MONTE CARLO INVESTIGATIONS OF THE EFFECT OF SKIN PIGMENTATION ON PULSE OXIMETER ACCURACY

By

Raghda Al-Halawani

A thesis submitted for the degree of Doctor of Philosophy

Supervisors: Professor Panicos Kyriacou and Dr Meha Qassem

School of Science and Technology

Research Centre for Biomedical Engineering

City St George's, University of London

2025

DECLARATION

I sincerely declare that the dissertation presented here is solely my own work, conducted in strict adherence to the regulations outlined by City St George's, University of London. All references to textbooks, theses, and published materials subject to copyright are cited, with careful acknowledgment of the title and authors. In cases where collaborative work has been completed, due credit has been provided to the respective collaborator(s). The content within the dissertation is entirely original and has not been previously submitted, either in whole or in part, for the fulfilment of any academic or professional degree.

I hereby authorise the Librarian at City St George's, University of London, to exercise discretion in permitting partial or complete reproduction of the thesis without requiring additional consent from the author. This authorisation extends solely to the creation of single copies intended for study purposes, with the understanding that proper acknowledgment will be maintained as a standard practice.

SIGNED: RAGHDA AL-HALAWANI

I dedicate this thesis to my mother, Mona Abou Yousef, and my father, Dr. Sami Al-Halawani.

ACKNOWLEDGEMENTS

I would like to start by thanking my supervisors Professor Panicos Kyriacou and Dr Meha Qassem, whose unwavering guidance, support, and contributions to this work have been invaluable. Their mentorship, which extended beyond technical aspects, encouragement, and inspiring stories are amongst many things that have helped me grow on a personal and professional level. My time and experience in the research centre have been truly fulfilling, as it not only allowed me to achieve a PhD, but also experience being a researcher beyond the laboratory setting. With them, I would like to extend my thanks to Dr James May, who has also played a crucial role in part of my academic journey with his invaluable support and assistance.

I would also like to express my gratitude for my friends in the RCBE lab. The bond we have shared throughout the past years is something I will always treasure, and I will never forget the laughter and the time we have spent together, both in and out of the lab. You have all made this journey so special, thank you for being such a kind, supportive, and unforgettable team. Equally important are my friends outside of the lab, who always fill my life with joy and remind me that, like family, I can always count on them especially in stressful times.

Without a doubt, I could not have completed this milestone without my incredible support system. To my husband, Ahmed, for pushing me to persevere in times of struggle, for lifting me up when I could not see the light at the end of the tunnel, and for always believing in me. To my nephews and nieces, who always inspire me to be a better role model, and to my sisters, Rouda, Rouba, and Roua, who have been my greatest cheerleaders from near or far in every opportunity I have embraced. By the grace of Allah, I have felt the presence of my parents through you all when I needed their comfort.

Mama and Baba (Senior Dr. Al-Halawani). Even though you are not here with me physically, I know you are always watching over me. Everything I have achieved is built on the foundation you gave me, so I know that I would not be where I am today without you. For that, I am forever thankful. I love you both so much.

ABSTRACT

Photoplethysmography (PPG) has been hailed as a non-invasive and low-cost optical measurement technique. It is used for a wide range of applications in clinical settings and wearable devices by monitoring the pulsations associated with changes in blood volume in a peripheral vascular bed. However, one unresolved limitation of PPG is the effect of skin pigmentation on the signal and its impact on pulse oximetry. While this phenomenon was first revealed in the 1980s, numerous publications since the COVID-19 pandemic have led this topic to resurface. The causes of discrepancies found in oxygen saturation measurement by pulse oximetry (SpO2), specifically its overestimation of true SaO2 in individuals with darker skin, are still unclear and require further research.

The interchangeable relationship between in vivo and in-silico studies supports the utilisation of Monte Carlo (MC) models, a computational tool which has been extensively used to predict and analyse the optical interactions within multiple tissue layers. Hence, this thesis focuses on presenting several novel MC models, which simulate different skin pigmentations in the finger. Different optical parameters are predicted and used to quantify the effect of skin pigmentation on the PPG output. The first model examines melanin concentration in the visible range in the epidermis, which is then expanded to include a multilayer finger model in both reflectance and transmittance modes. The third model evaluates the impact of melanin on simulated pulse oximeter calibration algorithms, and finally, simulations of PPG signals are presented. Overall, the computational results show that skin pigmentation may influence a range of optical parameters, with some more significantly than others. Most importantly, the simulations qualitatively reproduced the overestimation of SaO2 as pigmentation increased, highlighting that a one-algorithm-fits-all approach may not be suitable. Software-based corrective measures may be required to minimise SpO2 bias between populations.

Table of Contents

List of Symbols and Acronyms

n	Refractive index
λ	Wavelength
μ_a	Absorption coefficient
μ_s	Scattering coefficient
μ_t	Attenuation coefficient
t	Tissue thickness
s	Source-detector separation
nm	Nanometres
mm^{-1}	Per millimetre
g	Anisotropy factor
NA	Numerical aperture
φ	Azimuthal angle
θ	Angle of deflection
u_x, u_y, u_z	Direction cosines with respect to the x, y, and z axes
x, y, z	Cartesian coordinates
ε	Molar extinction coefficient
C	Concentration
v_{mel}	Volume fraction of melanosomes
l	Photon step size
L	Photon pathlength
A	Absorbance
R	Reflectance
I_o	Incident light intensity
I_t	Transmitted light intensity
MC	Monte Carlo
DPF	Differential pathlength factor
PPG	Photoplethysmography
w	Photon weight
wa	Weight absorbed
ξ	Random number

List of Figures

List of Tables

List of Publications

• Journal publications

Kyriacou PA, Charlton PH, Al-Halawani R, Shelley KH. Inaccuracy of pulse oximetry with dark skin pigmentation: clinical implications and need for improvement. Br J Anaesth. 2023 Jan;130(1):e33-e36. doi: 10.1016/j.bja.2022.03.011. Epub 2022 Apr 14. PMID: 35430087.

Al-Halawani R, Charlton PH, Qassem M, Kyriacou PA. A review of the effect of skin pigmentation on pulse oximeter accuracy. Physiol Meas. 2023 Jun 1;44(5):05TR01. doi: 10.1088/1361-6579/acd51a. PMID: 37172609; PMCID: PMC10391744.

Al-Halawani R, Qassem M, Kyriacou PA. Monte Carlo simulation of the effect of melanin concentration on light-tissue interactions in transmittance and reflectance finger photoplethysmography. Sci Rep. 2024 Apr 8;14(1):8145. doi: 10.1038/s41598-024-58435-7. PMID: 38584229; PMCID: PMC10999454.

Gidado, I., Al-Halawani, R., Qassem, M. *et al.* Development and Analysis of a Multi-Wavelength Near-Infrared Sensor for Monitoring Skin Hydration and Validation Using Monte Carlo Simulation. *Photonic Sens* **14**, 240306 (2024). https://doi.org/10.1007/s13320-024-0719-z.

Al-Halawani R, Qassem M, Kyriacou PA. Monte Carlo simulation of the effect of melanin concentration on light-tissue interactions for transmittance pulse oximetry measurement. J Biomed Opt. 2024 Jun;29(Suppl 3):S33305. doi: 10.1117/1.JBO.29.S3.S33305. Epub 2024 Aug 13. PMID: 39139814; PMCID: PMC11321364.

Al-Halawani, R.; Qassem, M.; Kyriacou, P.A. Analysis of the Effect of Skin Pigmentation and Oxygen Saturation on Monte Carlo-Simulated Reflectance Photoplethysmography Signals. *Sensors* **2025**, *25*, 372. https://doi.org/10.3390/s25020372

Al-Halawani, R.; Qassem, M.; Kyriacou, P.A. Monte Carlo Simulation of the Effect of Melanin Concentration on Light–Tissue Interactions in Reflectance Pulse Oximetry. *Sensors* **2025**, *25*, 559. https://doi.org/10.3390/s25020559

- **Conference proceedings**

Al-Halawani R, Chatterjee S, Kyriacou PA. "Monte Carlo Simulation of the Effect of Human Skin Melanin in Light-Tissue Interactions." 2022 44th Annual International Conference of the IEEE Engineering in Medicine & Biology Society (EMBC) (2022): 1598-1601.

Al-Halawani, R., Qassem, M., May, J.M., Kyriacou, P.A. (2024). Monte Carlo Simulated Photoplethysmography Signals for the Validation of an in Vitro Wrist Phantom. In: Jarm, T., Šmerc, R., Mahnič-Kalamiza, S. (eds) 9th European Medical and Biological Engineering Conference. EMBEC 2024. IFMBE Proceedings, vol 113. Springer, Cham. https://doi.org/10.1007/978-3-031-61628-0_15

CHAPTER 1: INTRODUCTION

A pulse oximeter is a non-invasive and low-cost optical device, based on a two wavelength photoplethysmography (PPG) system, used for the continuous monitoring of arterial oxygenation. Pulse oximetry has been found to work on the finger, the ear, the bridge of the nose, the nasal septum, the temple over the temporal artery, and on the foot or palm in infants. Arterial oxygen saturation measurement plays a central role in the diagnosis of sleep-related respiratory disorders such as obstructive sleep apnoea (OSA), monitoring and treatment of respiratory diseases by detecting hypoxaemia, assisting the titration of supplemental oxygen treatment in preterm neonates, and many more [1]. Pulse oximetry is now routinely used in a wide range of clinical settings, ranging from hospital care to primary care to home monitoring [2-11]. It has shown to be an effective tool for identifying the need for hospitalisation in initially non-severe and possibly high-risk COVID-19 patients, or for discharging known or suspected COVID-19 patients [12-28] [12], [13], [14], [15], [16], [17], [18], [19], [20], [21], [22], [23], [24], [25], [26], [27], [28]. Hence, pulse oximetry is now widely used in clinical and consumer settings [23], underlining the need to ensure it is as accurate and reliable as possible. Figure 1-1 provides a succinct summary of the key events in the history of pulse oximeter technology.

However, there are rising concerns of the differing performance of pulse oximeters in patients with different skin pigmentations [17], [28-96]. While this concept is not new, its importance increased during the COVID-19 pandemic [18], since the deterioration of blood oxygenation is one of the primary symptoms of the virus in severe cases. The limitations of pulse oximetry, including the impact of ambient light, difficulties in obtaining measurements during low perfusion and motion, etc., are known [97] and guidance on how to minimise their effect is available [98]. However, the increased mortality rate amongst ethnic minority patients since 2020 from the COVID-19 outbreak has raised the question of whether differential accuracy of pulse oximetry due to skin pigmentation may be a contributing factor to this health inequality. Consequently, this thesis sets to explore how this issue can be addressed computationally.

1851: Beer-Lambert law [99].

1864: Georg Gabriel Stokes discovers a pigment that is the oxygen carrier in blood [100].

1864: Felix Hoppe-Seyler purifies the pigment and calls it haemoglobin [101].

1887-90: Carl Gustav Hufner studies absorption spectra of haemoglobin [102].

1931: Ludwig Nicolai investigates the quantitative spectrophotometry of light transmitted through human tissues [103].

1934: Kurt Kramer (1906-85) makes precise measurements of the oxygen saturation of blood flowing through cuvettes [104].

1939-45: World War II: great military interest in oximetry in pilots at high altitude [105].

1940: JR Squire passes red and infrared light through the finger web for the continuous monitoring of oxygenation; it requires compression of tissues to create a bloodless field for calibration [106].

1940-42: Glen Millikan coins the term oximeter and develops the Millikan oximeter [107].

1948-50: Earl Wood develops Wood's ear oximeter [108].

1964: Robert Shaw develops the eight-wavelength ear oximeter [105].

1970: Hewlett-Packard market the eight-wavelength ear oximeter [105].

1971: Takuo Aoyagi uses the pulsatility of the absorption signal to separate absorption due to the arterial blood from that of other tissues [105].

1974: Aoyagi develops the prototype pulse oximeter using incandescent light source, filters, and analogue electronics [109].

1975: First commercially available pulse oximeter [110].

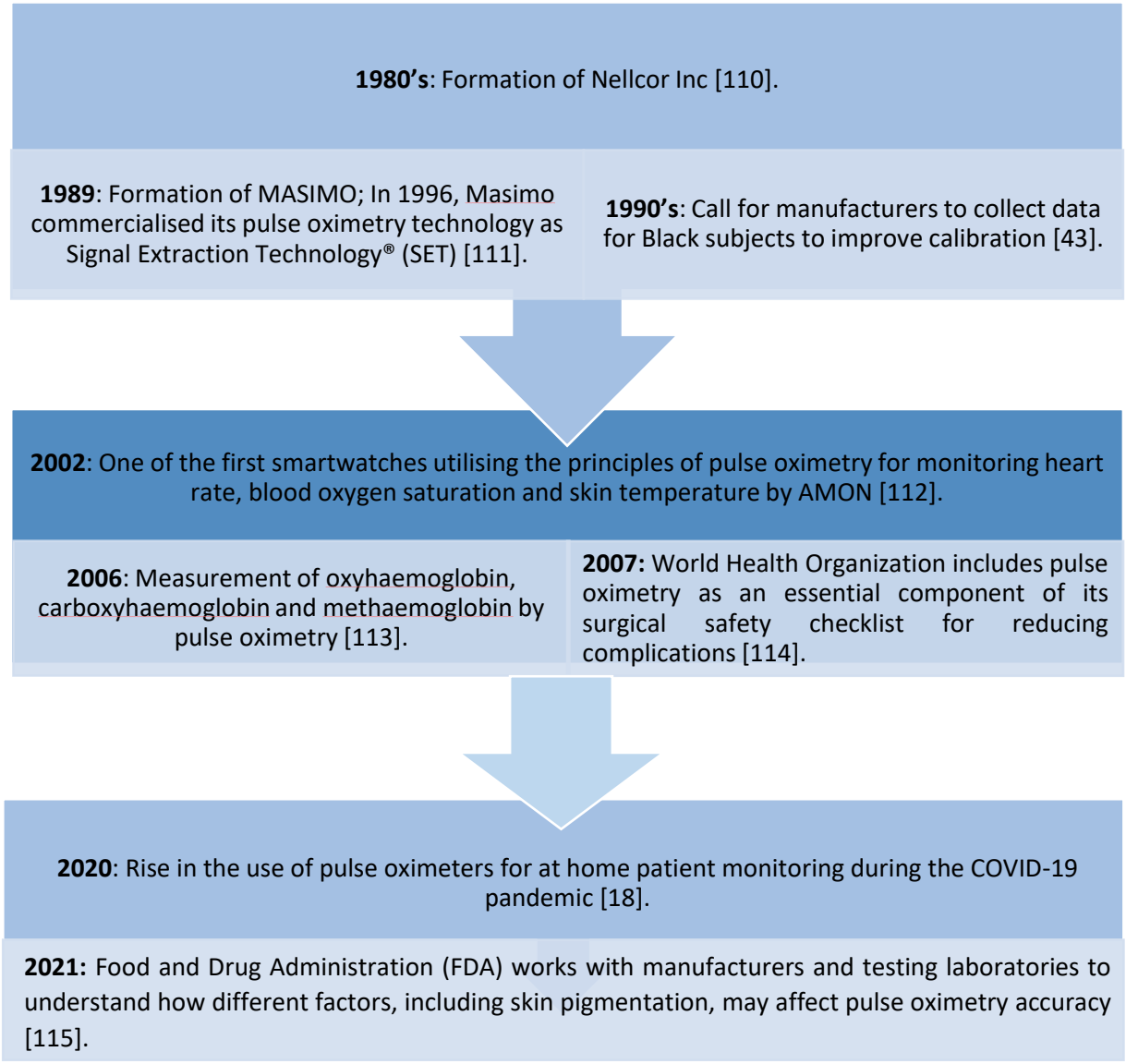

Figure 1-1. Key events in the history of pulse oximeter technology.

1.1. Aims and Objectives

The primary aim of this project is to investigate the complex light-tissue interactions in pulse oximetry and PPG, firstly by focusing on how varying melanin concentrations in the epidermis influence these interactions. By developing a detailed and novel computational model in MATLAB, this project seeks to determine if adjustments in sensor specifications or calibration algorithms are necessary to ensure more accurate readings across diverse skin pigmentation levels. An integral part of this investigation is the creation of a fully functional three-dimensional (3D) and validated Monte Carlo (MC) simulation to model photon migration and analyse various and relevant optical parameters of interest. After that, the model will aim to provide a more realistic representation of light-tissue interactions by simulating a human finger at different melanin concentrations, wavelengths, and PPG sensor configurations, incorporating all relevant layers and main physiological constituents. This framework leads to further studies exploring the combined effect of oxygen saturation and melanin concentration on light-tissue interactions for pulse oximetry in both transmittance and reflectance PPG modes utilising red (660 nm) and infrared (940 nm) wavelengths. Calibration curves will be generated to understand the impact of these confounding factors on pulse oximeter algorithms across different skin types, particularly light, moderate, and dark skin, and to analyse how bias magnitude varies between them. Lastly, this thesis will present its most novel study examining the impact of skin pigmentation on Monte Carlo simulated PPG signals, with a focus on how pigmentation affects key PPG signal characteristics. Overall, this work sets to determine whether software and post-processing adjustments are required in current pulse oximeters to accommodate for accurate physiological monitoring irrespective of skin pigmentation, and to promote inclusive engineering practises in healthcare.

1.2. Contributions to research

In pursuing these aims and objectives, this thesis makes several novel contributions that extend both the methodological foundations of biomedical optics modelling using the MC technique and the practical understanding of pigmentation-related bias in pulse oximetry:

a) **Development of a novel computational foundation model** – The validated 3D Monte Carlo framework provides a versatile platform that can be adapted for a wide range of

biomedical optics applications beyond pulse oximetry, enabling controlled investigations of light–tissue interactions in complex multilayered structures.

b) **Isolated study of melanin's optical role** – A controlled approach to allow a clearer interpretation of melanin's contribution to measurement bias irrespective of other confounding factors under different sensor configurations.

c) **Wavelength-specific insights into SpO_2 estimation** – A detailed analysis of optical parameters at red and infrared wavelengths, with direct implications for the ratio-of-ratios method used in pulse oximetry. This enables an improved understanding of how pigmentation-dependent attenuation alters SpO_2 accuracy across different skin tones.

d) **Implications for pulse oximeter algorithms** – Results highlight the need for recalibration or post-processing adjustments in current algorithms to mitigate skin pigmentation bias.

e) **Novel integration of epidermal optical properties, elastic properties of blood vessels, and simulation of PPG signals** – For the first time, the model generates PPG signals using the MC technique by implementing more realistic epidermal optical properties using L*a*b* characterisation, and the elastic deformation of custom-made arterial vessel channels in the dermis.

1.3. Thesis outline

Chapter 1: Introduction

This chapter provides an overview of the key events in pulse oximetry. With an expanded role in assessing and monitoring COVID-19 patients, concerns regarding its accuracy in patients with different skin pigmentation levels are highlighted to identify the key motivation of this thesis. The aims and objectives of the thesis are also outlined to provide an overall scope of the work presented.

Chapter 2: Tissue Optics and Mechanisms of Light-Tissue Interactions

This chapter outlines the mechanisms of light-tissue interactions, including absorption, scattering, reflection, and transmission, to establish a foundational understanding of how light behaves within biological tissue. It also presents the mathematical equations governing these mechanisms for bio-optical modelling, along with key principles such as Snell's law, the Beer-Lambert Law (BLL) and its modified form (MBLL).

Chapter 3: Background Physiology: Skin Pigmentation

This chapter delves into the physiological basis of skin pigmentation, focusing on the interplay of biological factors such as melanin, keratin, carotene, and haemoglobin, which collectively form skin's colour and appearance. Several factors affecting skin pigmentation and the concentration and distribution of melanin is discussed, including its impact on light absorption and scattering and hence, the optical properties of the epidermis.

Chapter 4: The Principles and Limitations of Pulse Oximetry

This chapter explores the principles, methods, and limitations of pulse oximetry, including the operating wavelengths and modalities. Although pulse oximeters have largely replaced blood gas analysis, its limitations are critically examined, including its susceptibility to interference from external light, movement, poor perfusion, etc., that may distort readings. These limitations underscore the need for empirical calibration and careful interpretation of SpO_2 readings amongst different skin types.

Chapter 5: The Effect of Skin Pigmentation on Pulse Oximeter Accuracy

This chapter examines how skin pigmentation has influenced the accuracy of pulse oximetry from retrospective and prospective studies through a literature review search across several databases. Most studies reveal a consistent overestimation of SpO_2 in darker-skinned individuals and higher prevalence of occult hypoxemia in comparison to lightly skinned individuals. Additionally, the chapter discusses methodological limitations in pulse oximeter studies, including inconsistent standards for classifying skin pigmentation and underrepresentation of darker-skinned subjects, which reduce statistical certainty.

Chapter 6: Modelling Skin Pigmentation using the Monte Carlo technique

This chapter offers a comprehensive literature review of the use of Monte Carlo technique for modelling skin pigmentation. It examines the different methodologies employed across various medical applications, providing insights that will guide the modelling approach used in this thesis.

Chapter 7: Development of the Monte Carlo Model

This chapter outlines the foundational methodology employed in the subsequent studies, detailing the step-by-step process of developing the Monte Carlo model with a specific focus on the human finger as the primary anatomical region of interest. It also includes the optical properties of each layer in the model, enabling the simulation of light-tissue interactions across visible and near-infrared wavelengths. Whilst the majority of the steps discussed here remain consistent across all the studies presented in this thesis, some modifications to this methodology are noted in their respective chapters.

Chapter 8: Monte Carlo Simulation of the Effect of Human Skin Melanin on Light-Tissue Interactions Using a Monolayer Skin Model

In this chapter, a monolayer Monte Carlo model is developed to first explore the light-tissue interactions in the epidermis, which is the skin layer responsible for characterising skin pigmentation. Three wavelengths, specifically blue, green, and red are simulated to analyse the impact of light absorption by different concentrations of melanin in the visible range.

Chapter 9: Monte Carlo Simulation of the Effect of Melanin Concentration on Light-Tissue Interactions in Transmittance and Reflectance Finger Photoplethysmography

This chapter presents an investigation into the influence of melanin concentration on light-tissue interactions within a multi-layered finger model with light, moderate, and dark epidermis. The study aims to provide foundational insights into how melanin alone impacts

key optical parameters including absorbance, detected intensity, optical pathlength, and penetration depth at 660 nm and 940 nm in transmittance and reflectance modes.

Chapter 10: Monte Carlo Simulation of the Effect of Melanin Concentration on Light-Tissue Interactions for Transmittance and Reflectance Pulse Oximetry Measurement

This chapter examines the impact of melanin concentration on pulse oximetry through a Monte Carlo simulation in transmittance and reflectance modes. Some optical parameters are used to calculate the ratio between pulsatile and non-pulsatile light absorbance at 660 nm and 940 nm. Monte Carlo simulated calibration curves are plotted for light, moderate, and dark skin, showing notable differences in pulse oximeter algorithms based on skin type. The study recommends the necessity for tailored calibration algorithms particularly with the rising use pulse oximeters at home and consumer wearables.

Chapter 11: Monte Carlo Simulated Photoplethysmography Signals

This chapter presents a preliminary study to generate Monte Carlo simulated PPG signals based on an in vitro wrist phantom set up. The methodology includes the development of a wrist phantom using SolidWorks and MATLAB, with optical properties characterised using spectrophotometry and mechanical properties derived to simulate changes in blood pressure. This study guides the methodology for assessing the effect of skin pigmentation on MC-simulated finger PPG signals more accurately than previous studies due to advances anatomical structure and optical characterisation.

Chapter 12: Analysis of the Effect of Skin Pigmentation on Simulated Transmittance and Reflectance Photoplethysmography Signals using the Monte Carlo Technique

This chapter investigates the impact of skin pigmentation on Monte Carlo-simulated PPG signals in transmittance and reflectance mode. This study fills a gap in existing research by directly analysing how skin pigmentation affects PPG signal characteristics prior to calibration processing. A further innovation in this study is the advancement in skin pigmentation modelling through spectrophotometrically derived optical properties, replacing analytical

equations and values extracted from the literature as shown in other studies. This approach aims to strengthen the accuracy and relevance of findings related to the influence of skin pigmentation on PPG signals.

Chapter 13: Discussions & Conclusions

This chapter discusses the results from all studies presented in this thesis, highlighting the key findings from the Monte Carlo simulations on the impact of skin pigmentation on PPG signals and pulse oximeter accuracy. The studies show the necessity of considering skin pigmentation in device calibration to improve diagnostic reliability. Additionally, the chapter acknowledges the limitations of the model and suggests areas for future research to enhance the equity of healthcare technologies.

CHAPTER 2: TISSUE OPTICS AND MECHANISMS OF LIGHT-TISSUE INTERACTIONS

The core principles of the work presented in this thesis focuses on utilising light to obtain quantitative and qualitative information related to our health. Light spans a broad spectrum of wavelengths, each serving their own purpose in biological and medical applications by interacting uniquely with tissue (Figure 2-1). Different wavelengths exhibit distinct behaviours due to variations in reflection, absorption, and scattering. For instance, shorter wavelengths such as ultraviolet (UV), blue, and green light are strongly absorbed by superficial components such as melanin and other epidermal proteins, resulting in limited penetration into deeper layers [99]. Conversely, longer wavelengths in the red and near-infrared (NIR) regions experience lower absorption by these chromophores, allowing them to penetrate more deeply into tissue [100]. These wavelength-dependent interactions form the basis for numerous medical and optical applications, including pulse oximetry [101], phototherapy [102], tissue imaging [103], etc., enabling selective targeting of specific tissue layers or components. Therefore, understanding how light interacts with biological tissue is essential for making informed decisions to achieve the desired output.

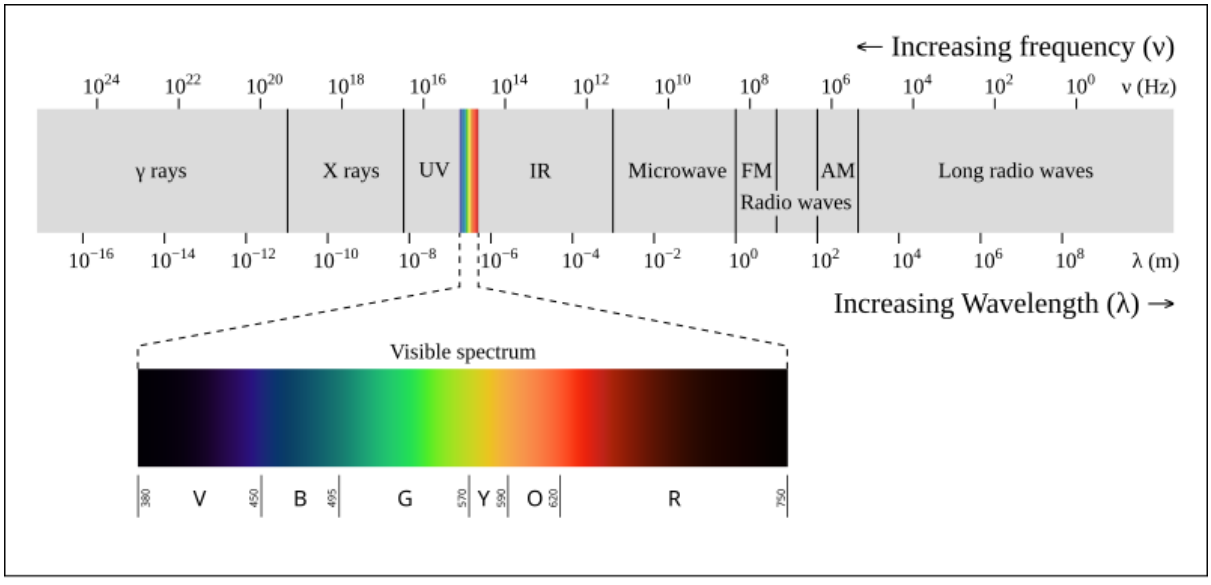

Figure 2-1. Electromagnetic spectrum with wavelength and frequency bands. Extracted from [121].

2.1. Reflection

When light interacts with biological tissues, it can undergo two main types of reflection, including specular reflection and diffuse reflection. Firstly, specular reflection occurs when light strikes at an angle on a smooth surface such as the outermost layer of the skin, and is reflected at an equal but opposite angle. This phenomenon, described by the law of reflection, was formally documented by the Greek philosopher Euclid around 300 BC in his book *Catoptrics* [104], which states that the angle of incidence (θ_i) equals the angle of reflection (θ_r). Specular reflection is closely related to Fresnel reflection which occurs at the boundary between two media with different refractive indices (n) and describes the fraction of light that is reflected rather than transmitted, depending on the angle of incidence and the refractive indices of the media. The remaining light, which is the reflected intensity subtracted from the intensity of light (equal to unity) is then refracted (or transmitted) to the other medium. The angle of refraction (or transmission, θ_t) is determined by Snell's law, which was introduced by the Dutch mathematician and physicist Willebrord Snellius in 1621 [105]. The law dictates how light bends when propagating between media with different refractive indices by demonstrating that ratio of the sine of the angles of incidence and transmission is equal to the ratio of the refractive indices of the materials at the interface [106] (Figure 2-2):

$$n_{air} \sin \theta_i = n_{tissue} \sin \theta_t \quad (2\text{-}1)$$

The amount of light that is reflected is determined by the reflection coefficient (R). When light of any wavelength is incident at any angle below or above 90°, the reflection coefficient is given by [106]:

$$R = \left| \frac{n_i \cos \theta_i - n_t \cos \theta_t}{n_i \cos \theta_i + n_t \cos \theta_t} \right|^2 \quad (2\text{-}2)$$

However, when light is incident perpendicularly to the tissue surface, the reflection coefficient, simplifies to [106]:

$$R_n = \left(\frac{n_i - n_t}{n_i + n_t} \right)^2 \quad (2\text{-}3)$$

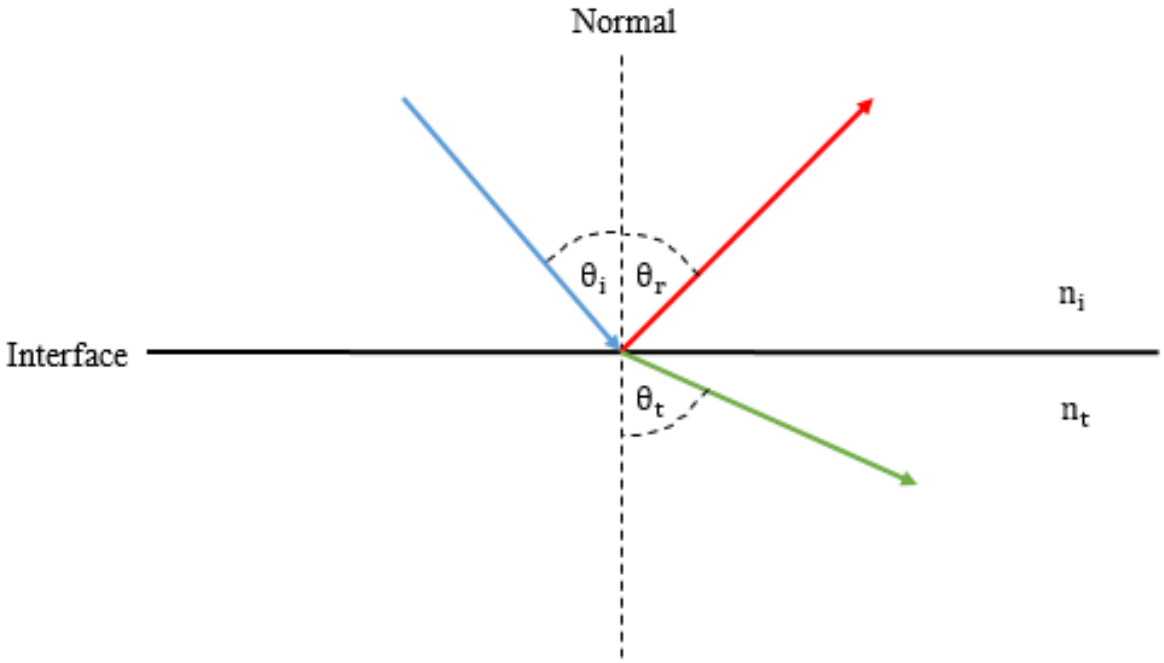

Figure 2-2. Diagrammatic representation of Snell's law, with incident ray (blue), reflected ray (red), and refracted ray (green), with their respective angle relative to the normal. The first medium is characterised by the refractive index $\boldsymbol{n_i}$, and the second medium by $\boldsymbol{n_t}$.

Another type of reflection is diffuse reflection, which occurs when light interacts with a rough or irregular surface, causing it to scatter in multiple directions. Biological tissues are inherently heterogeneous, with complex structures such as collagen fibres, cellular matrices, and blood vessels, which contribute to this form of reflection. Diffuse reflection is measured using diffuse reflectance spectroscopy, where the intensity of reflected light across wavelengths is analysed using a spectrophotometer. This data provides insights into tissue properties such as absorption and scattering coefficients (μ_a, μ_s).

Additionally, light interacting with tissue can be partially absorbed by chromophores before being reflected, which alters its intensity and spectral composition. In biological tissues, Fresnel reflection is particularly significant at interfaces such as the skin-air boundary or within layered tissue structures. The interplay of specular reflection, diffuse reflection, and Fresnel reflection contributes to the overall light-tissue interaction, enabling diagnostic techniques such as reflectance spectroscopy and Laser Doppler Flowmetry (LDF) to extract tissue-specific optical properties.

2.2.Absorption and the Beer Lambert Law

The principles governing light propagation through a medium was first introduced by Pierre Bouguer in 1729 [1]. He introduced the concept that light loses intensity as it propagates through a medium, with this attenuation being proportional to the pathlength of the light within the medium. Although Bouguer did not explicitly formulate a law, his observations laid the groundwork for understanding how the medium's properties and the distance travelled by light influence its intensity. This proportional relationship was later refined and formalised by Johann Heinrich Lambert, who expanded on Bouguer's findings in 1760 [107].

August Beer expanded on Bouguer's and Lambert's findings by introducing a relationship between light attenuation and the concentration of absorbing substances in a solution. In 1852, Beer demonstrated that the transmittance of light through a solution remains constant as long as the product of the solution's concentration and the optical pathlength remains unchanged. He quantified how the amount of light absorbed by a medium is directly proportional to the concentration of the absorbing molecules, establishing a key link between chemical composition and optical properties. This addition complemented Lambert's earlier work, leading to the combined Beer Lambert Law (BLL), which mathematically describes absorbance as a function of both the absorber's concentration (C), absorption per mole (ε) and the medium's thickness (d) [107]:

$$A = \varepsilon\, C\, d = \mu_a\, d \tag{2-4}$$

The light that is transmitted and detected by the photodetector after travelling through the medium is calculated [107] (Figure 2-3):

$$I_t = I_0 e^{(-\varepsilon C d)} = I_0 e^{(-\mu_a d)} \tag{2-5}$$

Where I_t = transmitted intensity, and I_0 = incident intensity. Absorbance (A) can also be derived by taking the negative logarithm of transmittance (T), which is given by the ratio of transmitted to incident intensity [107]:

$$A = -\log\left({}^{I_t}/_{I_0}\right) = -\log(T) \tag{2-6}$$

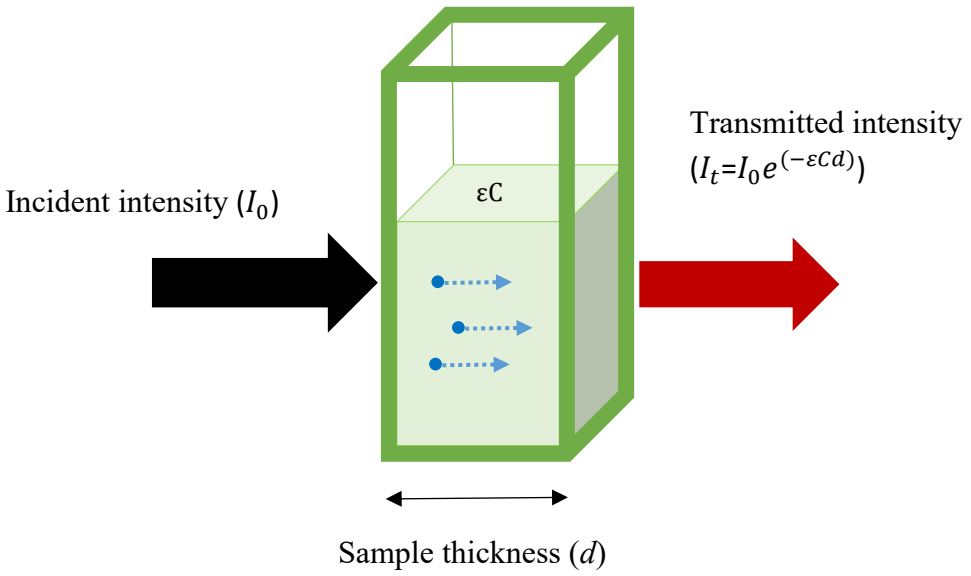

Figure 2-3. Diagrammatic representation of light transmission in a solution with a given molarity and concentration. Light enters the medium and travels a distance equivalent to the thickness of the medium under the generic Beer Lambert law (absorbing only medium).

All tissue chromophores can absorb a certain number of photons per unit distance as characterised by the absorption coefficient (μ_a), which is wavelength dependant. In biological tissues, light absorption occurs through radiative and/or non-radiative processes, each playing a distinct role in how tissues interact with light and convert its energy. Firstly, radiative absorption involves the excitation of a molecule to a higher energy state followed by the re-emission of energy as light. This process occurs in fluorescence and phosphorescence, where absorbed photons cause certain chromophores to emit light of a longer wavelength. Fluorescence imaging leverages this principle to highlight specific biological components or detect metabolic activity in tissues. Hence, they are particularly useful in diagnostic imaging because the emitted light provides information about the molecular composition and environment of the tissue. Non-radiative absorption, on the other hand, involves the dissipation of absorbed light energy through mechanisms other than light emission. In tissues, this energy is primarily converted into heat through vibrational relaxation or transferred to nearby molecules through collisional processes [108]. For example, water and lipids absorb light in the infrared range and convert it to heat, which can be utilised in therapeutic applications such as hyperthermia to treat certain pathologies [109]. Similarly, melanin dissipates energy non-radioactively when it absorbs UV or visible light to protect deeper tissues from damage.

2.3.Scattering and Modified Beer Lambert Law

In the context of biological applications, the Beer Lambert law is often modified to account for scattering effects in turbid media like tissue. David Delpy et al. [110] adapted this law to account for light scattering in biological tissues, resulting in the Modified Beer Lambert Law (MBLL). This updated formulation forms the foundation of many optical techniques, including spectrophotometry, photoplethysmography, etc, as they are required for understanding changes in intensity in highly scattering media. As a result the simplified form of the MBLL equation is given by [107]:

$$A = \varepsilon\, C\, L + G = \mu_a\, L + G \tag{2-7}$$

In this case, the G-value is a parameter that quantifies the light loss due to scattering. It accounts for the effects of scattering that alter the pathlength (L) due to the continuous redirection of light as it travels through the tissue. In practical terms, G is a constant or parameter that can be determined for specific tissues or experimental setups by measuring total attenuation in a sample using diffuse reflectance spectroscopy, separating the absorption contribution, and attributing the remainder to scattering loses. A larger G-value may indicate greater scattering, leading to more light loss, while a smaller G-value suggests that scattering effects are less significant.

To model the angular distribution of photons based on their tendency to travel in a particular direction requires the implementation of the Henyey-Greenstein phase function. This function is used to describe the relationship between the angle of deflection and the anisotropic factor (g) which determines photon directionality and ranges between -1 and 1. The equation is given by [111]:

$$\mathrm{p}(\cos\theta) = \frac{1-\mathrm{g}^2}{4\pi(1-2\mathrm{g}\cos\theta+\mathrm{g}^2)^{\frac{3}{2}}} \tag{2-8}$$

When g = -1, backscattering occurs. Rayleigh scattering occurs when g = 0 because it is isotropic, meaning that photons are deflected equally in all directions. However, when g ≅ 1, scattering is anisotropic, which results in Mie scattering, and so deflections occur in a more forward direction.

Additionally, the optical pathlength here is denoted by *L* as photons do not follow a straight path whilst travelling through a highly scattering medium. Hence, the distance that the photons

travel is not equal to the thickness of the medium (d) as explained in the formula of the Beer Lambert Law in its generic form. The relationship between these two quantities is quantified by the differential pathlength factor (DPF), a unitless parameter which calculates the ratio between the physical pathlength (d) and the geometrical pathlength (L) [107] (Figure 2-4):

$$DPF = L / d \tag{2-9}$$

When DPF = 1, the equation is reduced to L = d (BLL), however when DPF > 1, this implies that L > d (MBLL).

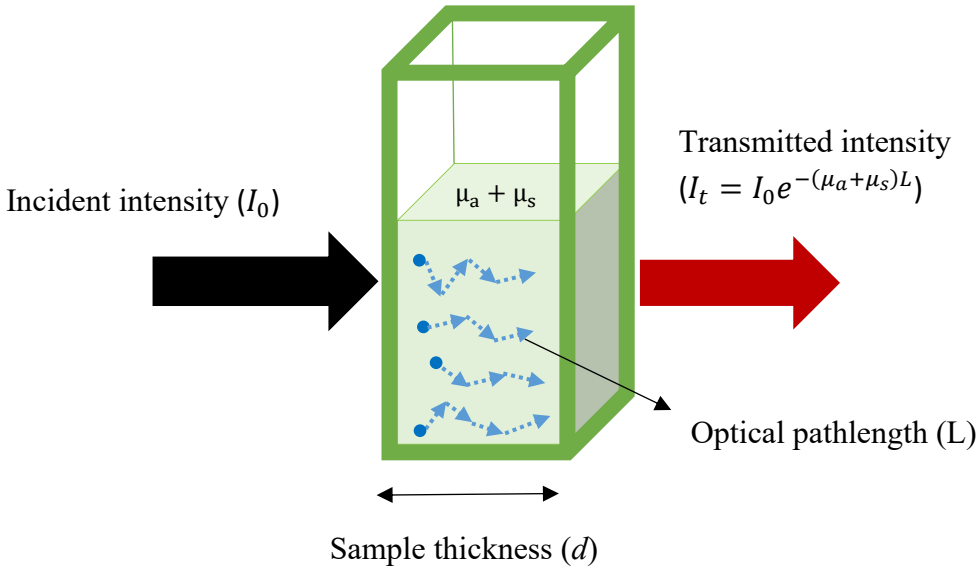

Figure 2-4. Diagrammatic representation of light transmission in a highly scattering medium, which is characterised by the absorption and scattering coefficient. The light travels in random directions until it is detected, causing the optical pathlength to exceed the thickness of the medium.

Similar to the absorption coefficient, the scattering coefficient (μ_s) defines the number of scattering events per unit distance, and is also wavelength dependant. As previously mentioned, Rayleigh and Mie scattering are two types of scattering which occur based on the particle size of the structures within the tissue relative to wavelength. Rayleigh scattering occurs when light interacts with particles much smaller than its wavelength, such as molecules or small organelles [112]. It is more pronounced at shorter wavelengths (e.g., blue light) [113] as the intensity of scattering is inversely proportional to the fourth power of the wavelength. It will become evident in this thesis how Rayleigh scattering plays a negligible role compared to other scattering mechanisms of photons due to the choice of wavelengths utilised in the studies.

Moreover, the most dominant scattering in biological tissue is known as Mie scattering, which occurs when the scattering particles are similar in size to the wavelength of light [112]. Unlike Rayleigh scattering, Mie scattering does not strongly favour shorter wavelengths and instead can scatter light across a wide range of angles (Figure 2-5). This is essential as light behaves in an anisotropic manner in tissue, especially at longer wavelengths.

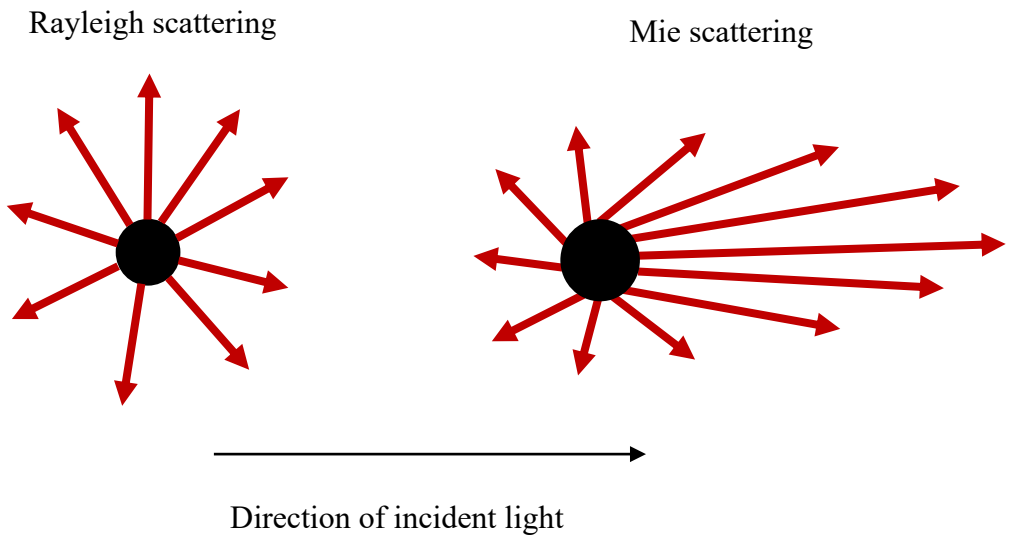

Figure 2-5. Diagrammatic representation of the directionality of photons during Rayleigh and Mie scattering.

2.4.Summary

This chapter has discussed the different mechanisms driving the interactions of light with biological tissues, focusing on how light absorption, reflection, and scattering and their types affect bio-optical processes. Light of different wavelengths interact with tissues in distinct ways and offer advantages in different medical applications depending on the smoothness or roughness of the tissue, the concentration of certain chromophores and the level of heterogeneity. As outlined, these mechanisms are governed by well-known laws in the field of optics such as Snell's law, the Beer-Lambert Law and its modified form.

CHAPTER 3: BACKGROUND PHYSIOLOGY: SKIN PIGMENTATION

Skin pigmentation is determined by the type, quantity, and distribution of melanin, a natural pigment which plays a primary role in defining skin colour [114]. The key microstructures involved in melanin synthesis include melanocytes, melanosomes, and keratinocytes, all of which contribute to pigmentation and skin protection. The following subsections provide an in-depth explanation of each of these terms, other factors affecting skin pigmentation, its effect on the optical properties of the epidermis, and the current methods used to measure skin pigmentation.

3.1.The production of human skin pigmentation

Upon exposure to stimuli such as UV radiation or changes in hormone levels including thyroxin, oestrogen, etc., melanocytes, which are specialised cells in the basal layer of the epidermis, respond by producing melanin. The pigment is synthesised via an enzymatic pathway involving tyrosinase, which converts the amino acid tyrosine into melanin [115]. There are two main types of melanin: eumelanin, which produces brown to black pigmentation and offers strong UV protection, and pheomelanin, which produces yellow to reddish hues and provides less UV protection [116]. The synthesis and regulation of melanin are influenced by genetic and environmental factors which makes skin colour either constitutive or facultative, respectively.

Moreover, melanosomes are organelles within melanocytes which store and transport melanin after it is synthesised to nearby keratinocytes. These organelles undergo maturation, gradually accumulating melanin through a cellular process of exocytosis and phagocytosis. Exocytosis involves the releasing of melanosomes from the melanocyte, and phagocytosis involves the absorption of the melanosomes by keratinocytes [117]. The melanin in these melanosomes is distributed throughout the epidermis, where it forms a protective shield around the nuclei of the keratinocytes to protect them from UV-induced DNA damage and influences the appearance of visible skin colour.

As keratinocytes proliferate through mitosis (cell division) in the basal layer, they migrate upwards towards the surface of the skin. During this process, the keratinocytes undergo a series of changes in structure and function, also known as differentiation. These changes include the accumulation of keratin, a protein that strengthens the skin, as well as the absorption of melanin

from the melanocytes. As keratinocytes move towards the skin's surface, they become flattened and eventually die, forming the stratum corneum, the outermost protective layer of dead cells, known as corneocytes. This final layer acts as a durable barrier, preventing harmful pathogens from entering the body and reducing water loss [116], [118].

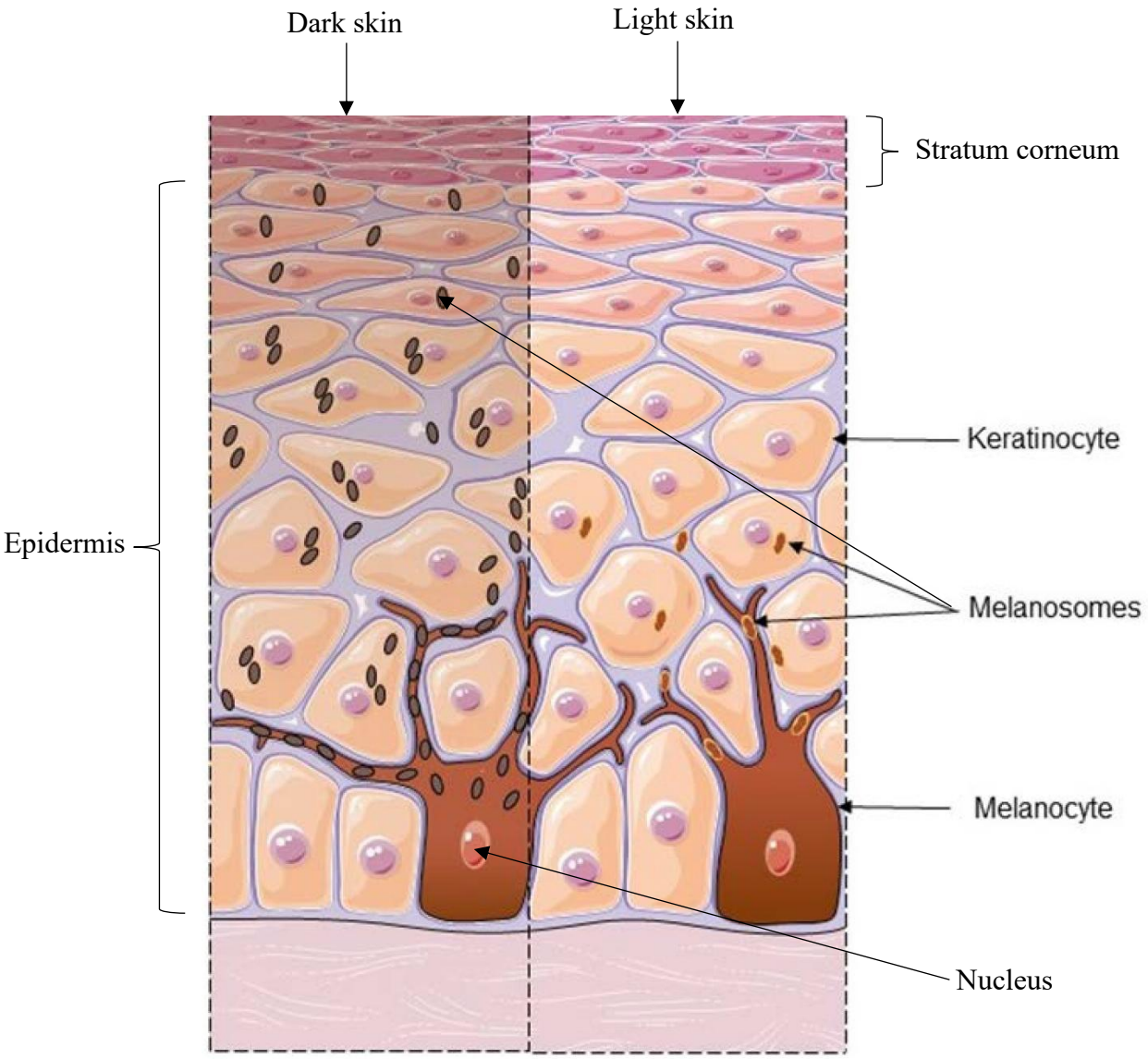

Figure 3-1. Structural components in the epidermis contributing to skin pigmentation in light and dark skin. Adapted from [137]**.**

3.2. Determinants of skin pigmentation and appearance and its influence on the optical properties skin

Skin is the largest, most highly complex organ, and its colour and appearance are influenced by several factors. In addition to the presence of melanin and keratin, carotene, haemoglobin, and other characteristics that differ with race such as hydration, texture, and homogeneity, also play a role in how we see skin colour. For example, carotene is a pigment stored in the stratum corneum of the skin, and while it does not directly affect melanin production, it can alter the skin's appearance by adding a subtle yellow-orange hue, especially in moderate skin tones [119]. Similarly, haemoglobin affects skin colour appearance primarily by influencing the redness or pinkish hue of the skin, depending on the level of oxygen in the blood and the proximity of blood vessels to the skin surface especially in lighter skin tones. The number of melanocytes does not account for the differences in skin colour, but rather, it is the variation in size, quantity, location, and distribution of melanosomes that contributes to the formation of skin colour [120], [121], [122]. In lighter skin, melanosomes are smaller, found in clusters, degrade more quickly relative to more pigmented skin [123], and are synthesised in very acidic conditions [124], [125], [126]. Contrastingly, melanosomes are larger, more dispersed along the basal layer, and synthesise at a higher pH of 6.8 in darkly pigmented skin [123].

As previously mentioned, natural melanin levels are determined by genetics, but can be influenced by quality of life, hormones, extrinsic and intrinsic aging, and skin pigment disorders, all of which alter the absorption coefficient and scattering coefficient of skin over time. The human skin is made up of multiple layers, each with their own distinctive optical properties that govern the absorption and scattering mechanisms of light. Depending on the subject, it is important to select an appropriate measurement site to obtain reliable bio-optical data [127]. This may differ from one patient to another, especially for those with dark skin pigmentation, as they are more prone to post-inflammatory hypopigmentation or hyperpigmentation relative to individuals with lighter skin [128]. Additionally, the colour of the nail bed in a Black person is much lighter than their skin, and so the behaviour of light through a finger using transmittance mode pulse oximetry may differ relative to the behaviour of light through a palm using reflectance mode pulse oximetry. Although skin pigmentation may appear evenly distributed to the human eye, it is not homogenous at the microscopic level. This variation makes selecting an appropriate measurement site particularly challenging with individuals who have skin pigmentation disorders, such as vitiligo or melasma.

The volume fraction of melanosomes in the epidermis layer of human skin ranges between 1% – 43% for very fair to very dark pigmentation, which in turn, represents a large variation in the average epidermal absorption coefficient [129]. It is important to note that these values would vary between subjects in the same skin pigmentation group, and that they also may not be entirely representative as such equations may be oversimplified. However, from a quantitative standpoint, these values may be indicative of the magnitude of the optical properties of the epidermis as melanin concentration varies. The absorption coefficient quantifies the extent to which photons are absorbed per unit distance within a medium. A higher absorption coefficient typically correlates with increased overall absorbance, as seen in individuals with darker skin due to greater melanin concentration. Although research on the absorption spectra of melanin across different concentrations is limited, one study measured natural melanin concentrations ranging from 0.1 to 0.8 g/L [130] (Figure 3-2). The results demonstrated significant absorption in the ultraviolet and blue light regions (200 nm – 400 nm), which gradually decreased across the visible spectrum toward red and near-infrared wavelengths. In this thesis, the primary focus is to explore the light-tissue interactions using red (660 nm) and near-infrared (940 nm) light sources, which are the most common wavelengths utilised in pulse oximetry. The data indicates that at higher melanin concentrations, absorption increases in the red spectrum, particularly at 0.8 g/L, while absorption in the near-infrared region remains relatively unaffected. These findings provide a foundational basis for interpreting the forthcoming Monte Carlo simulations of the finger model under varying epidermal melanin concentrations for the wavelengths of interest.

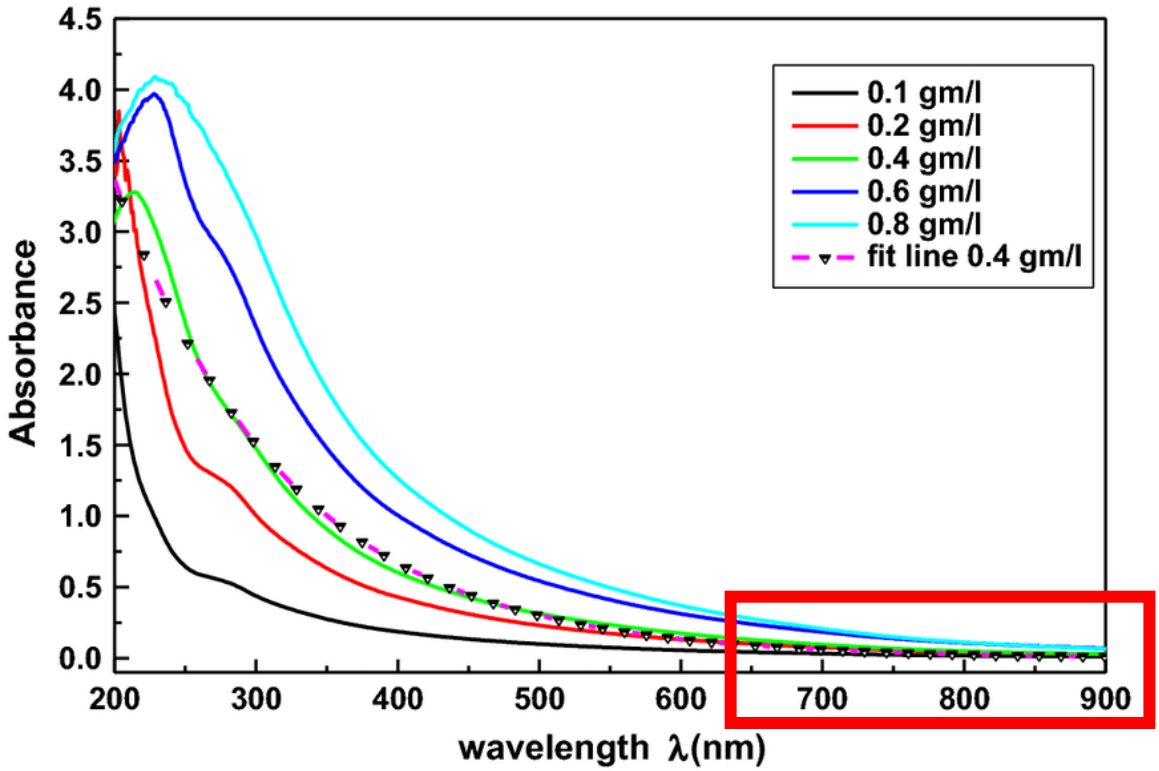

Figure 3-2. Absorbance spectra of different concentrations of synthetic melanin between 200 nm - 900 nm. The wavelength range of interest is highlighted by the red box. Adapted from [149].

Furthermore, the amount of light reflected from within or on the tissue surface contributes to the magnitude of light intensity output. As mentioned in Chapter 2.1, the amount of diffuse reflection that takes place is influenced by the optical and geometric properties of human skin i.e., the refractive index and angle of incidence [131]. Lighter skin types possess a low absorption coefficient and hence, more light can escape via diffuse reflectance. However, dark skin types have a high absorption coefficient, reducing the amount of diffuse reflectance, and tend to have a low scattering coefficient due to reduced blood supply to the skin. As a result, surface reflection relies on the combined effects of absorption and scattering based on skin pigmentation, hydration, sebum production, collagen network, and skin homogeneity.

Overall, it is important to distinguish between the characteristics of skin and their optical properties to understand the underpinning cause of overestimation of oxygen saturation in darkly pigmented subjects. It is possible that the distribution of melanin, colour, or racial differences, together or individually, are resulting in the inaccuracies observed in pulse oximetry measurement. The effect of each of these contributors on the optical properties of

skin must be studied in vivo and in vitro, to provide insights on computational outcomes from in silico models.

3.3. Measuring skin pigmentation

Accurate characterisation of skin pigmentation is critical for experimental and simulation studies, particularly for applications like pulse oximetry, where pigmentation is proposed to influence light-tissue interactions. Various qualitative and quantitative methods have been developed to stratify skin pigmentation, each with their advantages and limitations. These methods are broadly categorised as ‘subjective’ or ‘objective’ approaches depending on their underlying principles. Subjective methods rely on human perception and interpretation and include visual comparisons or colour scales. However, objective methods utilise instruments and standardised measurements such as spectrophotometers to quantify skin pigmentation. By combining both types of methods, researchers and clinicians can leverage the practicality of subjective assessments alongside the rigour of objective quantification. A comprehensive overview of the several subjective and objective methods for stratifying skin pigmentation is available on the Open Oximetry Group webpage [132], some of which are outlined in Table 3-1.

Among the commonly used subjective scales are the Fitzpatrick Skin Phototype Scale (FST), the Felix Von Luschan Chromatic Scale, the Munsell colour system, the Massey Scale, and the Monk Scale. The Fitzpatrick scale categorises skin into six types ranging between skin types I-VI and is widely used in dermatology. Traditionally, it is used to evaluate parameters related to predicting the skin's reaction to ultraviolet light [133]. As a result, it may not account for all aspects of skin colour, such as undertones, redness, or colour evenness [134]. This approach risks introducing bias into the subjective stratification of skin pigmentation, which may reduce the reliability and applicability of traditional phototyping in clinical research. Although strong correlations have been observed between the melanin index (MI) and individual typology angle (ITA°) values with the Fitzpatrick scale [135], there is some evidence that criticises the use of FST in non-dermatological research. For instance, a study by He et al. showed that patient self-reported race and pigmentary phenotypes are inaccurate predictors of sun sensitivity as defined by Fitzpatrick scale [136]. Moreover, another study presented by Pershing et al. employed reflectance spectrophotometry to quantify skin pigmentation in anatomical sites that are both

protected and unprotected from UV radiation [137]. With a motivation to assess the correlation between objective skin pigmentation stratification methods and the Fitzpatrick scale, they found that in some cases there is a lack of complete agreement between the phenotype group assigned to the patient by the clinician and the spectra obtained.

Similarly, the Von Luschan Scale uses visual comparison against 36 coloured tiles, providing finer stratification than Fitzpatrick, but still relying on subjective interpretation and environmental lighting. Treesirichod et al. [138] demonstrated a statistically significant correlation between skin colour evaluation using this skin colour scale chart and measurements obtained from the Mexameter MX18 (Courage & Khazaka electronic GmbH, Cologne, Germany), a narrowband reflectance spectrophotometer. They reported correlation coefficients of 0.9 and 0.86 for the melanin and erythema indices, respectively, suggesting that such colour scales can serve as practical tools for skin pigmentation stratification. In effect, this can offer a cost-effective alternative to expensive, maintenance-intensive spectrophotometric devices, even though objective methods were still deemed more reliable for precision. The study also revealed congruence between Fitzpatrick skin phototypes III–V and the Von Luschan colour ranges assessed, with increasing scale values aligning with higher Mexameter-measured indices. Future research should explore the interpersonal and intrapersonal variability within the scale and include participants across all Fitzpatrick phototypes for a comprehensive evaluation.

Moreover, some other scales including the Monk Skin Tone Scale (MST) and Massey Scale have attempted to address inclusivity gaps in older scales such as the above. The MST was developed by Dr. Ellis Monk in collaboration with Google, who divided skin into 10 shades. They used standardised photographic references in response to challenges in AI and technology systems that were often trained on biased datasets. In one study, it was reported to have the strongest correlation with variations in pulse oximetry bias when examining the impact of skin tone on SpO_2 accuracy in critically ill patients [80]. This may show some promise in future studies, considering that the Monk Scale is one of the newest colour scales introduced in the field of skin pigmentation measurement. The Massey Scale adopts a similar principle, also focusing on pigmentation through photographic comparisons but instead under controlled lighting. It is particularly relevant for light-tissue interaction studies but is similarly constrained by observer interpretation and lighting variability. Both methods remain partly subjective and

lack validation against quantitative measures, which further highlights the superiority of objective measurement of pigmentation.

As previously mentioned, the use of spectrophotometric data bridges the gap between subjective visual assessment and objective reproducible results as demonstrated by the Munsell colour system. It includes descriptions of 10 hues arranged in a circular plane to define the colour and the level of colour using 10 divisions. Another parameter 'value' measures lightness or darkness on a vertical scale from 0 (black) to 10 (white), and 'chroma' indicates the colour's dullness (0) or vividness (14). These are combined into a notation, such as ' 5R 6/12,' which could describe a bright/moderate red with moderate lightness and high saturation. Then, spectrophotometric devices are used to measure hue, value, and chroma to support the validation of these parameters that are selected through human assessment. This method has demonstrated higher intraclass correlation coefficients (ICC) compared to classifications based on race and ethnicity, indicating its potential as a reliable tool for quantifying skin pigmentation [139].

Lastly, methods that exclusively rely on spectrophotometry include the ITA° scale, and advanced devices such as the Konica Minolta CM-700d (Konica Minolta Ltd, Tokyo, Japan), the Dermaspectrometer (Delfin Technologies Ltd, Kuopio, Finland), and the Mexameter MX 18 as mentioned above. The ITA° scale measures the angle formed between the reflectance of skin at specific wavelengths and a baseline in the colour space, ranging from very light to dark skin tones:

$$\text{ITA}° = \tan^{-1}\left(\frac{L^* - 50}{b^*}\right) * \frac{180}{\pi} \quad (3\text{-}1)$$

Where L^* represents lightness, and b^* is the blue to yellow component from the L*a*b* colour space. a^* is the green to red component, and although it is not considered in the equation, it is still part of the overall colour space used to define the skin colour in its entirety. Colourimeters, such as the Konica Minolta CM-700d express skin pigmentation in colour spaces like L*a*b*, meanwhile the Dermaspectrometer measures reflected light across a spectrum for melanin and haemoglobin.

In clinical and research contexts, choosing the appropriate tool depends on the study's objectives. Portable devices like colourimeters are ideal for quick field assessments, while spectrophotometers are indispensable for in-depth optical analyses. By using objective systems

validated against standardised metrics, bias that is inherent in visual assessments can be minimised. However, it is important to recognise that subjective methods also offer certain advantages when used appropriately and should not be entirely disregarded. These methods can be valuable in contexts where more detailed or personalised evaluation is necessary, or where objective tools may not be easily accessible. Therefore, while objective measures provide high precision, subjective scales can still have a role in skin pigmentation stratification.

Table 3-1: The different methods for stratifying skin pigmentation.

Fitzpatrick skin phototype scale [140]	
Von Luschan Chromatic Scale [132]	
Monk Skin Tone Scale (MST Scale) [132]	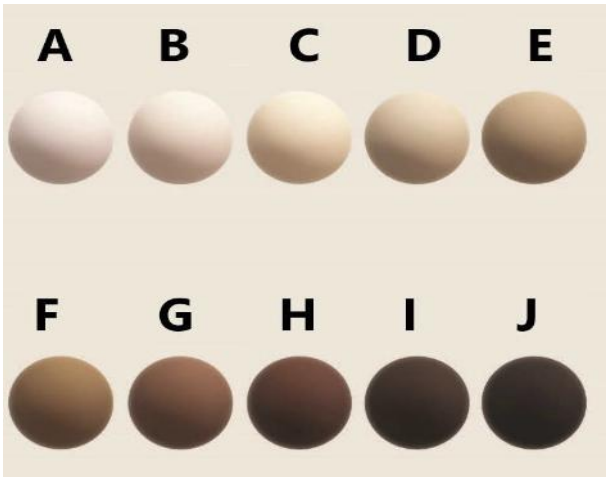

Massey Scale [132]	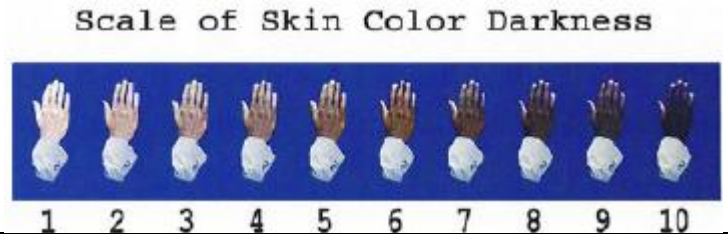
Munsell Colour chart [132]	
L*a*b* Scale [141]	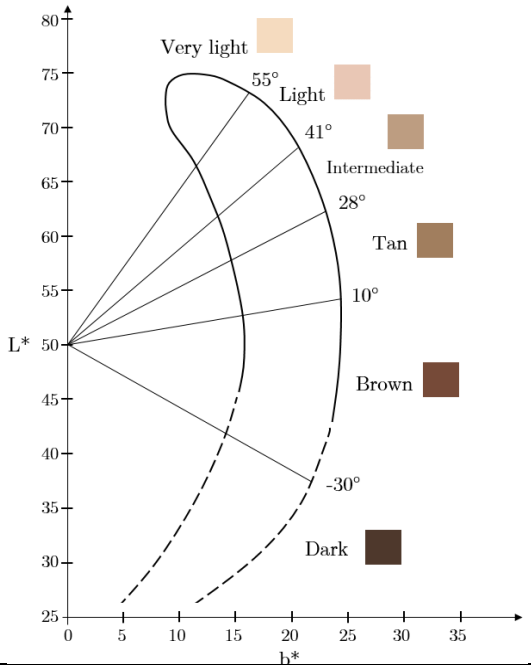

Konica Minolta CM-700d [132]	
Dermaspectrometer [132]	
Mexameter MX 18 [132]	

3.4.Summary

This chapter explored the determinants of skin pigmentation, focusing on melanin production and distribution, alongside other factors such as carotene, haemoglobin, and structural attributes like hydration and texture. These factors influence skin appearance and the optical properties of the skin, which are crucial for understanding light-tissue interactions, particularly in applications like pulse oximetry. Various methods to measure skin pigmentation were reviewed, including subjective scales and objective tools and devices, each with advantages and limitations. The importance of selecting an appropriate method based on the study's context was emphasised, acknowledging that while objective measures are generally more precise, subjective approaches remain valuable in specific scenarios.

CHAPTER 4: PULSE OXIMETRY: PRINCIPLES AND LIMITATIONS

Understanding the principles of pulse oximetry and the limitations of the device go hand in hand. While this thesis focuses on skin pigmentation as a confounding factor for SpO_2, there are many other factors affecting the accuracy of these measurements and hence, have been minimised since its commercialisation in 1975. This chapter provides a comprehensive scope of pulse oximeters and sheds light on the extent to which they can be improved based on their working principle.

4.1.The gold standard: Blood gas analysis

Blood gas analysis is currently the gold standard for blood oxygenation measurement. It was the only (invasive) method available in assessing blood oxygenation before the introduction of non-invasive blood oxygenation measurements as it requires a blood sample. Blood gas analysers consist of three electrodes that measure pH, partial pressure of carbon dioxide ($PACO_2$) and partial pressure of oxygen (PAO_2) at 37°C using extracted blood samples [142].

Two main indicators are used to reveal the amount of oxygen present in blood, namely functional arterial oxygen saturation (SaO_2) and fractional arterial oxygen saturation (FrO_2). Both indices represent the percentage content of oxygen-bound haemoglobin (HbO_2) against the total haemoglobin present. This is typically performed by measuring the concentration of the different haemoglobin species of interest. SaO_2, expressed as a percentage, is then determined by the ratio of HbO_2 concentration over the sum concentration of HbO_2 and deoxyhaemoglobin (HHb) in blood,

$$SaO_2 = \frac{[HbO_2]}{[HbO_2]+[HHb]} \tag{4-1}$$

Similarly, FrO_2 is determined by the proportion of oxygenated haemoglobin over the total concentration of all haemoglobin species,

$$FrO_2 = \frac{[HbO_2]}{[HbO_2]+[HHb]+[COHb]+[MetHb]} \tag{4-2}$$

Where [COHb], and [MetHb] are respectively the concentrations of carboxyhaemoglobin and methaemoglobin. FrO_2 is a more accurate method for determining oxygenation of blood, especially when the presence of other dyshaemoglobins (haemoglobins that do not bind to oxygen) is suspected due to particular physiological cues or pathological conditions.

4.2. Oxygen saturation by pulse oximetry

Pulse oximeters (Figure 4-1) provide a continuous non-invasive means for measuring oxygen saturation, usually at peripheral sites such as the finger. The device estimates functional arterial oxygen saturation by measuring changes in light absorbance in the arterioles over time, as they contain a higher concentration of HbO_2 relative to HHb. The photoplethysmogram is used to detect blood volume changes and to differentiate between absorbance of arterial blood and other absorbers (skin, bone, venous blood). A good choice of wavelength is where there are large differences in the extinction coefficients of HbO_2 and HHb [143] (Figure 4-2). Another criterion for the wavelength selection is the relative flatness of the absorption spectra around the chosen wavelength [144], [145], and as a result, 660 nm and 940 nm are widely used and well-suited as light sources in pulse oximeters. Measurement of arterial oxygen saturation by pulse oximetry is denoted by SpO_2, while the term SaO_2 is generally reserved for arterial oxygen saturation measured by blood gas analysis in extracted blood [146].

Figure 4-1. A pulse oximeter device for the non-invasive measurement of arterial oxygen saturation, available from pharmacies for home monitoring.

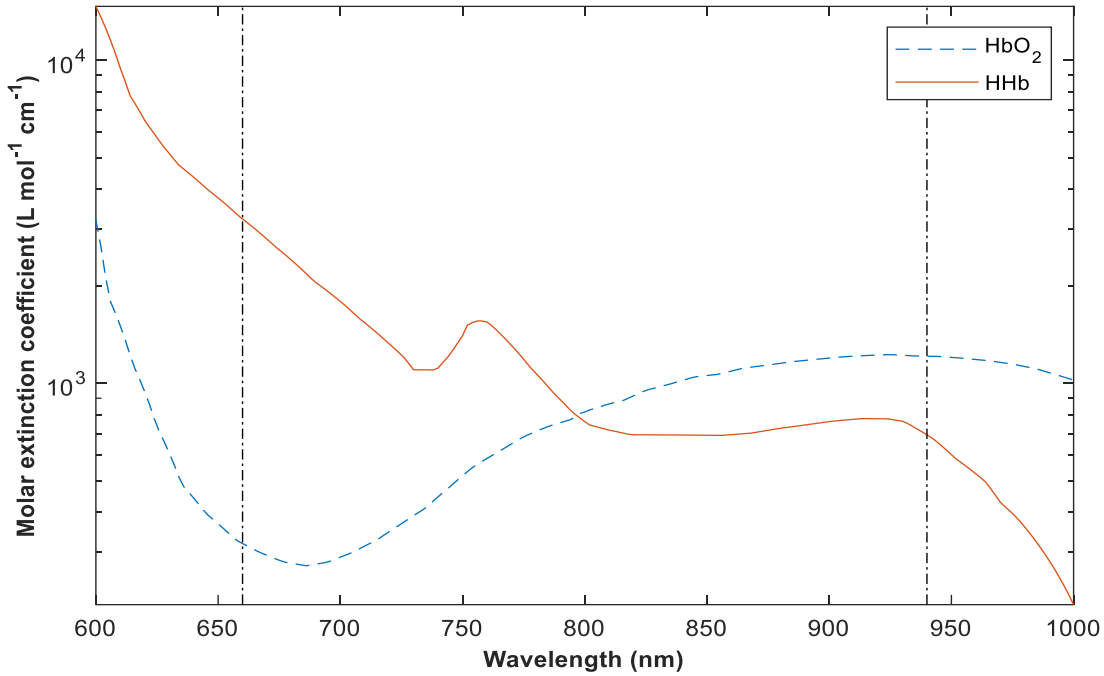

Figure 4-2. Absorption spectra of oxygenated (HbO_2) and deoxygenated (HHb) haemoglobin between the visible and near-infrared region. Molar extinction coefficients of both haemoglobin species are shown with respect to the wavelengths of interest in pulse. Extracted from [1].

The Beer Lambert law, in principle, can be used to estimate SpO_2 from the two PPG signals measured by a pulse oximeter as described in [146]. Briefly, to do so, the Beer Lambert Law is applied: (i) to measurements taken at points of minimum and maximum absorptions during the cardiac cycle (Figure 4-3), producing a pair of equations allowing the variables I_0 and C to be eliminated; and (ii) to two PPG signals obtained using two wavelengths of light. This produces an equation which relates measurements from the PPG signals to the ratio of the extinction coefficients at the two wavelengths (if the pathlength, d, is assumed constant at the two wavelengths). Since the extinction coefficients at the two wavelengths are determined by SaO_2 (the variable of interest) and the extinction coefficients of haemoglobin and oxyhaemoglobin (which are constant), this would allow for SaO_2 to be calculated directly from measurements from the two PPG signals.

However, we know that the pathlength d is not constant and instead it varies between wavelengths because of light-scattering (L). When using the modified Beer Lambert law, SpO_2 can no longer be calculated directly from measurements from two PPG signals because the optical pathlengths at the two wavelengths cannot be assumed to be equal. Additionally, pulse

oximeters are not based on the absolute measurement of μ_a and G, as they vary with wavelength, anatomical location, and the inter and intra variability of skin components between individuals, such as melanin, which affects these parameters. Theoretically, the modified Beer Lambert law would be utilised if the pulse oximeter did not present these limitations for obtaining accurate SpO_2 measurements. Since the optical parameters μ_a, L, and G cannot be directly measured, the concentration of oxyhaemoglobin and deoxyhaemoglobin cannot also be measured to calculate SaO_2. As a result, pulse oximetry is based on the simple version of the Beer Lambert law, which takes the ratio between incident and transmitted intensity at both operating wavelengths, and then used to calculate the "red: infrared ratio" (R):

$$R = \frac{\frac{AC_{660}}{DC_{660}}}{\frac{AC_{940}}{DC_{940}}} \tag{4-3}$$

where AC_{660} and DC_{660} represent the alternating current and direct current from tissue layers at 660 nm (a red wavelength) respectively, and likewise for AC_{940} and DC_{940} at 940 nm (an infrared wavelength). This equation is robust as it assumes that non-pulsatile absorbers such as melanin or static tissue structures such as bone, affect the AC and DC signals at each wavelength in a proportional manner i.e., that their impact can be approximated as a multiplicative scaling factor applied to both AC and DC at 660 nm and 940 nm. When the AC component is divided by the DC component at each wavelength, these scaling factors cancel out, and when the two normalised values are divided to compute R, the result is ideally independent of factors like pigmentation, tissue thickness, etc. Therefore, this assumption only holds reasonably well when the attenuation from pigmentation and other static tissue components affects AC and DC equally at a given wavelength, and when the relative spectral effect is small or consistent across individuals. Manufacturers calibrate pulse oximeters empirically by correlating the measured ratio (R) of AC/DC signals (Figure 4-3).

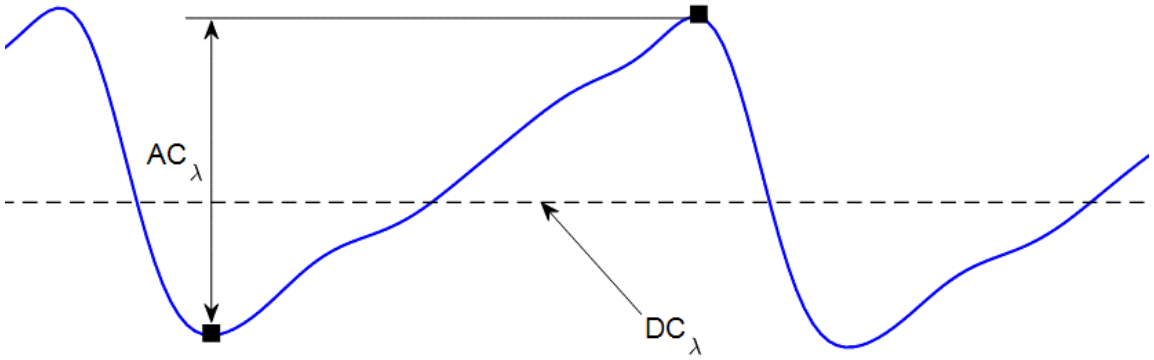

Figure 4-3. PPG parameters used for the calculation of the ratio of ratios (R). The AC amplitude at a generic wavelength λ is obtained from the difference between minimum and maximum absorption (squares) during the cardiac cycle. The DC component is the average light intensity. These two parameters are extracted from red and infrared wavelengths for calculation of the ratio of ratios (R). Extracted from [1].

Moreover, most modern pulse oximeters convert these ratios to SpO_2 using a "look-up table" [143].This approach assumes that the relationship between R and SaO_2 is constant across different individuals, which would be a reasonable assumption if not accounting for the limitations mentioned above, and if the magnitude of absorbance and the optical pathlength is not influenced by the presence of melanin in tissue. However, knowing the differences in the arrangement and concentration of melanosomes between individuals with different skin pigmentation (Chapter 3.2), there is expected to be greater levels of light absorption by individuals with dark skin due to an increase in μ_a [147]. Additionally, the type of light scattering, i.e., Rayleigh and Mie scattering (Chapter 2.3), can vary in different skin tones [148], with the size of scatterers being larger in individuals with darker skin, resulting in more forward (Mie) scattering in comparison to those with light skin tones. Therefore, current practises for pulse oximeter calibration may not be captured for wide populations.

4.3. Modalities of pulse oximetry

The pulse oximeter optical sensor can be either configured to operate in transmittance mode or in reflectance mode (Figure 4-4). In transmittance mode, the source and detector are placed opposite to one another across the surface of the region of interest (ROI), most commonly the

finger. Therefore, the optical path length is affected by the amount of light scattering within the tissue, as well as the tissue thickness, which alters the distance between the fixed source and detector. However, in reflectance mode, the source and detector are placed adjacent to each other, and the light detected is back scattered and reflected within the tissue. Reflectance PPG offers greater flexibility than transmittance PPG regarding the position of the sensors in different anatomical locations, such as the forehead. The source-detector separation can be altered by changing the distance between the source and detector, resulting in differences in the behaviour of light. For instance, if the desired outcome is to achieve maximum photon penetration depth, the source-detector separation can be increased to see the interaction of infrared light with deeper tissue. In both modalities, the light-tissue interactions that take place vary depending on the wavelength of the light source, which alters the optical properties of the tissue components.

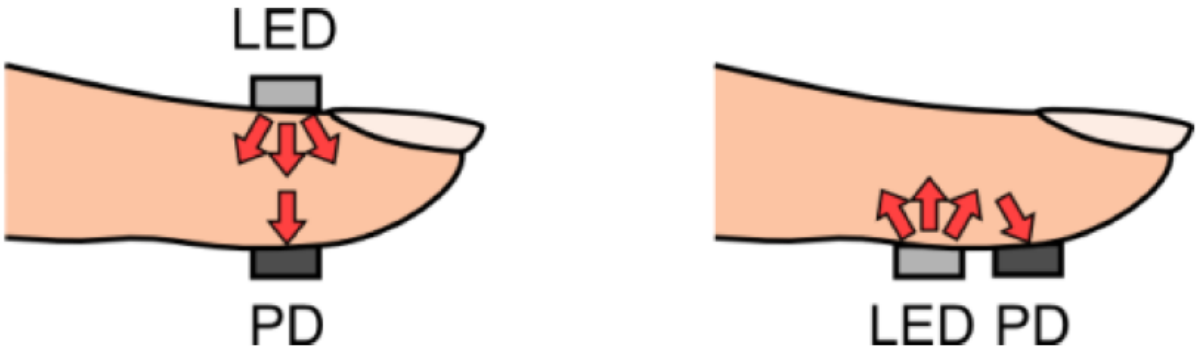

Figure 4-4. Sensor configurations of pulse oximetry. Left: Transmission mode. Right: Reflectance mode. Extracted from [167].

4.4. Limitations of pulse oximetry

It is important to acknowledge the limitations and assumptions of pulse oximetry before delving further into the impact and/or possible causes of skin pigmentation on the accuracy of pulse oximetry measurement. This is because inaccurate measurements may result from a combination of certain conditions, rather than the presence of either condition alone.

Since pulse oximeters only account for haemoglobin species that are bounded with deoxygenated and oxygenated haemoglobin, other dyshaemoglobins such as carboxyhaemoglobin (COHb) and methaemoglobin (MetHb) (eq. 4-2), may be present in the

blood due to higher concentrations or partial pressures of carbon monoxide and/or other gases and chemical compounds). The most common case is carboxyhaemoglobin, which is a molecule of haemoglobin that has bound reversibly with carbon monoxide (CO). In the visible range of the light spectrum, COHb presents a very similar absorption profile to oxyhaemoglobin, thus making it very difficult to distinguish between the two haemoglobins. This does not cause any particular concern in healthy subjects, but, in particular cases such as carbon monoxide poisoning or smokers, COHb may be present in higher concentrations in blood. This could potentially result in erroneous SpO_2 estimations, although they have been seen to minimally effect measurements of SpO_2 [149].

Furthermore, accurate estimation of blood oxygen saturation may be compromised under conditions of poor blood perfusion. To estimate SpO_2 accurately, pulse oximeters rely on the optical measurements of arterial pulsations (i.e., PPG signals) within the tissue bed. However, these pulsations only make up 2% - 5% of the total optical absorption profile recorded and are significantly dependent on an adequate blood flow/supply to the measurement area. When blood flow to certain anatomical areas is compromised due to, for instance, hypovolaemia, hypotension or hypothermia, the arterial pulsations recorded by the pulse oximeter may be significantly reduced or disappear, causing inaccurate SpO_2 measurements. A reasonable solution is to move the sensor from a peripheral site, such as the finger to a more central location with adequate perfusion. However, this may be not ideal in cases of severe critical illness such as patients experiencing a high degree of hypoperfusion. Another cause of falsely low SpO_2 is changes in venous volume due to venous pulsations, which can result from several scenarios including tightly placed finger probes, or again, in critically ill-patients suffering from heart complications.

Pulse oximeters are well known to provide inaccurate readings when the light absorption profile of red and/or infrared light is corrupted. Nail polish and artificial fingernails have been reported to affect pulse oximeter readings measured at the fingertips. More specifically, dark colours of nail polish such as black or blue can cause false readings and lead to inaccuracies [150], [151], [152]. As this is a well-known limitation of pulse oximetry, removing nail polish or changing the measurement site can eliminate this particular issue. Contrarily to the popular understanding that nail polish causes false SpO_2 readings, some studies have determined a limited or insignificant impact on SpO_2 readings [153], [154], [155]. However, the reported differences in the literature may be due to methodological differences and more standardised

studies are required to assess the existence of such interference across different pulse oximeter manufactures, nail polish colours, and larger populations.

Another limitation is the effect of light pollution (ambient light) [156], [157], [158]. Any external light, aside from the discrete wavelengths employed by the instrument, can interfere with measurement if it reaches the photodetector. Usually, ambient light pollution may cause offsets in the sensor or cause additional issues due to the flickering of lamps at 50 Hz (i.e., this frequency may vary across different countries), thus introducing unwanted noise in the PPG signals, which can possibly lead to erroneous SpO_2 values. For this reason, pulse oximetry sensors should be optically insulated from any external light, and they should be positioned carefully to avoid ambient light reaching the photodetector. Using filtered photodetectors may alleviate the problem, but any light component in the red to the near-infrared range of the spectrum (i.e., the effective range used in pulse oximetry) can still enter the sensor if not properly screened. Also, if pulse oximetry sensors are not properly positioned on the measurement tissue, mismatches in the red and infrared absorption (penumbra effect) may cause false SpO_2 readings. The penumbra effect re-emphasises the importance of correct probe positioning. Inappropriate probe placement leads to error readings, especially on the small fingers of neonates and infants. This effect occurs when the probe is not symmetrically placed, such that the pathlength between the two LEDs and the photodetector is unequal, causing one wavelength to be 'overloaded'. Also, the emitted light can be projected tangentially to the detector (in reflectance probes), sometimes without crossing an arterial bed, leading to optical shunting. Therefore, repositioning of the probe often leads to improvement in saturation readings.

Furthermore, one of the "nemesis" of pulse oximetry is sensor/tissue movement artefact and this should be limited during measurements [159], [160], [161]. Good probe design and attachment as per application needs can help mitigate against this. Random extra-arterial movements can be easily recognised, but periodical movements, synchronous with the cardiac cycle, can be erroneously interpreted as 'signal' by the instrument and cause inaccurate SpO_2 measurements. Advancements in signal processing techniques and technologies have helped to minimise the issue of movement artefacts in pulse oximetry [162], [163], [164]. Some proprietary algorithms such as the Masimo Signal Extraction (SET®) [165] are already incorporated in modern pulse oximeters and are showing a robust estimation of SpO_2 during motion [7].

Lastly, pulse oximeter readings can be impacted by intravenous and intradermal dyes (methylene blue, indocyanine green, patent blue, nitrobenzene and indigo carmine), which are used to identify anatomical structures (e.g., cancerous tissue, lymph nodes, etc.) in diagnostic imaging or surgical operations. Usage of pulse oximeters during or shortly after the induction of these dyes has shown to have resulted in falsely low SpO_2 values without actual desaturation. These errors occur as the pulse oximeter cannot distinguish between the absorption of light by intravenous dye and the absorption by haemoglobin species. For example, methylene blue has its peak spectral absorption at 668nm, hence it absorbs most of the light emitted by the red emitter. This absorption is interpreted by the pulse oximeter as the presence of reduced haemoglobin, leading to inaccurate estimation of SpO_2 [166], [167]. Therefore, caution must be taken when performing dye injections with concomitant pulse oximetry measurements.

In conventional practice, the effects of light scattering are accounted for via empirical calibration of the oximeter device, which appears to work well, but only up to a certain point [143]. This is an unavoidable limitation of pulse oximeters as they can only be as accurate as their empirical calibration curves. These calibration curves are obtained from healthy subjects by measuring the red: infrared ratio (eq. (4-3)) while varying the inspired fraction of oxygen and, simultaneously, measuring SaO_2 by blood-gas analysis and collecting dual-wavelength PPG signals. Understandably, researchers and pulse oximetry manufacturers are limited in the degree of hypoxaemia inducible in these volunteers, to a SaO_2 of approximately 70% to 75%. Therefore, the shape of the calibration curve below these levels must be extrapolated, with potential implications for the accuracy of pulse oximetry at low saturation levels. One of the limitations of this traditional calibration method is the limited range of oxygen saturation that can be acquired. Ethical issues prevent intentional desaturation of healthy subjects below a certain point due to risk of hypoxic brain damage. Also, another potential limitation of such calibration studies between the years of 2020 and 2024 is perhaps the lack of balance between participating volunteers from all categories of skin pigmentation. Notably, the assumptions inherently made during an empirical calibration are valid only for a limited range of saturations and become invalid under extreme conditions.

While pulse oximetry has proven to be a reliable and non-invasive method for measuring oxygen saturation, it is not without its limitations. As the technology continues to evolve, future improvements must consider these limitations and seek more accurate, robust methods for algorithms that can accommodate the complexities of human physiology, including variations in skin pigmentation, blood flow dynamics, and environmental conditions.

4.5.Summary

This chapter provides an overview of pulse oximetry, detailing its working principle and the limitations associated with the technology, particularly in relation to skin pigmentation. Pulse oximeters work by estimating blood oxygen saturation (SpO_2) through changes in light absorption in blood vessels, using two wavelengths of light (660 nm and 940 nm). However, several factors can affect the accuracy of these measurements, such as the impact of skin pigmentation on light absorption and scattering. Individuals with darker skin tones typically experience higher light absorption, which can influence SpO_2 readings. The limitations of pulse oximetry include the potential interference of dyshaemoglobins like COHb and MetHb, which can lead to inaccurate readings. Poor blood perfusion may also compromise accuracy, as can the presence of nail polish or artificial nails, and many more. The chapter highlights the need for improved calibration methods that account for skin pigmentation differences, aiming to enhance the overall accuracy of pulse oximetry.

CHAPTER 5: THE EFFECT OF SKIN PIGMENTATION ON PULSE OXIMETER ACCURACY

Differences between arterial oxygen saturation measured by blood gas analysis and pulse oximetry was documented soon after their invention in the 1980's [29], [30], [31], yet the challenges imposed on the measurement due to skin pigmentation remains neither fully corrected nor fully understood. A summary of the studies which compared the accuracy of pulse oximeters in groups of different race or skin pigmentation is provided in Table 5-1. These were identified via several databases including PubMed, Web of Science, and Google Scholar, IEEE Xplore, and Scopus using the following search terms/phrases: 'pulse oximeter skin pigmentation', 'racial bias in pulse oximetry', 'pulse oximetry COVID-19', and 'silent hypoxaemia'. Sources that were not identified using the search terms were retrieved from the references of identified publications. To be included, studies had to compare SpO_2 against reference SaO_2 measurements obtained via blood gas analysis on subjects with different skin pigmentation types/levels, even if there was no clinical or statistical significance between the two variables. This was done to make explicit the lack of consensus in the field, emphasising the importance of approaching the research hypothesis without assumption or bias. Hence, drawing attention to these inconsistencies contextualises the rationale for this research.

5.1. Overestimation of arterial oxygen saturation

The mean difference between blood oxygen saturation measurements obtained by the two approaches is the 'bias', hence, 'mean bias' was referred to the average bias recorded within a racial subgroup. Out of the 38 studies identified in Table 5-1, 26 studies found that SpO_2 was overestimated in those with darker skin relative to reference SaO_2 measurements obtained by blood gas analysis [32], [33], [34], [36], [37], [38], [39], [40], [41], [43], [46], [47], [48], [49], [53], [54], [55], [56], [62], [73], [75], [76], [77], [78], [79], [80]. Additionally, over half (53%) of the studies documented an increase in bias for subjects from all racial sub groups as they became less saturated [33], [34], [35], [37], [38], [39], [40], [41], [43], [47], [48], [49], [53], [55], [61], [70], [74], [76], [78], [79]. For White subjects, bias values were observed between -0.35% and 3.2% and between 0.6% and 5.1% for Black subjects. Precision, which is given by the standard deviation (SD), was found to range between 1.8% and 6.3% for White subjects and between 2.7% and 9.1% for Black subjects. Evidently, bias and precision are seen to have

a wider range in Black subjects relative to White subjects, which indicates that some pulse oximetry measurements are more accurate in individuals with light/fair skin.

In infants, a 1.5-fold overestimation of SpO_2 was observed in Black infants relative to White infants for a SaO_2 range between 85% and 100% [47] and approximately three times more for a SaO_2 range between 70% and 100% [75]. However, some biases in infants may be caused by cyanosis and not skin pigmentation [168], [169] although cyanosis is often observed differently in people with different skin tones (blue/purple in fair skin, grey/green in intermediate skin, and grey/white in dark skin). A mixture of foetal haemoglobin (HbF) and adult haemoglobin (HbA) could result in an underestimation of SpO_2 of 3% - 4%, or rotation of sensors every 12 hours (to avoid skin injury) can cause inaccurate readings, as well as increase in melanin production following treatment in Black and Asian patients after phototherapy for jaundice patients [47]. Such considerations are as important for rectifying bias caused in Black subjects, specifically hypoxic patients. Hence, more work must be done on investigating bias at low arterial oxygen saturations (<90%), as this may provide some explanation about the overestimation of SpO_2, and the occurrence of suboptimal function, which was observed two times more frequently in Black patients relative to White patients [36].

Moreover, pulse oximeters were found to have a root-mean squared error (A_{rms}) of more than 3% in infants overall, with a greater discrepancy in Black infants (9.5% for Black infants and 8.9% for White infants) [47]. Other studies recorded root-mean square values less than 3% (1.35% for White patients and 1.42% for Black patients using the Masimo SET) [52], (1.08% for White patients, 1.13% for Asian patients, and 1.56% for Black patients) [38], (1.64% for light pigmented patients and 1.71% for dark pigmented patients) [79]. There is a greater urgency to address the huge inaccuracies observed in infants relative to adults [92], and to perform thorough testing of consumer marketed pulse oximeters, including new generation models [170], in order to prevent misleading interpretation of pulse oximeters readings, especially by home users [54]. The OpenOximetry.org Project is actively working to better understand the impact of skin pigmentation on oximeter accuracy and to develop new strategies to eliminate this source of error [132]. This includes laboratory testing on human subjects to determine the performance of existing oximeters used in a laboratory setting, whether they perform differently in some patients in a clinical setting, and raw data mainly from the University of California and San Franscisco (UCSF) hypoxia lab.

5.2. Incidence of hypoxaemia

As expected, the overestimation of SpO_2 in Black subjects leads to an increased incidence of occult hypoxaemia (SaO_2<88% yet SpO_2=92%-96%) [38], [43], [45], [46], [47], [48], [70], [71], [73], [76] ([42] is a notable exception). Occult hypoxaemia was found to occur three times more frequently in Black subjects than in White subjects [46], [73], two times more frequently in Black subjects than in White subjects [71], and in 9.2% of Black infants and 7.7% of White infants [47]. Infants spend much of their hospitalisation period with oxygen saturations above 85%, so any small change in bias is critical, and can have adverse effects on mortality post-surgery [96]. Relying on pulse oximeters to triage patients and adjust supplemental O_2 may place Black patients with increased hypoxaemia at risk [45].

To correct for these levels of hypoxaemia amongst different racial groups, SpO_2 targets of 92% and 95% were found to be reliable in predicting a satisfactory level of oxygenation in White and Black patients respectively [43]. These thresholds were determined for patients who recorded a PaO_2 of 60mmHg or above, however, it was more difficult to correct hypoxaemia while avoiding O_2 toxicity for Black patients who recorded an average PaO_2 level of 83 ± 31 mmHg [43], [58]. In another study, these results were also consistent after the exclusion of patients with high COHb (seen to overestimate SpO_2 [36]), diabetes, and adjusting for age and sex and cardiovascular score, which indicates that the inaccuracies appear to be related to skin pigmentation. It is important to note that not all Black patients had occult hypoxaemia, but it is clear that there is a variation in risk due to race [73], extending to greater organ dysfunction and higher in hospital mortality, even when age, sex, and sequential organ failure assessment (SOFA) score were adjusted [48]. Similarly in another retrospective study, Black patients diagnosed with Covid-19 were always at risk of unrecognised oxygen treatment eligibility based on pulse oximetry measurement [72].

5.3. Methodologies

Conventionally, skin pigmentation is described by self-report or ethnic classification, without consideration of environmental factors affecting the quantity and distribution of melanin in the epidermis, such as exposure to ultraviolet A and B radiation. Some studies whose methods and/or outcomes did not comply with the United States Food and Drug Administration (FDA) were identified. According to regulations in 2022, 15% of the participant pool should be darkly

pigmented. This requirement was met in some studies including [42], [48], [80] (White pool=65.5%, Black pool 29.6%; White pool=55.44%, Black pool=44.56%;White pool=43.75%, Black pool=44.53%), but not in other studies including [38], [46], [55], [67]. Despite this, the inaccuracies seen in Black or darkly skinned subjects mentioned above did not change, although it was difficult to make conclusive statements in studies with a small number of volunteers [30].

The magnitude of the biases may have occurred due to a number of reasons. Firstly, some studies did not obtain simultaneous SpO_2-SaO_2 pairs as conducted in [37], since SaO_2 measurements are prone to fluctuations over short periods of time. Instead, some measurements were taken 1 minute apart [75], 4 minutes apart [38], 5 minutes apart [80] 7.5 minutes apart [55], 10 minutes apart [73], and up to 30 minutes apart [53]. It is also important to consider that breathing variations, body temperature, anaemia, excessive motion, high levels of COHb and MetHb [36], incorrectly applied probes/probe type [41], blood gas contamination by air in syringe [47], and perfusion status [54], may have resulted in a small bias difference, especially in critically-ill patients [38].

Furthermore, some studies used the Fitzpatrick scale (as currently recommended by the FDA) to categorise skin tones [37], [67], [79], [80], [81], while others chose to use the Munsell chart [36], [39], [41], [82] or Monk scale [80], [83]. Only three studies quantified pigment using reflectance spectrophotometry, chromametry, and Individual Topology Angle, respectively [35], [78], [80], which is the most objective method for classifying different skin colours, and now gaining huge attention in this research space. The remainder of the studies stratified skin pigmentation based on ethnicity, race, or other visual scales.

5.4. Statistical significance

While most of the data and information presented in this section share similar trends, not all these studies showed statistically significant differences. From Table 5-1, 22 out of 38 studies (58%) concluded that their results showed a statistically significant relationship between skin pigmentation and overestimated SpO_2 in subjects with darker skin [30], [31], [32], [34], [36], [40], [41], [43], [46], [47], [48], [49], [53], [54], [55], [71], [72], [73], [76], [78], [79], [80]. Some studies were either not able to conclude statistical significance due to limiting factors (e.g., sample size), or simply did not mention the statistical significance of the data [29], [33],

[38], [61], [62]. Additionally, there appears to be no clear guidelines for determining the level of clinically significant inaccuracy (or difference in accuracies). For instance, the differences in accuracy between groups were deemed to be clinically significant in Wiles et al. [38] and Volgyesi et al. [74], and clinically insignificant in Bothma et al. [35], Adler et al. [36], and Baker and Wilson [52], despite both sharing overlapping limits of agreement. Overall, the data from these studies indicate that at least some pulse oximeters are less accurate in people with darker skin pigmentation.

Table 5-1: Pertinent studies that compared the accuracy of pulse oximeters in groups of different race or skin pigmentation (available to access).

Study	**No. subjects**	**Setting**	**Method for stratifying skin pigmentation**	**Statistical information**	**Findings**
Wang *et al.* (1985) [29]	31 "pigmented patients"	Not available	Not available	Not available	Biox III oximeter gave readings that closely approximated oxygen saturation measurements from arterial blood, confirming the usefulness of non-invasive oximetry even in pigmented patients.
Gabrielczyk & Buist (1988) [30]	21 (4 "racially pigmented")	Post-cardiac surgery	Unclear	*Bias $\pm$ SD (Overall): +0.6$\pm$1.6%	Statistically insignificant difference in accuracy of SpO_2 between skin pigmentations.
Cecil *et al.* (1988) [31]	152 (136 White, 1 Asian, 15 Black)	Not stated	Scale of 1 to 3 – Light, medium, or dark pigment	*Bias (Overall): Nellcor, +0.59%. Ohmeda, -0.897%	Both oximeters displayed a statistically significant, but clinically insignificant bias when compared with arterial blood oxyhaemoglobin. Greater accuracy in SpO_2 measurements taken from Black patients was observed by the Ohmeda oximeter.
Ries *et al.* (1989) [32]	187 Distribution of racial groups not	Laboratory	Munsell colour system	*Bias (Overall): Ohmeda, +1.4%. Hewlett Packard, -	Readings were slightly less accurate in patient groups with darker skin, suggesting that dark skin colour may. affect the performance and

	stated			0.6%	accuracy of ear oximeters.
Jubran & Tobin (1990) [43]	54 (29 Black, 25 White)	Intensive Care	Visual	*Bias ± SD (White): 2.2±1.8% *Bias ± SD (Black): 3.3±2.7%	SpO_2 was less accurate and less precise in Black patients.
Cahan et al (1990) [33]	28 (22 White, 6 Black)	Hypoxia Laboratory	Unclear	*Bias ± SD (White): 1.9±5.1% *Bias ± SD (Black): 5.1±4.6%	Pulse oximetry values can be higher in Black subjects than in White subjects, especially at saturations below 80%.
Lee *et al.* (1993) [34]	33 (22 Chinese, 6 Malaysian, 5 Indian)	Intensive Care	Race	*Bias ± SD (Overall): +0.82±2.6% Range: -4.9% - 10.5%	SpO_2 was most accurate in Chinese patients, and less accurate (greater overestimation) in Malaysian and Indian patients. It was also less accurate at low saturations and in patients with elevated bilirubin levels.
Bothma *et al.* (1996) [35]	100 darkly pigmented adults	Intensive Care	Reflectance spectrophotometer	*Bias (Overall): -1.0% - 1.2% LOA: -6.6% - 6.6% across all pulse oximeters SD: 1.9% – 2.4%	The accuracy of pulse oximetry is not adversely affected by skin pigmentation, and it remains a useful oxygenation-monitoring device in darkly pigmented patients.

				across all pulse oximeters	
Adler *et al.* (1998) [36]	278 (34 Dark, 101 Intermediate, 143 Light)	Emergency Department	Munsell colour system	*Bias ± SD (Light): +2.5±4.6% *Bias ± SD (Intermediate): +2.8±5.2% *Bias ± SD (Dark): +2.2±3.7%	The accuracy and precision of SpO_2 was not affected by skin pigmentation. Signal quality was poorer in a great proportion of patients with dark skin pigmentation than intermediate or light.
Bickler *et al.* (2005) [40]	21 (11 Dark, 10 Light)	Hypoxia Laboratory	Race	*Bias ± SD (Light): +0.37±3.20% *Bias ± SD (Dark): +3.56±2.45%	SpO_2 was less accurate (greater overestimation) in Darkly pigmented subjects. This bias was greater at lower saturations, and differed between pulse oximeters.
Feiner *et al.* (2007) [41]	36 (17 Dark, 7 Intermediate, 12 Light)	Hypoxia Laboratory	Race	*Bias range for intermediate and dark skin: +4.5% – +4.9% (SaO_2 = 60% - 70%) +2.4% – +3.6% (SaO_2 = 70% - 80%)	SpO_2 was less accurate (overestimation) in subjects with Dark and Intermediate pigmentation at lower saturations for five out of six combinations of pulse oximeters and probe types (the exception being the Masimo Radical with adhesive probe).

Witting *et al.* (2008) [62]	837 (577 African American, 260 White)	Emergency department	Self-report	Not available	African American group without hypoxaemia was associated with a 0.8-unit increase in SpO_2 values, and without a change in precision. African American females and White females had an average SpO_2 higher than African American men and White men, respectively. Clinicians should regard these findings with particular significance.
Foglia *et al.* (2017) [39]	35 (14 Dark, 21 Light)	Infants with congenital heart disease	Munsell colour system	*Bias ± SD (Overall): Nellcor, +3.9 ± 2.0% Masimo, +0.8±2.4%	No significant difference in SpO_2 accuracy between patients with Dark and Light pigmentation.
Ebmeier *et al.* (2018) [37]	394 Distribution of racial groups not stated	Intensive Care	Fitzpatrick scale	*Bias (Light vs. Medium): -0.9% *Bias (Light vs. Dark): -2.4% LOA: -4.4% – 4.4%	The accuracy of SpO_2 was influenced by skin pigmentation and pulse oximeter model (Masimo underestimating, Philips overestimating).
Murphy & Omar (2018) [63]	146 (6 Light, 111 Medium, 29 Dark)	Intensive Care	Massey New Immigrant Survey skin colour scale	*Bias ± SD (Overall): +1.64±0.15 g/dL LOA (Overall): -1.05 g/dL – 4.33 g/dL	The degree of skin pigmentation does not appear to influence the magnitude of bias, rather the increasing severity of illness and decreasing lower mean arterial blood

					pressure.
Smith & Hofmeyr (2019) [61]	220 12 Type I, 28 Type II, 69 Type III, 45 Type IV, 28 Type V, and 38 Type VI	Perioperative areas e.g. pre-assessment clinics, recovery rooms, operating theatres and intensive care units	Fitzpatrick scale	*Bias (Overall): -0.55% LOA: -3.25% – 2.16%	Darker skin pigmentation showed no trend to an effect on the accuracy of oxygen saturation measured using portable fingertip pulse oximeter and a conventional bedside pulse oximeter.
Sjoding *et al.* (2020) [73]	10,001 (1,326 Black, 8,675 White)	Intensive Care, and Inpatients receiving oxygen	Race	Not available	SpO_2 was less accurate (overestimation) in Black than White patients. Hidden hypoxemia (arterial oxygen saturation of <88% and SpO_2 of 92-96%) was nearly three times as common in Black than White patients.
Valbuena *et al.* (2021) [46]	372 (65 Asian, 51 Black, 70 Hispanic, 186 White)	Intensive Care	Race	Incidence of occult hypoxaemia: 10.2% (White), 21.5% (Black), 8.6% (Hispanic), and 9.2% (Asian)	Hidden hypoxemia (blood gas arterial oxygen saturation of <88% and SpO_2 of 92-96%) was more common in Black patients than Asian, Hispanic or White patients.

Vesoulis *et al.* (2021) [47]	294 (124 Black, 170 White)	Neonatal Intensive Care	Race	*Bias (White): +0.72% *Bias (Black): +1.73%	SpO_2 was less accurate (overestimation) in Black than White patients. Hidden hypoxemia (arterial oxygen saturation of <85% and SpO_2 ≥90%) was more common (although not significantly so) in Black than White patients.
Okunlola *et al.* (2021) [54]	491 (108 Dark, 383 Light)	Hypoxia Laboratory	Unclear	Not available	SpO_2 was less accurate (overestimation) in Dark than Light to Medium skin pigmentations.
Wong *et al.* (2021) [48]	87,971 (1,919 Asian, 26,032 Black, 2,397 Hispanic, 57,632 White)	Intensive Care and other Hospital Wards	Race	Proportion of patients with hidden hypoxaemia: White: 4.9% Asian: 4.9% Hispanic: 6.0% Black: 6.9%	The incidence of hidden hypoxemia (arterial oxygen saturation of <88% and SpO_2 ≥88%) was greatest in Black, then Hispanic, Asian and finally White patients. It was associated with greater organ dysfunction 24 hours later, and higher in-hospital mortality.
Bangash *et al.* (2021) [55]	16,818 (81.2% White, 11.7% Asian, 4.0% Black, 3.2% Other ethnicities)	Hospital	Ethnicity	Relative to White patients: *Bias (Asian): 0.5pp greater *Bias (Black): 0.8pp	Pulse oximetry tends to overestimate O_2 saturation, and this is more pronounced in patients of Black ethnicity. These differences resulted in 6.1% vs. 8.7% of White vs. Black patients classified as normoxic on SpO_2 who

				greater *Bias (Other): 0.3pp greater	were hypoxic on the gold standard SaO_2 reading.
Shi *et al.* (2022) [49]	6,505 (4,897 adults and 1,608 children) Distribution of racial groups not stated	27 out of 32 in hospital, none at home	15 studies measured skin pigmentation and 22 referred only to ethnicity	*Bias±SD (Light): -0.35±1.49% LOA (Light): -1.87 – 4.09 *Bias ± SD (Intermediate): -0.58±1.47% LOA (Intermediate): -3.46 – 2.30 *Bias ± SD (Dark): +1.11±1.52% LOA (Dark): -3.27 – 2.58	Pulse oximetry may overestimate oxygen saturation in people with dark skin and people whose ethnicity is reported as Black/African American, compared with SaO_2, although the overestimation may be quite small in hospital settings. The clinical importance of any overestimation will depend on the particular clinical circumstance.
Barker & Wilson (2022) [52]	75 (39 Black, 36 White)	Hypoxia Laboratory	Unclear	*Bias±SD (White): -0.05±1.35% Arms (White): 1.35% *Bias±SD (Black):	There was no clinically significant difference in the accuracy or bias between Black and White subjects monitored with Masimo SET pulse oximetry.

				-0.2±1.40% Accuracy (Black): 1.42%	
Crooks *et al.* (2022) [53]	2997 Distribution of ethnic groups not stated	Hospital	Ethnicity	*Bias (White): +3.2% *Bias (Asian): +5.1% *Bias (Black): +5.4% *Bias (Mixed): +6.9%	Pulse oximetry overestimated arterial oxygen saturations compared to blood gas measurement across all ethnicity groups when SpO_2 measurements were below 90%, and underestimated these when SpO_2 measurements were above 95%. However, individuals with Black, Asian or mixed ethnicity had a higher reading for oxygen saturation as measured by pulse oximetry than blood gas compared to individuals with a White ethnicity.
Wiles *et al.* (2022) [38]	178 (126 White, 30 South Asian, 13 Black, and 9 other ethnic origin)	Intensive Care	Ethnicity	**Bias (White): -0.25% LOA (White): -4.75% – 4.23% **Bias (South Asian):	Bias was greater in patients of non-White ethnic origin. The study also found that pulse oximetry is less accurate in patients diagnosed with COVID-19 and receiving mechanical ventilation.

				-0.96% LOA (South Asian): -5.62% – 3.71% **Bias (Black): -1.72% LOA (Black): -6.8% – 3.36% **Bias (Other): -1.21% LOA (Other): -5.48% – 3.05%	
Henry *et al.* (2022) [70]	26,603 (24,493 White, 1,263 Black, 574 Asian, 273 American Indian)	Intensive Care	Self-identification	Proportion of patients occult hypoxaemia: White (3.6%), Black (6.2%), Asian and American Indian (6.6%)	Occult hypoxemia is more common in Black patients compared with White patients and is associated with increased mortality, suggesting potentially important outcome implications for undetected hypoxemia. It is imperative to validate pulse oximetry with expanded racial inclusion.
Burnett et al. (2022) [71]	151,070 (16,011 Black, 21,223 Hispanic,	Unclear	Self-identification	*Bias±SD (White): -0.20±6.3% *Bias±SD (Hispanic):	Self-reported Black and Hispanic race/ethnicity are associated with a greater prevalence of intraoperative occult

	70,722 White, 8,121 Asian, 34,993 other)			+0.5±7.9% *Bias ± SD (Asian): +0.2±6.5% *Bias ± SD (Other): +0.1±5.9% *Bias ± SD (Black): +0.6±9.1%	hypoxemia in the SpO_2 range of 92% to 100% when compared with self-reported White race/ethnicity.
Fawzy et al. (2022) [72]	1216 (63 Asian, 478 Black, 215 Hispanic, and 460 White)	Referral centres and community hospitals	Self-identification	**Bias (Relative to White Patients) Asian: -1.73% Hispanic: -1.13% Black: -1.23%	Pulse oximetry overestimated arterial oxygen saturation among Asian, Black, and Hispanic patients (ethnic minority groups) compared with White patients with COVID-19. This contributes to missed or delayed recognition of eligibility to receive COVID-19 therapies.
Ruppel et al. (2023) [75]	774 (201 Black/African American, 573 White)	Children's hospital	Race	*Mean bias (range): White: +0.88% (0.63% – 1.13%) Black/African American: +2.61% (2.19% – 3.04%)	Overestimating of SpO_2 in patients with darker skin can be attributed to the light absorption properties of melanin at higher concentrations. Future studies should employ direct measurement of skin pigmentation.

Savorgnan et al. (2023) [76]	2713 (1663 Black, 1050 White)	Children's hospital	Race	Proportion of patients with occult hypoxaemia: White: 4% Black: 12%	Reliance on pulse oximetry may place Black pediatric patients at increased risk of occult hypoxaemia due to higher incidence of increased bias.
Meira e Cruz et al (2023) [77]	24 (16 Non Black, 8 Black)	Hospital setting	Race	*Bias between non Black and Black patients at 70% and 100% oxygen saturation: +0.7%. Accuracy between 90% - 100% oxygen saturation (Non black, Black): 1.57%, 1.73% Accuracy between 70% - 79% oxygen saturation (Non black, Black): 2.71%, 2.84%	Bias and accuracy differences between the two racial groups was not statistically significant. Patented design ensures that the readings are obtained from the palmar aspect of the finger, which generally has less pigment than the back of the hand.

Fawzy et al. (2023) [78]	12 (7 light skin, 5 dark skin)	Academic medical centre	Chromameter	*Bias (Light): 0.34%, (Dark): 1.05% Accuracy (Light): 1.97%, (Dark): 4.15%	With objectively measured skin pigmentation, pulse oximeter bias was greater among darkly pigmented patients, especially at lower oxygen saturation levels.
Khanna et al. (2023) [79]	131 patients	Unclear	5-level stratification system: Light, medium-light, medium (Light, Type I-III), medium dark, dark (Dark, Type IV-V)	*Bias between 70% - 80% oxygen saturation: (Light): +0.30%, (Dark): +0.58% Overall accuracy: (Light): 1.64%, (Dark): 1.71%	Performance of pulse oximeter meets medical grade standard although bias difference between light and dark pigmented groups was statistically significant at low saturations. Further research is required to evaluate design elements to improve performance.
Hao et al. (2024) [80]	128 (56 White, 57 Black, 15 other, including those who self-identified as Asian or from two or more	Intensive care unit	Fitzpatrick scale, Monk scale, Von Luschan, reflectance colourimetry, reflectance	**Bias between light and dark skin tones using the Monk scale (best relationship with differences in pulse oximeter bias):	Pulse oximeter bias was greater in darker skin toned patients, however, due to the large variation in pulse oximeter data, skin tone is unlikely to be the sole contributor to performance discrepancies.

	ethnicities)		spectrophotometry	-2.40% LOA: -4.32% – -0.48%	
Leeb et al. (2024) [81]	34 (8 Caucasian, 9 Asian, 7 Black, 5 Hispanic, 5 multiethnic)	Laboratory	Fitzpatrick scale and Individual Topology Angle	No quoted data, but forest plots showed wide range in bias and accuracy especially in darker individuals	The Fitzpatrick scale miscategorised individuals and not recommended for use in such studies. 9 out of 11 pulse oximeters performed poorly in dark skinned individuals, and 5 had accuracy levels above 3%.
Haxha et al. (2024) [82]	20 (7 White, 7 Brown, 6 Black)	University laboratory	Munsell colour system	*SpO_2 ±SD at 100% oxygen saturation White: 99.29 ± 1.11% Brown: 99.86 ± 0.38% Black: 99.29 ± 0.49%	No significance in SpO_2 measurement between different pigmentation level across the three commercial pulse oximeters. The custom pulse oximeter only had an infrared LED source, so it is no surprise that mean SpO_2 was very similar between the three skin categories.
Blaney et al. (2024) [83]	11	Laboratory	Monk scale	No quoted data, but when comparing the use of a single and dual detectors at melanin	Dual ratio pulse oximeter approach may compensate for subject specific differences in individuals such as skin pigmentation, in comparion to traditional single distance pulse oximeters. However, haemodynamic

				concentrations of 1% and 43% (Very light – very dark skin), the single detector approach showed greater differences in uncalibrated SpO_2 in comparison to the dual detector approach.	heterogeneity may play a bigger role in SpO_2 discrepancies in comparison to differences in melanin.

LOA: Limits of agreement, SD: Standard deviation, pp: Percentage points, *Bias= SpO_2 - SaO_2, **Bias= SaO_2 - SpO_2

5.5.Summary

In this chapter, the literature concerning the effect of skin pigmentation on pulse oximeter accuracy was presented and has shown that discrepancies in SpO_2 measurement in individuals with darker skin pigmentation remains inconclusive. From this review, 80% of the studies found that SpO_2 was overestimated in darker-skinned individuals, especially at lower oxygen saturation levels, including wider precision and bias ranges in comparison to White subjects. Furthermore, occult hypoxaemia was found to occur more frequent in Black patients, raising concerns about delayed treatment and increased mortality rates. However, methodological inconsistencies, including insufficient representation of dark-skinned subjects and variable skin stratification techniques increases ambiguity and may justify some of the statistically insignificant biases. The lack of standardised guidelines for clinical significance and variability in pulse oximeter performance underscores the need for further research to understand the possible underlying causes of these inaccurate measurements.

CHAPTER 6: MODELLING SKIN PIGMENTATION USING THE MONTE CARLO TECHNIQUE

Monte Carlo modelling is a powerful computational technique widely used in biomedical optics to model light–tissue interactions. Its significance lies in its ability to account for complex tissue geometries and stochastic light scattering and absorption events. They are also useful for a range of applications, such as predicting the distribution of tissue chromophores [171], deriving the optical properties of tissue layers and constituents [172], and analysing photon behaviour in complex biological structures and different sensor configurations [173]. Meglinski and Doronin [174] state the advantages of the MC method over other methods used to model light-tissue interactions. For instance, in comparison to the random walk model, it considers biological heterogeneity, which arises from the non-uniform composition of blood and skin pigment distributions, and more. Other advantages include the ability to produce accurate results whilst offering flexibility with regards to the size, shape and position of the optical source and detector. Moreover, the diffusion theory neglects the 'ballistic' nature of photon propagation in a medium dominated by scattering [175], which is an essential representation of biological tissue. Nevertheless, the main drawback with MC simulations could be its long computation time, however this is not considered to be a fundamental problem owing to advances in computer technology. A summary of the advantages and limitations of the Monte Carlo method for simulating light-tissue interactions over other techniques is presented in Table 6-1.

Table 6-1: Comparison between different computational methods for modelling light-tissue interactions.

Method	Advantages	Limitations	Relevance to Study
Monte Carlo simulation (MCS)	Highly accurate for modelling complex tissue structures and heterogeneous tissue properties [176]. Capable of accounting for scattering, absorption, and tissue heterogeneity, providing a statistically detailed simulation of light transport and interaction [177].	Can be computationally expensive, requiring significant computational resources and time [178].	Provides high accuracy and reproducible outcomes by running a very high number of photon iterations, making it ideal for studying their stochastic nature in light–tissue interactions as pigmentation changes.
Finite element method (FEM)	Suitable for solving complex systems particularly in laser-based applications [179], [180].	Less accurate in modelling light scattering and absorption compared to MCS [181].	FEM can be less suited for pulse oximetry applications to model the complex scattering events in tissues such as skin.
Finite different method (FDM)	Useful for solving the light diffusion equation in simple tissue models and to achieve a balance between accuracy and computational efficiency [182].	Assumes constant tissue properties, limiting its application in heterogeneous tissues like skin [183].	FDM is more suited for simpler models of tissue and may be faster for initial simulations but lacks the precision needed for accurately modelling light absorption and scattering in tissues like skin with varying pigmentation.
Diffusion approximation	Computationally efficient for modelling light transport in scattering media especially in deep tissue [184].	Less accurate for tissues with high absorbing properties [185].	Diffusion approximation is better suited for modelling light in deep tissues rather than superficial layers, which is the main focus of this study. Like FEM, it is also not ideal for predicting radiative transport in turbid media such as the human finger.

From Chapter 3, we established that skin pigmentation is a complex structure, making it important to understand how it can be modelled within the capabilities of Monte Carlo simulations. Monte Carlo methods are highly versatile in simulating different anatomical regions. Therefore, this chapter will explore how skin pigmentation has been modelled in various tissue sites beyond the finger. The skin is the largest organ in the human body, making pigmentation a potential confounding factor for accurate PPG acquisition beyond finger oximetry, for instance in applications such as cerebral oximetry [186], [187]. It has been referenced as a tool to better understand sensor reflectivity and its impact on cerebral light-tissue interactions, in combination with in vitro experiments utilising tissue mimicking phantoms [188].

In order to justify the methodological approach employed to incorporate skin pigmentation in the models presented in this thesis, a review of the literature looking at modelling skin pigmentation using the Monte Carlo technique is conducted. Similar to the search method employed in Chapter 5, the same databases were used with the following search terms to identify the relevant sources: ‘skin pigmentation’, ‘Monte Carlo simulation’, ‘melanin’. Some of the studies that were not retrieved via the databases were also found from some of the identified publications. The inclusion criteria for this review involved studies that developed Monte Carlo models of pigmented skin in any anatomical region.

6.1.Literature search outcomes

A total of 388 sources were identified across four databases, including 320 from Google Scholar, 17 from PubMed, 44 from Scopus, and 7 from IEEE Xplore. Titles and abstracts were initially screened, eliminating 229 sources. Additional exclusions were made for studies not in English (3), animal-based research (7), ocular oximetry applications (11) as they are unrelated to skin modelling, duplicates (25), and unavailable sources (10). Further removals included studies using diffuse approximation models (4) which assume a simplified light propagation approach, the Kubelka-Munk theory (1), and research employing the inverse Monte Carlo method to calculate melanin concentration (32), which is different from the forward simulations required for the studies in this thesis. Additionally, theses were also excluded to prioritise peer-reviewed research (21), leaving 45 sources for review and analysis. Of these studies, seven maintained a constant melanin concentration or skin type ranging from light to moderate skin [173], [189], [190, p. 12 - 194], but were still included as their methodological approach for representing skin pigmentation was relevant to the scope of this Chapter. The

remaining 38 sources modelled a range of skin pigmentation levels/groups, sharing some similarities in their approach [64], [171], [195-230]. A table summarising the applications and the range of skin types considered in the models are presented below in chronological order by year of publication (Table 6-2).

Table 6-2: Pertinent studies that modelled skin pigmentation using the Monte Carlo technique (available to access).

Study	Application	Skin type range
Meglinski (2001) [192]	Study how different optical properties (e.g., blood volume, oxygenation, melanin, and water content) affect skin reflectance for in non-invasive optical diagnostics.	10% melanin concentration
Reuss (2005) [64]	Investigate how melanin absorption affects SpO_2 calibration in reflectance pulse oximetry.	5%, 10%, 20% melanin concentrations.
Chen et al (2007) [171]	Investigate the effect of melanin content and distribution on skin reflectance and fluorescence spectra for non-invasive skin diagnostics, vitiligo assessment, and melanin quantification.	Normal skin: (Slightly increased melanin content). Vitiligo skin: (lower melanin content). Blue vitiligo skin: Melanin relocated to the dermis instead of the epidermis.
Ramella-Roman & Hidler (2008) [211]	Estimate skin oxygen saturation using reflectance spectroscopy while accounting for melanin's effect on optical absorption.	No range specified.
Fredriksson et al (2009) [212]	To model how melanin concentration affects Laser Doppler Flowmetry (LDF) measurements of skin microcirculation.	0% to 50% melanin concentrations, from very light to very dark skin.
Swearingen et al (2010) [203]	Improves Monte Carlo simulations for applications in non-invasive skin diagnostics, laser treatments, and optical imaging.	Different concentrations of oxyhaemoglobin, deoxyhaemoglobin, melanin, and bilirubin are varied to simulate numerous skin colour (exact number not stated).
Maeda et al (2010) [194]	Improve the accuracy of spectral reflectance modelling for skin tissue for skin optics research, dermatology, and cosmetics.	Exact melanin range is not stated. The study was conducted on Japanese skin, so melanin concentration can be assumed moderate (10 – 15%).
Liu et al (2011) [199]	A fibre-based tissue oxygenation monitor with integrated scattering corrections to improve accuracy in skin measurements.	Volunteers categorised as white, brown, and black.
Yudovsky et al (2012) [215]	Separate the effects of melanin absorption in the epidermis from	Melanin molarity: 0.01 and 0.06 μM = Light

	blood absorption in the dermis to improve tissue oxygenation measurements.	and dark skin.
Okamoto et al (2013) [228]	Investigates how melanin concentration, particle size, and refractive index influence skin reflectance for cosmetic science, particularly foundation makeup for covering hyperpigmentation.	5% to 10% melanin concentrations.
Quintanar et al (2013) [196]	Calibrate a pulse oximeter for different melanin concentrations and skin thicknesses, and photodynamic therapy.	3.8%, 13.5%, and 30.5% melanin concentration = Light, moderate, and dark pigmented, respectively
Karsten & Singh (2013) [197]	Quantify the effect of epidermal absorption and thickness on fluence rate loss and adjust treatment time accordingly based on skin type.	No range specified (3)
Denstedt et al (2014) [205]	To extract spectral features from hyperspectral imaging of tissue and correlate them with physical parameters such as melanin concentration, oxygenation, and blood volume.	0.5% and 6% melanin concentrations.
Huang et al (2015) [221]	Reduce measurement artifacts caused by melanin concentration, scattering, and blood absorption using a multispectral imaging algorithm for noncontact and quantitative assessment of cutaneous tissue oxygen saturation.	Melanin concentrations: 2% (Caucasians), 13% (Asians), 30% (Africans).
Zhao et al (2016) [190]	Model in vivo Raman spectroscopy of skin and analyse how light propagates and is absorbed in different layers of skin, particularly in the epidermis and dermis. Relevant to skin cancer diagnosis.	Light skin
Ghassemi et al (2016) [198]	Investigate the effect of melanin content on laser-induced heating in breast cancer imaging.	Melanin concentrations: 1% (Type II - Light skin), 13.5% (Type IV - moderate skin), 30.5% (Type VI - dark skin)
Akaho et al (2017) [195]	Analyse the relationship between dark circles and chromophore concentrations (e.g., melanin, haemoglobin) for cosmetic applications.	1% - 10% melanin concentration

Mustafa et al (2017) [219]	Analyse how melanin and hydration affect near-infrared (NIR) reflectance for body fat measurement in neonates.	Melanin concentrations: 1% and 30% = Caucasian and African skin, respectively
Burns et al (2018) [214]	Evaluate light absorption at different melanin levels and explore ways to improve laser therapy outcomes for darker skin tones.	Melanin concentrations: 4%, 15%, and 50% = Lightly, moderately, and heavily pigmented skin
Li et al (2018) [218]	Develop an optimised version of the Kubelka-Munk Genetic Algorithm (KMGA) for fast multispectral skin lesion assessment.	1% - 43% melanin concentrations
Hung et al (2019) [189]	Track how UV light interacts with skin layers and calculate the absorbed UV power at different hair follicle depths.	Caucasian skin types I-II
Chatterjee & Kyriacou (2019) [173]	Analyse light-tissue interactions in reflectance and transmittance PPG.	10% melanin concentration
Verdel et al (2019) [206]	Combining Pulsed Photothermal Radiometry (PPTR) and Diffuse Reflectance Spectroscopy (DRS) with Monte Carlo modelling to assess optical and physiological properties of skin such as melanin concentration, blood content, etc.	1.3% - 1.9% melanin concentrations (Caucasian skin).
Naglič et al (2019) [224]	Monitoring physiological changes in skin reflectance from melanin variations due to sun exposure.	No exact range specified. Example values from figures suggest melanin concentrations of around 0.5% and 1.5%.
Zhang et al (2019) [225]	A correction model to account for melanin's inhomogeneous distribution for reflectance spectroscopy in heavily pigmented skin.	No exact range specified but simulates dark skin types IV-VI.
Chatterjee et al (2020) [191]	Investigate the origins of the PPG signal by focusing on the impact of absorbance, reflectance, and penetration depth at multiple wavelengths and different skin layers.	10% melanin concentration
Ying et al (2020) [193]	Investigate the effect of melanin distribution on laser therapy for port wine stain treatment and improve parameter selection for laser thermotherapy.	5% melanin concentration
Hernández-Quintanar et al	Improve accuracy of pulse oximetry measurements by	Melanin concentrations: 3.5% (lightly

(2020) [222]	accounting for skin thickness and melanin content.	pigmented skin), 13.5% (moderately pigmented skin), 30.5% (strongly pigmented skin)
Robbins et al (2021) [202]	Enabling non-invasive monitoring of tumour response to chemotherapy in patients with different skin tones.	Absorption coefficients of 0.01 to 2 mm^{-1} are simulated to cover light to dark skin types. Instead of defining melanin as a fixed percentage, the study estimates melanin content dynamically using a melanin index (MI).
Boonya-Ananta et al (2021) [204]	Evaluates how skin tone and obesity affect the accuracy of PPG-based heart rate sensors in Apple Watch S5, Fitbit Versa 2, and Polar M600.	Melanin concentrations: 3% (Type I), 10% (Type II), 16% (Type III), 23% (type IV), 32% (Type V), and 42% (Type VI).
Dremin et al (2021) [213]	Assess how melanin concentration affects LDF and tissue reflectance oximetry measurements.	1% to 45% melanin concentrations, from very light to very dark skin.
Colas et al (2021) [220]	Quantify skin layer contributions in light transport simulations to improve non-invasive skin cancer diagnostics and estimate optical properties of different skin layers.	Melanin concentrations: 1% (Phototype I, very fair), 4% (Phototype II, fair), 8% (Phototype III, moderately fair), and 11% (Phototype IV, dark).
Fine et al (2022) [201]	Investigate the effect of age, skin tone, and device wavelength on PPG signal strength and feature extraction for blood pressure estimation.	3% - 30% melanin concentrations.
Althobaiti (2022) [207]	Optimise a dual-channel near-infrared (NIR) glucose sensor for different skin colours for signal-to-noise ratio (SNR) and dermis sensitivity.	Melanin concentrations: 2%, 10%, 20%, and 30%, representing various skin tones from light to dark.
Nishidate (2022) [210]	Estimation of blood oxygen saturation and haemoglobin concentration in skin using an RGB camera.	1% to 10% melanin concentrations.
Harrison-Smith et al (2022) [231]	Investigate and reduce racial bias in transcutaneous bilirubin and pulse oximetry measurements.	Light, mixed, and dark skin. No exact values specified.
Hou et al (2022) [227]	Investigates how optical property changes (due to ischemia and	Melanin concentrations: 2% (Caucasian), 13%

	hyperemia) affect NADH fluorescence measurements.	(Asian), 30% (African)
Arefin et al (2022) [229]	Investigate racial bias in pulse oximeter calibration by assessing how different racial enrolment distributions impact SpO_2 calibration accuracy.	Melanin concentration is stochastically sampled to create 1200+ skin pigmentation models a range of pigmentation levels. No exact range specified.
Chen et al (2023) [200]	To correct melanin and haemoglobin absorption in a non-invasive method to measure bilirubin concentration in adults for liver monitoring.	Absorption coefficients of 0.01 to 2 mm^{-1} are simulated to cover light to dark skin types
Bolic (2023) [223]	Analyse the effects of melanin concentration and air gap depth on the accuracy of reflectance-mode pulse oximeters.	Melanin concentrations: 0.3%, 3%, 8%, 12%, and 16%.
Else et al (2024) [209]	Investigate how skin melanin concentration affects photoacoustic imaging (PAI) and blood oxygenation measurements.	2% to 40% melanin concentrations (Skin Types I – VI).
Larsson et al (2024) [216]	Estimate blood oxygen saturation in real time from multispectral imaging for clinical applications such as ischemia detection, microcirculatory studies, and wound healing assessment.	Melanin molarity (μM) is randomised. No exact values specified.
Van Lankveld et al (2024) [226]	Evaluates the effect of skin pigmentation on light penetration and energy deposition in the brain at different wavelengths.	Caucasian (light), Asian (medium), and African (dark). No exact range specified.
Narayana Swamy et al (2024) [230]	Provide solutions for overestimated oxygen saturation in heavily pigmented skin types via pulse oximeter design.	5% and 25% melanin concentrations (Light (Type II) and dark (Type V), respectively).
Reiser et al (2025) [208]	Assess signal loss due to melanin absorption, compare different calibration models, and suggest improvements for skin colour-adapted pulse oximeter calibration	Melanin concentrations: 2.55%, 5.5%, 10.5%, 15.5%, 20.5%, 25.5%, and 30.5%, representing various skin tones from light to dark.

6.2.Optical characterisation of the epidermis

Accurate characterisation of epidermal optical properties is fundamental to Monte Carlo modelling of skin pigmentation. The ability to simulate light-tissue interactions depends on defining absorption and scattering coefficients and other optical properties that represent the epidermis as realistically as possible. There are three primary approaches to obtaining this data: analytical equations, experimental values from the literature, and hybrid methods that incorporate elements of both. Each approach presents distinct advantages and limitations, which must be critically evaluated to determine their applicability in each modelling framework.

6.2.1. Analytical equations

Analytical equations are mathematical formulations that are used to describe relationships based on theoretical models and empirical data from absorption spectra. From this, the absorption coefficients of dominant chromophore/s responsible for skin pigmentation are computed [64], [173], [189], [191], [194], [195], [200], [202], [203], [206], [207], [210], [214], [215], [216], [218], [224], [225], [230]. The epidermal absorption coefficient is at least characterised by a fraction of the absorption coefficient of melanin ($\mu_a melanin$) to simulate different skin types, allowing for the baseline characterisation of the epidermis without the presence of other chromophores [64], [195], [210], [218]:

$$\mu_a epi\ (\lambda) = v_{mel} \times \mu_a melanin\ (\lambda) \tag{6-1}$$

Where v_{mel} is the volume fraction of melanosomes and,

$$\mu_a melanin\ (\lambda)\ [\mathrm{mm}^{-1}] = 6.6 \times 10^{10} \lambda^{-3.33} \tag{6-2}$$

calibrated between 300 – 1100 nm [129] and used to optically characterise melanin in a number of studies [173], [191], [200], [207], [224], [227], [230]. Yudovsky et al adopted the same principle by defining the extinction coefficient of the epidermis (ε_{mel}) as a function of wavelength and chromophore concentration (C_{mel}) [215]:

$$\mu_a epi\ (\lambda) = C_{mel} \times \varepsilon_{mel}\ (\lambda) \tag{6-3}$$

Where ε_{mel} can be calculated using the empirical equation [171], [221]:

$$\varepsilon_{mel} = 1.7 \times 10^{11} \lambda^{-3.48} \quad (6\text{-}4)$$

Nevertheless, accounting for absorption of light by multiple chromophores in the epidermis provides a more physiologically accurate representation of how light interacts with skin. While melanin is the dominant absorber in the visible and near-infrared spectrum, water absorption becomes significant at longer wavelengths. Neglecting water content, for example, could lead to errors in absorption calculations at wavelengths such as 940 nm, where water contributes substantially to light attenuation. Additionally, many studies report cumulative absorption coefficients for the epidermis, which inherently include contributions from water and other absorbers, such as bilirubin, carotene, etc. As a result, this creates better alignment of simulated optical property values with experimental data by utilising the eq. (6-5), adapted from eq. (6-1) [173], [191], [206], [207], [214], [219], [220], [227], [230]. Since the sum of all tissue chromophore concentrations is equal to 1, the volume fractions of melanin and water are subtracted from 1 to calculate the contribution of background absorption:

$$\mu_a epi\ (\lambda) = v_{mel} \times \mu_a melanin\ (\lambda) + v_{water} \times \mu_a water\ (\lambda) + (1 - v_{water} - v_{mel}) \times \mu_a baseline \quad (6\text{-}5)$$

While accurately distinguishing the baseline absorption coefficient values for a melanin-free epidermis and a blood-free dermis has been challenging, the baseline absorption for both layers is approximated. The following equation is based on measurements of bloodless rat skin using an integrating sphere calibrated with phantom measurements, also between 350 nm - 1100 nm [129], [224]:

$$\mu_a baseline = 0.0244 + 8.53 e^{\frac{154-\lambda}{66.2}} \quad (6\text{-}6)$$

Additional data was collected between 450 nm and 750 nm using in vitro neonatal skin samples to improve the relevance of sample characterisation to human skin after accounting for excess absorption due to residual haemoglobin and bilirubin. From this data, the following baseline equation was derived [129]:

$$\mu_a baseline = 7.84 \times 10^{8} \lambda^{-3.255} \quad (6\text{-}7)$$

At 660 nm, skin baseline calculations are 0.0285 mm^{-1} and 0.521 mm^{-1}, and 0.0245 mm^{-1} and 0.165 mm^{-1} at 940 nm, using eq. (6-6) and eq. (6-7), respectively. Optically, rat skin and neonatal skin exhibit strong similarities, so it is unsurprising that their baseline values at the two wavelengths are nearly identical when using eq. (6-6). Nevertheless, these calculated baseline values account for absorption by other chromophores more accurately due to the wavelength dependence of melanin, in comparison to assuming a constant background absorption level, as conducted by Denstedt et al, which does not account for wavelength dependence [205]:

$$\mu_a epi\ (\lambda) = \mu_a background + v_{mel} \times \mu_a melanin\ (\lambda) \quad (6\text{-}8)$$

Where $\mu_a background$ was set to 25 mm^{-1}

The equivalent equation for multiple chromophore absorption with the extinction coefficient and concentration of a substance is [200], [203], [213]:

$$\mu_a epi\ (\lambda) = C_{mel} \times \varepsilon_{mel}\ (\lambda) + C_{water} \times \varepsilon_{water}(\lambda) + \sum_n^i C_{i\ldots n} \times \varepsilon_{i\ldots n}(\lambda) \quad (6\text{-}9)$$

for *n* number of chromophores.

While the benefits of accounting for other skin chromophores have been highlighted, this approach also adds complexity, as each chromophore must be assigned a specific concentration, which can vary between individuals and anatomical locations. This could explain why Harrison-Smith et al [217] and Arefin et al [229] stochastically assigned a combination of different melanin, haemoglobin, and bilirubin properties to each 'patient' to model more realistic inter-patient variability. This way, when physical tissue samples are not accessible, more representative cohorts can be simulated, accounting for skin optical differences as discussed in Chapter 3.

Other specific equations were used to calculate the absorption coefficient of the epidermis for different applications. For instance, Larsson et al used an equation that also follows an inverse power-law dependency on wavelength, in addition to a pre-defined proportionality constant (*k*) related to the specific absorption properties of melanin [216]:

$$\mu_a epi\ (\lambda) = v_{mel} \times k(\frac{\lambda}{\lambda_0})^{-3.3} \quad (6\text{-}10)$$

Where k was 39 mm^{-1} and λ_0 is the reference wavelength in nanometres.

While this equation may be computationally efficient in capturing melanin's spectral behaviour, additional work may be required to define k for other chromophores. Also, its empirical nature implies that it may not generalise well beyond certain wavelengths, with the reference wavelength being 550 nm. The equation's inapplicability becomes more apparent for NIR tissue characterisation at even shorter wavelengths, such as UV. Huang et al focused on modelling light tissue interactions in this range (280 nm – 400 nm) and used data from previous work to form the following equations [189]:

$$\mu_a epi\ (\lambda) = -1.125 + \frac{1011}{\lambda - 265.8} \tag{6-11a}$$

$$\mu_s epi\ (\lambda) = \mu_s dermis\ (\lambda) = 600.26e^{-0.005\lambda} \tag{6-11b}$$

$$n_{epi}(\lambda) = 1.395 + \frac{26.57}{\lambda} + \frac{0.2203}{\lambda^{3.5}} \tag{6-11c}$$

$$g_{epi}(\lambda) = 0.62 + 2.9 \times 10^{-4}\lambda \tag{6-11d}$$

Although they do not account for changes in skin pigmentation and only Caucasian skin, these equations present the utilisation of spectra to derive equations that define the relationship between not only the absorption coefficients of the epidermis, but also the scattering coefficient, refractive index, and anisotropy factor of the epidermis. Yet, scattering is often approximated using dermal properties rather than those specific to the epidermis. This assumption can be problematic, as the structural and compositional differences between the epidermis and dermis result in distinct scattering behaviours.

Furthermore, distinguishing between eumelanin and pheomelanin absorption (Chapter 3.1) can provide a more detailed representation of pigmentation variability as they both have different spectral absorption and scattering properties. However, as the case with accounting for other chromophores, accurate concentrations and ratios of these components for different individuals, as well as the limited availability of spectral data for pheomelanin, may complicate the methodological approach for later analysis. These melanin components were not modelled separately in any of the studies using analytical equations for optical property classification, however they can be considered in skin pigmentation modelling in the basal layer of the epidermis [232]:

$$\mu_a eu\ (\lambda) = 6.6 \times 10^{10} \lambda^{-3.33} \quad \text{(6-12a)}$$

$$\mu_a pheo\ (\lambda) = 2.9 \times 10^{14} \lambda^{-4.75} \quad \text{(6-12b)}$$

Evidently, Jacques et al [129] characterise melanin based on brown and black colouration (eq. (6-2)) which can be reasonable for simulating a range of skin pigmentation levels by varying concentration. The yellow to reddish hue from pheomelanin can change the optical behaviour of the epidermis, but implementing exact concentrations of each component may be more applicable to skin cancer or UV-induced diagnoses. Overall, these equations offer a structured and theoretically grounded means of estimating optical properties, but they can be constrained by the wavelength ranges for which they were originally calibrated. From all the equations utilised in the above studies, Jacques' equations show to be well-suited for pulse oximetry modelling, as they provide the most reliable representation of melanin's absorption behaviour across red and infrared wavelengths.

6.2.2. Spectrophotometry measurements

An alternative approach to these mathematical formulations is the use of optical properties derived from experimental literature [190], [194], [196], [197], [198], [199], [201], [204], [208], [209], [211], [217], [222], [223], [228], [229]. Empirical measurements of skin optical properties provide direct estimates of absorption and scattering coefficients, which may be considered more representative of real tissue behaviour than theoretically derived values. However, the reliability of these literature-derived properties is highly dependent on the experimental conditions under which they are obtained. Differences in measurement techniques, subject demographics, and chromophore isolation methods contribute to substantial variability in reported values. For instance, cumulative absorption coefficients can be a challenge when attempting to parameterise them separately in a Monte Carlo model, as the relative contributions of each chromophore may not be explicitly stated. However, having more than one approach to characterise tissue optically can provide a means of numerical validation. Using melanin absorption coefficient data from Alhallak [233] and Jacques equation (eq. (6-5)), $\mu_a melanin$ values can be calculated and compared at specific wavelengths. As shown in Table 6-3, the values from the literature and calculations are in broad agreement with each other, although comparisons with other sources can help reinforce confidence in the values to

be inputted in the model. Similarly, optical properties that are correlated with different melanin concentration levels or skin groups may serve as a benchmark for calculated epidermal absorption coefficients [201], [233] (Table 6-4 and Table 6-5).

Table 6-3: Comparison between calculated and spectroscopy- based melanin absorption coefficients at different wavelengths.

Wavelength (nm)	532	755	1,064
$\mu_a melanin$ from literature [mm^{-1}]	55.5	16.3	5.0
$\mu_a melanin$ from calculations (eq (6-2)) [mm^{-1}]	55.2	17.2	5.5

Table 6-4: Optical properties of the epidermis extracted from [201].

		515 nm	660 nm	880 nm
$\mu_a[\mathrm{mm}^{-1}]$	v_{mel} = 3%	0.196	0.086	0.033
	v_{mel} = 10%	0.628	0.275	0.106
	v_{mel} = 20%	1.243	0.544	0.209
	v_{mel} = 30%	1.858	0.813	0.313
$\mu_s[\mathrm{mm}^{-1}]$		38.84	30.30	22.73

Table 6-5: Optical properties of the epidermis extracted from [233].

		585 nm	595 nm	810 nm	940 nm	1064 nm
$\mu_a[\mathrm{mm}^{-1}]$	Light	6.071	5.738	2.065	1.266	0.845
	Moderate	20.15	19.045	6.824	4.162	2.759
	Heavy	38.252	36.153	12.944	7.885	5.220
$\mu_s[\mathrm{mm}^{-1}]$		15.606	14.869	14.802	10.527	8.137
g		0.8	0.8	0.91	0.91	0.91

Similar to Huang et al study (eqs. (6-11a) – (6-11d)), the scattering and anisotropy values are assumed constant for all skin levels/groups, highlighting the complexities of characterising

these optical properties which rely on structural variations at the microscopic level. Hence, it is easier to obtain absorption coefficients for different skin colours because absorption is primarily dictated by the concentration and spectral properties of well-defined chromophores, making it a more direct and quantifiable process following the simple Beer Lambert law. Furthermore, melanin's absorption can be measured using controlled techniques like diffuse reflectance spectroscopy [197], where the absorption spectra can be extracted from known melanin concentrations in isolated or reconstructed skin samples, which makes it possible to derive relatively consistent absorption coefficient values across different skin tones. Even so, scattering coefficient values cannot be stochastically varied based on trends, as their relationship with absorbance, transmittance, or reflectance may not follow a linear dependence on wavelength. Therefore, current Monte Carlo models may need to assume constant scattering coefficient values across all skin types until further advancements enable a more accurate representation of scattering behaviour for different levels skin pigmentation.

6.2.3. Hybrid approach

In attempt to address the limitations imposed by both methods, some models adopt a hybrid approach by combining analytical equations with literature-derived optical values to better define the optical properties of skin at specific wavelengths of interest and tissue layers that are not always accessible. A common example involves using calculated absorption coefficients for melanin while obtaining water absorption coefficients from experimental data [173], [191]. This method leverages the strengths of both approaches by combining the flexibility of theoretical models with the empirical accuracy of measured optical properties. However, it may introduce the risk of inconsistency if values from different sources are not fully compatible with each other. For instance, if melanin absorption is estimated based on a specific assumed concentration, while water absorption is taken from a study that used different baseline conditions, the resulting cumulative optical properties may not accurately reflect real epidermal tissue. Ensuring coherence between theoretical and empirical data is therefore crucial in hybrid modelling strategies, however, this cannot always be guaranteed due to the unavailability of data from the same setup with the specific tissue components required. Establishing such a dataset would provide a more reliable source of optical property values that can be used for analytical calculations, particularly when spectrometry-based equipment is unavailable.

6.2.4. Optical properties and skin classification systems

To establish a sense of familiarity across various biomedical research fields, some studies have attempted to bridge this gap by correlating optical properties with skin classification systems such as the Fitzpatrick scale [197], [198], [202], [204], [205], [206], [209], [213], [215], [220], [224], [225], [230]. This approach provides a practical framework for categorising skin types based on pigmentation characteristics, enabling the assignment of optical properties to pre-defined skin groups. For instance, Ajmal et al [204] used an epidermal absorption coefficient of 0.1865 mm^{-1} corresponding to FST I, and 2.4668 mm^{-1} for FST VI, which is particularly relevant in dermatological research. They further employed the Individual Typology Angle (ITA°) as an alternative classification metric, which offers a continuous rather than categorical representation of skin colour. While these classification methods facilitate structured modelling, their effectiveness depends on the accuracy of the underlying melanin concentration estimates. Since the Fitzpatrick scale was originally developed based on UV sensitivity rather than direct pigmentation measurements, its correlation with optical properties is not always straightforward but can be used as a guide for current regulations in skin stratification. Similarly, the ITA method, while more useful for quantitative validation purposes, relies on surface reflectance measurements that do not necessarily capture deeper melanin distributions.

6.3.Discussion

Owing to advancements in spectroscopy, Monte Carlo models have become increasingly capable of simulating a wide range of physiological parameters, enhancing their versatility in biomedical applications. By integrating spectroscopic data, these models can incorporate wavelength-dependent absorption and scattering properties of tissue and subcomponents, enabling more precise representations of skin and its influence on light propagation. This adaptability is particularly valuable in non-invasive diagnostic techniques, where subtle variations in tissue composition can significantly affect measurement accuracy. Early studies, like those by Reuss [64] and Meglinski [192], focused on melanin absorption's impact on reflectance and SpO_2 calibration but used limited concentration ranges. By the late 2000s, research expanded to non-invasive diagnostics and spectroscopy, incorporating broader melanin variations [171], [211] and other skin chromophores such as bilirubin [194], [203]. Post COVID-19, studies introduced dynamic melanin estimations [202] and addressed racial bias in device calibration [217], [229]. Machine learning and optimisation techniques have

further enhanced simulation accuracy and real-time analysis [218]. However, the reliability of these simulations depends on how the optical properties of the epidermis are characterised. The methodological approaches discussed above offer distinct advantages and limitations when applied to Monte Carlo modelling, so an analysis of these methods is essential to determine their suitability for representing skin pigmentation depending on the intended application.

Firstly, analytical equations have shown to provide a theoretical framework for calculating absorption and scattering coefficients but are limited by the wavelength range over which they are calibrated. Many studies use similar power-law equations for melanin absorption, allowing for comparability between different research works. Secondly, literature-derived optical properties, while empirically validated, often represent averaged values that may not fully capture individual variability, which highlights the difficulty of obtaining universally comparable optical properties. Other device-related methodological differences may include the choice of light source and detection system which further complicates comparisons, as some techniques measure total attenuation rather than pure absorption. Thirdly, hybrid methods attempt to integrate the strengths of both approaches, yet inconsistencies in parameter selection can introduce uncertainties in simulations. Stochastic sampling of chromophore concentrations can help address the limitation of lack of data on interindividual skin variability; however, it may impose challenges in output variable interpretation. In relation to pulse oximetry studies, the implementation of multiple physiological factors influencing light absorption may make it difficult to justify potential inaccuracies in simulated SpO_2. Hence, it is essential to isolate and analyse each confounding factor on SpO_2 measurement, such that any changes observed can be more reliably attributed to specific independent variables.

Beyond the inherent differences in the chemical composition of different skin types, other factors such as epidermal thickness must be considered. Changing the thickness of the epidermis also changes the probability of photons localising inside it. As a result, differences in output absorbance are likely, especially with transmittance mode pulse oximeters when used on dark skin individuals. In this case, the melanin index, which is a product of the epidermal thickness and the epidermal absorption coefficient, can be implemented in a Monte Carlo model [202]. A further consideration is the spatial distribution of melanin, which includes the modelling of melanosomes that are dispersed in a specific arrangement in the epidermis. From the literature, most models assumed a homogeneous melanin distribution, while the remainder accounted for non-uniform pigmentation patterns [171], [193], [196], [212], [214], [225].

Studies that incorporate heterogeneous melanin distributions provide a more physiologically realistic representation of skin, since melanin is not uniformly dispersed across the epidermis (Chapter 3). However, the extent to which such complexity improves simulation accuracy must be weighed against its impact on computational efficiency, although studies investigating skin disorders like vitiligo, should prioritise this type of accurate melanin distribution [171]. Therefore, the choice of melanin quantification metric, whether melanin concentration, melanin index, or melanin molarity, must be carefully considered based on the intended purpose of the model. Among the various equations used to compute the absorption coefficient of the epidermis using different melanin metrics, Jacques' equations remain one of the most widely used in Monte Carlo light tissue interactions, especially for pulse oximetry applications.

Overall, the progression of Monte Carlo modelling in skin pigmentation research has transitioned from basic reflectance simulations to highly detailed models integrating multiple physiological and optical parameters. The field has seen improvements in accuracy, the inclusion of a wider range of pigmentation levels, and a focus on mitigating biases in biomedical applications. While early studies provide foundational insights on skin pigmentation modelling, modern research now emphasises individualised and adaptable models, leading to more accurate diagnoses and device calibration. While no single approach provides a perfect solution, these advancements and considerations provide a guideline for selecting an appropriate methodological approach for modelling skin pigmentation using the Monte Carlo technique in the forthcoming studies. Currently, a combination of validated absorption coefficients and theoretically derived models appears to offer the most robust framework to understand the effect of skin pigmentation on SpO_2 outcomes.

6.4.Summary

This chapter provides a comprehensive literature review on how skin pigmentation is modelled using the Monte Carlo method. It examines studies that meet specific inclusion criteria, highlighting their medical applications and the range of simulated skin types. The studies use either analytical equations, literature-derived optical properties, or a combination of the two, to optically characterise the epidermal layer, which is responsible for skin pigmentation appearance. The advantages and limitations of each approach are critically analysed, offering insights into the most suitable method for skin modelling in the forthcoming studies.

CHAPTER 7: DEVELOPMENT OF THE MONTE CARLO MODEL

A Monte Carlo model simulates the path of virtual photon clusters as they travel through biological tissue with defined optical properties (μ_a, μ_s, g, n), as described in Chapter 2. Photons propagate in 3D space using a Cartesian coordinate system (*x, y, z*) and spherical polar coordinate system, which is essential for accurately illustrating the distribution of light in all possible directions in various tissue structures such as slabs, spheres, or cylinders. Both monolayer and multilayer models can be constructed to investigate light-tissue interactions in a single homogeneous layer, or to consider heterogeneity by combining multiple homogenous layers together in a specific arrangement which mimics the structure of the region of interest as much as possible.

7.1. Coordinate systems

Along with the Cartesian coordinate system, the Monte Carlo model also incorporates a spherical polar coordinate system to track photon movement within the tissue [234]. When they interact with scatterers in the tissue and its path changes, the resulting directional shift is first computed in the spherical polar system before being converted to the Cartesian coordinate system.

To represent the direction of a photon at any given point, a vector $\vec{r}$ is used. In the spherical polar coordinate system, this direction is defined by the deflection angle (θ), and the azimuthal angle (φ) as illustrated in Figure 7-1. In the Cartesian system, the position vector $\vec{r}$ forms angles with α, β, and γ with the x, y, and z axes, respectively. These relationships allow the transformation between the spherical polar and Cartesian coordinate systems through direction cosines given by u_x, u_y, u_z.

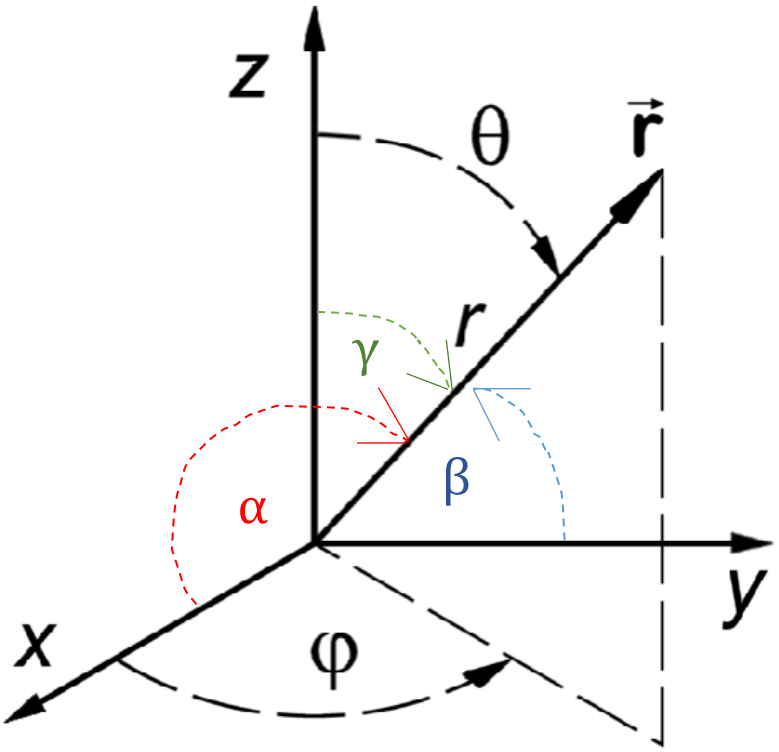

Figure 7-1. The relationship between the spherical polar coordinate and Cartesian coordinate system.

To derive the direction cosines, we must first calculate the length of the triangles formed by each axis relative to the vector $\vec{r}$, expressed in terms of the angles θ and φ. For the z-axis, the calculation of u_z is straightforward, as it corresponds to the projection of $\vec{r}$ along the z-axis, which is given by cos(θ). However, the calculations for the x and y components require more steps than this. As illustrated in Figure 7-2, the vector $\vec{r}$ creates both vertical and horizontal projections relative to the xy-plane. The vertical projection is common for both the x and y components, and the length of this projection in terms of θ is given by sin(θ). Then, to determine the x and y components of the horizontal projection in terms of φ with respect to $\vec{r}$, the following illustration can be used:

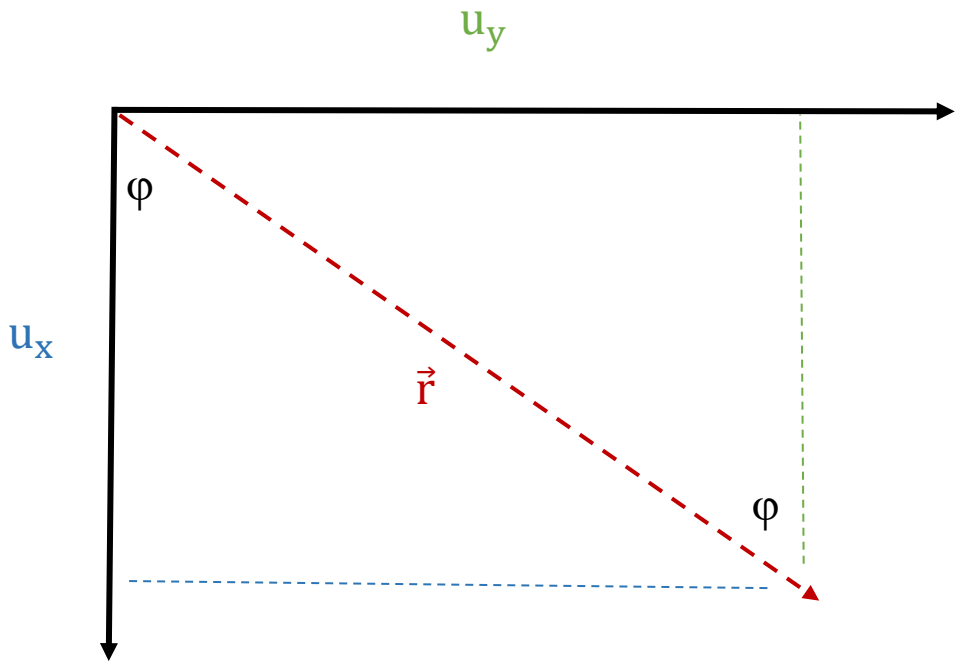

Figure 7-2. Two-dimensional geometric representation of photons travelling between the x and y planes. Trigonometric functions are used to calculate the x and y direction cosines using the azimuthal angle.

This gives trigonometric functions of $\cos\theta$ and $\sin\varphi$ in the x and y axes respectively, which when combined with the functions for $\vec{r}_{yz}$ and $\vec{r}_{xz}$, yields the following equations:

$$u_x = \cos\alpha = \sin\theta\cos\varphi \quad (7\text{-}1a)$$

$$u_y = \cos\beta = \sin\theta\sin\varphi \quad (7\text{-}1b)$$

$$u_z = \cos\gamma = \cos\theta \quad (7\text{-}1c)$$

Where $= 2\pi\xi$, a randomly generated azimuthal angle between 0 and 2π to represent a full circle.

7.2. Launching photons

Several optical sources can be modelled in a Monte Carlo simulation [234], however only an optical fibre and Gaussian beam is implemented for the studies presented in this thesis. Firstly, for the optical fibre, photons are emitted from a point source with initial position coordinates (0,0,0) for simplistic modelling. The numerical aperture (NA), which determines the range of angles over which the sensor can effectively collect/emit light, was set to 0.39 to implement a fibre with a half angle of approximately 45°:

$$\theta = 2n \sin^{-1} NA \quad (7\text{-}2a)$$

Where n = 1 (refractive index of air)

So that photons are emitted randomly from the optical fibre with the cone of acceptance, a pseudo random number generator (PRNG, ξ) is factored into the equation using the MATLAB function 'rand' [234]:

$$\theta = 2\xi n \sin^{-1} NA \quad (7\text{-}2b)$$

This function generates random numbers uniformly distributed between 0 and 1 meaning each value in the range has an equal chance of being selected. It uses a deterministic algorithm, such as the Mersenne Twister, which determines the entire sequence of numbers based on an initial 'seed' value. If the same seed is used with the same settings, the sequence of random numbers will be identical each time, making experiments reproducible. This is why if the same simulation is run multiple times, it will not produce the same exact data, but it should generate the same trends observed between different inputs and outputs.

Furthermore, in the case of a collimated Gaussian beam, the photons are launched perpendicularly to the tissue (θ = 0°), which results in initial direction cosines of (0,0,1) with respect to the x, y and z axes. After that, θ is generated by rearranging eq. (7-1c), which accounts for changes after a photon undergoes scattering.

The beam is modelled as emerging from a ring-shaped source located on the tissue surface, and follows a specific radial probability distribution function:

$$p(r) = \frac{e^{\frac{-r^2}{b^2}}}{\pi b^2} 2\pi r \quad (7\text{-}3a)$$

Where r is the radial distance from the centre of the beam, and b is the radius at which the intensity falls to $1/e^2$ of its central value.

To ensure proper normalisation i.e. the sum of the probabilities of all possible events is 1 or 100%, the probability function solved over the entire area of the beam:

$$P(r) = \int_0^\infty \frac{1}{\pi b^2} e^{\frac{-r^2}{b^2}} 2\pi r \, dr = \frac{1}{b^2} e^{\frac{-r^2}{b^2}} 2r \, dr \quad (7\text{-}3b)$$

The integration can be simplified by integrating by substitution:

$$u = \frac{r^2}{b^2} \Longrightarrow du = \frac{2r}{b^2} dr \tag{7-3c}$$

$$\int_0^\infty e^{-u}\, du \Longrightarrow -e^{-\infty} - (-e^{-0}) = 0 - (-1) = 1 \tag{7-3d}$$

$$\therefore$$

In practice, this means that photons in a Gaussian beam are more likely to be densely packed near the centre of the beam, with the likelihood decreasing as you move further away from the centre. The cumulative distribution function (CDF) helps model this by stating the likelihood that a photon will be within a certain distance from the centre of the beam.

After normalising the Gaussian distribution, the integral of P(r) gives the CDF; the probability that the photon's radial position *r* is less than or equal to a particular value, which in this case, to a random number (ξ) between 0 and 1:

$$\xi = 1 - e^{-\frac{{r_1}^2}{b^2}} \tag{7-3e}$$

Solving for *r* in terms of the random number, the equation for a randomly generated radius which follows the Gaussian distribution yields to:

$$r_1 = b\sqrt{-\ln\,(1-\xi)} \tag{7-3f}$$

However, because the random number is based on a uniform distribution, flipping the value of $1 - \xi$ to ξ does not affect the outcome when applying the −ln transformation. The uniform distribution ensures that both combinations are equally likely to take any value within the range 0 and 1. For example, if ξ =0.2, then $1 - \xi$ = 0.8. Applying the negative natural logarithm transformation to both would give:

−ln(0.2) = 1.6094, and

−ln(0.8) = 0.2231

So, even though the actual numbers are different, they both follow the same overall exponential distribution. Hence, the equation for r_1 can be rewritten as

$$r_1 = b\sqrt{-\ln\,(\xi)} \tag{7-3g}$$

Then, to determine the position of the incident photons, the x and y coordinates are calculated using basic trigonometric functions:

$$x = r_1 \cos \varphi \tag{7-4a}$$

$$y = r_1 \sin \varphi \tag{7-4b}$$

$$z = 0 \tag{7-4c}$$

7.3. Photon reflection

Wang et al [234] and Jacques et al [235] employ an 'implicit capture' approach by simulating photon clusters rather than individual photons to improve computational efficiency and reduce variance. Therefore, in this thesis, the term 'photon' refers to a cluster of photons, which is defined by its weight, position, and direction coordinates. The initial weight of the photon cluster is equal to unity, and upon interaction with the tissue, a portion of the photon's weight is reflected off the surface and at the boundary. The amount of the photon's weight that is reflected is governed by eqs. (2-2) and (2-3) depending on the angle of incidence. The weight of the photon entering the tissue is given by:

$$w = w_o - (w_o * R) \tag{7-5}$$

Now the photon is ready to travel a certain step size (l). This parameter is defined as the distance that a photon travels between two consecutive interactions in the tissue, and accounts for the contributions from the absorption and scattering properties, known as the attenuation coefficient (μ_t). The probability density function for the photon step size is given by:

$$p(l) = \mu_t e^{-\mu_t l} \tag{7-6a}$$

Similar to the process for normalising the probability distribution of r in accordance with a Gaussian distribution, this is done also for $p(l)$. However, the difference here is that photon step size is bounded by the properties of the medium l_1 , while in theory, photons can be anywhere within the infinite space surrounding the centre of the beam. The PDF is integrated as follows:

$$P(l) = \int_0^{l_1} \mu_t e^{-\mu_t l}\, dl \tag{7-6b}$$

$$\Longrightarrow P(l) = \frac{\cancel{\mu_t} e^{-\mu_t l}}{\cancel{-\mu_t}} = -e^{-\mu_t l_1} - (-e^{-\mu_t 0}) = -e^{-\mu_t l_1} + 1 \tag{7-6c}$$

Once again, to generate a random step size based on the CDF:

$$1-e^{-\mu_t l_1} = \xi \tag{7-6d}$$

Rearrange for l_1:

$$l_1 = -\frac{\ln(1-\xi)}{\mu_t} = -\frac{\ln(\xi)}{\mu_t} \tag{7-6e}$$

This is used to calculate the new position coordinates (x_2, y_2, z_2) along with the direction cosines in each respective axis:

$$x_2(q) = x + l_q * u_x \tag{7-7a}$$

$$y_2(q) = y + l_q * u_y \tag{7-7b}$$

$$z_2(q) = z + l_q * u_z \tag{7-7c}$$

Where q is dependent on the optical properties of the tissue layer that the photon is positioned in in a heterogenous model. After each step, the photon undergoes absorption and scattering simultaneously.

Finally, internal reflection is accounted for in the model by checking if total internal reflection is achieved, or if the photon it is travelling only in the z direction i.e., the absolute value of u_z is equal to 1, which inverts the current z coordinate and u_z value.

7.4. Photon absorption and scattering

7.4.1. Scattering

Next, two of the most critical light-tissue interaction mechanisms – scattering and absorption– need to be modelled. In the Monte Carlo simulation, scattering is modelled based on the Henyey-Greenstein phase function, as presented by eq. (2-8) in Chapter 2.3. As we know, the polar angle and the azimuthal angle are the two angles used to define the new direction of the photon. The Henyey-Greenstein function helps us decide the polar angle based on the scattering properties of the medium, however, the azimuthal angle is used to define the rotation of the photon around its original direction. This is also assumed to be randomly and uniformly

distributed between 0 and $2\boldsymbol{\pi}$, which means that scattering has no preferred direction in the *x-y* plane.

In the Henyey Greenstein function, the '$4\boldsymbol{\pi}$' in the denominator accounts for all the angles around a sphere in 3D space. For modelling light scattering, this is important to ensure light is scattered in all possible directions. However, in Monte Carlo simulations, the photon is rotated through the azimuthal angle, which has a maximum value of $2\boldsymbol{\pi}$. To calculate a randomly generated scattering angle:

$$\cos\theta = \frac{1}{2g}\left[1 + g^2 - \left(\frac{1-g^2}{1-g+2g\xi}\right)^2\right] \tag{7-8a}$$

Using the geometric relationship between *cos(θ)* and $sin(\theta)$ for a circle:

$$sin\theta = \sqrt{1 - cos^2\theta} \tag{7-8b}$$

The new direction cosines can be calculated after a scattering event to update the value of u_x, u_y, and u_z [236]:

$$u_x{}' = \frac{sin\,\theta(u_x u_z\, cos\,\varphi - u_y\, sin\,\varphi)}{\sqrt{1-u_z{}^2}} + u_x\, cos\,\theta \tag{7-8c}$$

$$u_y{}' = \frac{sin\,\theta(u_y u_z\, cos\,\varphi + u_x\, sin\,\varphi)}{\sqrt{1-u_z{}^2}} + u_y\, cos\,\theta \tag{7-8d}$$

$$u_z{}' = -\,sin\,\theta\, cos\,\varphi\sqrt{1-u_z{}^2} + u_z\, cos\,\theta \tag{7-8e}$$

However, if the photons are extremely close to the z axis, the direction cosines given by eqs. (7-1a) and (7-1b) are used for u_{x1} and u_{y1}, respectively. For u_{z1}, this is given by eq. (7-1c), except that the sign of the vector was considered positive (+1) if the photon was towards the tissue surface, and negative (-1) if the photon was away from the tissue surface.

7.4.2. Absorption

For absorption, implicit photon capture is employed in the forthcoming MC models as mentioned above. Implicit and explicit capture methods differ primarily in how photon

absorption is modelled and recorded. Implicit capture gradually reduces the photon's weight during propagation by subtracting a fraction of the current weight of the photon at each interaction. This fraction is characterised by the albedo (Λ), a dimensionless parameter which quantifies the relative dominance of absorption and scattering in a specific medium/tissue layer:

$$wa = \left(\frac{\mu_a}{\mu_a+\mu_s}\right) * w = \left(\frac{\mu_a}{\mu_t}\right) * w = \Lambda * w \quad (7\text{-}9a)$$

$$w_{new} = w - wa \quad (7\text{-}9b)$$

This approach is computationally efficient, providing a smooth representation of cumulative energy deposition suitable for bulk tissue simulations. In contrast, explicit capture models absorption by nullifying the weight of the photon if it experiences absorption at any interaction. This method is ideal for applications such as photothermal therapy, where understanding where photons are absorbed and how much energy is deposited is critical. The location of absorption is tracked, but no energy remains in the photon after it is absorbed. However, in the employed model, if the weight of the photon cluster does not exceed the pre-defined weight threshold of 0.0001, its intensity is considered negligible due to continuous absorption and may be terminated. To address potential bias arising from photon termination at low energies that may not contribute meaningfully to the overall simulation, a probabilistic method called Russian roulette is used. With this approach, there is a chance that a photon with a weight below the threshold will survive by checking if a random number is less than 0.1, which will increase its weight by a factor of 10, or otherwise set to zero (photon termination). When a photon is terminated, a new photon is launched, and the simulation continues until the desired number of detected photons is reached or launched.

7.5. Photon detection

Another condition for terminating photon propagation is when the photon is detected. Detection occurs when the photon's position and direction align with the detection area of a ring-shaped detector placed on the tissue surface. Depending on the setup, the detector may be positioned on the same side as the photon source, in which case reflectance is measured, or on the opposite side, where transmittance is measured. Once a photon is detected, its propagation is halted, and

several variables of interest are updated. These include the total reflectance or transmittance, optical pathlength, photon weight (intensity), number of scattering events, absorbed weight in the tissue layers, distribution of scattering centres, penetration depth, etc.

Transmittance and reflectance sensor geometries are described in Chapter 4. In transmittance geometry, the detector is positioned at (0,0,*t*) where *t* is the thickness of the tissue, and in reflectance mode, the detector is positioned at (*s*,0,0), where *s* is the source-detector separation. As described above, photon trajectories are simulated based on step sizes defined by the MC algorithm, and photons that satisfy the detection criteria are recorded by the detector. In transmissive geometry, a conditional if loop statement is used to check whether the current *z* coordinate (z_2) of the photon is equal to or greater than the thickness of the tissue (*t*). This determines whether the photon is transmitted, and now to check if the photon was detected, some calculations are conducted. The step size at this point can be calculated using the following equation:

$$z + lu_z = t \tag{7-10a}$$

$$\Longrightarrow$$

$$l = \frac{t-z}{u_z} \tag{7-10b}$$

Substituting this into the equations for x_2 and y_2, the position coordinates of the photons in the x and y axes can be calculated and denoted by x_3 and y_3:

$$x_3 = (t - z) * \frac{u_x}{u_z} + x \tag{7-10c}$$

$$y_3 = (t - z) * \frac{u_y}{u_z} + y \tag{7-10d}$$

These values are then used to check if the photon 'fits' into the ring-shaped detected which has a circular cross section:

$$(x_3)^2 + (y_3)^2 < r^2 \tag{7-10e}$$

Similar calculations are completed for deriving the equation for the detection criteria of the photodetector in reflectance mode, except that z_2 is equal or less than zero as the photon is backscattered:

$$x_3 = z * \frac{u_x}{u_z} + x \tag{7-10f}$$

$$y_3 = z * \frac{u_y}{u_z} + y \tag{7-10g}$$

The entire procedure was completed for a certain number of photons (N) depending on the application and is summarised in Figure 7-3. The parameter Q, referred to as a 'convergence rate' by Subhasri et al. [237], is used as a proxy to measure simulation stability based on output variance. As Q decreases, the statistical noise in the simulation also decreases and hence predicts more reproducible outcomes:

$$Q \propto 1/\sqrt{N} \tag{7-11}$$

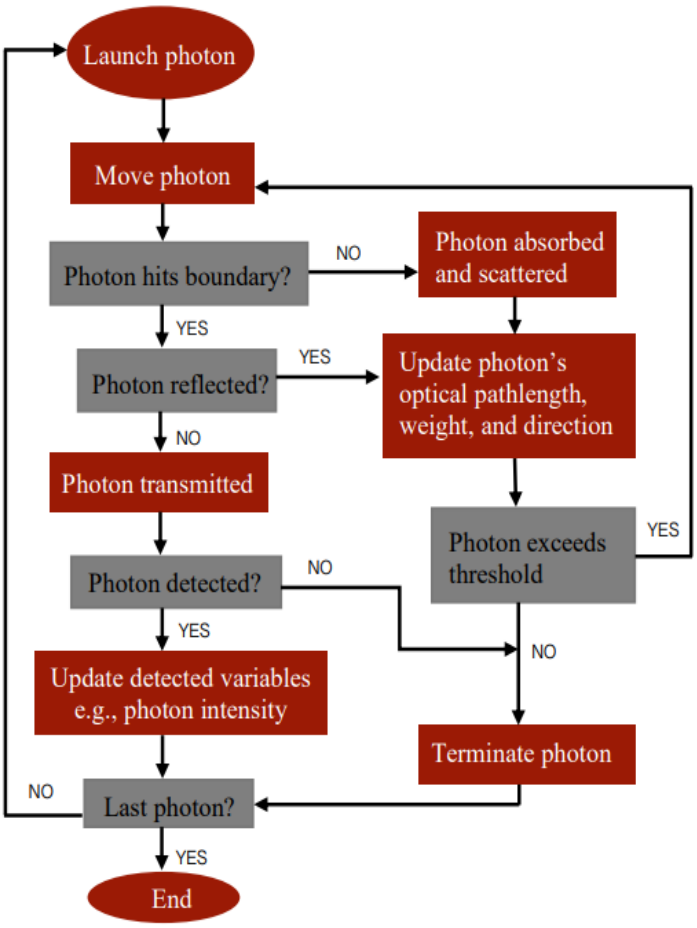

Figure 7-3. Monte Carlo algorithm, which governs the movement of photons between the source and detector in both transmittance and reflectance PPG modes. Adapted from [191].

7.6.Summary

This chapter outlines the methodology to develop a Monte Carlo model and simulate photon transport in biological tissue. The model utilises both Cartesian and spherical polar coordinate systems to track photon trajectories between scattering events in single or multi-layered tissue structures. The framework for the implementation of different optical sources are provided, including the generation of random angular distributions to simulate the stochastic nature of photons. Key light-tissue interactions such as scattering, absorption, and reflection are modelled using probability-based methods such as the Henyey-Greenstein phase function, implicit photon capture, and Russian roulette. Additionally, all the mathematical formulations for defining photon position in 3D space and the photon detection criteria are provided to generate data for different optical parameters of interest. These elements are collated into a Monte Carlo flowchart algorithm, which encompasses all the mechanisms governing photon movement as they travel from the source to the detector.

CHAPTER 8: MONTE CARLO SIMULATION OF THE EFFECT OF HUMAN SKIN MELANIN IN LIGHT-TISSUE INTERACTIONS USING A MONOLAYER SKIN MODEL

8.1.Introduction

The behaviour of light in human skin using the Monte Carlo technique has been explored in the literature [171], [173], [194], [204], [229], [238], [239], [240], [241], [242], [243], [244], [245], some with a main focus on the effect of melanin and skin pigmentation on PPG [171], [204], [229], [244], [245]. Previous chapters have explored the principles and mechanisms of light propagation in biological tissues, with a focus on its application in pulse oximetry. Building on this foundation and using the methodology outlined in Chapter 7, this chapter introduces a monolayer model of the epidermis to simulate changes in melanin concentration and predict certain optical parameter using the Monte Carlo technique. Starting with a simplified model of the human finger, the aim is to examine how melanin concentration acts as a confounding factor in light-tissue interactions and how they could affect the accuracy of key parameters of interest. Another key motivation of this study is to validate the behaviour of the monolayer model by analysing its outputs in response to changes in optical properties, while ensuring that the model adheres to the principles of the Beer Lambert and modified Beer Lambert laws.

8.2. Method for execution

The model defined an epidermal layer with four distinct melanin concentrations ranging from 5% to 20%, in 5% increments. To calculate the absorption coefficient of the various pigmented epidermal layers, the baseline skin calculation, the absorption coefficient of melanin, and the melanin concentration expressed as a decimal percentage were combined (eqs. (6-1), (6-2), and (6-7)).

The reduced scattering coefficients and anisotropy factors of the epidermis were obtained from the literature, as well as the refractive index of 1.4 representing skin. Three wavelengths, specifically blue, green, and red (450 nm, 550 nm, 650 nm) were simulated in this study to investigate the behaviour of low and high melanin concentrations within the visible light range, a region known for its high absorption by melanin.

The sensor setup consisted of a point light source emitting the specified wavelengths and a photodetector with a radius of 0.1 mm placed adjacent to the light source in reflectance mode. Therefore, the initial coordinates of the photons were (0,0,0) and the initial directions cosines were (0,0,1). Photons approaching the detector within a cone of acceptance of 45° were classified as detected photons in their assigned vector, and eq. (7-2b) was used to define the angle of projection, which was randomly simulated.

In this study, the model predicted optical pathlength, detected intensity, absorbance, and penetration depth at 0.5 mm, 0.75 mm, and 1 mm source-detector separations. The photon trajectories were recorded and changes in their "weighting" were used to analyse intensity and absorbance from one million incident photons. Additional details, including the equations used to record reflected photons and absorption, scattering, and reflection events, can be found in Chapter 7. The optical properties of the epidermal layer at all three wavelengths and melanin concentrations are provided in Table 8-1.

Table 8-1: Optical properties of the epidermis with different melanosome volume fractions at 450 nm, 550 nm, and 650 nm.

λ (nm)	v_{mel} (%)	μ_a (mm^{-1}) [129]	μ_s (mm^{-1}) [191]	g [191]
450				
	5	4.99	58.09	0.838
	10	9.81		
	15	14.6		
	20	19.4		
550				
	5	2.56	41.40	0.886
	10	5.03		
	15	7.49		
	20	9.96		
650				
	5	1.47	29.77	0.913
	10	2.88		

	15	4.29		
	20	5.71		

8.3. Results

8.3.1. Model verification

The Monte Carlo model was successfully verified as the expected trends in reflectance was achieved (Figure 8-1). Firstly, an exponential decrease in reflectance was observed as the absorption coefficient increased between 1 mm^{-1} and 5 mm^{-1}. Evidently, this trend adheres to the principles of the Beer Lambert Law (BLL), which confirms the negative exponential relationship between the attenuation of light as the medium's capacity to absorb more light increases i.e., has a greater absorption coefficient. In reflectance mode PPG, an increase in the scattering coefficient leads to a higher rate of light scattering and hence the light becomes redirected in various directions instead of following a straight path. Lastly, a lower anisotropy factor shows higher reflectance as the photons are travelling in a more backwards direction towards the photodiode.

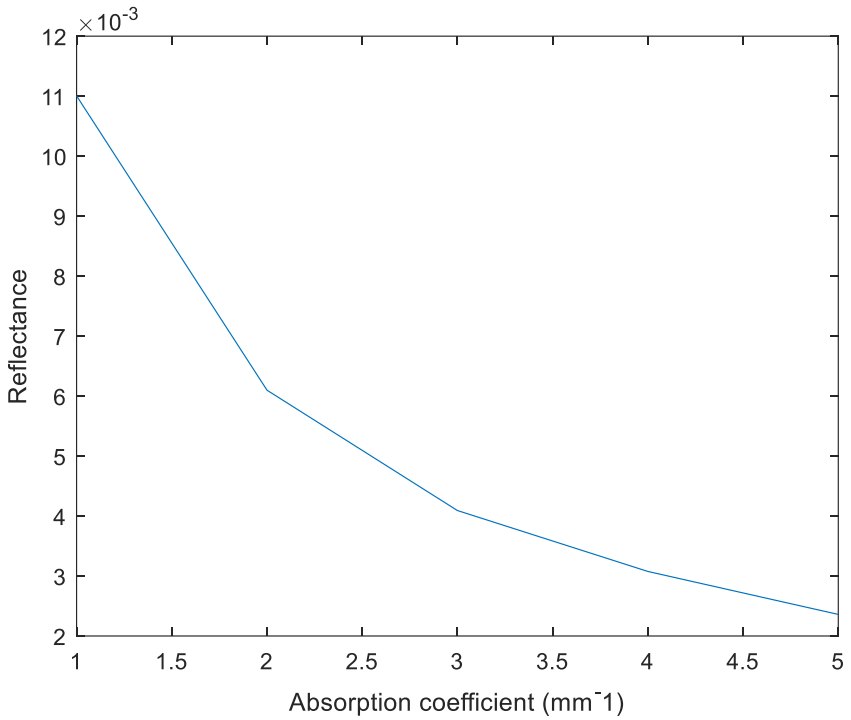

(a)

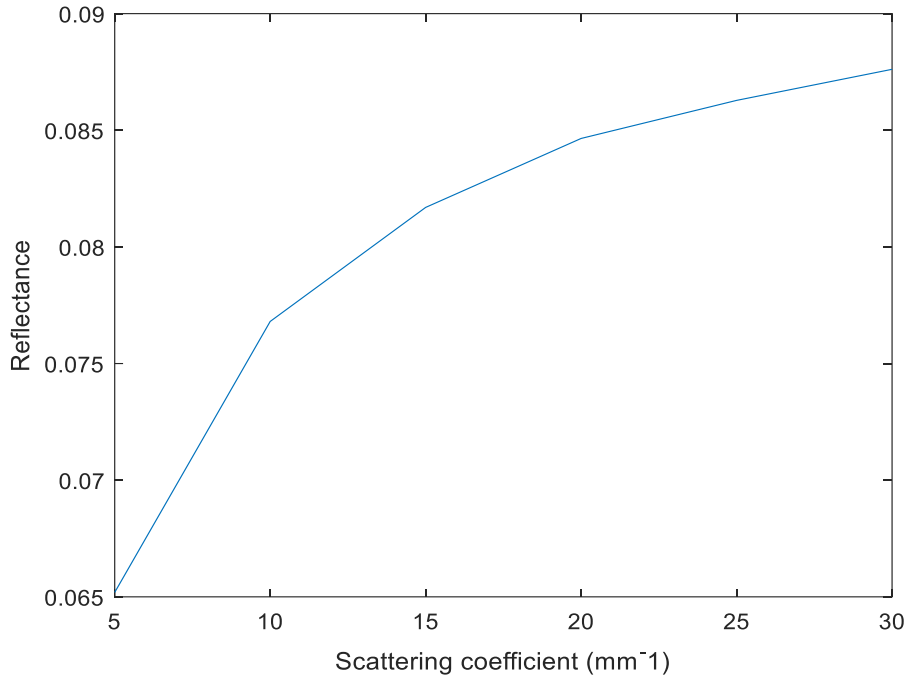

(b)

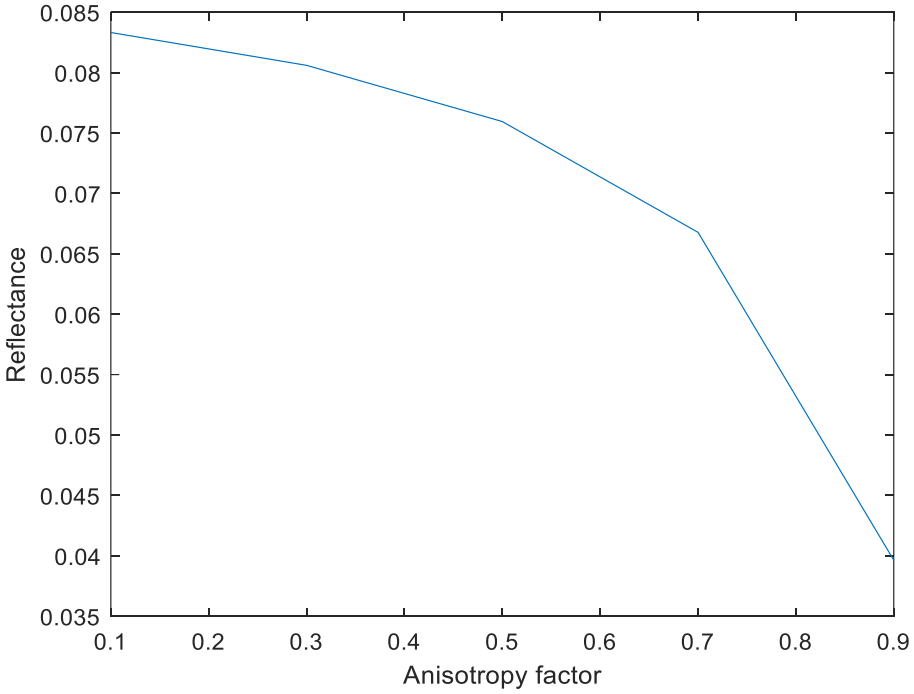

(c)

Figure 8-1. Verification of the Monte Carlo model in reflectance mode. (a) The effect of the absorption coefficient on output reflectance. (b) The effect of the scattering coefficient on output reflectance. (c) The effect of the anisotropy factor on output reflectance.

Another model validation approach was to replicate the set up by Wang et al [234] and compare diffuse transmittance data. The following parameters were inputted into the model, and run 10 times for 50,000 detected photons to compute average diffuse transmittance and error: n = 1, μ_a = 1 mm^{-1}, μ_s = 9 mm^{-1}, g = 0.75, and t = 0.2 mm. As shown in Figure 8-2a, the data from the developed model is in great agreement with those obtained by Wang et al and other previous studies.

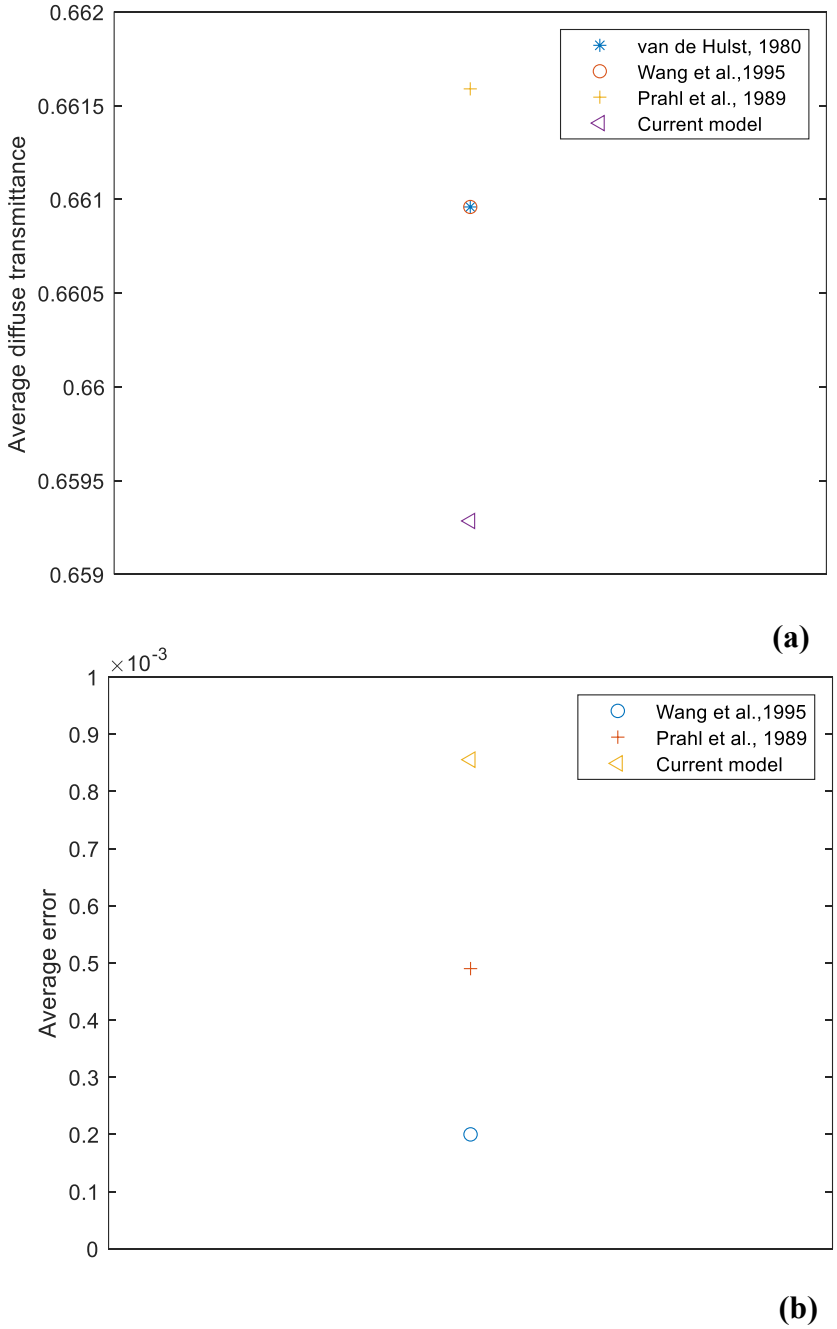

Figure 8-2: Verification of the Monte Carlo in transmittance mode by comparing output diffuse transmittance from the current model to other studies. (a) Average diffuse transmittance computed after 10 simulation runs. (b) Average error.

8.3.2. Photon intensity and absorbance

For each combination of melanin concentration, wavelength, and source-detector separation, the number of photons detected from the one million launched varied based on absorption and scattering effects, as illustrated in Figure 8-3. Although the changes in source-detector separation were small, reducing this distance incrementally enhanced the visualisation of detection trends and photon paths [246]. This effect was particularly evident at shorter wavelengths, especially for a source-detector separation of 1 mm and melanin concentrations of 15 % – 20 %. At higher melanin levels, photon detection was limited for certain conditions, such as blue light at 15 % and 20 % melanin when s = 0.75 mm, 10 % – 20 % when s = 1 mm, and green light at 20% melanin when s =1 mm. However, the model successfully outputted all the independent variables of interest using one million red photons, highlighting the lower absorption susceptibility of red light to varying melanin concentrations compared to blue and green light in the visible spectrum. For instance, even at low melanin concentrations, representative of lightly pigmented subjects, red photon detection is approximately 50 times higher than blue light and twice as high as green light when s = 1 mm. While the number of detected photons serves as an indicator of light behaviour, its primary role in the simulation is to normalise the predicted outcomes, ensuring consistency across scenarios for comparative analysis by calculating averages. In practical applications, the focus shifts to the intensity of the detected photons, as this reveals the total absorbance taking place during photon travel between the source and detector. This intensity also provides insight into the PPG amplitude, which will be examined in greater detail in subsequent chapters.

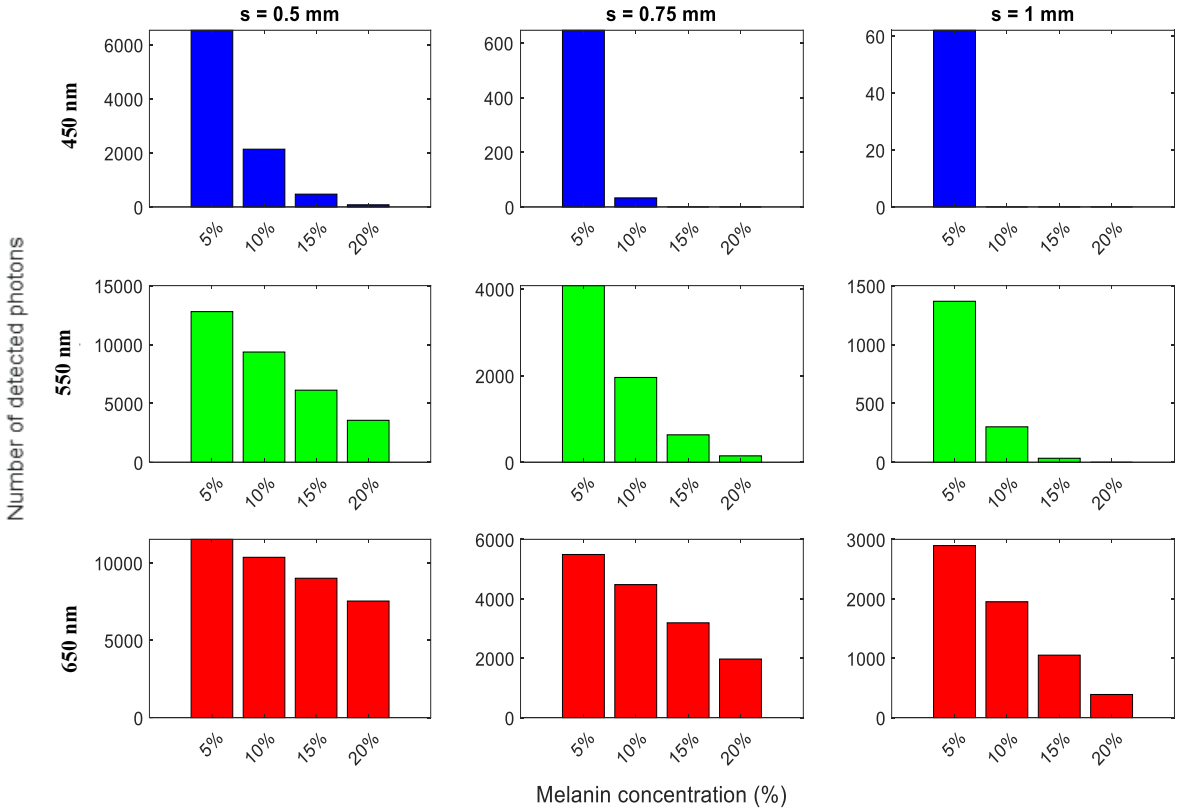

Figure 8-3. The effect of wavelength, source-detector separation, and melanin concentration of the number of detected photons from the Monte Carlo simulation.

Figure 8-4 shows the photon profiles of the light that travelled through the epidermis and returned to the photodetector. As the photons moved in 3D space, their *x, y*, and *z* coordinates were updated at every scattering event until they were detected, where their trajectory was recorded in three separate vectors. To visualise the "banana shape" path of the photons as they travelled between the source and the detector in reflectance mode, the lateral (*x*) plane is plotted against the perpendicular (*z*) plane. Densely scattered regions appear as clustered points, but as melanin concentration and/or source-detector separation increase, the banana shape becomes more defined. This is particularly noticeable at shorter wavelengths, greater source-detector separations, and higher melanin concentrations, such as for blue light when s =1 mm at 20 % melanin concentration.

For a fixed source-detector separation, photons are seen to penetrate deeper into the epidermis as wavelength increases, as suggested by the magnitude of values in the perpendicular plane. At 650 nm, photons are more likely to travel beyond the thickness of the epidermis (0.25 mm), resulting in higher intensity due to reduced fractional absorption and increased photon

weighting. Furthermore, for a given wavelength, there is a reduction in the scattering density and photon dispersion within the *x* and *z* planes as the separation increases, especially at higher melanin concentrations. This likely results from the greater distance that the photons must travel to reach the detector within the specified angles of acceptance, which becomes more challenging in highly pigmented skin where absorption increases by approximately 4–5 times per unit distance (Table 8-1).

In agreement with these findings are the trends in total absorbance and detected intensity shown in Figure 8-5 where absorption is compromised at longer wavelengths, leading to higher detected intensities which diminish exponentially as melanin concentration increases. The intensity of red light is approximately 15 % – 17 % greater than green light across the three source-detector separations and 98 % – 99 % greater than blue light as a result of very low/no detected photons in most scenarios. While these differences may vary with a larger number of incident photons, they reflect distinct light-tissue interactions in the epidermis at shorter wavelengths. This is evident in the steep gradient of melanin's absorption spectrum, even at low concentrations, and the differences in scattering coefficients, which are approximately 1.4 and 1.9 times higher for blue light compared to green and red light, respectively. This could explain why green and red light sources are the most commonly used wavelengths from the visible spectrum for obtaining PPG measurements, including in pulse oximeters [247], [248].

Overall, these results highlight the importance of wavelength and source-detector separation selection in sensor design and development, particularly for users with darker skin pigmentation.

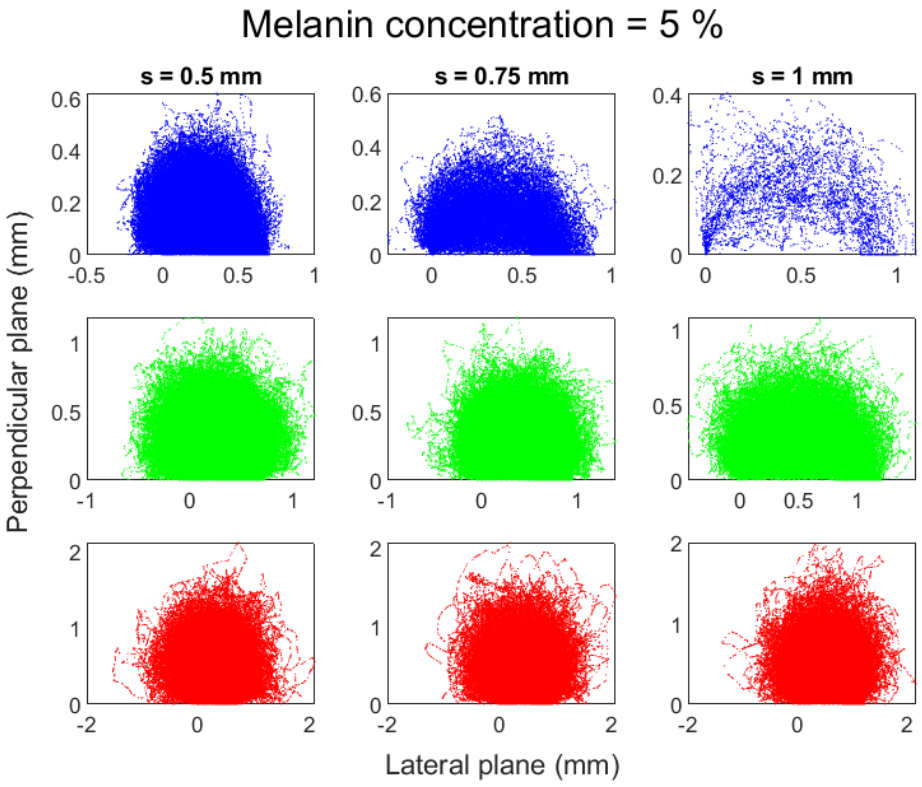
Melanin concentration = 5 %
s = 0.5 mm
s = 0.75 mm
s = 1 mm
Perpendicular plane (mm)
Lateral plane (mm)

(a)

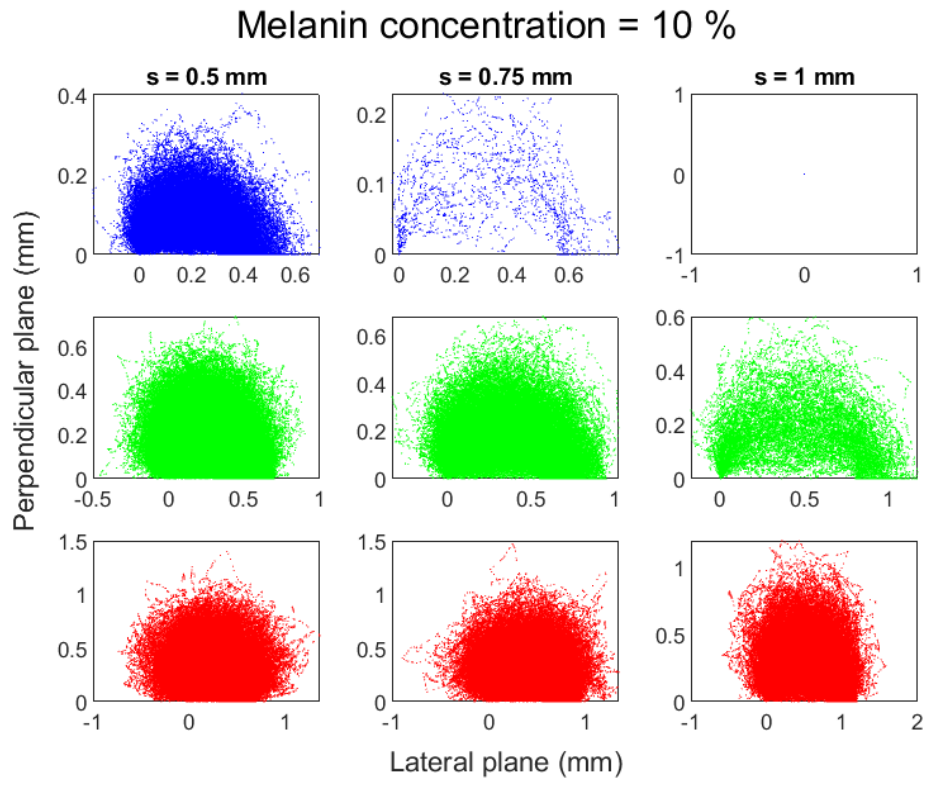
Melanin concentration = 10 %
s = 0.5 mm
s = 0.75 mm
s = 1 mm
Perpendicular plane (mm)
Lateral plane (mm)

(b)

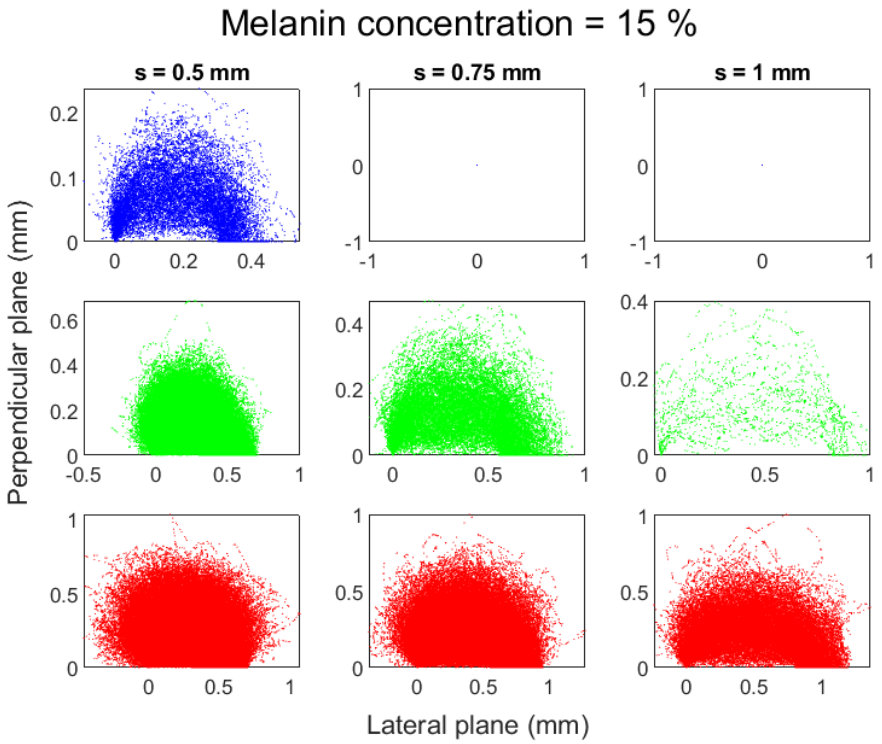

(c)

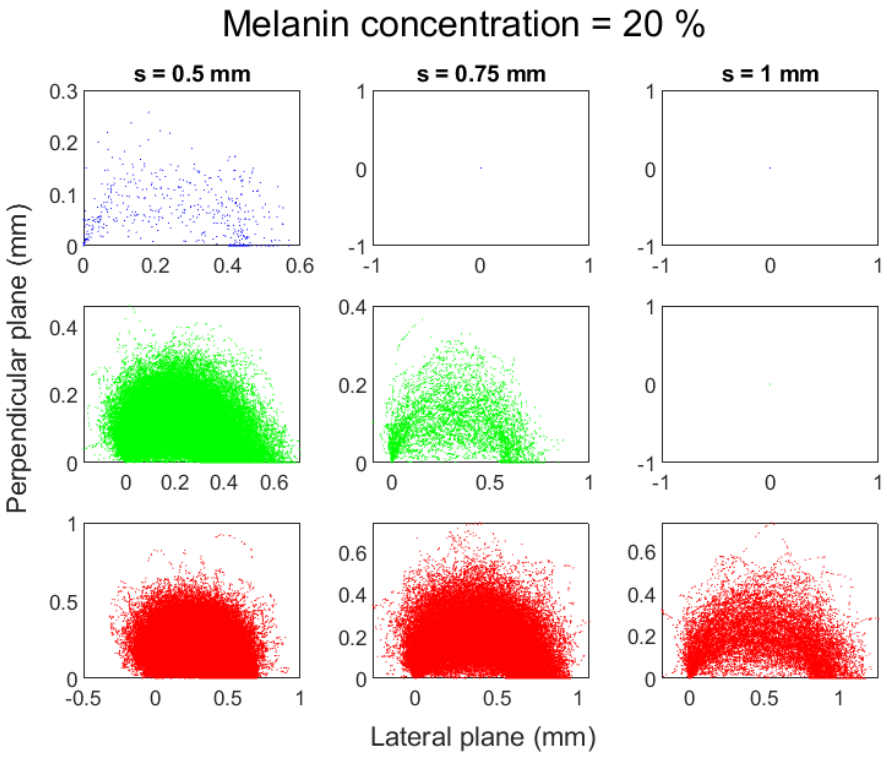

(d)

Figure 8-4. Photon propagation in reflectance mode at blue, green, and red wavelengths (rows) and 0.5 mm, 0.75 mm, and 1 mm source-detector separations (columns). (a) 5% melanin concentration. (b) 10% melanin concentration. (c) 15% melanin concentration. (d) 20% melanin concentration.

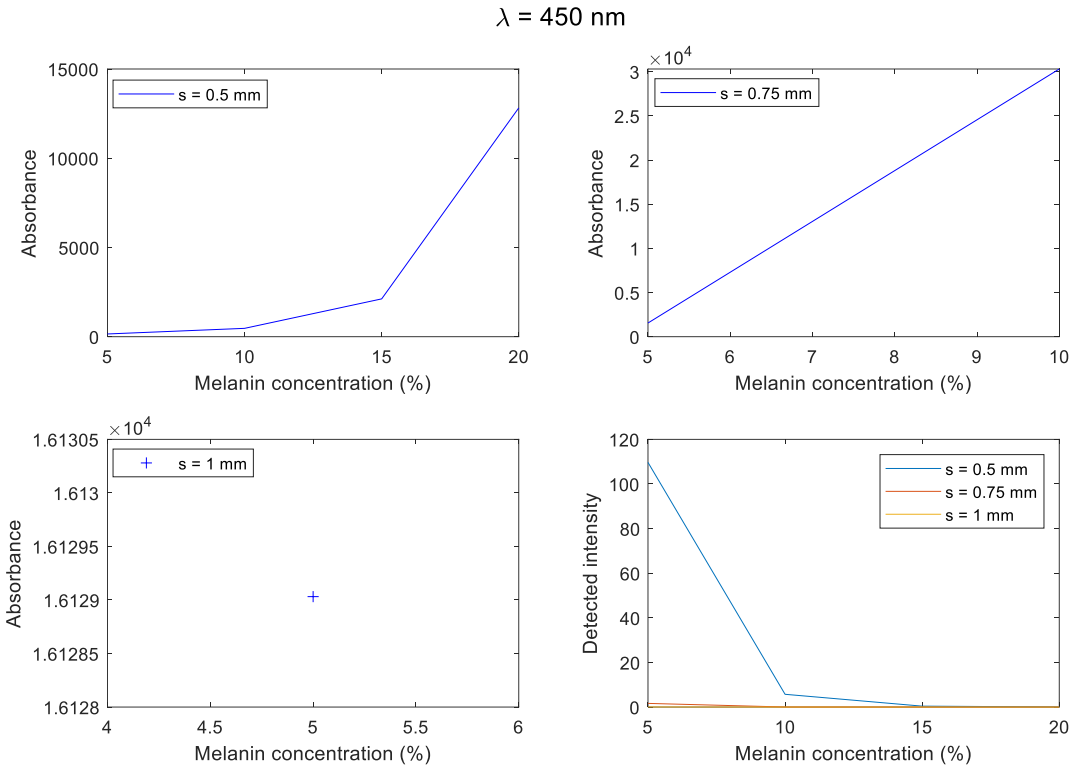
λ = 450 nm
s = 0.5 mm
Absorbance
Melanin concentration (%)
s = 0.75 mm
Absorbance
Melanin concentration (%)
s = 1 mm
Absorbance
Melanin concentration (%)
s = 0.5 mm
s = 0.75 mm
s = 1 mm
Detected intensity
Melanin concentration (%)

(a)

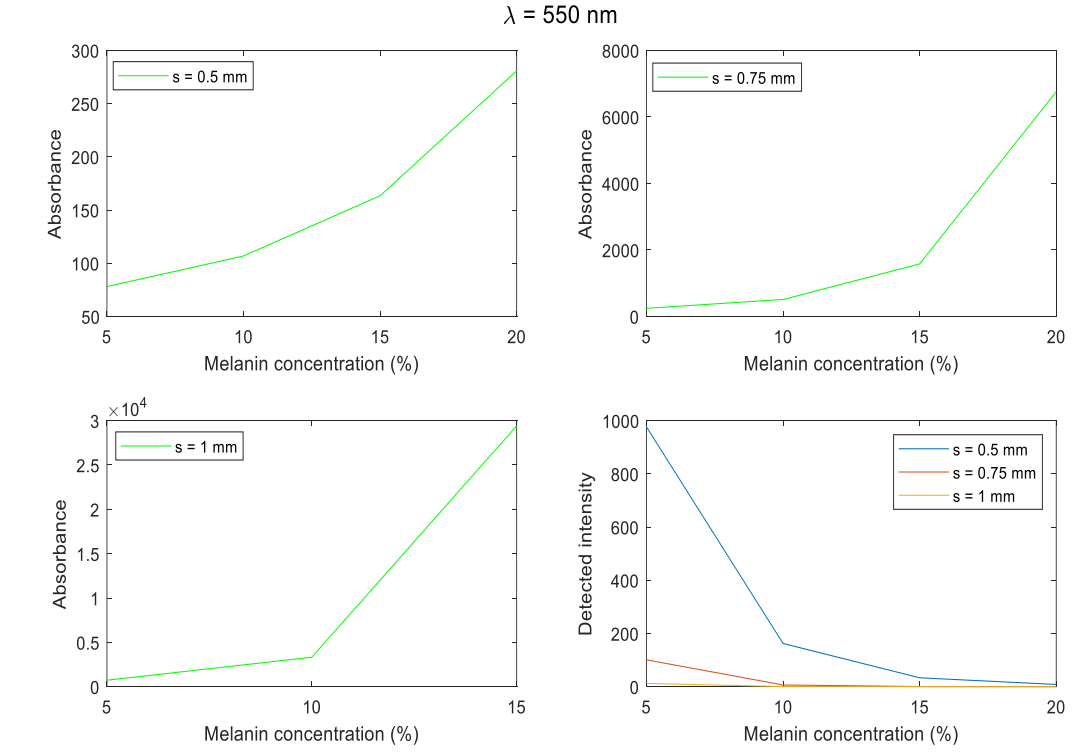
λ = 550 nm
s = 0.5 mm
Absorbance
Melanin concentration (%)
s = 0.75 mm
Absorbance
Melanin concentration (%)
s = 1 mm
Absorbance
Melanin concentration (%)
s = 0.5 mm
s = 0.75 mm
s = 1 mm
Detected intensity
Melanin concentration (%)

(b)

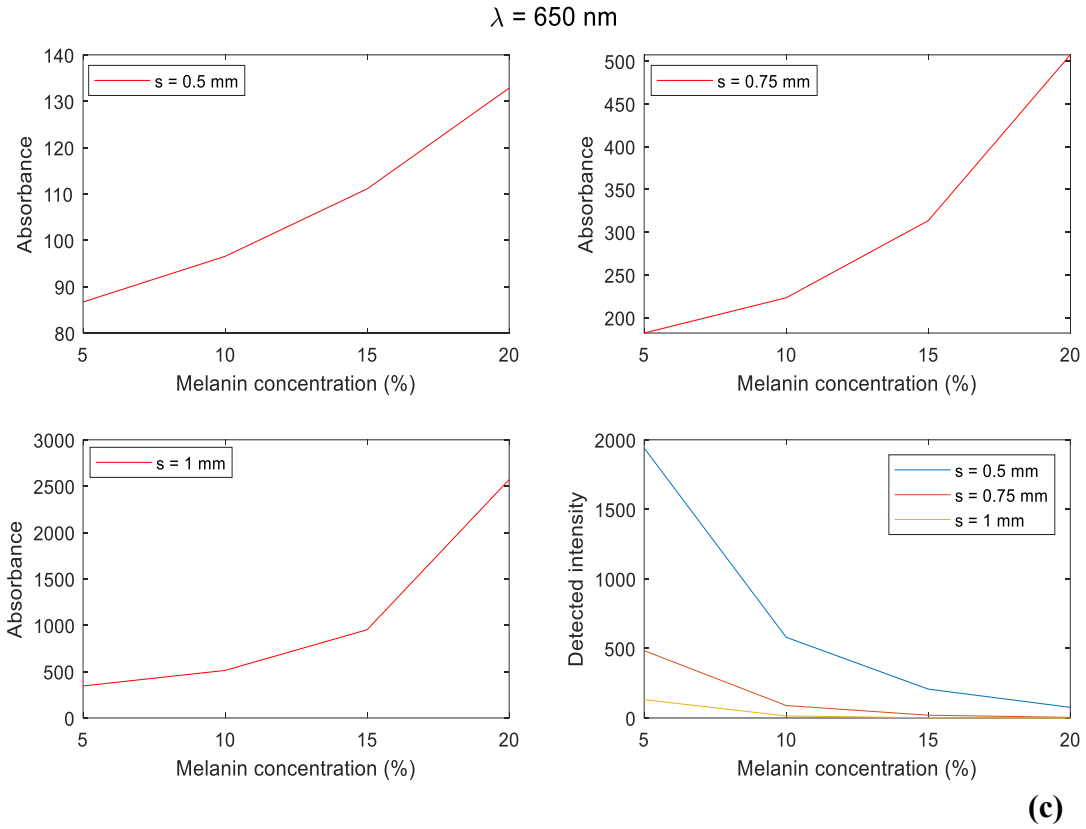

Figure 8-5. The effect of melanin concentration on absorbance and detected intensity at 0.5 mm, 0.75 mm, and 1 mm source-detector separations. (a) Blue light. (b) Green light. (c) Red light.

8.3.3. Optical pathlength and photon penetration depth

The optical pathlength of photons is a critical parameter in biomedical optics as it directly influences how light interacts with tissue and determines the extent of absorption and scattering. The mean distance travelled by each detected photon from the source was calculated to distinguish the relationship between optical pathlength and melanin concentration. Figure 8-6 illustrates that the mean optical pathlength decreases as melanin concentration increases, and even more at shorter source-detector separations. Similar trends were observed for green and blue light in the generated data, although only red light is presented here for completeness across all scenarios. As expected, photons scatter more when they must travel longer distances to detectors positioned further from the source, leading to an increased random walk in various directions. The ratios between the maximum and minimum values of the optical pathlength

corresponding to light and darker skin also vary with source-detector separation: approximately 1.6 when s = 0.5 mm, 1.69 when s = 0.75 mm, and 1.87 when s = 1 mm.

Additionally, red photons exhibit the highest mean optical pathlength which decreases with shorter wavelengths (Figure 8-6b) which could be attributed to differences in absorption rates between the three wavelengths at a fixed melanin concentration. Evidently, red light is absorbed less by melanin, allowing it to travel longer distances, whereas blue light is absorbed more readily, resulting in shorter pathlengths. These findings correlate with differences in the differential pathlength factor (Figure 8-7) which, as discussed in Chapter 2, helps quantify the effective distance travelled by photons relative to the physical separation of the source and detector. Expected trends are demonstrated as the optical pathlength and the DPF are directly proportional to each other for a fixed source-detector separation. However, the DPF at 650 nm increases as the source-detector separation decreases since the mean optical pathlength is equal to the DPF when s = 1 mm (eq. (2-9)). Therefore, when the source-detector separation is reduced to 0.5, the DPF value effectively doubles due to the division by the smaller separation distance. These results show that the DPF provides insight into the extent of scattering and absorption relative to the separation distance, allowing for the normalisation of optical pathlengths across different measurement setups. This normalisation is crucial for ensuring consistent interpretation of tissue optics, particularly in applications like PPG for accurate physiological assessment.

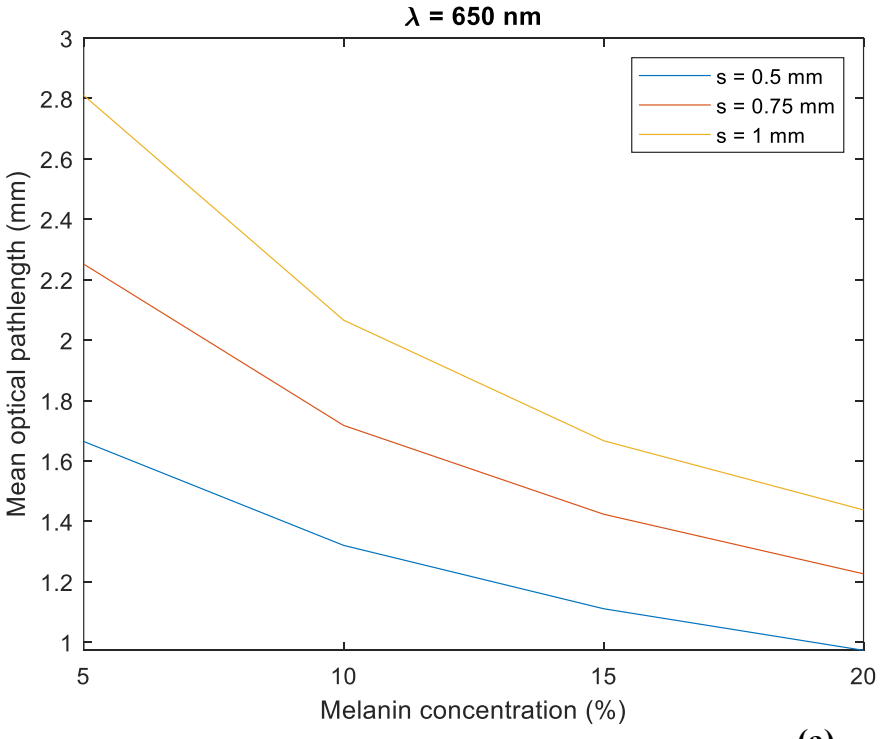

(a)

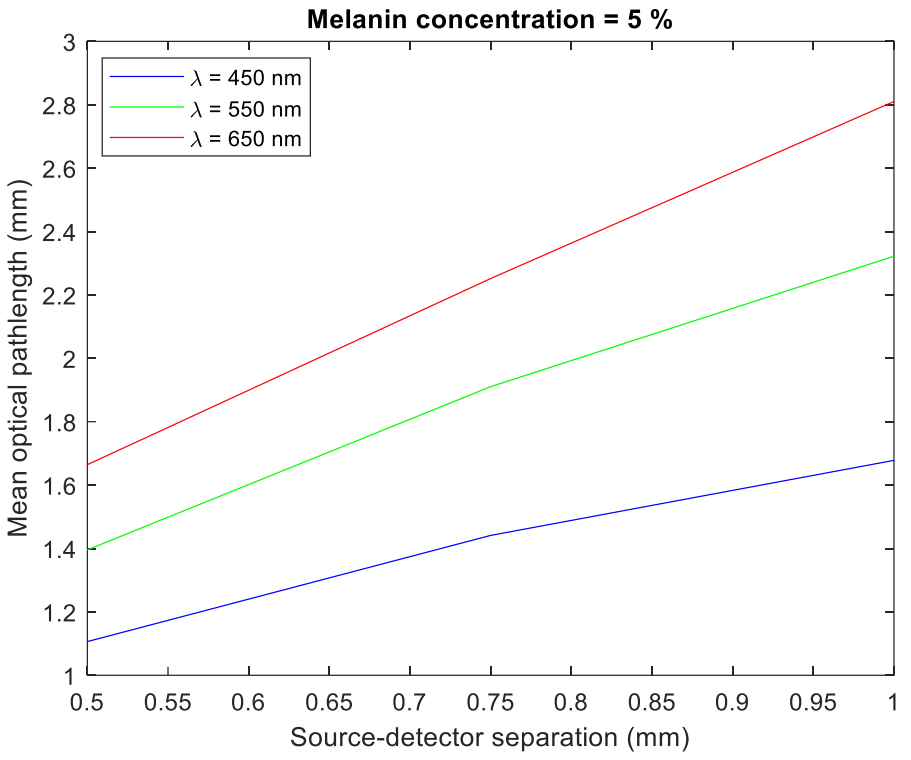

(b)

Figure 8-6. Mean optical pathlength. (a) The effect of melanin concentration and the source-detector separation using red light. (b) The effect of the source-detector separation and wavelength for light skin.

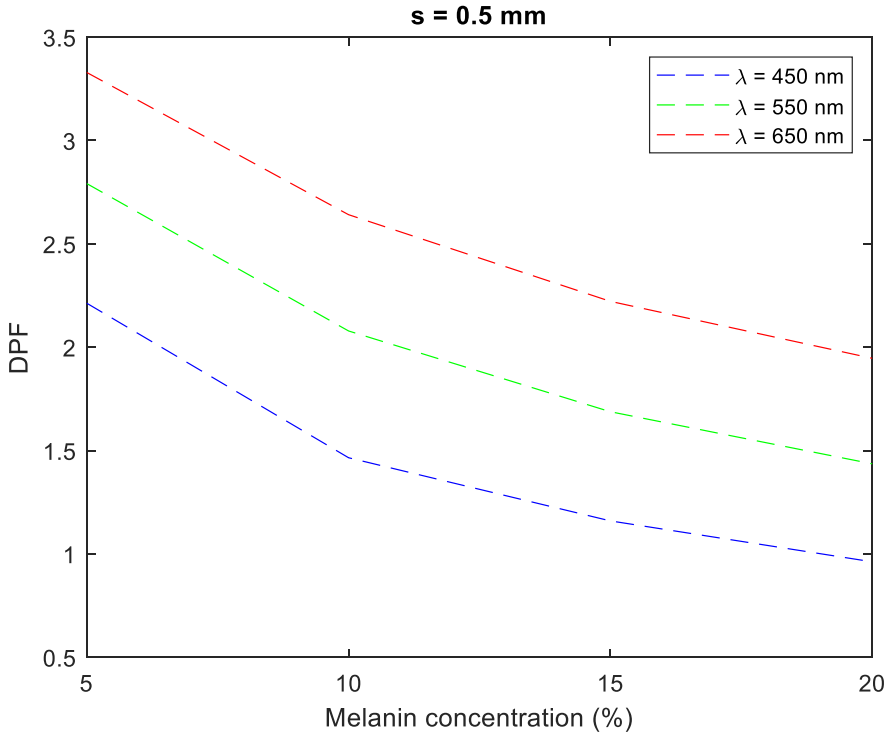

(a)

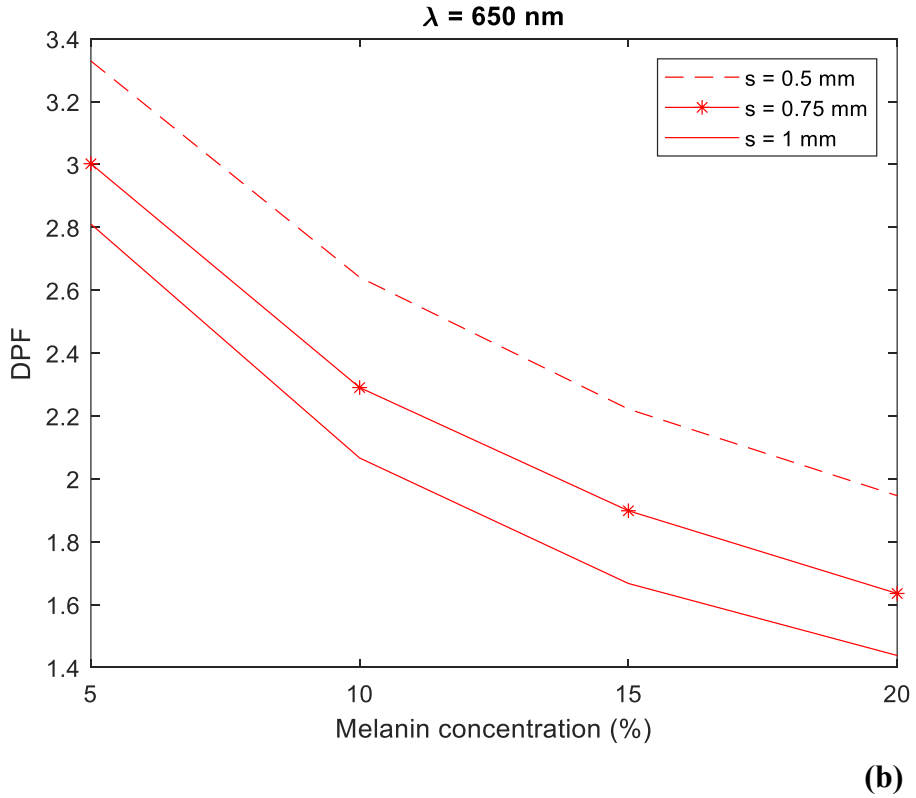

Figure 8-7. Differential pathlength factor. (a) The effect of melanin concentration and wavelength at a fixed source-detector separation of 0.5 mm. (b) The effect of melanin concentration and the source-detector separation at a fixed wavelength of 650 nm.

Lastly, in conjunction with the optical pathlength is the higher probability of photons penetrating deeper into the medium as shown earlier in the photon profiles, and now quantified by the mean penetration depth in Figure 8-8. The results indicate that even at a low melanin concentration of 5%, information obtained from a blue light source is largely confined to the superficial layers at the given source-detector separations. In contrast, green and red light can provide insights into their behaviour in deeper layers of the skin, including the dermal layers. However, mean penetration depth is compromised by nearly two times between the epidermis with 5% and 20% melanin concentration, making the retrieval of bio-optical information from darker pigmented skin significantly more challenging and potentially contributing to inaccuracies in optical measurements.

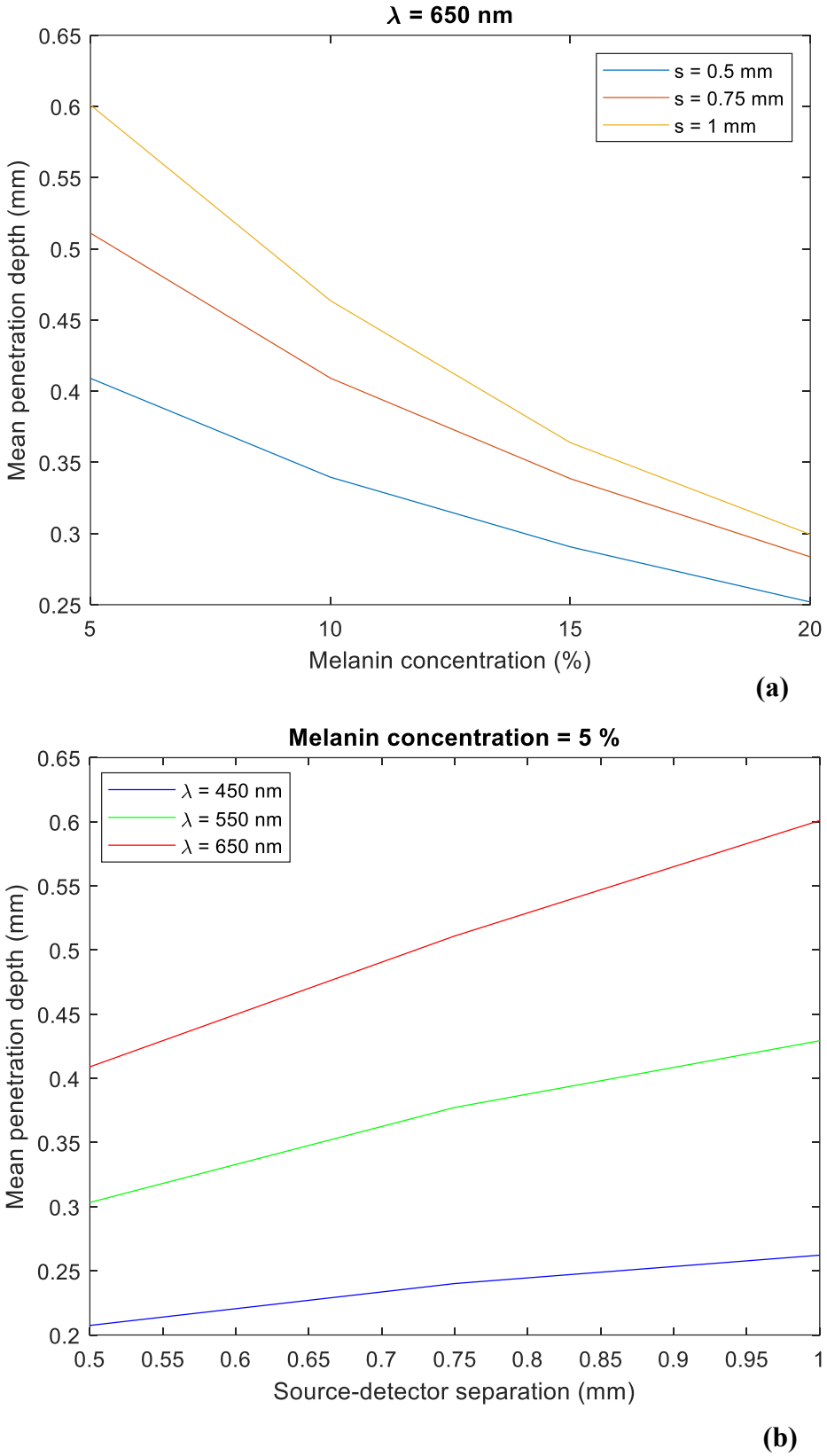

Figure 8-8. Mean penetration depth. (a) The effect of melanin concentration and the source-detector separation at a fixed wavelength of 650 nm. (b) The effect of source-detector and wavelength for light skin.

8.4.Summary

This chapter builds upon the foundational principles of light propagation in biological tissues and focuses on simulating light-tissue interactions in a monolayer model of the epidermis. Using the Monte Carlo technique, the study explored the impact of varying melanin concentrations on some optical parameters of interest with blue, green, and red light sources at three source-detector separations. The findings highlighted the influence of melanin concentration, wavelength selection, and source-detector spacing on photon behaviour, with higher melanin levels, shorter wavelengths, and longer spacing reducing photon detection. This study also validated the model's adherence to the Beer Lambert and modified Beer Lambert laws, confirming its reliability for simulating light propagation in more complex models of the finger. While the results have suggested how melanin concentration affects absorbance on the DC component of a PPG signal, the implications of the results remain unknown for the AC component since the optical properties of blood were not defined.

CHAPTER 9: MONTE CARLO SIMULATION OF THE EFFECT OF MELANIN CONCENTRATION ON LIGHT-TISSUE INTERACTIONS IN TRANSMITTANCE AND FINGER PHOTOPLETHYSMOGRAPHY

9.1.Introduction

The interaction of light with biological tissues involves contributions from multiple layers in the specific region of interest, with each layer having distinct structural, mechanical and optical properties. While it has been acknowledged that the light-tissue interactions in the epidermis can be primarily influenced by melanin concentration, deeper layers of the finger such as the dermis, subcutaneous fat, muscle, and bone also play critical roles. Understanding how light propagates through these layers is essential for improving bio-optical measurements, and is particularly relevant for potential hardware and/or software optimisation [177] to minimise inaccurate outcomes across a range of pigmentation levels.

The importance of MC simulations for understanding the effect of optical (e.g., wavelength, beam size, etc.) and non-optical (e.g., thickness of the tissue layer) input parameters on some optical parameters have been highlighted in Chapter 8. Building on this knowledge, the simulation of a multilayer model of the human finger is presented in this chapter to provide a more anatomically realistic representation of light-tissue interactions for the application of pulse oximetry.

9.2. Method for execution

The MC model simulated red (660 nm) and infrared (940 nm) light sources to replicate the multiplexing of the two operating wavelengths in pulse oximeters. Here, the light is emitted from a 1 mm radius beam based on a Gaussian distribution, and the photodetector also has a radius of 1 mm and an acceptance angle of 90°. Reflectance and transmittance sensor configurations are simulated to explore the behaviour of light for PPG based sensing in wearables and in clinical settings. Similarly to the previous chapter, the source-detector separation was varied between 1 mm – 9 mm in increments of 2 mm by changing the distance of the photodetector relative to the light source in the *x* direction, i.e. across the width of the finger model for reflectance mode. In transmittance mode, the source is placed in the dorsal (top) face of the skin and the photodetector is placed directly below the source on the ventral

(bottom) face of the skin. Fat, muscle, and bone are positioned in alternate order between the skin layers, which include six sublayers: stratum corneum, epidermis, papillary dermis, upper blood net dermis, reticular dermis, and deep blood net dermis (Figure 9-1).

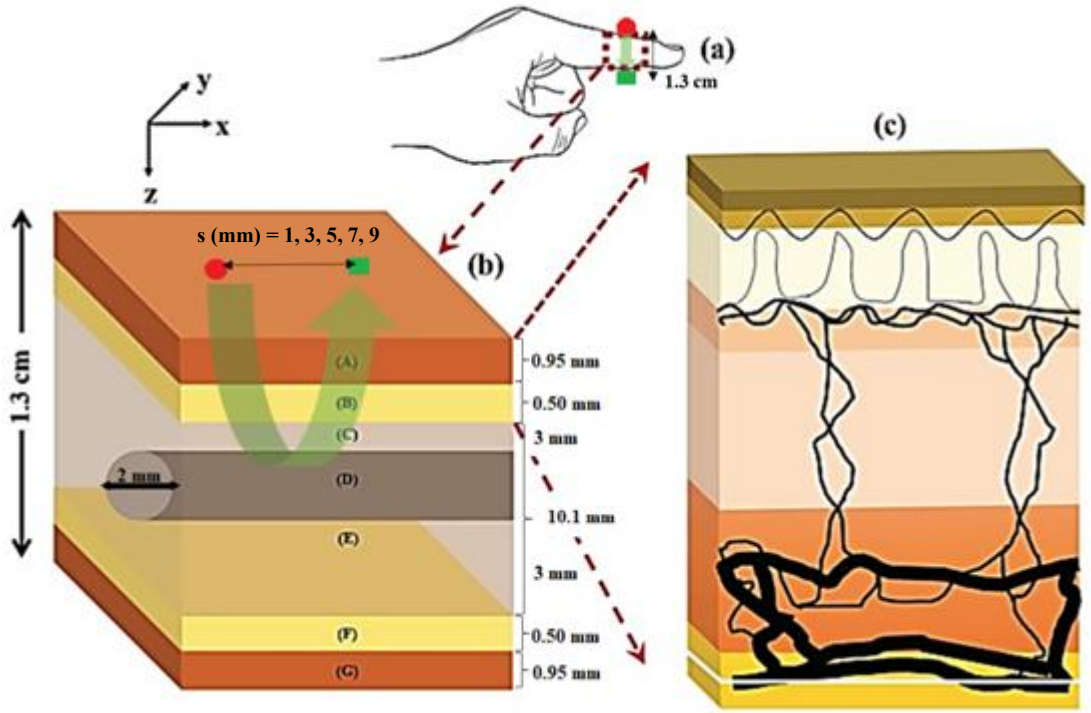

Figure 9-1. Block representation of the finger. (a) The region of interest with transmittance sensor configuration (source and detector placed opposite to each other across the finger). (b) Illustrates the different layers of the finger with their corresponding thicknesses: A & G are skin layers, B & F are fat layers, and C & E are muscle layers containing a cylindrical bone D. The reflectance sensor configuration is also illustrated (source and detector are placed adjacent to each other) with source-detector separations between 1 mm – 9 mm in 2 mm increments. (c) Skin structure comprising of 6 layers – stratum corneum, epidermis, papillary dermis, upper blood net dermis, reticular dermis, deep blood net dermis, connected to the sub dermis (fat layer). Green arrows show the overall trajectory of the photons in both PPG modes. Adapted from [191].

To simulate different skin colour groups, three distinct skin types were categorised according to the Fitzpatrick scale and characterised by the volume fraction of melanosomes in the epidermis. These are 2.55% for light skin (Type I-II), 15.5% for moderate skin (Type IV-V), and 30.5% for dark skin (Type VI) [249], which are used to calculate the three absorption coefficients of the epidermis using eqs. (6-5) and (6-7).

Skin phototype III is not simulated as the melanosome volume for this scale was not available, which was acceptable for the purposes of this study as the analysis of the light-tissue interactions between distinct skin groups could still be achieved.

The diastolic optical properties, blood volumes, and water concentration values for each skin sublayer are defined from the literature. To simulate cardiac pulsatility, the systolic blood volume is assumed to be two times the diastolic blood volume [250], which is divided equally between arterial and venous blood [251]. This assumption was considered viable due to its applicability in previous studies also exploring pulse oximeter modelling and light-tissue interactions [173], [250] based on reproducing the conditions of Schmitt et al validation study with human pulse oximetry data [252]. Additionally, contributions from venous pulsations have been hypothesised and measured in some studies [253], [254], indicating that venous blood may influence PPG signals under certain conditions. Consequently, modelling an equal split allowed for the understanding of the extent of this influence and its implications for SaO_2 estimation.

The absorption coefficients of arterial and venous blood accounted for changes in arterial and venous oxygenation, using the following equation:

$$\mu_{a_{derm(n)}} = v_{A\,(n)}(sat_A \times \mu_{a_{Hbo}} + (1 - sat_A) \times \mu_{a_{HHb}}) + v_{V(n)}(sat_V \times \mu_{a_{Hbo}} + (1 - sat_V) \times \mu_{a_{HHb}}) + \mu_{a_w} \times v_{w(n)} + (1 - (v_{A(n)} + v_{V(n)} + v_{w(n)})) \times \mu_{a_{baseline}} \quad (9\text{-}1)$$

where,

$derm(n)$ is the nth sublayer of the dermis: papillary dermis (1), upper blood net dermis (2), reticular dermis (3), and deep blood net dermis (4)

sat_A is arterial oxygen saturation, ranging between 70% and 100%

sat_V is venous oxygen saturation, which is assumed 10% than sat_A [255]

v_v is the volume fraction of venous blood

v_A is the volume fraction of arterial blood

$\mu_{a_{Hbo}}$ is the absorption coefficient of oxyhaemoglobin (mm^{-1})

$\mu_{a_{HHb}}$ is the absorption coefficient of deoxyhaemoglobin (mm^{-1})

Lastly, to calculate the magnitude of the AC and DC components at a single point in time, the generated intensities during diastole and systole are used to calculate transmittance and reflectance by computing the ratio between output and input intensity. As illustrated in Figure 9-2, the AC component is calculated by subtracting the systolic intensity by the diastolic intensity, and the DC component is given by the systolic intensity:

$$AC = I_d - I_s \tag{9-2a}$$

$$DC = I_s \tag{9-2b}$$

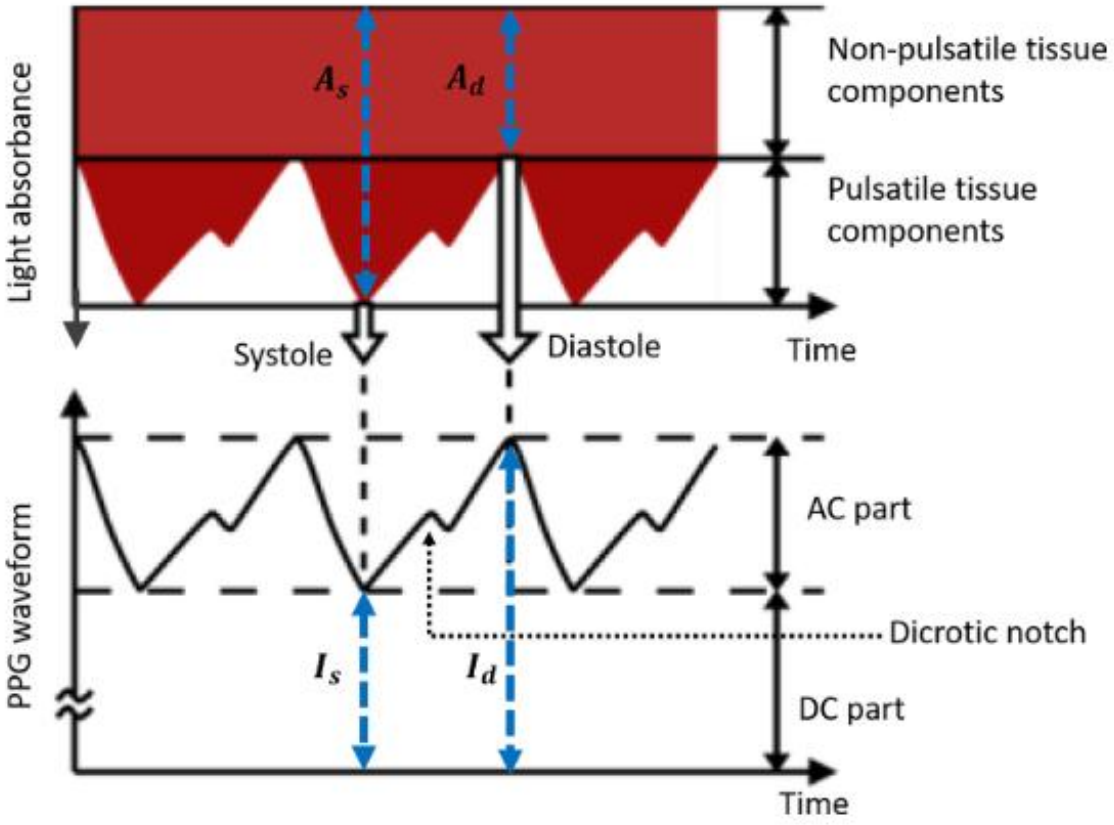

Figure 9-2. Schematic of the PPG waveform produced as a result of light absorbance during systole and diastole (A_s and A_d). The corresponding light intensities are denoted by I_s and I_d, used for the calculation of the pulsatile AC component and non-pulsatile DC component from the Monte Carlo simulation. Extracted from [1].

All the optical properties that are either calculated or extracted from the literature are outlined in Table 9-1 and inputted into the model. The model assumes a uniform refractive index of 1.4 within each tissue layer, meaning photons travel in straight lines until they are scattered. The tissue layer boundaries are treated as smooth, with photons reflecting according to Fresnel's law. The calculated absorption coefficient values of light, moderate, and dark skin correlated with the data trends produced by Patwardhan et al [256].

Table 9-1: Optical properties of all the tissue layer/components in the simulated finger model at 660 nm and 940 nm. Blood and water concentrations of the skin sublayers are also included.

Tissue layer/component	μ_a **(mm^{-1})**		μ_s **(mm^{-1})**		g [191]		v_b **(%)** [257]	v_w **(%)** [257]
Wavelength (nm)	660	940	660	940	660	940		
Stratum corneum	0.0495 [129]	0.0170 [129]	25.62 [258]	5.68 [258]	0.91	0.94	0	5
Epidermis	-	-					0	20
Light skin	0.7275 [129]	0.2297 [129]					-	-
Moderate skin	4.2100 [129]	1.3023 [129]					-	-
Dark skin	8.2438 [129]	2.5447 [129]					-	-
Papillary dermis	0.0331	0.0465					4	50
Upper blood net dermis	0.0728	0.2094					30	60

Reticular dermis	0.0228	0.0486					4	60
Deep blood net dermis	0.0331	0.0859					10	70
Fat	0.0104 [258], [259]	0.0170 [258], [259]	6.20 [258], [259]	5.42 [258], [259]	0.90	0.90	-	-
Muscle	0.0816 [258], [259]	0.0401 [258], [259]	8.61 [258], [259]	5.81 [258], [259]	0.88	0.91	-	-
Bone	0.0351 [260]	0.0457 [260]	34.45 [260]	24.70 [260]	0.92	0.93	-	-
Oxygenated blood (HbO2) [261]	0.15	0.65	87.61	66.08	0.983	0.981	-	-
Deoxygenated blood (HHb) [261]	1.64	0.43	81.45	49.66	0.986	0.978	-	-
Water [262]	0.00036	0.0274	-	-	-	-	-	-

9.3. Results

9.3.1. Transmittance PPG

The photon profiles of red and infrared light for light, moderate, and dark skin in transmittance mode are presented in Figure 9-3. Similarly, by tracking and recording the trajectory of detected photons, the profiles were constructed using a histogram of 200 bins to generate a heat map, which enabled direct comparisons in the behaviour of light in the finger model between the two wavelengths across the different skin types. From the data, out of the ten million red photons launched at the tissue surface, 1791 were detected by light skin, 341 by moderate skin, and 55 by dark skin. Conversely, in the case of infrared light, light, moderate, and dark skin

detected 9655, 6846, and 4408 respectively, all during diastole. Notably, with red light, the number of detected photons vary significantly with melanin concentration, resulting in contrasting scattering patterns relative to infrared light. The scattering density is very pronounced in the dermal layers near the source and the photodetector, as well as the muscle and bone layer as shown by the brighter white/yellow regions. The influence of melanin concentration on the number of detected photons and scattering events appeared to be less prominent with infrared light, suggesting the relatively minimal impact of skin type on photon propagation at longer wavelengths.

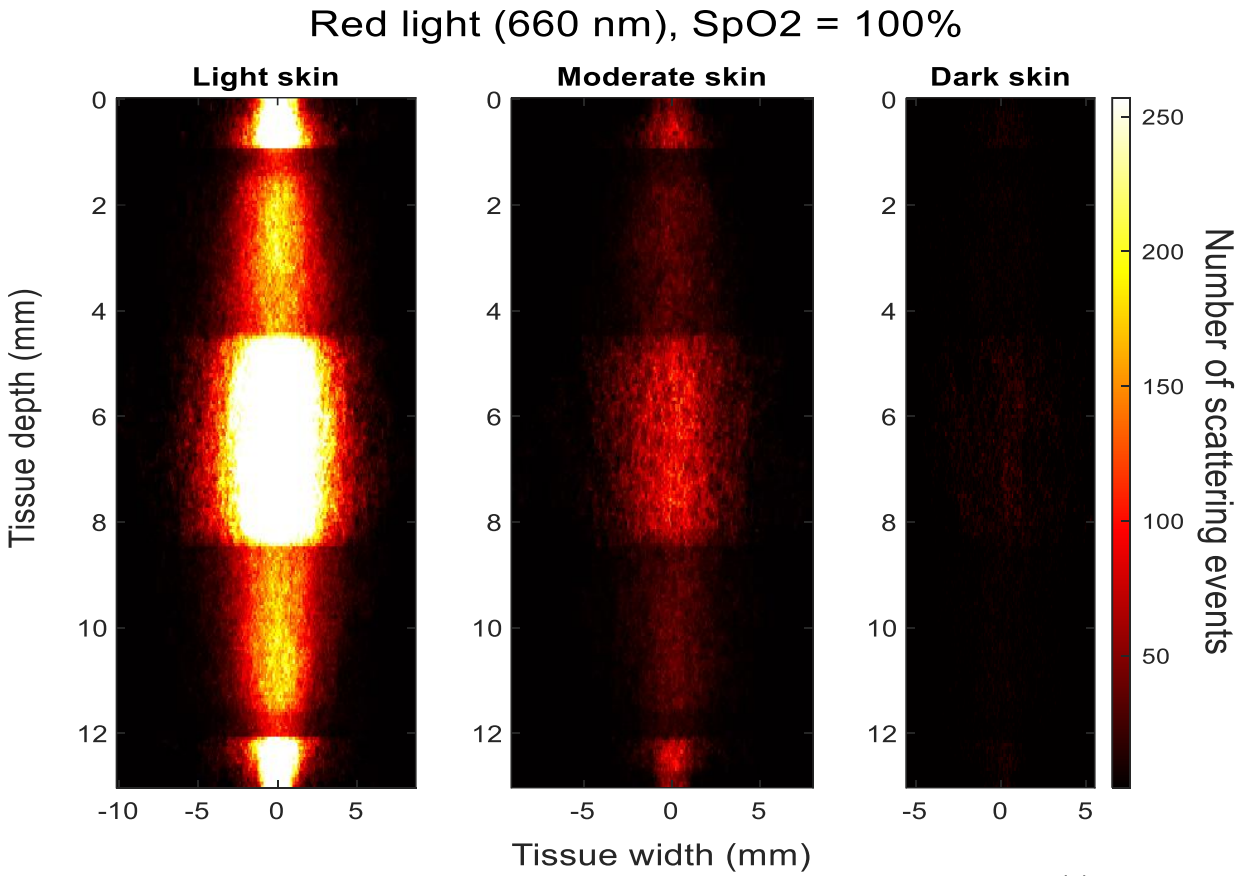

(a)

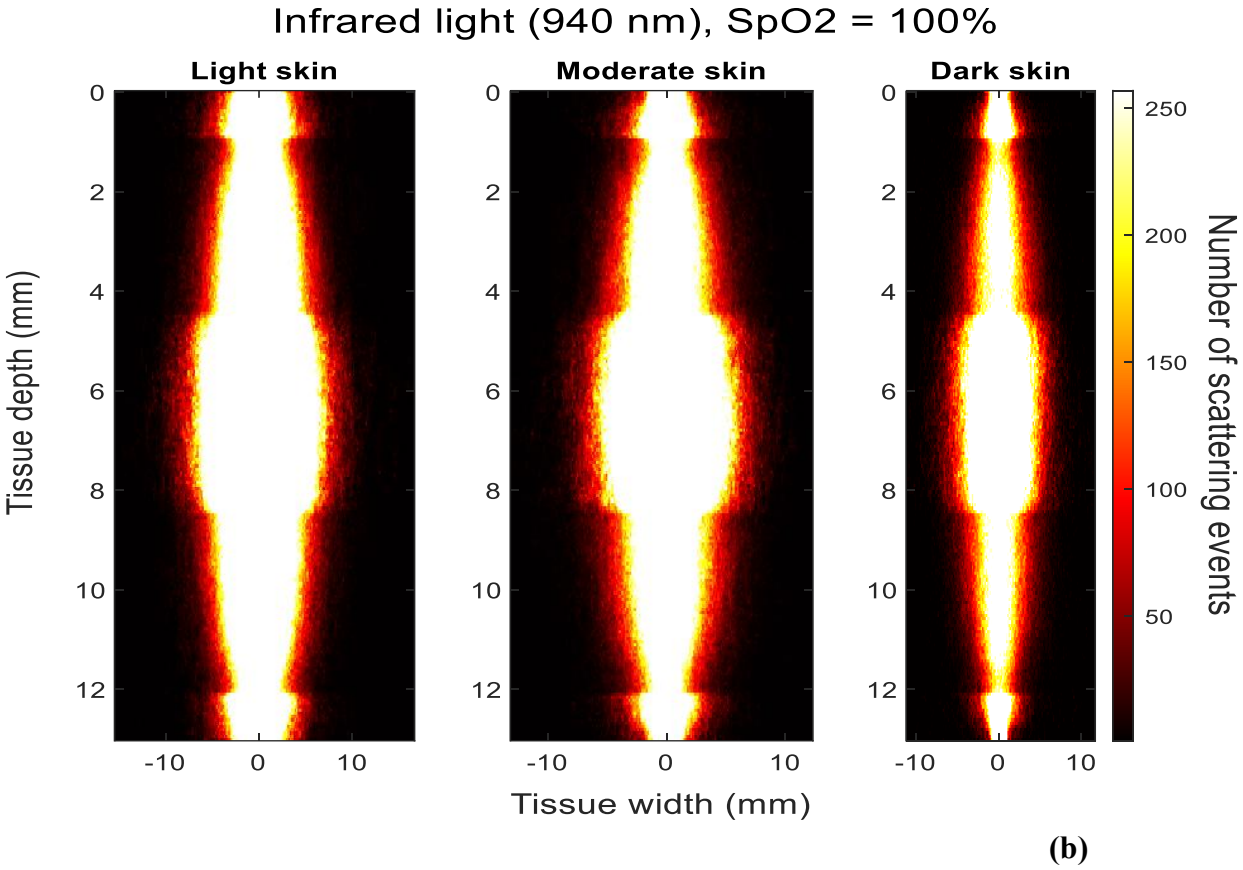

Figure 9-3. Photon propagation profiles of detected photons in transmittance PPG for light, moderate, and dark skin using a (a) 660 nm light source and (b) 940 nm light source.

In Figure 9-4, the results demonstrate the magnitudes of AC and DC components for a static point in a PPG signal for red and infrared light across light, moderate, and dark skin. Transmittance, calculated by taking the ratio of detected intensity to the incident intensity, indicates the portion of light that passes through the finger model and is received by the photodetector. The data clearly illustrates that both AC and DC transmittance values decrease with increasing melanin concentration. As anticipated, the AC component is significantly smaller than the DC component at both wavelengths, reflecting the relatively small amplitude of AC outputs in PPG signals. However, the AC and DC values for red light are notably smaller compared to infrared light, and hence, a logarithmic scale is used to visualise the differences in transmittance as melanin concentration changes. The decreasing difference between the AC and DC components becomes evident as melanin concentration increases, and that overall, red

light is most absorbed by dark skin (v_{mel} = 30.5%). Nevertheless, the AC and DC components exhibit a consistent difference in magnitude with increasing melanin concentration for infrared light, further suggesting its limited influence at 940 nm.

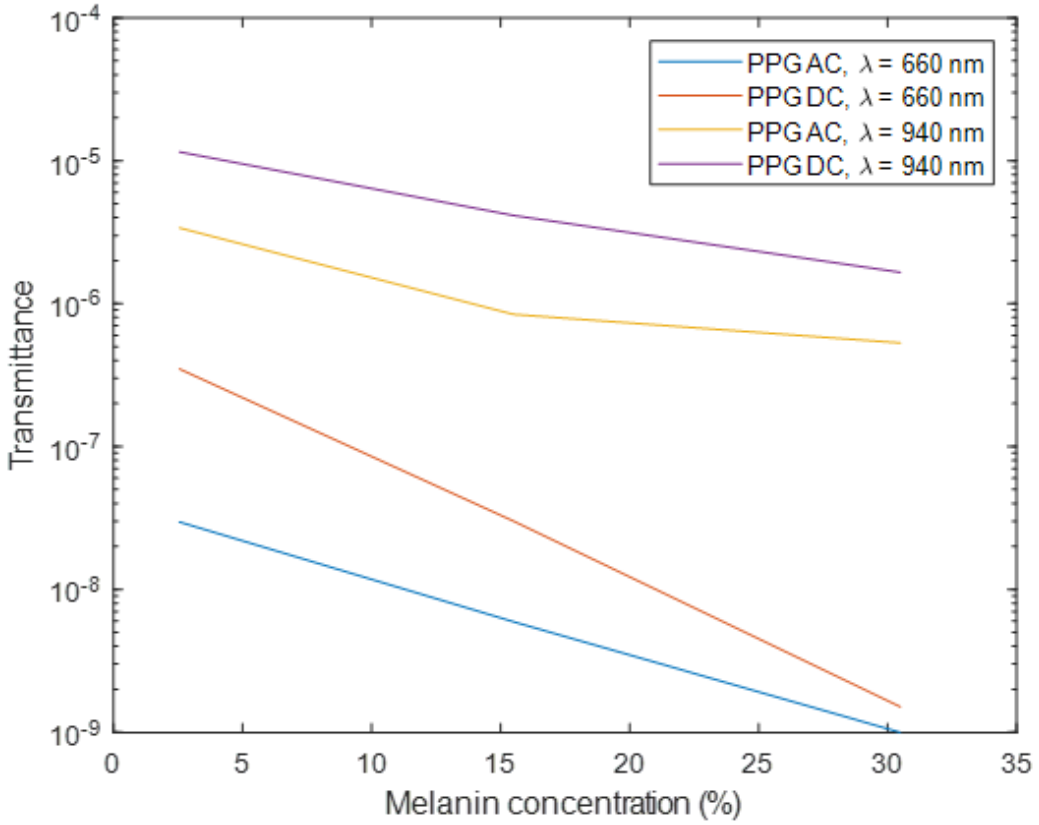

Figure 9-4. Calculated AC and DC transmittance values for light, moderate, and dark skin at 660 nm and 940 nm in logarithmic scale.

Moreover, the relative absorbance of detected photons per layer for red and infrared light in both systolic and diastolic states are presented in Figure 9-5. Hence, the distribution of absorption in all the layers of the finger model are presented based on the concentration of melanin. For the epidermal layer, it is evident that the dark epidermis exhibits the highest relative absorbance, followed by the moderate epidermis and the light epidermis for both wavelengths. For red light, relative absorbance is approximately 78%, 68%, and 36% respectively, while for infrared light, relative absorbance is 56%, 45%, and 16% respectively during diastole. For all skin types, the stratum corneum is seen to have the lowest relative absorbance at both wavelengths. In the dermal layers, relative absorbance during systole is greater than diastole due to increased blood volume, which increases the capacity of the dermis to absorb more photons. Overall, as the relative absorbance in the epidermis increases due to increasing melanin concentration, the relative absorbance in the dermal layers as well as fat,

muscle, and bone layers decreases, which were in agreement with work by Chatterjee et al [173].

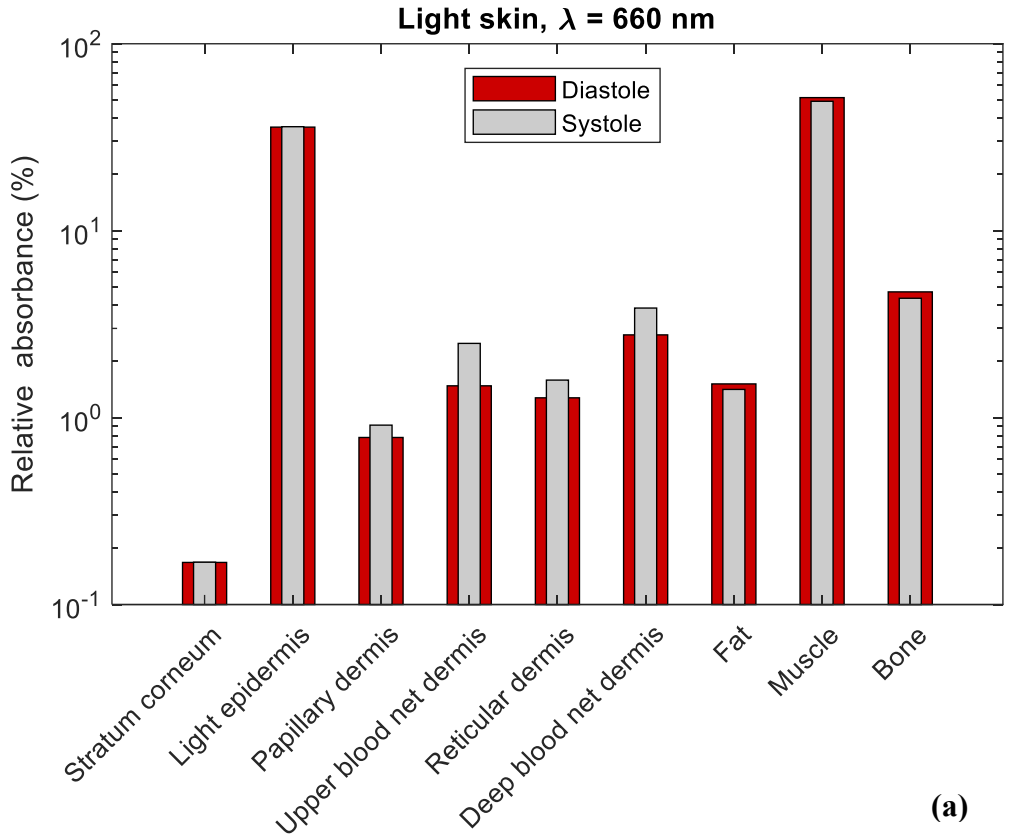

(a)

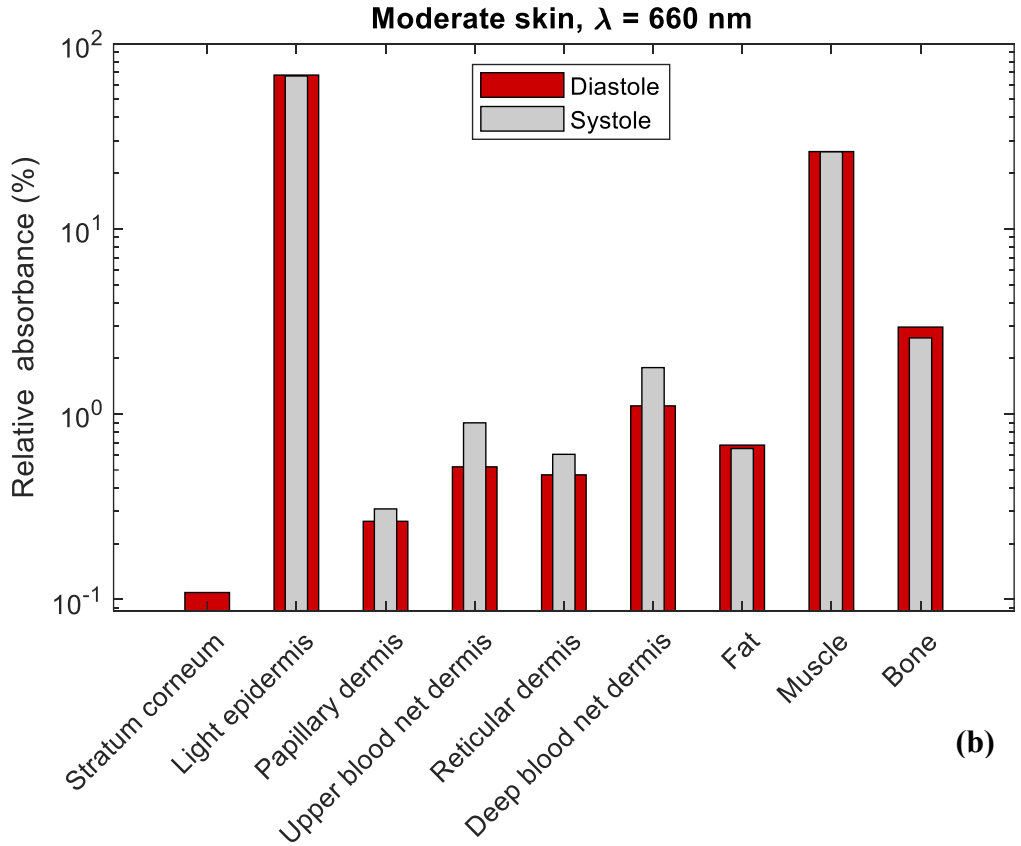

(b)

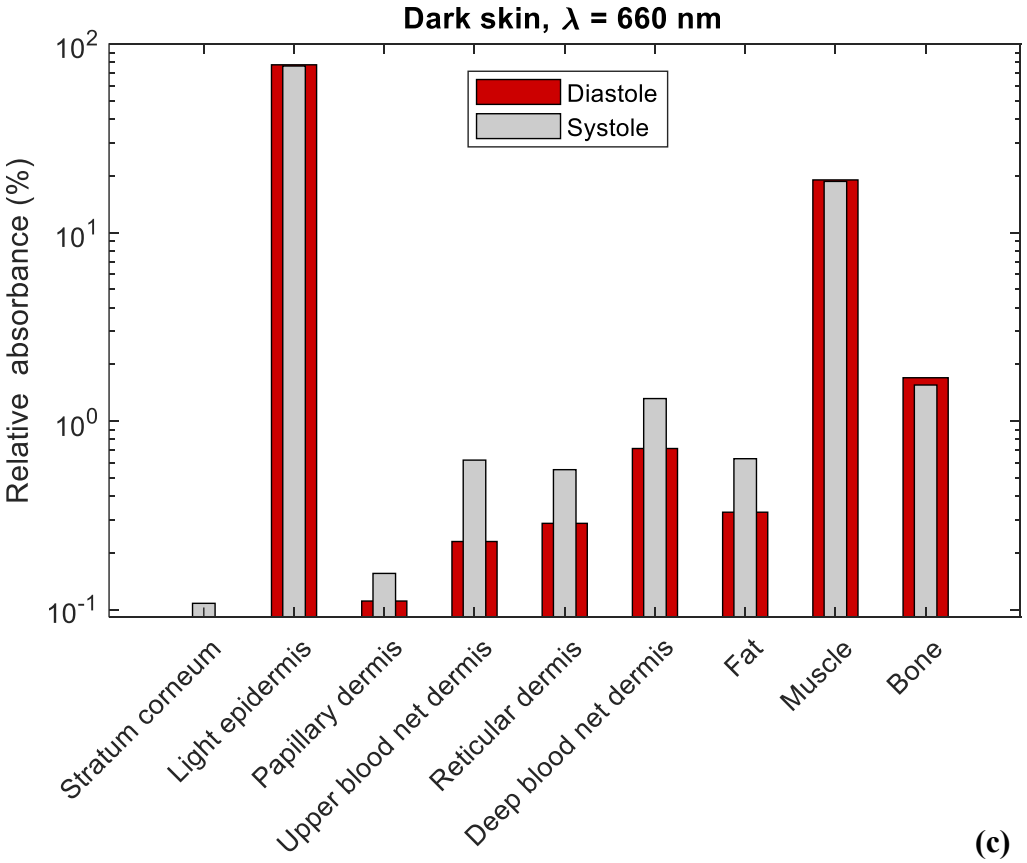
Dark skin, λ = 660 nm
Diastole
Systole
Relative absorbance (%)
10^2
10^1
10^0
10^-1
Stratum corneum
Light epidermis
Papillary dermis
Upper blood net dermis
Reticular dermis
Deep blood net dermis
Fat
Muscle
Bone

(c)

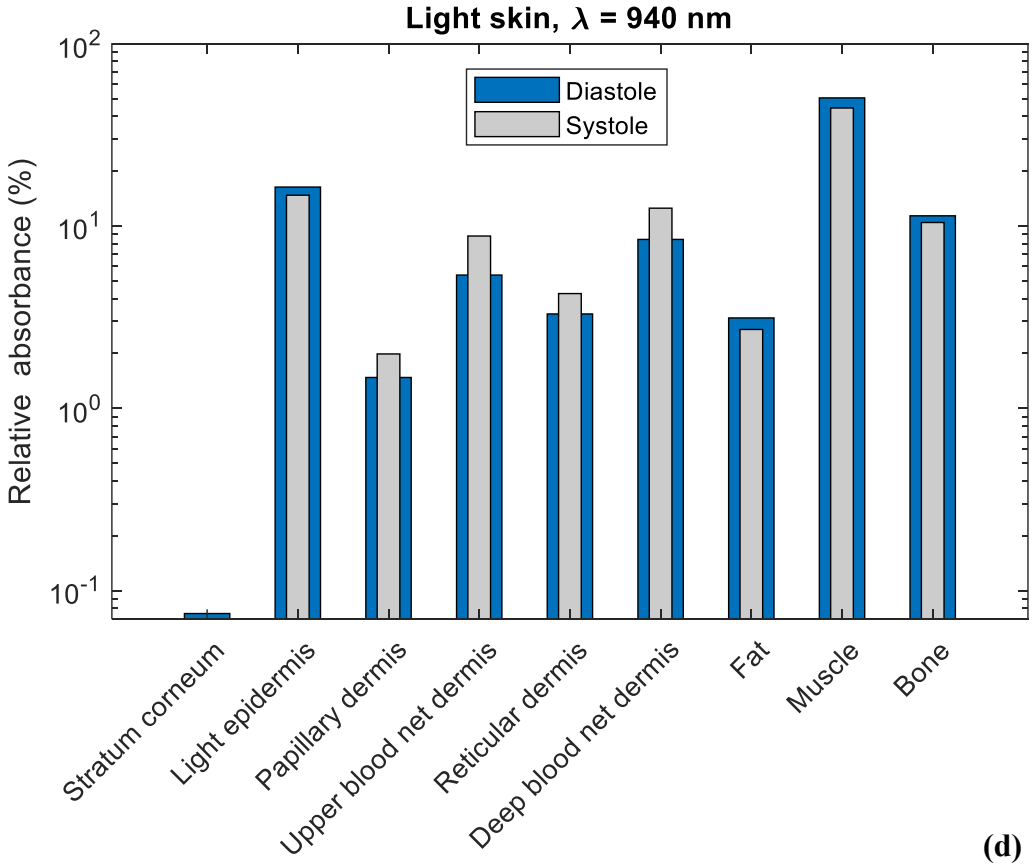
Light skin, λ = 940 nm
Diastole
Systole
Relative absorbance (%)
10^2
10^1
10^0
10^-1
Stratum corneum
Light epidermis
Papillary dermis
Upper blood net dermis
Reticular dermis
Deep blood net dermis
Fat
Muscle
Bone

(d)

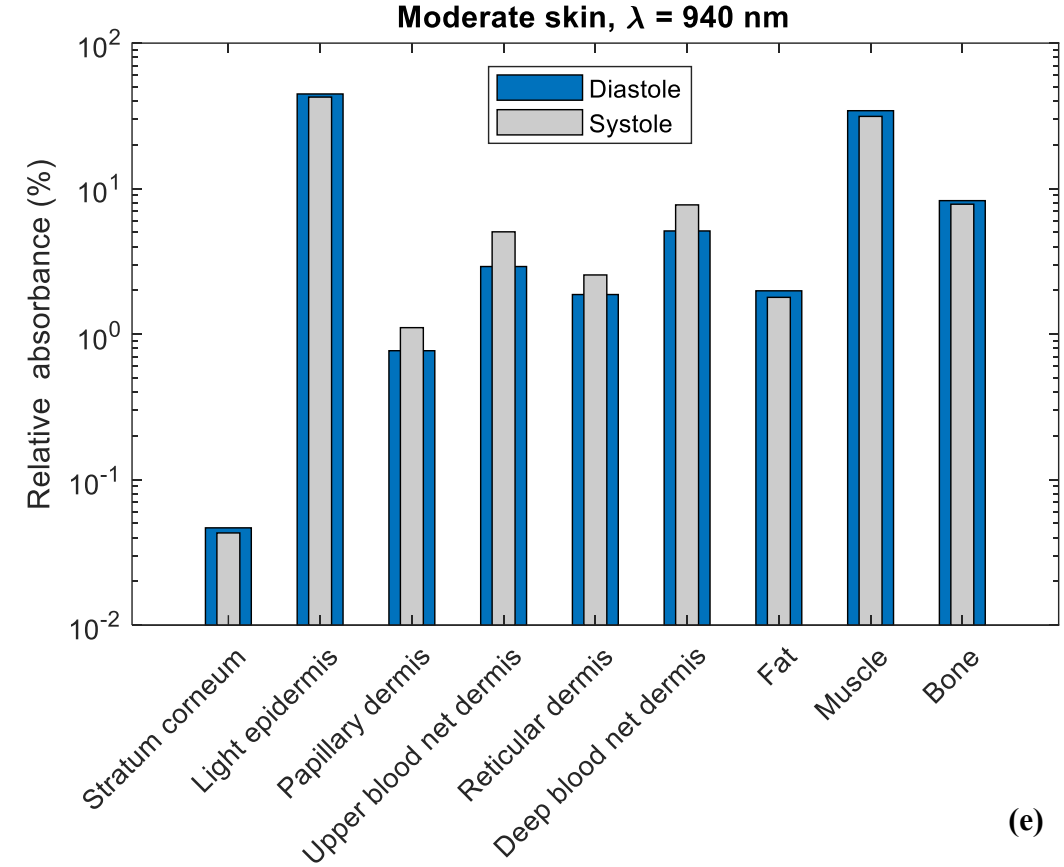

(e)

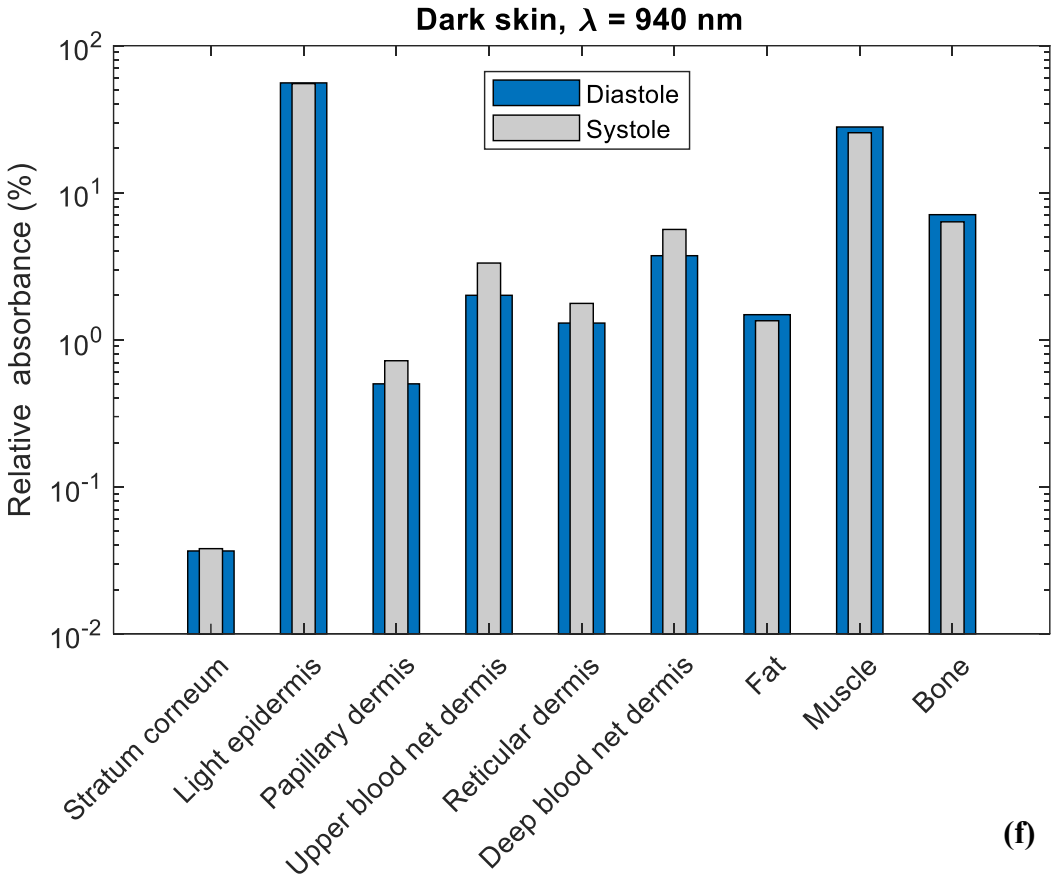

(f)

Figure 9-5. Relative absorbance of detected photons in each sublayer of the simulated finger model at diastolic and systolic states for light, moderate, and dark skin for (a)-(c) red light and (d)-(f) infrared light.

9.3.2. Reflectance PPG

The photon profiles for light, moderate, and dark skin are presented for red and infrared light across five different source-detector separations (1 mm, 3 mm, 5 mm, 7 mm, and 9 mm) in Figure 9-6. As the case with the photon profiles in transmission mode, only the trajectory of the photons that have been detected are shown, and not the photons that have been absorbed or internally reflected when they entered the tissue. The horizontal lines indicate the boundary of each layer of the finger model.

The profiles at 660 nm show that there is an inverse relationship between the source-detector separation and the number of detected photons and scattering events for each skin type. Additionally, photon density is immensely reduced starting from moderate skin when s = 5 mm and beyond. This implies that the photons are unable to travel long distances between the source and detector before being completely absorbed, a phenomenon that intensifies with higher concentrations of melanin. However, for infrared light, slight differences in the scattering density are also observed among the three skin types at smaller source-detector separations, such as 1 mm and 3 mm. Even when the separation is 9 mm, 4790 infrared photons are detected by dark skin in comparison to 173 red photons, indicating the greater probability of red-light absorption at higher melanin concentrations. In comparison to absorption, scattering is the more dominant mechanism of the light-tissue interactions with infrared compared to red light, irrespective of the skin type, even at large-source detector separations.

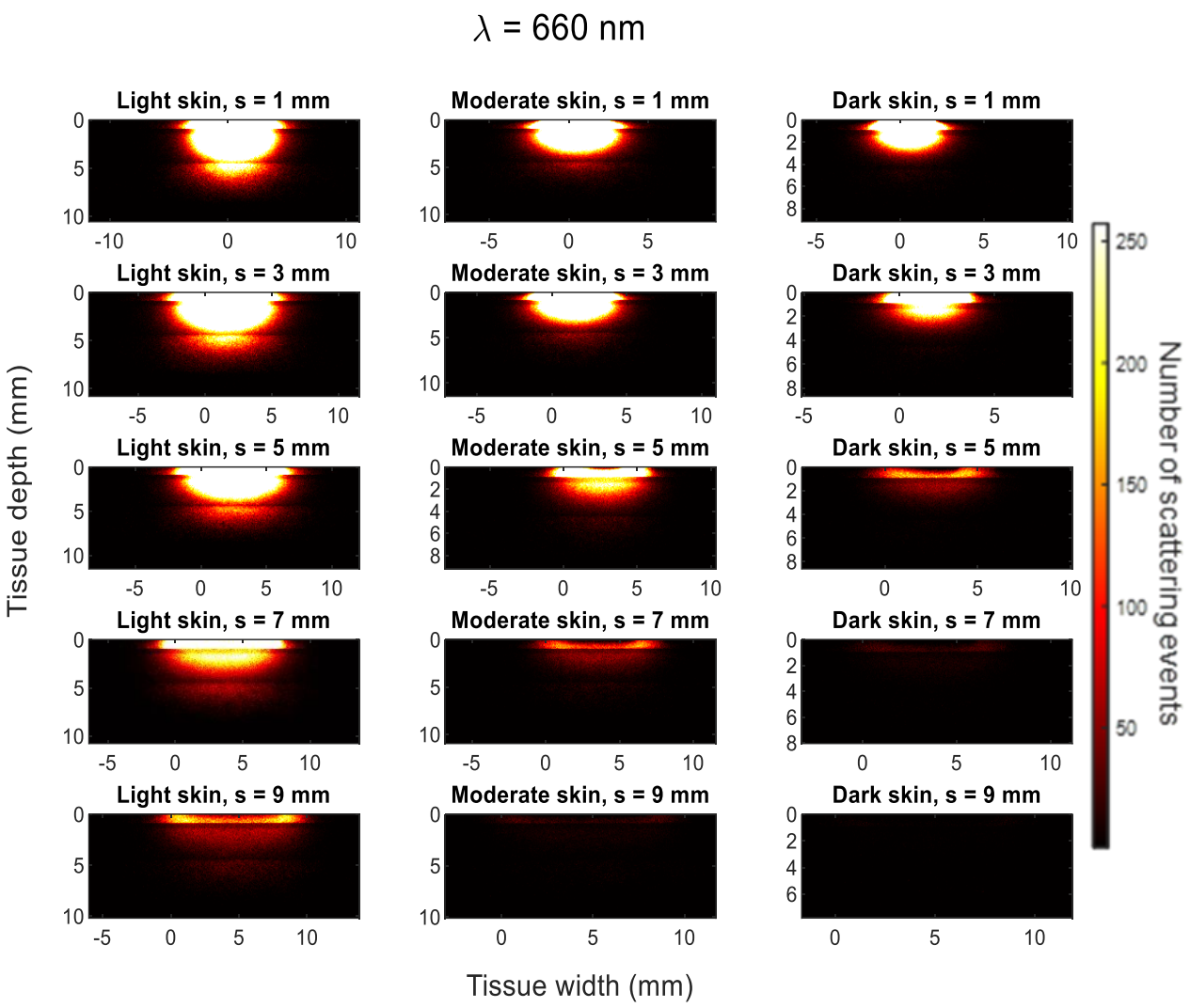
λ = 660 nm
Light skin, s = 1 mm
Moderate skin, s = 1 mm
Dark skin, s = 1 mm
Light skin, s = 3 mm
Moderate skin, s = 3 mm
Dark skin, s = 3 mm
Light skin, s = 5 mm
Moderate skin, s = 5 mm
Dark skin, s = 5 mm
Light skin, s = 7 mm
Moderate skin, s = 7 mm
Dark skin, s = 7 mm
Light skin, s = 9 mm
Moderate skin, s = 9 mm
Dark skin, s = 9 mm
Tissue depth (mm)
Tissue width (mm)
Number of scattering events

(a)

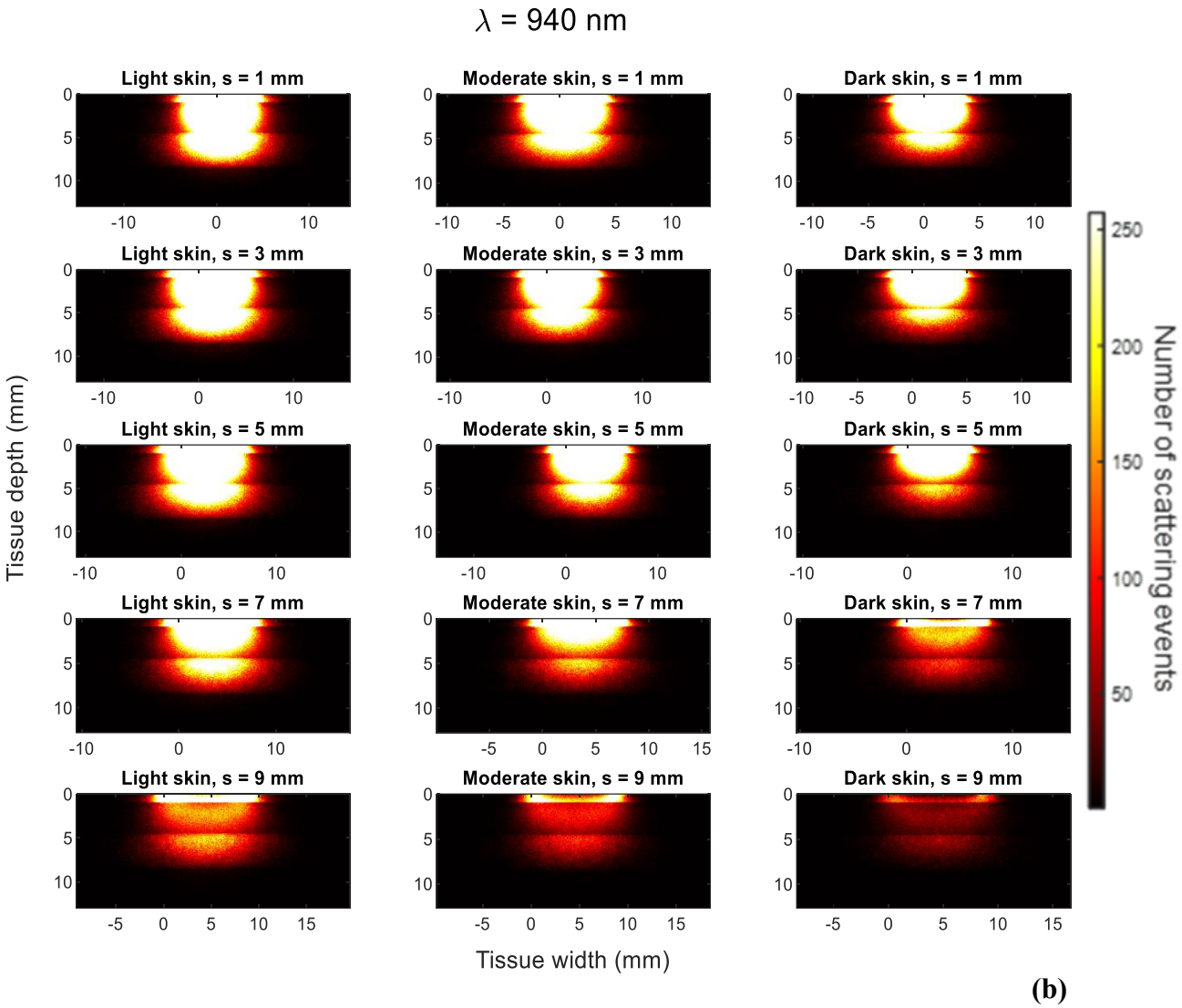

Figure 9-6. Photon propagation profiles of detected photons in reflectance PPG for light, moderate, and dark skin using a (A) 660 nm light source and (B) 940 nm light source across a source-detector separation range of 1 mm – 9 mm. Brighter regions illustrate the high density of scattering events.

Furthermore, Figure 9-7 provides information on the mean optical pathlength for each skin type at both red and infrared wavelengths, against source-detector separations between 1 mm and 9 mm. At both wavelengths, there is a directly proportional relationship between the source-detector separation and the mean optical pathlength, and an inversely proportional relationship between melanin concentration and mean optical pathlength. However, it is important to note that the mean optical pathlength is consistently higher for infrared light compared to red light, as indicated by the respective magnitude ranges on the y-axes of the figures. This suggests that, on average, there is a greater tendency for infrared photons to scatter, which increases the total distance they travel before reaching the photodetector,

regardless of skin type. These findings correlate directly with the behaviour of the photons observed in Figure 9-8, showing the increase in photon penetration depth as the source-detector separation increases for both red and infrared wavelengths. These findings align with the trends observed in the monolayer model outcomes simulated in Chapter 8, suggesting the impact of differently pigmented skin on the overall light-tissue interactions in a multilayered finger model.

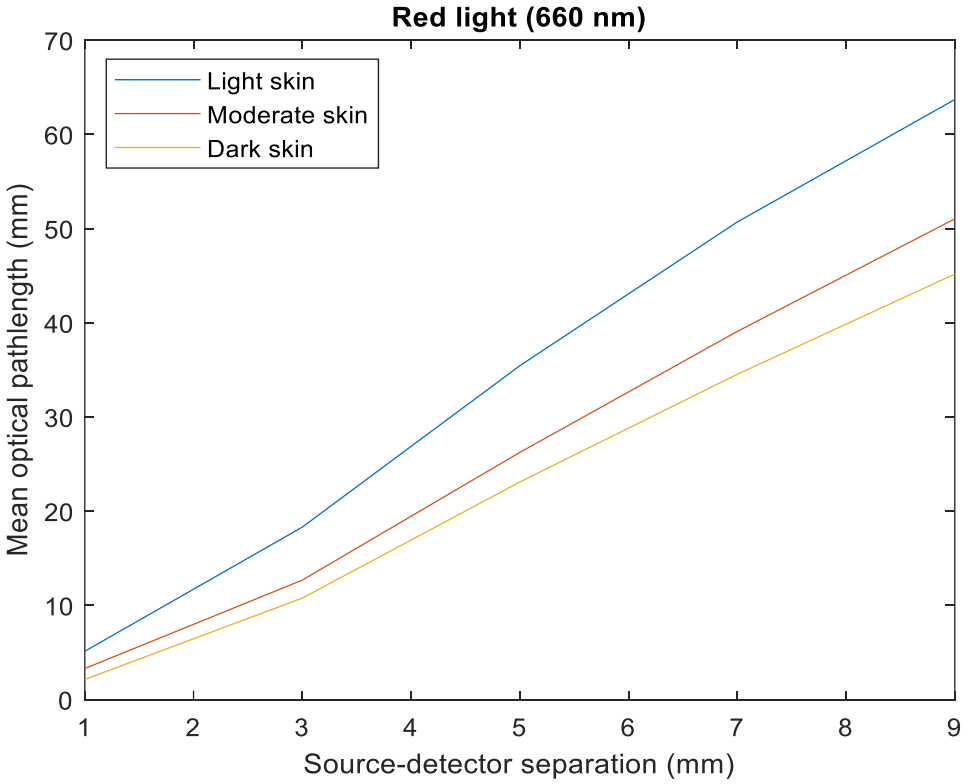

(a)

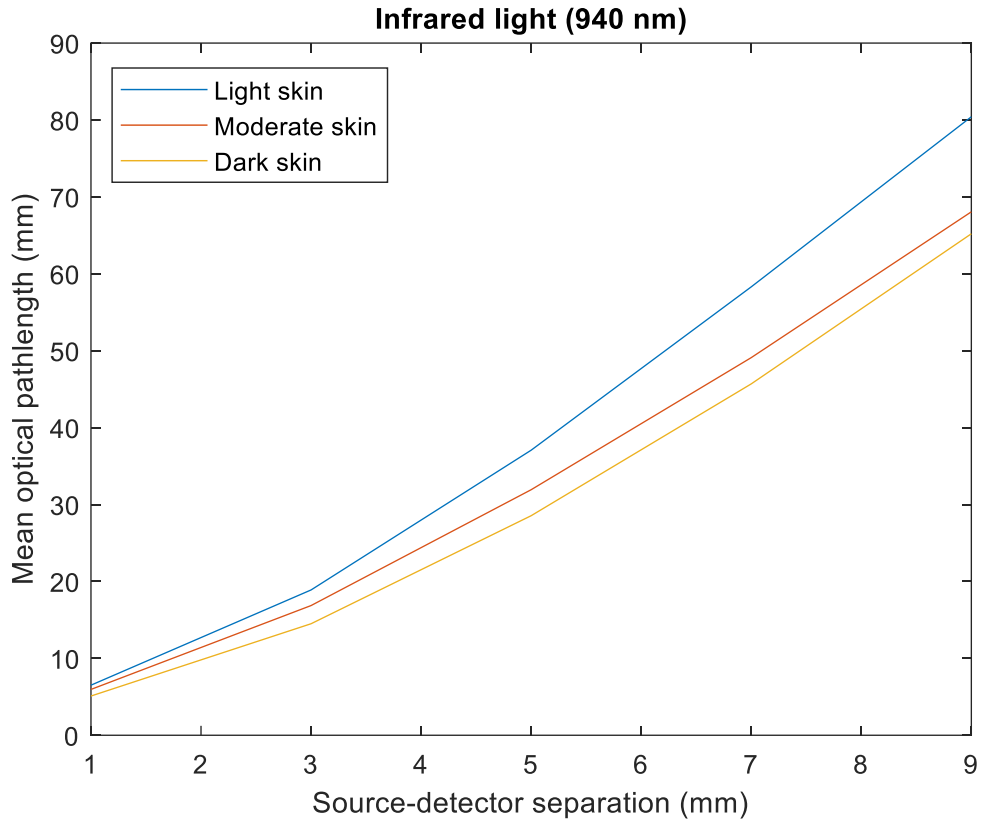

(b)

Figure 9-7. Mean optical pathlength for light, moderate, and dark skin across a source-detector separation range of 1 mm – 9 mm at (a) 660 nm and (b) 940 nm.

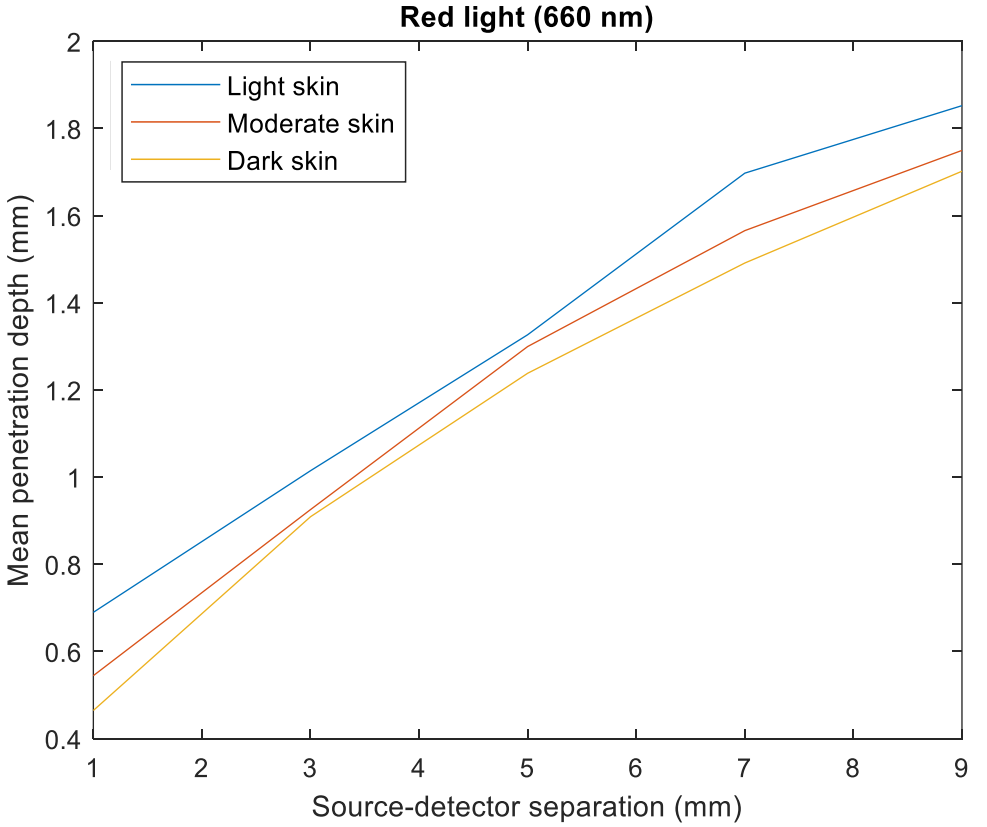

(a)

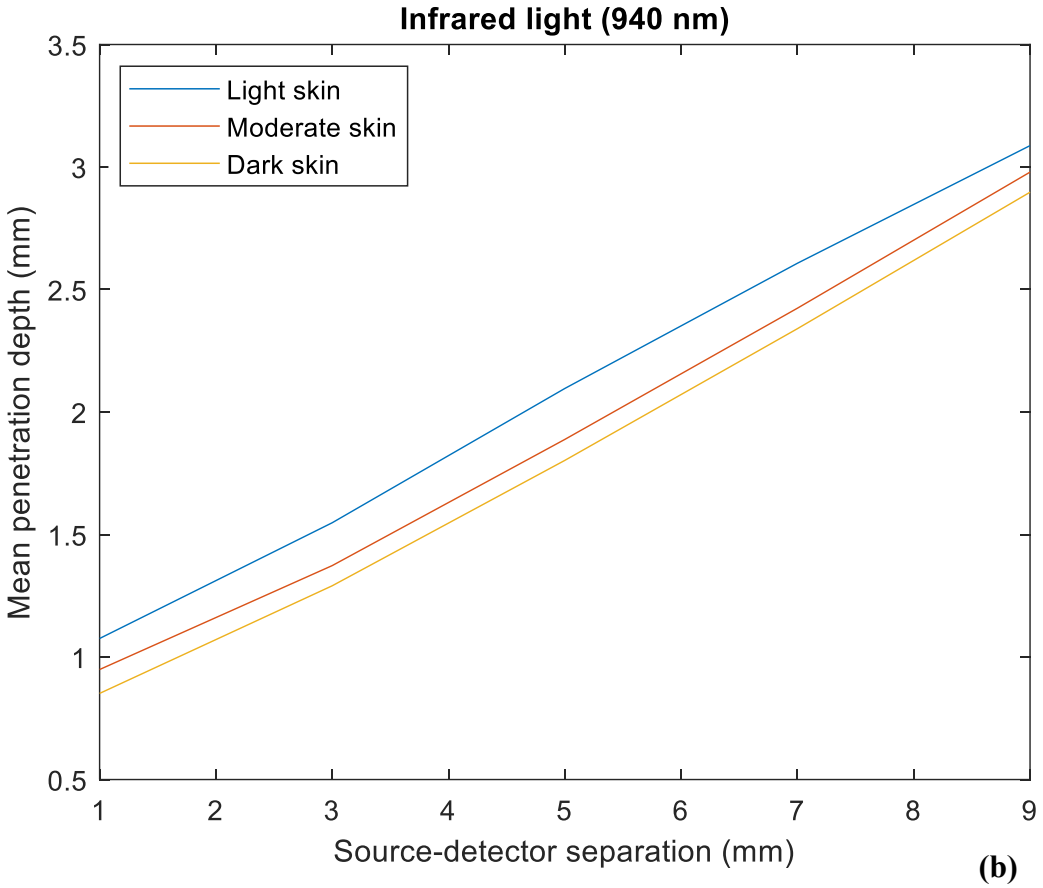

Figure 9-8. Mean photon penetration depth for light, moderate, and dark skin across a source-detector separation range of 1 mm – 9 mm at (a) 660 nm and (b) 940 nm.

Lastly, Figure 9-9 presents the AC and DC components of an instantaneous point in a simulated PPG signal for red and infrared light. Results for light, moderate, and dark skin are shown as the source-detector separation varies from 1 mm to 9 mm. Similar to the previous observations with transmittance AC and DC, the results reveal how the reflectance AC and DC components of the PPG are compromised as a result of increased melanin concentration. Notably, there is a sharp decline in the DC component at both wavelengths beyond a source-detector separation of 1 mm, and an even significant drop in the AC component beyond 5 mm. Also, the AC component (solid lines) does not decrease monotonically beyond a source-separation distance of 5 mm, owing to a lack of detected photons propagating in the dermal layers and not from differences in skin pigmentation. However, the difference between these PPG components in transmittance and reflectance lies in their magnitudes, ranging between 10^{-5} and 10^{-7} for transmittance and 10^{-2} and 10^{-3} for reflectance.

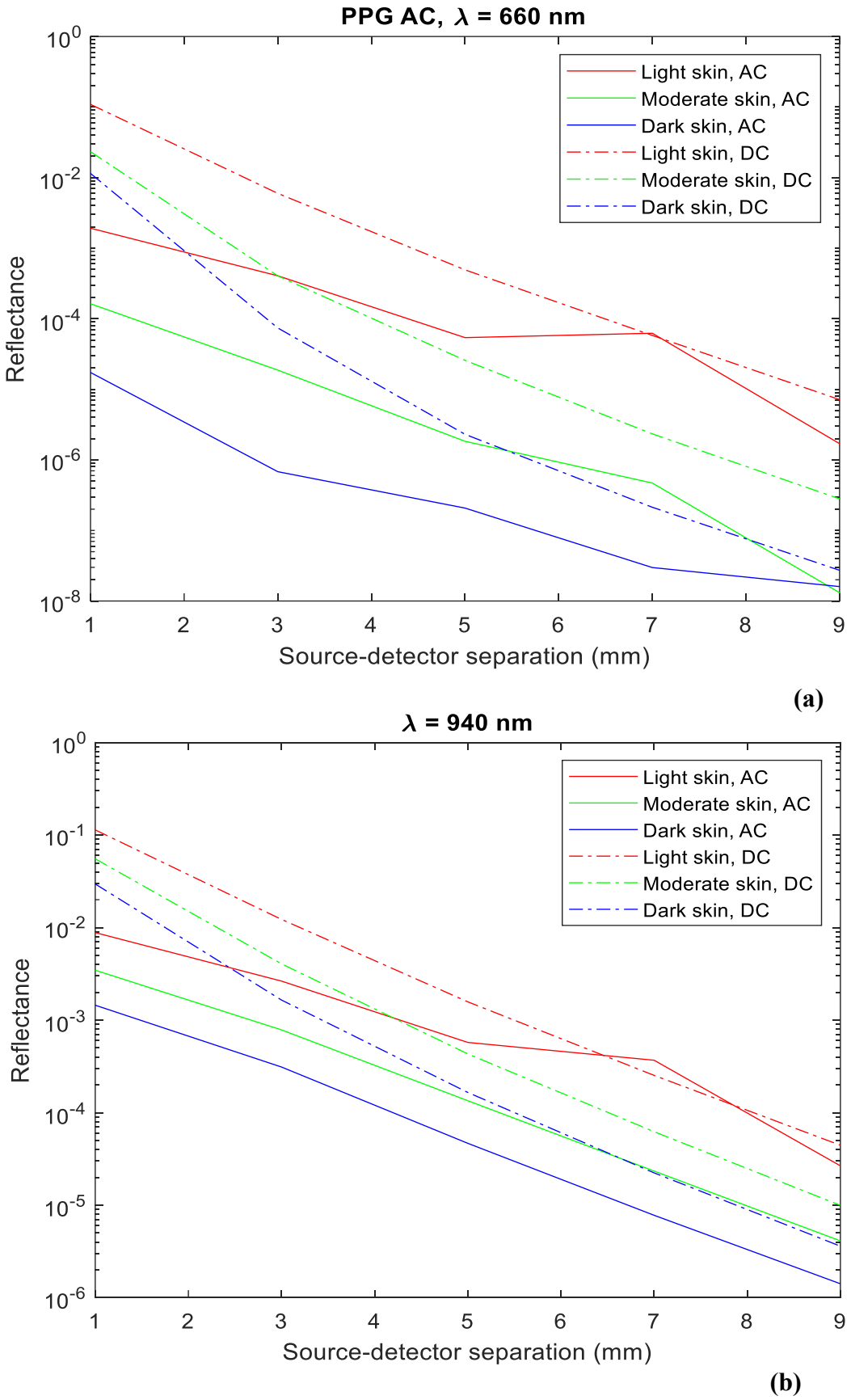

Figure 9-9. Calculated AC and DC reflectance values for light, moderate, and dark skin across a source-detector separation range of 1 mm – 9 mm. (a) AC and DC, 660 nm and (b) AC and DC, 940 nm.

9.3.3. Statistical analysis

The following section presents an evaluation of the results presented of in sections 9.3.1 and 9.3.2 for further analysis. The specific outputs of interests are a) the number of detected photons in transmittance and reflectance PPG, b) mean optical pathlength in reflectance PPG, c) mean penetration depth in reflectance PPG and, d) AC/DC ratio in reflectance mode.

To evaluate the certainty of the simulations, the convergence rate (Q), given by the inverse square root of the number of detected photons (N), is calculated to select the results to be further discussed and analysed. Therefore, any results with a convergence rate less than 0.001 ($N < 1{,}000{,}000$), were omitted because they did not yield reproducible results when ran 3 times, including all those in transmittance (Table 9-2). Calculation of the AC/DC ratio was completed for all skin types in reflectance when s = 1 mm and 3 mm.

For the analysis of transmittance PPG, the number of detected photons is indicative of the quality of the PPG signal, which is observed for both red and infrared light across the three skin types. However, this decrease is more pronounced at 660 nm, evident by the smaller percentage values in moderate and dark skin pigmentation relative to light pigmentation (19% and 3.1% vs. 71% and 46%). This aligns with the decline in the DC intensity, resulting from increased levels of absorption of higher concentrations of melanin.

Table 9-2: The number of detected photons and convergence rate in transmittance mode for light, moderate, and dark skin at 660 nm and 940 nm.

Transmittance PPG						
	Number of detected photons (percentage as compared to light skin at the respective wavelength, %)			Convergence rate (Q)		
	Light	Moderate	Dark	Light	Moderate	Dark
660 nm	1791 (100)	341 (19)	55 (3.1)	0.024	0.054	0.135
940 nm	9655 (100)	6846 (71)	4408 (46)	0.010	0.012	0.015

Furthermore, similar trends in the number of detected photons are observed in reflectance mode across the selected source-detector distances (Figure 9-10). Firstly, the relative percentage

range of detected photons in moderate and dark skin is notably greater in comparison to transmittance PPG. This results from photons being less susceptible to repeated absorption and scattering due to the relatively short distances in which they have travelled (in comparison to 13 mm in transmission).

Moreover, the statistics also present the increase in reflectance from moderate and dark skin types relative to light skin at both wavelengths as the source-detector separation increases. This demonstrates the influence of the separation distance and changes in melanin concentration on predicted 'amplitudes'. In the context of finger probe designs, which have been seen to produce high-quality PPG signals at separation distances between 2 mm and 6 mm [263], the relative reflectance between skin types becomes a critical factor, particularly for dark skin at 660 nm. Whilst majority of the data follows a linear trend, model accuracy is once against compromised beyond a source-detector separation of 7 mm at darker skin types and shorter wavelengths due to small photon detection, resulting in fluctuations in relative reflectance as shown in Figure 9-10.

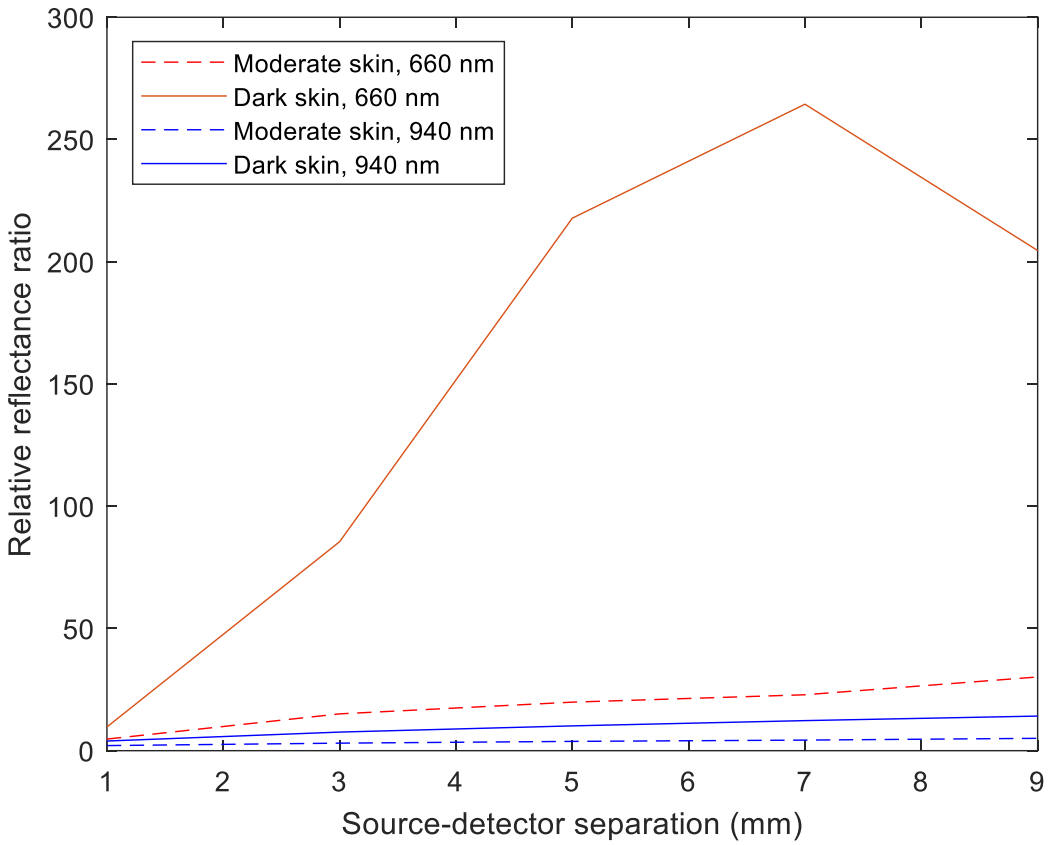

Figure 9-10. Reflectance ratio by moderate and dark skin relative to light skin at 660 nm and 940 nm.

Determining the percentage difference between two data sets provides insight into their proximity (inferred by a small percentage difference), or divergence (inferred by a large percentage difference). Table 9-3 and Table 9-4 display the relative percentage differences in the mean penetration depth and mean optical pathlength among the three skin type combinations, wavelengths, and source-detector separations.

When taking measurements from a finger using a PPG reflectance sensor, a source-detector separation of 3 mm is considered as an optimal distance to minimise saturated light [263]. At this distance, there is a 2.75% difference in mean penetration depth between light and dark skin with red light, and 4.53% with infrared light. This indicates that penetration depth is limited irrespective of melanin concentration, relative to the greater depth in which infrared light can travel in light skin. Overall, the percentage difference between moderate and dark skin is seen to exhibit the lowest percentage. The highest difference is observed between light and dark skin at both wavelengths, which aligns with the approximately 2 and 12 times increase in melanin concentration between the two skin group combinations, respectively.

Furthermore, the average percentage difference in mean optical pathlength between light and dark skin across all separations is almost 2.5 times greater than that between moderate and dark skin at both wavelengths. Evidently, dark skin yields the shortest optical pathlength as a result of its higher absorption rate, causing photons to be terminated more rapidly compared to light and moderate skin. However, this relationship gradually weakens with an increase in the source-detector separation and suggests that there is no one correlation between photon pathlength and penetration depth with infrared light.

Table 9-3: Percentage difference in mean penetration depth between light, moderate, and dark skin across a source-detector separation range of 1 mm – 9 mm (%).

Wavelength (nm)		Skin type combination	Percentage difference in mean penetration depth (%)					Mean % difference across all *sds*
	Source-detector separation		1	3	5	7	9	

	(sds, mm)							
660								
		Light – Moderate	5.89	2.30	0.516	2.02	1.43	2.43
		Light – Dark	9.76	2.75	1.72	3.23	2.12	3.92
		Moderate – Dark	3.96	0.447	1.21	1.22	0.692	1.51
940								
		Light – Moderate	3.13	2.99	2.61	1.82	0.892	2.29
		Light – Dark	5.82	4.53	3.76	2.69	1.59	3.68
		Moderate – Dark	2.71	1.55	1.16	0.877	0.697	1.39

Table 9-4: Percentage difference in mean optical pathlength between light, moderate, and dark skin across a source-detector separation range of 1 mm – 9 mm (%).

Wavelength (nm)		Skin type combination	Percentage difference in mean optical pathlength (%)					Mean % difference across all *sds*
	Source-detector separation (sds, mm)		1	3	5	7	9	
660								
		Light – Moderate	10.8	9.03	7.57	6.47	5.52	7.88
		Light –	20.5	12.9	10.6	9.48	8.51	12.4

		Dark						
		Moderate – Dark	10.7	4.07	3.18	3.09	3.05	4.81
940								
		Light – Moderate	2.26	2.84	3.72	4.28	4.16	3.45
		Light – Dark	6.09	6.58	6.49	6.07	5.22	6.09
		Moderate – Dark	3.86	3.77	2.79	1.81	1.07	2.49

Lastly, the AC/DC ratios across the three skin types, both wavelengths, and at source-detector separations of 1 mm and 3 mm, are shown in Figure 9-11. For red and infrared light, the AC/DC ratio is highest for light skin, followed by moderate skin, and then dark skin. Notably, the AC/DC ratios are higher at 940 nm compared to 660 nm, with a narrower difference in magnitude between the three skin types. It becomes evident that skin type, particularly with red light, significantly reduces AC reflectance in comparison to infrared light, resulting in a larger gap between the AC and DC components. Consequently, when a smaller AC value is divided by a relatively similar (and larger) DC value between all skin types, it results in an overall reduced ratio. This suggests that the perfusion index (PI, ratio between AC and DC components) at 660 nm is more impacted by changes in melanin concentration and the source-detector separations. Since the AC/DC ratio is an important parameter in photoplethysmography that is often analysed to assess the strength or amplitude of the pulsatile component, changes in this ratio due to differences in skin pigmentation must be accounted for. Therefore, while a reduced AC/DC ratio may indicate poor pulsatile signal quality potentially due to weakened arterial flow, in this instance, it may be due to interference from the patient's skin colour.

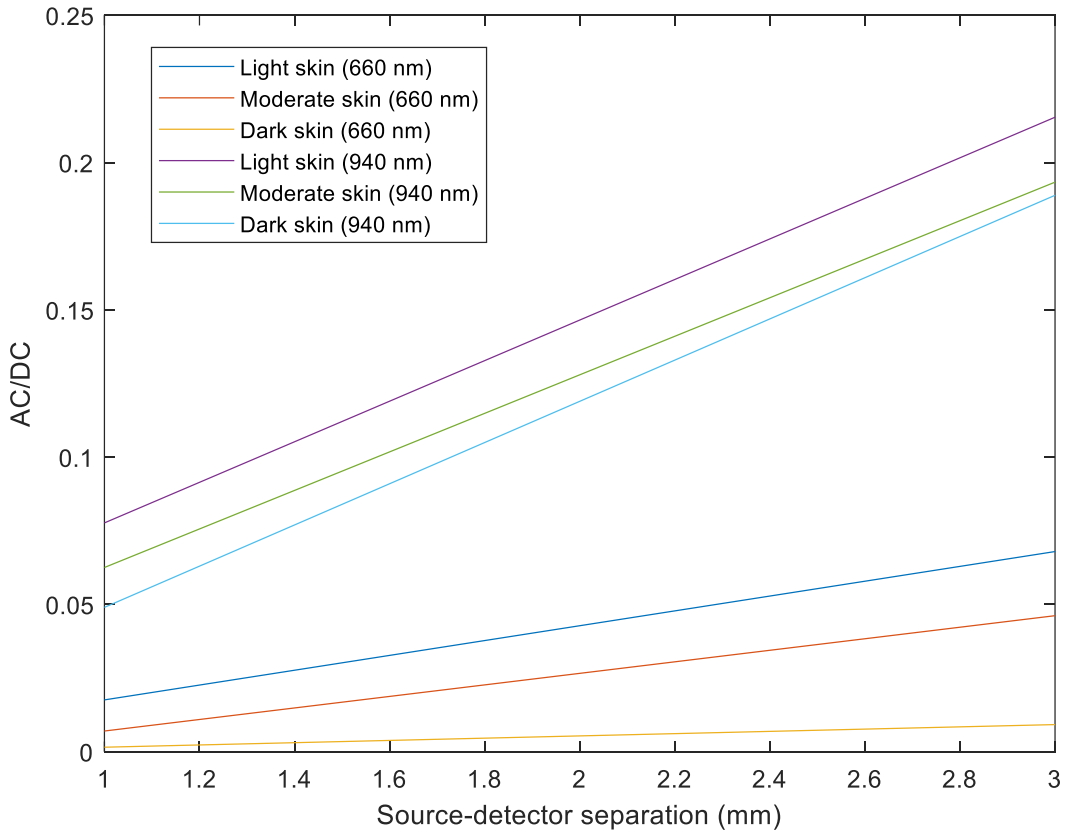

Figure 9-11. AC/DC ratio for light, moderate, and dark skin at source-detector separations of 1 mm and 3 mm for red (660 nm) and infrared (940 nm) light.

9.4.Summary

The current model has provided valuable insights into the interaction between red and infrared light with a heterogeneous model of the finger. Three epidermal melanin concentration levels were simulated, allowing for the preliminary replication of different skin pigmentation groups based on the Fitzpatrick scale, a common method for stratifying skin colour. The study's exploration of light-tissue interactions suggests the extent of light absorption in transmittance versus reflectance across three skin types, with implications for computational resources when simulating skin pigmentation's impact on PPG -based applications. For example, in future simulations, an equal and substantial number of photons needs to be detected in both transmittance and reflectance PPG modes across all skin types to produce more accurate outcomes. This ensures the development of a more robust model before delving further into the potential reasons for inaccuracy in PPG measurement due to differences in skin pigmentation as observed in some clinical studies. The presented model is useful for examining specific application parameters in pulse oximetry, such as the ratio of ratios.

CHAPTER 10: MONTE CARLO SIMULATION OF THE EFFECT OF MELANIN CONCENTRATION ON LIGHT-TISSUE INTERACTIONS FOR TRANSMITTANCE AND REFLECTANCE PULSE OXIMETRY MEASUREMENT

10.1.Introduction

The need to assess the performance of pulse oximeters gained huge attention over the past four years, with the motivation to build upon findings firstly reported by Sjoding et al [73]. Their study highlighted a significant disparity in the detection of occult hypoxemia between Black patients and White patients, with Black patients exhibiting nearly three times the frequency of undetected hypoxaemia when using pulse oximeters. In the wake of these findings, both pulse oximetry companies and research laboratories have undertaken comprehensive retesting of various over-the-counter and commercial pulse oximeters to assess their accuracy particularly in individuals with darker skin pigmentation [264]. While some have shown through their studies that the accuracy of their devices are not affected by melanin [52], [265], [266], the majority have yielded a mix of opinions regarding their statistical and clinical significance. Hence, this has shifted the focus to investigating the potential sources of inaccuracy in pulse oximetry, primarily from an engineering hardware perspective in an effort to unravel the underlying issues.

Considering the influence of different skin pigmentation levels on red-light detection from Chapter 8 and 9, there is other research to suggest that bias associated with skin pigment, inherent in some currently available pulse oximeters, could be effectively mitigated when using narrowband light sources [267]. The rationale behind this lies in the fact that light emitting diodes (LEDs), with their distinct spectral responses, emit a range of wavelengths and not only the peak wavelength of light. This broader spectrum of emitted light can lead to varying interactions with melanin content in the skin, especially at higher concentrations. Furthermore, research by Cabanas et al [268] has continued to support this hypothesis, by reinforcing the idea that monochromatic light sources can minimise the positive bias associated with individuals with darker skin pigmentation. Overall, these suggestions align with the notion that by employing specific wavelengths of light that are less sensitive to changes in skin colour, pulse oximeters can offer more accurate and reliable readings for diverse groups of individuals.

In the context of pulse oximetry and the challenges associated with skin pigmentation, computational models utilising the Monte Carlo technique have shown to be crucial for

predicting the outcomes of complex systems, as previously discussed. The limited research on the absorption spectra of different melanin concentrations, combined with the standardised calibration algorithms primarily designed and tested on individuals with lighter skin, underscores the need for these types of simulations. Some research has explored how variations in melanin concentration could impact levels of bias ($SpO_2 - SaO_2$) or the implications of the differences in important parameters such as the perfusion index between light and dark skin [223], [229], [269], [270]. As discussed in Chapter 6, Arefin et al [229] utilised the Monte Carlo technique to conduct random sampling on various concentrations of melanin, blood, and bilirubin concentrations. These samples represented a cohort that aligns with Food and Drug Administration (FDA) regulations for pulse oximeter calibration i.e., for 20% of the participant pool to be darkly pigmented. Their findings showed overestimation of SpO_2 in Black subjects by presenting the level of bias, which was seen to decrease when the calibration process involved distributions with a greater enrolment of individuals with higher levels of pigmentation. Furthermore, results observed by Hu et al [270] and Reiser et al [208] on reflectance pulse oximetry were consistent with each other. Both studies showed that a) the AC and DC ratios increased with decreasing melanin concentration and b) the effect of melanin concentration on the red-light PPG characteristics should be paid more attention when predicting blood oxygen saturation. This highlights computationally that melanin concentration may have a similar effect on SpO_2 measurement in both the wrist and finger for transmittance and reflectance pulse oximeter modes.

Evidently, all studies have contributed to some of the concerns regarding pulse oximeter design or have shed light on potential sources of systematic errors that might lead to the overestimation of oxygen saturation in individuals with darker skin pigmentation. However, they highlight the need for refinement of calibration algorithms for pulse oximeters to accommodate diverse skin pigments. Therefore, the aim of the study presented in this chapter is to generate simulated pulse oximetry calibration curves for individuals with light, moderate, and dark skin pigmentation in transmittance and reflectance pulse oximetry modes using the previous multi-layered Monte Carlo model of the finger in Chapter 9. Transmittance mode is used to compare findings with common medical-grade pulse oximeters, while reflectance mode is included to assess inaccuracies caused by skin pigmentation despite their reliance on interactions with the skin's superficial layers. The novelty in this approach lies in the validation of the simulated outcomes which: a) provide computational evidence to support the data trends observed in

clinical studies, b) better identify the impact of skin pigmentation on SpO_2 accuracy, and c) suggest practical solutions for future improvements in current calibration algorithms.

10.2.Method for execution

The same finger model structure, simulation of the epidermal layers, optical properties of the tissue layers, wavelengths, and PPG configurations are applied in this study. However, unlike in Chapter 9 where the SpO_2 level was fixed at 100%, this chapter investigates the combined effects of melanin concentration and varying oxygen saturation levels. As pulse oximeters are typically calibrated for SpO_2 levels between 70% and 100%, arterial oxygen saturation levels within this range are simulated in 5% increments. To improve computational efficiency, parallel computing is employed to run 10 single photons at a time (for a computer with 10 cores). Then, the simulations are run until one million photons are detected for each combination of melanin concentration and SpO_2 level (42 combinations between both transmittance and reflectance modes). This way, all the results, irrespective of melanin level, can be directly compared as they have the same number of generated outcomes. Launching the same number of photons will impact the quality and reliability of the data depending on the number of photons that survive and become detected, as seen in Chapters 8 and 9.

The systolic and diastolic output intensities were utilised to derive the AC and DC components, which were subsequently used to calculate the perfusion index at 660 nm and 940 nm. These values are then divided to obtain the simulated ratio of ratios (eq. (4-3)) for each of the seven oxygen saturation levels, which are then plotted to generate simulated calibration curves for each skin type in both transmittance and reflectance modes.

10.3.Results

10.3.1. Transmittance pulse oximetry

Using the data generated from the Monte Carlo simulation, three calibration curves were obtained for light, moderate, and dark skin in Figure 10-1. The solid lines represent the lines of best fit (LOBF) for each simulated (dashed) algorithm curve, to replicate those integrated in pulse oximeters. These calibration curves illustrate the correlation between the non-invasive

measurement of arterial oxygen saturation and the ratio of ratios. As shown, moderate and dark skin calibration curves are shifted with respect to the simulated calibration curve for light skin and the commercial pulse oximeter. This occurs from a relatively greater increase in absorption of red light as melanin concentration increases for each oxygen saturation level compared to infrared light (

Table **10-1**). According to the calculation of the ratio of ratios the value of R decreases if the normalised transmittance in the red wavelength (numerator) decreases and is divided by slight variations in larger normalised transmittance values from the infrared wavelength (denominator). The raw AC/DC values at 660 nm demonstrate a clear trend where the perfusion index decreases with increasing melanin concentration and oxygen saturation. This trend is consistent with the known absorption characteristics of haemoglobin and melanin. At 660 nm, deoxyhaemoglobin absorbs more light, and higher melanin concentrations result in increased absorption, thus reducing the detected signal. On the other hand, the signal at 940 nm appears less influenced by melanin. This is expected because the absorption of light by melanin is significantly lower at this wavelength compared to 660 nm (**Figure 3-2** [130]). Additionally, at a haematocrit level of 45%, oxyhaemoglobin and deoxyhaemoglobin have similar absorption coefficients at 940 nm (0.65 mm^{-1} and 0.43 mm^{-1}, respectively [261]), in comparison to 0.15 and 1.64 at 660 nm. Hence, the infrared signal is more stable across different levels of oxygen saturation and melanin concentration. From these findings, it becomes apparent that skin pigmentation influences pulse oximeter calibration algorithms, and that a single algorithm may not be suitable for all skin types. This is suggested by the varying behaviour of light in the presence of different epidermal melanin concentrations, especially in the visible region.

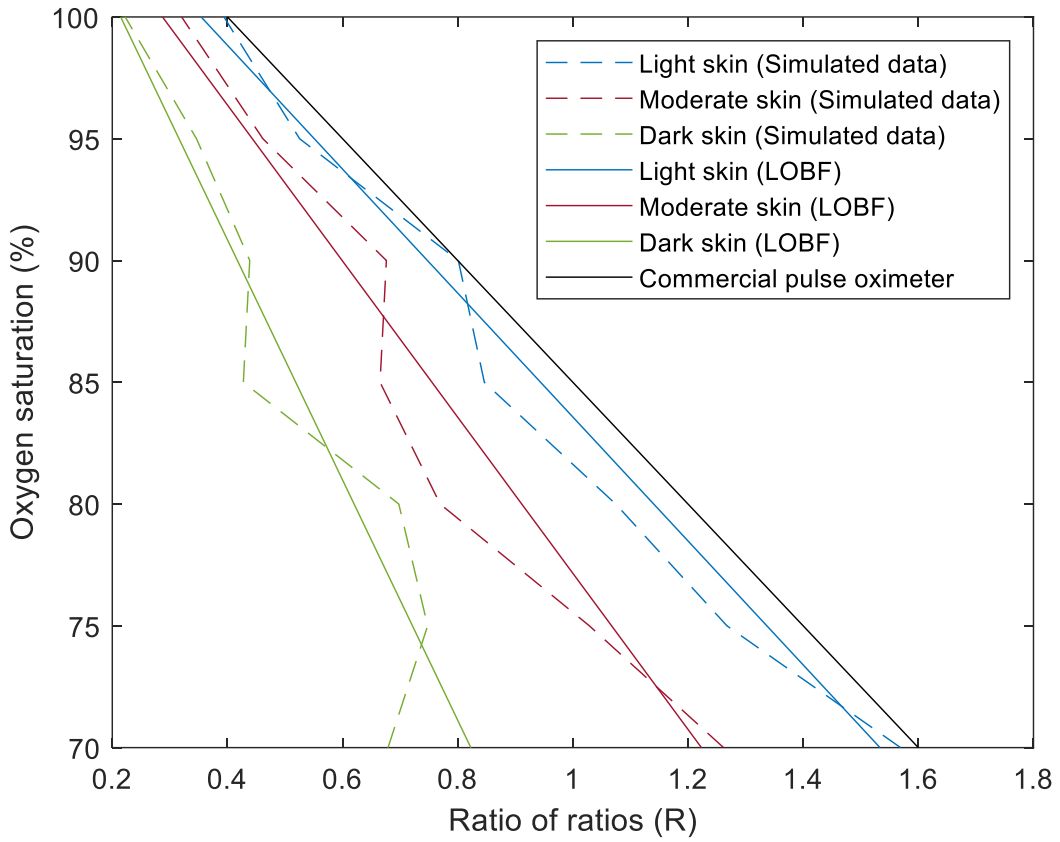

Figure 10-1. Simulated calibration curves for light, moderate, and dark skin in transmittance mode pulse oximetry. The dashed lines show the computed ratio of ratios using the simulated input and output intensities. The solid lines show the lines of best fit for each calibration curves, compared against a widely used algorithm in commercial pulse oximeters for many applications [209].

Table 10-1: Simulated raw AC/DC data at red (660 nm) and infrared (940 nm) wavelengths for all simulated SaO_2 values (70% - 100%) and skin types. The AC and DC components are calculated using output transmittance during systole and diastole.

Skin type	Red light (660 nm)						
	70%	75%	80%	85%	90%	95%	100%
Light	0.4398	0.3845	0.3232	0.2785	0.2631	0.1610	0.1192
Moderate	0.3012	0.2328	0.1759	0.1524	0.2495	0.1383	0.0831
Dark	0.2114	0.1758	0.1607	0.1316	0.1085	0.0811	0.0586
	Infrared light (940 nm)						

Light	0.2748	0.2973	0.2949	0.3227	0.3220	0. 3007	0.2967
Moderate	0.2340	0.2219	0.2240	0.2247	0.3618	0.2937	0.2543
Dark	0.3051	0.2305	0.2258	0.3015	0.2425	0.2296	0.2585

Commercial pulse oximeter	$\mathrm{SpO_2} = 110 - 25\mathrm{R}$	(10-1a)
Light skin	$\mathrm{SaO_2} = 109 - 25.95\mathrm{R}$	(10-1b)
Moderate skin	$\mathrm{SaO_2} = 109.2 - 32.69\mathrm{R}$	(10-1c)
Dark skin	$\mathrm{SaO_2} = 110.6 - 50.31\mathrm{R}$	(10-1d)

Following the simulation of the calibration curves for the three skin types, the level of bias was computed between light and dark skin to be compared against the bias observed in the cohort study conducted by Sjoding et al [73]. In this study, a total of 48,097 paired SpO_2 and SaO_2 readings were recorded between two cohorts, each within a 10-minute time period. SaO_2 was directly measured by co-oximetry and included carboxyhaemoglobin and methaemoglobin saturations.

For direct comparison between the computational and clinical datasets, SpO_2 was derived for light and dark skin using their respective simulated calibration equations (eqs. (10-1b) and (10-1d). Both equations were rearranged to calculate the ratio of ratios for SaO_2 values between 86% and 92%, as this covered the mean range for SpO_2 values between 89% and 96% from the cohort study. These R values were then substituted into eq. 10-1a, to calculate predicted SpO_2 based on skin type, and then to calculate the difference between true and non-invasive oxygenation. Table 10-2 and Table 10-3 show SaO_2 and SpO_2 data from the clinical and Monte Carlo simulation study for White (Light) and Black (Dark) subjects, respectively.

The larger bias observed in the Monte Carlo simulation results compared to the clinical study data can be attributed to the relative simplification and assumptions about tissue optical properties and physiological conditions. This may not fully capture the complexities and variability inherent in human subjects, especially those with darker skin pigmentation which can average out biases. Despite these differences, the similarity in the ratio between the two sets of data (6.6 for the clinical study and 5.47 for the simulation study) suggests that the

underlying trends and relationships are consistent across both methods, providing confidence in the overall validity of the simulation approach.

Table 10-2: Approximated mean and range of SaO_2 data for an SpO_2 range between 89% - 96% SpO_2 extracted from Sjoding et al cohort study who investigated occult hypoxemia in patients identifying as White or Black. Bias is calculated by subtracted SaO_2 from SpO_2, and the mean bias is calculated to provide a quantitative measure of the ratio of ratios between bias level in White and Black subjects.

SpO_2 (%)	SaO_2 (%) Mean (range)		Bias (SpO_2 – SaO_2, %) Mean (range)	
	White subjects	Black subjects	White subjects	Black subjects
89	88.5 (78 – 99)	86 (83 – 92)	0.5 (11 – -3)	3 (6 – -3)
90	89 (80 – 97.5)	87 (83 – 97)	1 (3 – -7.5)	3 (7 – -7)
91	91 (83 – 98)	87.5 (80 – 97.5)	0 (8 – -7)	3.5 (11 – -6.5)
92	92 (83.5 – 98.5)	89 (82.5 – 96)	0 (8.5 – -6.5)	4 (9.5 – -4)
93	93 (85 – 98)	90 (84 – 97.5)	0 (8 – -5)	3 (7 – -7)
94	93.5 (86 – 98)	91.5 (85 – 97)	0.5 (8 – -4)	2.5 (9 – -3)
95	94 (87 – 98.5)	92 (85.5 – 97)	1 (8 – -3.5)	3 (9.5 – -2)
96	94.5 (89 – 99)	92 (84 – 98)	1.5 (7 – -3)	4 (12 – -2)
			Mean bias (%)	
			0.5 (7.7 – -4.9)	**3.3 (8.9 – -4.3)**
			Ratio between mean biases	
			6.6	

Table 10-3: Simulated oxygen saturation (SpO_2) for light and dark skin. The computed ratio of ratios for a SaO_2 range between 86% and 92% are inputted in the commercial pulse oximeter equation to calculate predicted SpO_2 with current in-built algorithms. Bias is calculated for both skin types and used to determine the mean ratio between the biases.

True SaO_2 (input), %	Simulated SpO_2 (output), %		Bias (SpO_2 – SaO_2), %	
	Light skin	Dark skin	Light skin	Dark skin
86	87.8	96.8	1.8	10.8
87	88.8	97.3	1.8	10.3
88	89.8	97.8	1.8	9.8
89	90.7	98.3	1.7	9.3
90	91.7	98.8	1.7	8.8
91	92.7	99.2	1.7	8.3
92	93.6	99.8	1.6	7.8
			Mean bias (%)	
			1.7	**9.3**
			Ratio between mean biases	
			5.47	

Moreover, the feasibility of data manipulation to devise potential solutions for pulse oximeter calibration for moderate and dark skin pigmentation was explored. Given that current pulse oximeters exhibit minimal bias in light skin, this indicates that algorithms may be predominantly tailored to this demographic. Therefore, the light skin calibration curve served as a reference, and was used to calculate the ratios between the R values of light and moderate skin and light and dark skin at a reference SpO_2 of 100%. This was done to ensure that pulse oximeters meet the minimum requirement of providing accurate measurements in healthy individuals, irrespective of skin pigmentation level. These calculations yielded multipliers of 1.23 and 1.65, respectively. After initially applying these values across the total oxygen

saturation range, it became visually apparent that moderate skin closely aligned with the light skin calibration curve, but not for dark skin below 100% (Figure 10-2a). This observation suggested that a linear multiplier alone may not suffice for implementing an inherent correction in pulse oximeters for dark skin. Even at an oxygen saturation level of 90% (Figure 10-2b), a bias of 2.1% was recorded relative to light and moderate skin. Consequently, the ratios between the R values for light and dark skin were recalculated for the entire oxygen saturation range, as depicted in Figure 10-3a. Notably, these ratios suggested an exponential trend, which can be attributed to the decrease in the pathlength and photon penetration depth due to increased absorption (characterised by a higher absorption coefficient value), thus reducing the perfusion index, especially at higher oxygen saturation levels in the dermal layers (eq. (9-1)). The mean of these multipliers was equal to approximately 1.8, which was then applied to the original dark skin calibration curve, resulting in significant adjustments that brought all calibration algorithms for the three skin types into close proximity (Figure 10-3b). Hence, the adjustments suggest the feasibility of integrating corrective measures into pulse oximeter designs to safeguard SpO_2 accuracy against the influence of skin pigmentation.

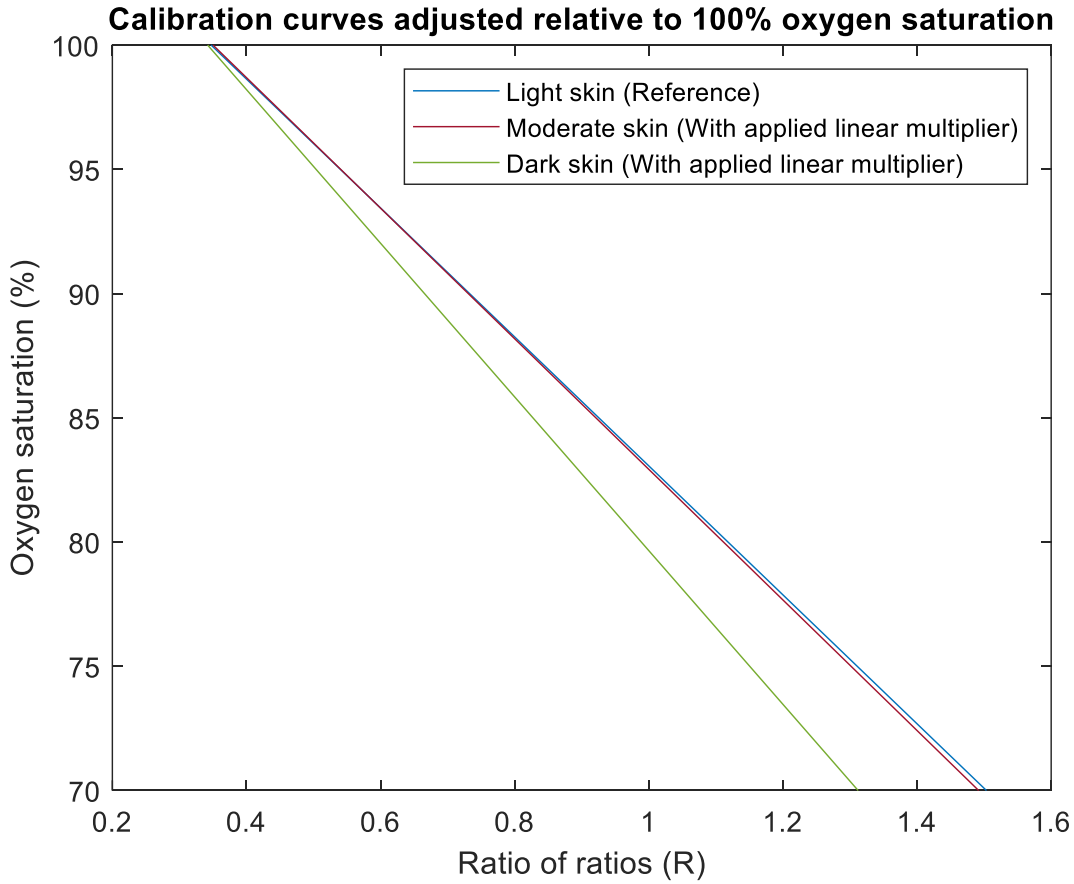

(a)

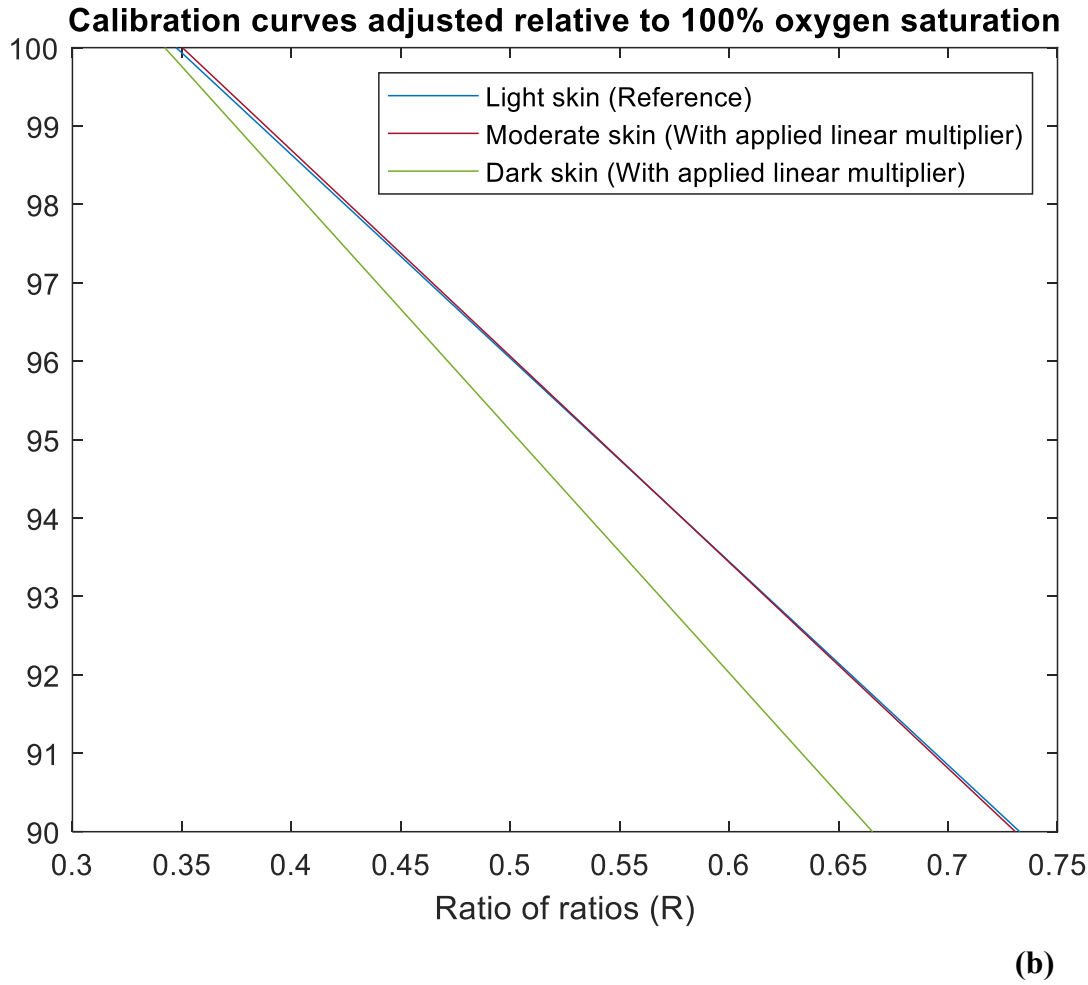

Figure 10-2. Adjusted calibration curves for moderate and dark skin with an applied linear multiplier relative to light skin at 100% oxygen saturation. (a) Adjusted calibration curves between 70% and 100% oxygen saturation. (b) Adjusted calibration curves between 90% and 100% oxygen saturation (range of interest). The data suggests that the dark skin calibration curve requires a non-linear re-adjustment.

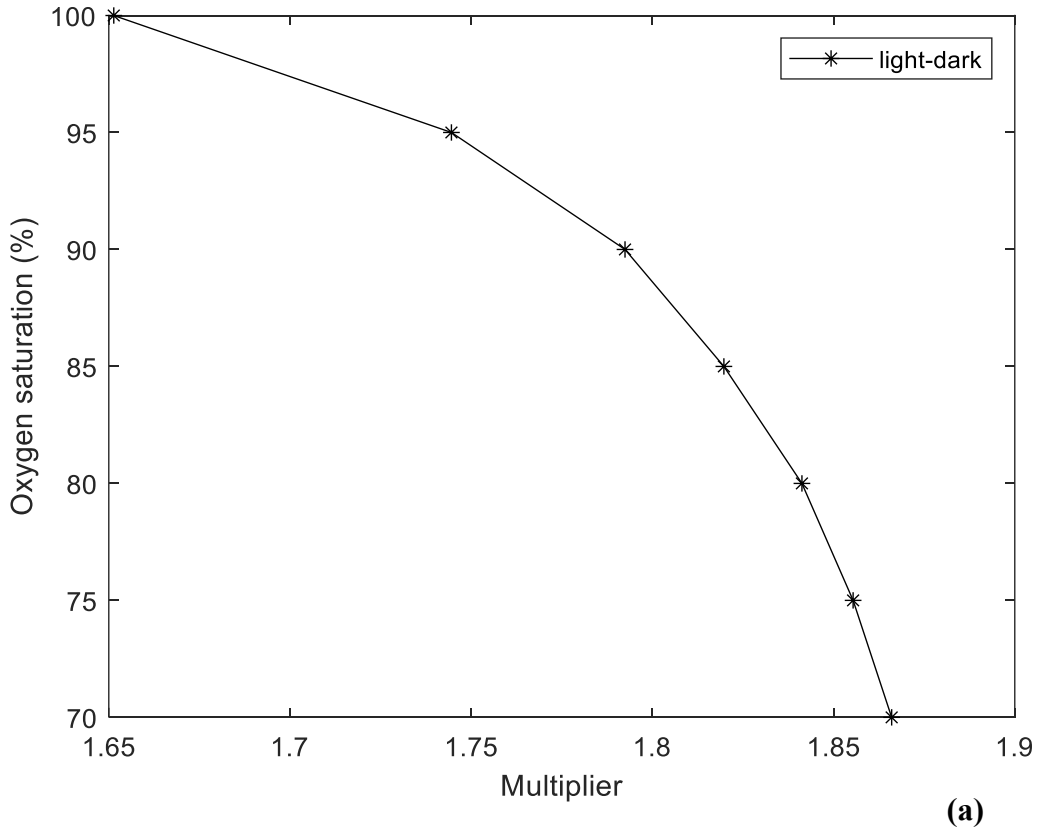
light-dark
Oxygen saturation (%)
Multiplier
100
95
90
85
80
75
70
1.65
1.7
1.75
1.8
1.85
1.9

(a)

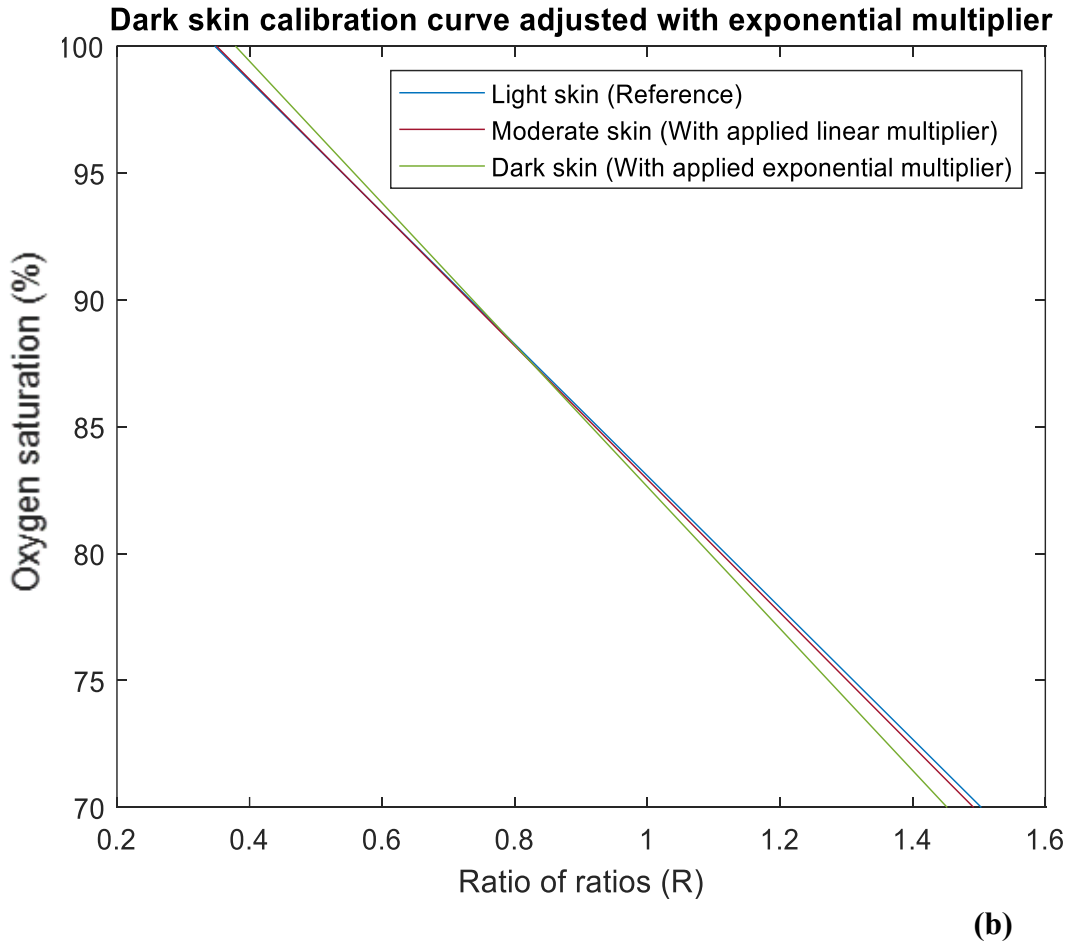
Dark skin calibration curve adjusted with exponential multiplier
Light skin (Reference)
Moderate skin (With applied linear multiplier)
Dark skin (With applied exponential multiplier)
Oxygen saturation (%)
Ratio of ratios (R)
100
95
90
85
80
75
70
0.2
0.4
0.6
0.8
1
1.2
1.4
1.6

(b)

Figure 10-3. Re-adjustment of the simulated calibration curve for dark skin. (a) Multiplication values for the ratio of ratios between light and dark skin across an oxygenation saturation range of 70% and 100%. (b) Adjusted dark skin calibration curve using the mean of the exponential multipliers. All simulated calibration curves now follow very similar algorithms, suggested by the integration of correctives measures.

10.3.2. Reflectance pulse oximetry

Similarly, three distinct calibration curves for light, moderate, and dark skin are generated from the MC model in reflectance mode (Figure 10-4). From this data, it is also evident that red light is highly absorbed by melanin in comparison to infrared light, especially at higher melanin concentrations. As a result, normalised reflectance at 660 nm reduces in magnitude as melanin concentration increases, and more so at lower oxygen saturation levels. With larger and less compromised normalised reflectance values at 940 nm across the simulated oxygen saturation range, a consistent reduction in the range of the ratio of ratios is observed. Moderate and dark skin calibration curves are shifted with respect to the light skin calibration curve due to changes in skin pigmentation for the same oxygen saturation level, thereby leading to inaccuracies and especially overestimation of SpO_2.

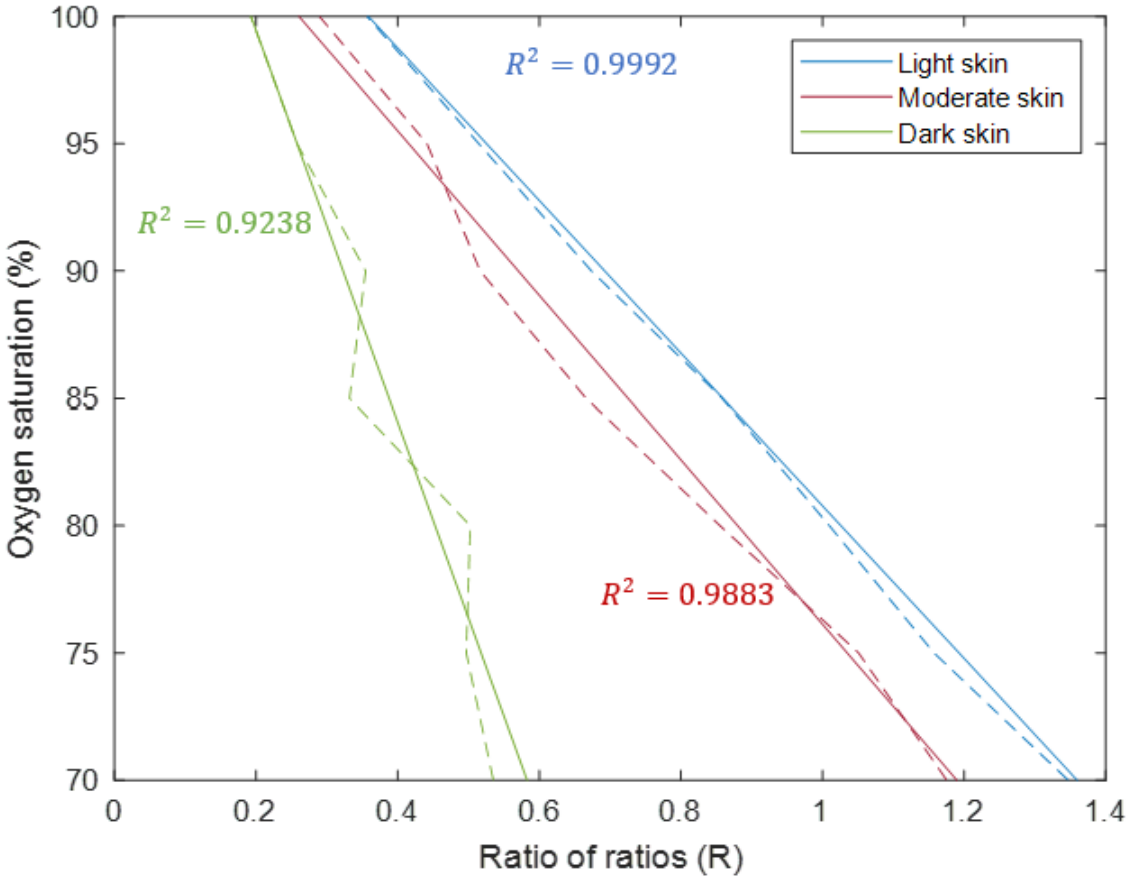

Figure 10-4. Simulated calibration curves for light, moderate, and dark skin. The dashed lines show the calculated ratio of ratios values from the raw intensity data, and the solid lines show the lines of best fit.

Once again, the results indicate that a single calibration algorithm may not allow for the accurate measurement of health metrics such as SpO_2 by smart wearable technologies on diverse skin pigmentations as is the case with transmittance pulse oximeters. Therefore, a similar approach of applying correction factors to the moderate and dark skin calibration curves was adopted. In doing so, correction factors of 1.21 and 2.17 were calculated, respectively, and applied to the original calibration curves (Figure 10-5). As shown, the simulated curves do not fully overlap with each other across the entire oxygen saturation range, unlike the behaviour observed with previous work on transmittance pulse oximeters. This discrepancy is possibly due to differences in light absorption and scattering that arise from variations in skin pigmentation as photon travel is primarily limited to the superficial layers, and where sensitivity could be heightened in the epidermis region from backscattering [271]. Therefore, in reflectance mode, there is a greater likelihood for photons to traverse a shorter depth before they are detected especially in darker skin types due to the increased absorption by higher melanin levels, and more so at shorter wavelengths. Hence, additional and/or alternative corrections could be explored by adjusting the source-detector separation for different skin types. By varying the separation distances for individuals with light, moderate, and dark skin, similar photon penetration depths can be achieved, which could ensure more consistent light interaction with specific regions of the tissue. This adjustment could help to normalise the calibration curves, potentially making post-processing corrective measures easier to implement.

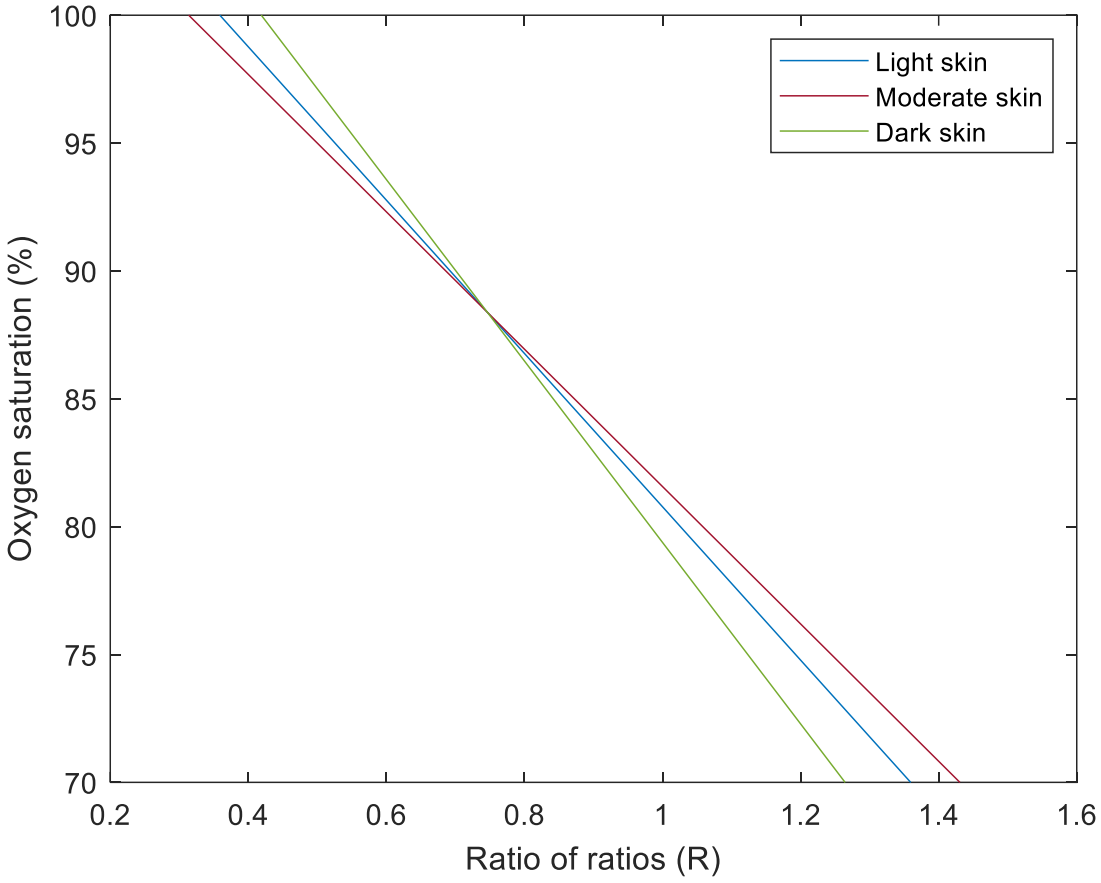

Figure 10-5. Adjustment of moderate and dark skin simulated calibration curves relative to light skin with applied corrective factors.

From the existing literature, it is known that reflectance pulse oximeters exhibit a decreased accuracy level of 3.5% compared to transmittance pulse oximeters of 3% [272]. Hence, part of the data analysis was to assess whether the computational outcomes in reflectance reflect this accuracy gap by comparing simulated calibration algorithms for light, moderate, and dark skin in transmittance mode (Figure 10-6). Visually, the simulated calibration curves suggest that the effect of melanin concentration on oxygen saturation measurement was significantly amplified in reflectance mode, and that pulse oximeter calibrations may indeed be calibrated on individuals from predominantly light-skinned populations due to the smaller gap between both modes. Furthermore, this accuracy consistently decreased with oxygen saturation as observed in studies on hypoxaemic patients [41], [268]. Like transmittance, the simulated calibration curves were defined by an equation with a linear function:

Light skin	$SpO_2 = 110.8 – 29.98 \times R$	(10-2a)
Moderate skin	$SpO_2 = 108.4 – 32.3 \times R$	(10-2b)
Dark skin	$SpO_2 = 114.9 – 76.99 \times R$	(10-2c)

Next, these equations were used to calculate the level of bias between reflectance and transmittance modes for each skin type i.e., light skin transmittance—light skin reflectance, etc. To do this, eq. (10-1b) was used as a reference as it closely matched the commonly used commercial pulse oximeter algorithm (eq. (10-1a)). The equation was rearranged to calculate the ratio of ratios values for a healthy SaO_2 range of 95–100% to understand the effect of melanin concentration independently of SpO_2 inaccuracies at lower oxygen saturation levels. These R values were then substituted into all other equations (eqs. (10-1c), (10-1d), (10-2a), (10-2b), and (10-2c)) to calculate bias as shown in Figure 10-6d. Evidently, light and moderate skin calibration exhibit a low level of bias across the SaO_2 range between −0.0154% and 0.6984%, and between 0.8884% and 0.9376%, respectively. This results in a root mean square error (RMSE) of 0.3956% and 0.9132% in comparison to 8.4111% for dark skin. However, it is important not to interpret this error by its absolute value until further computational investigation of dark skin simulation is conducted due to its more complex structure. Rather, this indicates the potential difference in bias between transmittance and reflectance pulse oximeters on skin types with high melanin concentrations.

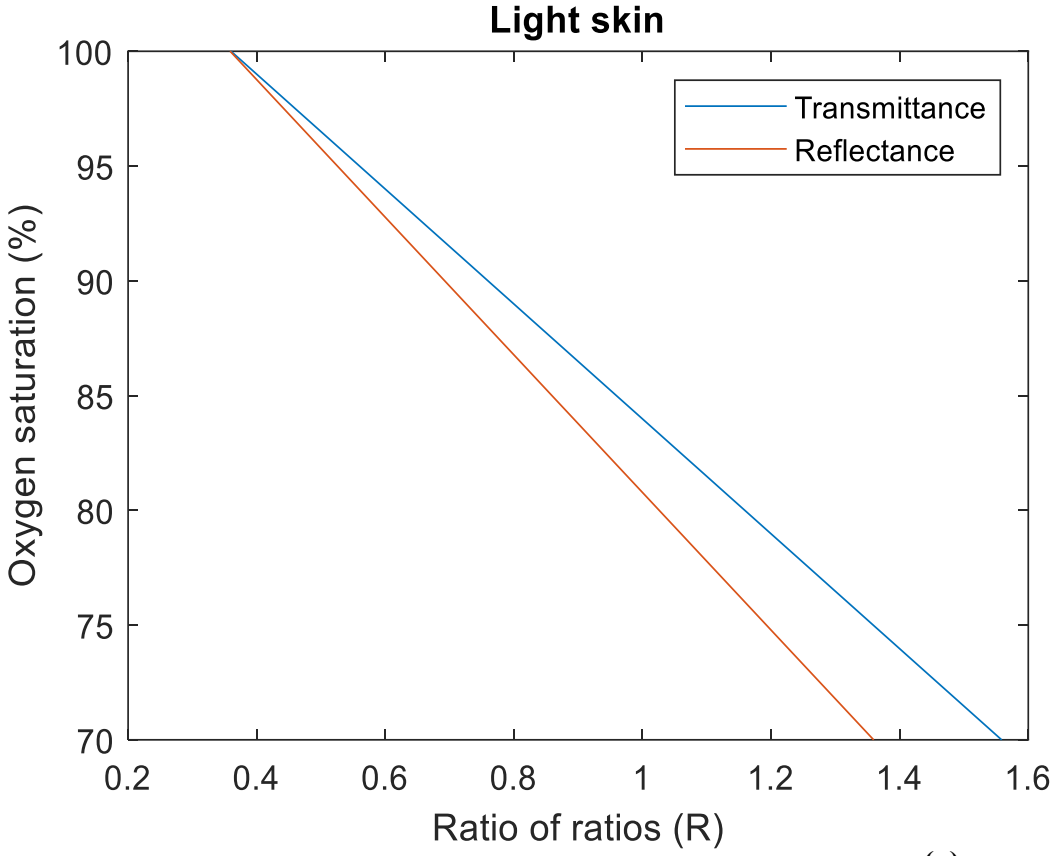
Light skin
Transmittance
Reflectance
Oxygen saturation (%)
Ratio of ratios (R)
100
95
90
85
80
75
70
0.2
0.4
0.6
0.8
1
1.2
1.4
1.6

(a)

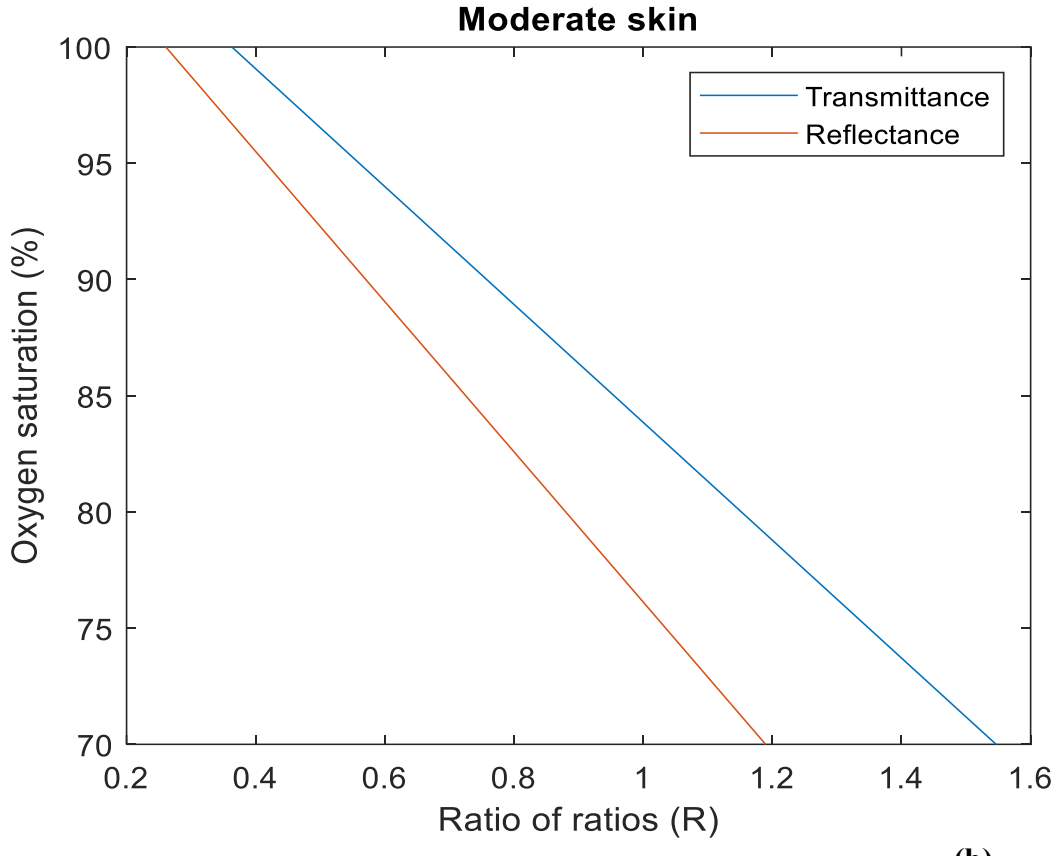
Moderate skin
Transmittance
Reflectance
Oxygen saturation (%)
Ratio of ratios (R)
100
95
90
85
80
75
70
0.2
0.4
0.6
0.8
1
1.2
1.4
1.6

(b)

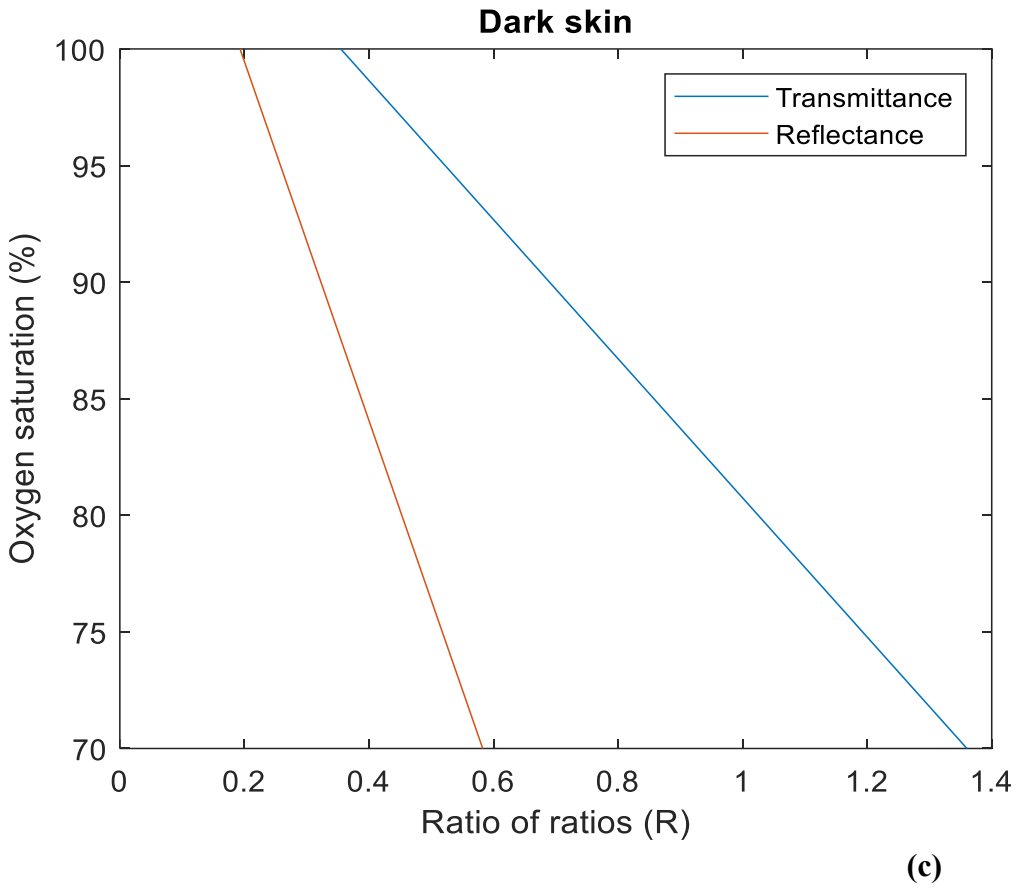

(c)

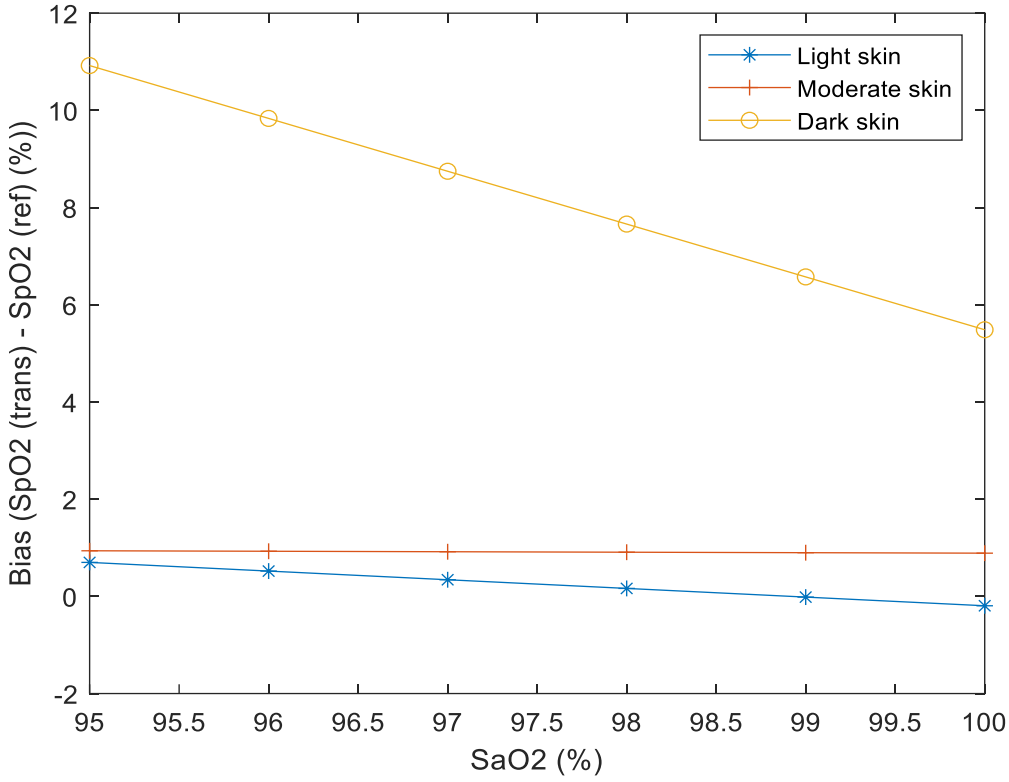

(d)

Figure 10-6. Simulated calibration curves in transmittance and reflectance mode pulse oximetry for (a) light skin, (b) moderate skin, and (c) dark skin. (d) Calculated bias between simulated transmittance and reflectance SpO_2 for healthy SaO_2 range (95 - 100%).

10.4.Summary

This chapter contributes to the scientific knowledge associated with pigmentation related bias in pulse oximeters through a Monte Carlo simulation. The simulated results in transmittance and reflectance modes have provided quantitative evidence to rectify the shift occurring in moderate and darker skin pigmentations, which, moving forward, can be considered by pulse oximeter manufacturers. This is especially the case for SpO_2 measurements derived from reflectance pulse oximeters considering the growing demand of consumer wearables. Hence, the retesting of pulse oximeters with additional in-built algorithm adjustments, as well as more precise in vitro and in vivo investigations, is encouraged. Future research will prioritise the development of more accurate models regarding the haemodynamic processes and skin pigmentation characterisation in the finger to explore the repeatability of the magnitude of these biases, and whether current recommendations are still viable.

CHAPTER 11: MONTE CARLO SIMULATED PHOTOPLETHYSMOGRAPHY SIGNALS FOR THE VALIDATION OF AN IN VITRO WRIST PHANTOM

11.1.Introduction

In the past decade, in vitro models have played a crucial role for the development of reliable consumer wearables, allowing users to monitor various health metrics in real time [273], [274]. Monte Carlo simulations emerge as a powerful tool in the realm of in vitro experimentation, offering a computational approach to assess the behaviour of light in biological systems under different physiological conditions [275]. In addition to simulating the stochastic nature of light in tissue, Monte Carlo simulations play a crucial role in validating and/or refining in vitro experiments [276]. By comparing data obtained from computational and experimental protocols, researchers can maintain the consistency of their in vitro findings, ensuring that simulations accurately represent the biological phenomena under investigation.

We have seen from Chapter 10 that pulse oximeter calibration algorithms may vary across different skin types. However, the variability between algorithms and the exact values of bias may not be realistic due to the method employed to model skin pigmentation, even though the trends may remain consistent. The difference in magnitude is important, as it can influence the type of adjustments required in pulse oximeters to minimise bias discrepancies. PPG analysis primarily focuses on the volumetric changes in blood during the cardiac cycle, and inaccuracies in SpO_2 measurements may arise from variations in the AC and DC components of the PPG signal as epidermal melanin content changes. Therefore, advances in the modelling of blood in the dermis and skin pigmentation in the epidermis are important in addressing these limitations from the previous model. Hence, this chapter will explore the modelling of blood in its dynamic form, laying the foundation for generating simulated PPG signals using a Monte Carlo simulation.

11.2.Method for execution

A radial artery with a 3 mm diameter, located at a 13 mm depth in a phantom body (40 mm x 100 mm x 40 mm) is designed using SolidWorks to create a basic replica of the human wrist. The phantom is fabricated by combining silicone with Sylgard 184 and catalyst for curing. Wavelength specific epolight dyes dissolved in acetone and titanium oxide (TiO_2) were

incorporated in specific concentrations to introduce absorbing and scattering properties to the phantom, respectively. Then, the optical characteristics of the silicon body and vessel were characterised using the LAMBDA 1050+ UV/VIS/NIR (L6020371/2) spectrophotometer at the Research Centre for Biomedical Engineering, City St George's, University of London. Spectra were collected across the range of 350 nm - 1000 nm by performing diffuse reflectance and diffuse transmittance measurements, which are then processed through an Inverse Adding-Doubling (IAD) algorithm to derive the absorption and scattering coefficients. The anisotropy values and refractive index of the tissue components were selected as according to the literature on reported values for human tissue [259], [277]. These determined the default optical properties of the model that are later presented in the results section.

The dimensions of the phantom are imported into MATLAB to provide the model with the coordinates of its vertices and faces using a computer aided design (CAD). Since the CAD file is saved in stereolithography (STL) format, it needs to be converted to represent the dimensions as x, y, and z coordinates, corresponding to points along the width, length, and depth of the phantom, and then stored in vectors. These vectors are used to set the boundary conditions governing photon absorption and scattering within the wrist phantom model as they travel between the source and the detector. This conversion enabled the model to be plotted and read in MATLAB for further analysis.

For this specific application, the source and the detector are placed 5 mm apart in reflectance mode, and positioned 20 mm in the lateral (x) and longitudinal (y) axes to mimick the position of a watch on the wrist phantom (Figure 11-1). Some information regarding the red light source and photodiode were extracted from the OSRAM SFH 7050A datasheet to be implemented in the Monte Carlo model, as outlined in Table 11-1. Since the active area of the red emitter was not stated, a Gaussian beam distribution was assumed for a source radius of 1 mm.

Table 11-1: Characteristics of the red light emitting diode (LED) and photodiode used in the sensor configuration for the simulated model of the wrist phantom.

	Red emitter	Photodiode
Wavelength of maximum sensitivity (nm)	660	900
Spectral range of sensitivity (nm)	643 – 677 (FWHM)	400 – 1100
Half angle (°)	60	90
Active area (mm^2)	-	1.51

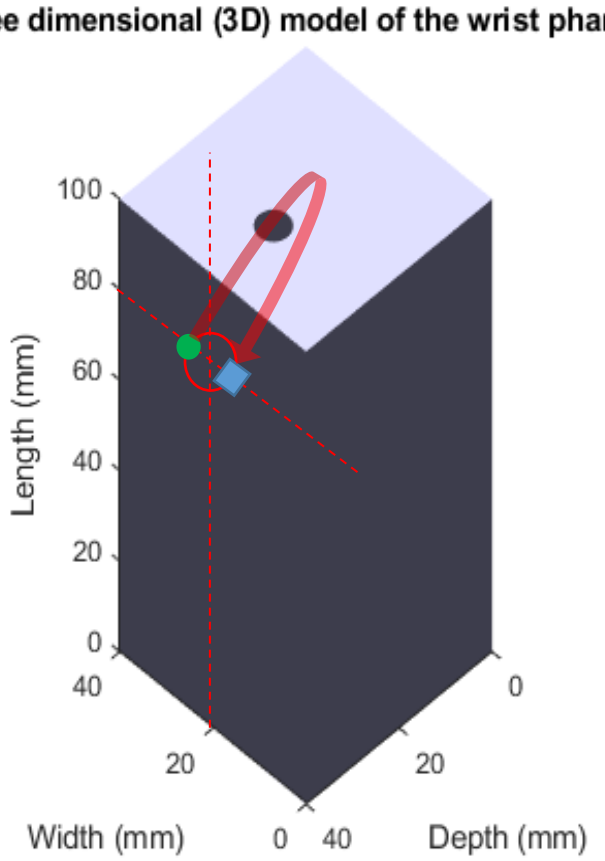

Figure 11-1. Three dimensional (3D) imported computer aided design (CAD) of the wrist phantom into MATLAB from SolidWorks. The location of the sensor area is denoted by the red circle, 20 mm from the x and y axes, and the red arrow denotes the trajectory of the photons as they travel between the light source (green circle) and photodiode (blue square). The black circle on the top face represents a blood vessel.

To generate a PPG signal, the volumetric blood flow was represented by adjusting the vessel diameters in response to changes in blood pressure, thereby introducing mechanical properties to the vessels through geometrical deformation. This was achieved by connecting a vessel to a syringe pump to induce inflation from increasing fluid levels. A pressure transducer is used to measure the internal pressure between 0 – 140 mmHg in increments of 20 mmHg. Vessel diameter changes were recorded using a digital microscope, and a precision ruler was used to measure the dimensions of the captured images [278]. Similar to the detection protocol employed in Chapter 10, the simulations were run until one million photons were detected for the different diameter values, generating predicted detected intensity and number of launched photons to calculate reflectance. These points were then combined to form one pulse in a photoplethysmogram.

11.3.Results

The optical and mechanical properties of the phantom and vessel were obtained to simulate the pulsatile component of the PPG signal. Table 11-2 presents the data obtained for the absorption coefficient, scattering coefficient, anisotropy factor, and refractive index at 660 nm. The refractive index of air was considered to account for surface reflection before the light entered the phantom body. Furthermore, the vessel diameter test described above was conducted and showed a positive linear relationship between internal pressure and vessel diameter (Figure 11-2). The line of best fit was used to calculate the diameters of the vessel (y) at any given input of blood pressure (x) accurate to three decimal places (Table 11-3). In this study, a hypertensive blood pressure waveform was inputted into the equation to extract ten diameter points. These were selected based on the pressure values that initiated crucial points of inflection in the PPG signal, e.g., before and after the systolic slope, etc.

Table 11-2: Optical properties of incident interface (air) and the components of the developed wrist phantom (vessel and phantom body) at 660 nm using the LAMBDA spectrophotometer at City, University of London

	μ_a	μ_s	g	n
Air	-	-	-	1
Vessel	0.5	30	0.9	-
Phantom body	0.00591	0.53	0.8	1.4

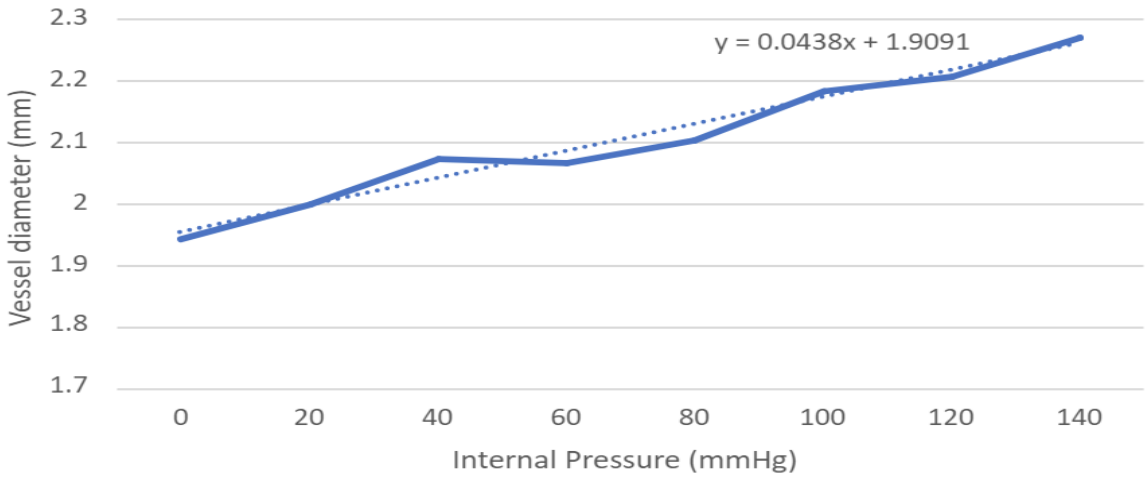

Figure 11-2. Changes in vessel diameter as blood pressure increases from 0 mmHg to 140 mmHg.

Table 11-3: Simulated vessel diameters corresponding to changes in blood pressure to replicate a pulsating vessel.

Data point	**1**	**2**	**3**	**4**	**5**	**6**	**7**	**8**	**9**	**10**
Blood pressure (mmHg)	154.049	158.499	167.827	171.141	168.023	162.136	161.522	158.923	158.175	155.598
Diameter (mm)	2.291	2.300	2.321	2.328	2.321	2.308	2.307	2.301	2.297	2.294

To accurately generate changes in reflectance for very similar magnitudes of vessel diameters, the simulation was run until one million photons were detected to reduce inaccuracy arising from random sampling. For example, 444,282,000 photons entered the phantom model until one million photons were detected for a vessel diameter of approximately 2.29 mm.

The simulated PPG pulse is shown in Figure 11-3 by the blue line, and exhibits key features of a typical PPG signal, including onsets, dicrotic notch, and systolic and diastolic peaks and slopes. However, to improve the smoothness of the pulse, spline interpolation was computed on the ten data points using an in-built function in MATLAB named ‘spline’. Two increment sizes, specifically 0.5 and 0.01 were used to smoothen the PPG signal, as shown by the orange and yellow lines, respectively. Evidently, using a smaller increment size is more ideal for achieving very smooth lines around the points of inflection. However, in instances where spline interpolation is not used, any desired number of diameter points can be simulated to capture the true characteristics of the PPG signal. On average, the computation time to simulate one diameter point was 13 minutes, although this is subject to change with different optical property values and number of detected photons.

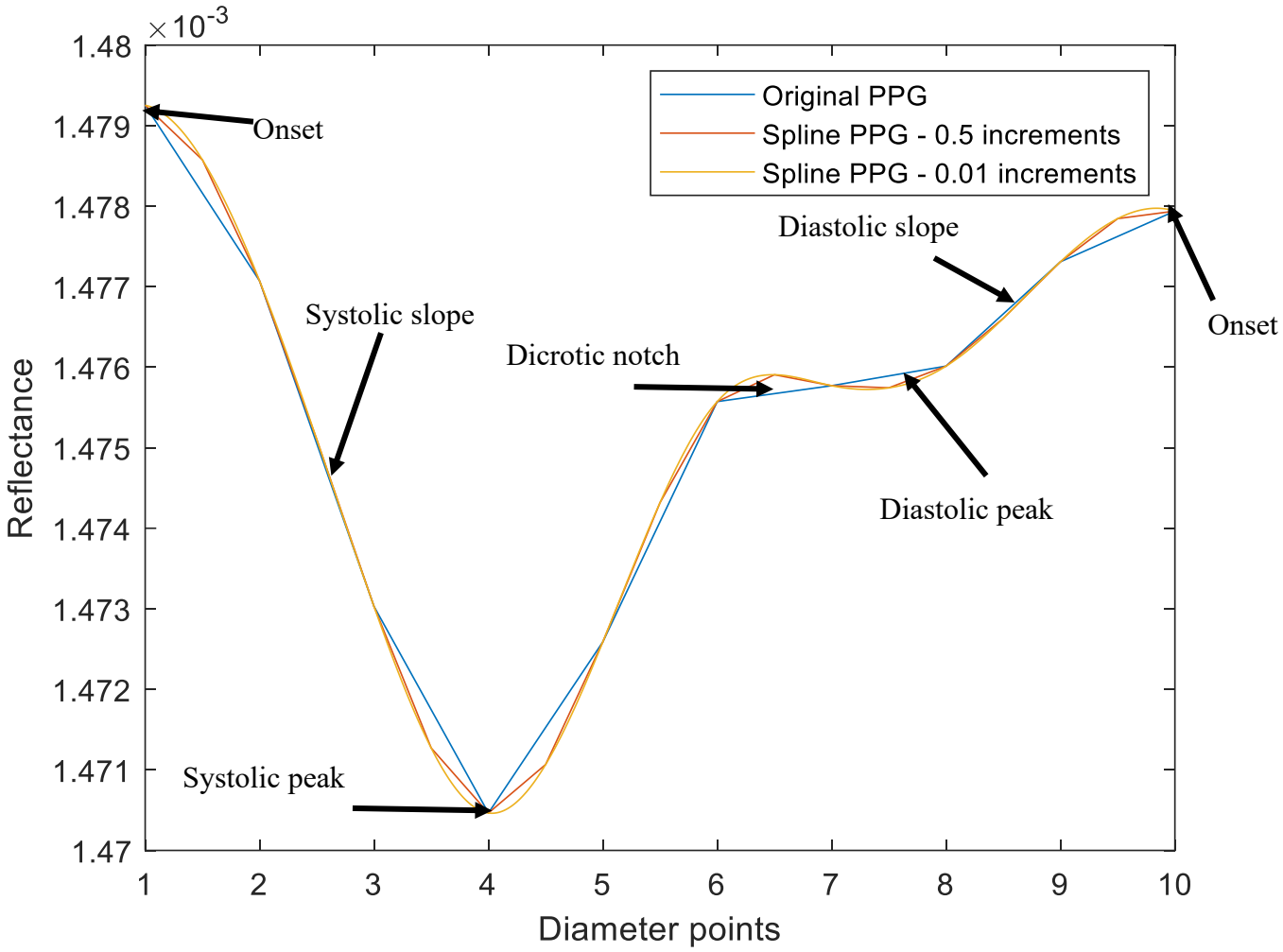

Figure 11-3. Monte Carlo simulated pulse of a PPG waveform. The blue line shows the initial simulated reflectance data using the 10 selected vessel diameters. The orange and yellow lines are generated using the 'spline' function in MATLAB to create a smoother morphology of original pulse, with 0.5 and 0.01 increments, respectively.

Lastly, the photons profile in the x-y plane, y-z plane, and the x-z plane show a bird's eye view, side sectional view, and cross section view of the phantom as the photons travelled between the source and the detector (Figure 11-4). As observed, detected photons have a high scattering density within and beyond the vessel, which increases the accuracy of the output reflectance values as sufficient information is received from the pulsating and deeper regions of the phantom model. Scattering density is compromised $\pm$10 mm along the width of the phantom relative to the sensor location which limits the trajectory of the photons between this space, and for approximately 50% of the length of the vessel. While this is appropriate for the current placement configuration of the sensor, it is important to note that if the source and detector are positioned parallel to the vessel in future simulations, the scattering density should be higher

along a larger portion of the vessel. This way, the detector will capture as much information as possible as the cross-sectional diameter changes with pressure, which reduces the level of noise in the simulated PPG signal.

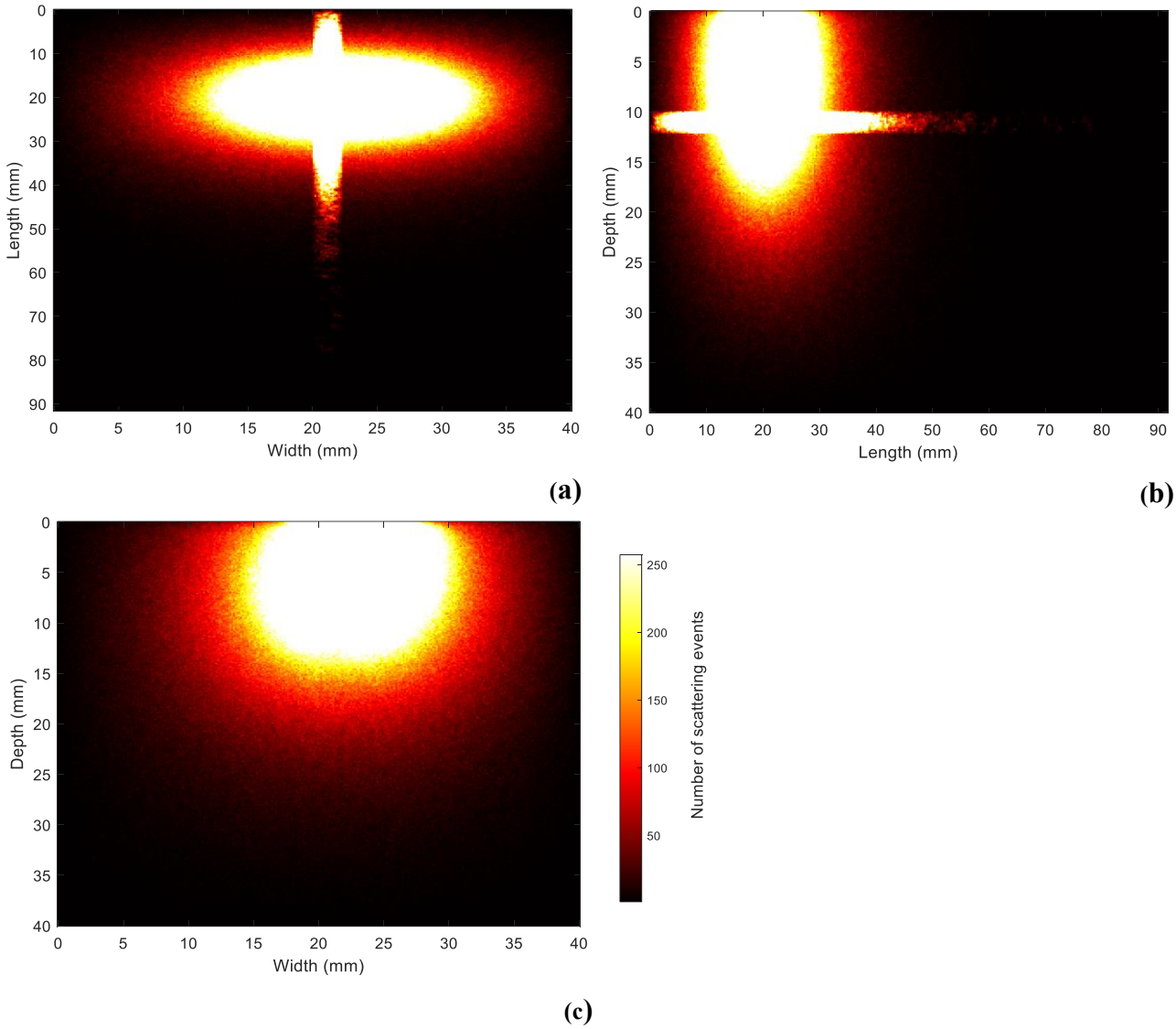

Figure 11-4. Photon profiles of the light tissue interactions in the wrist phantom model using red light (660 nm) at a source-detector separation of 5 mm. High scattering density is represented by the brighter regions (white/yellow), and quantified on the colour bar. Only the trajectory of the photons that are detected by the photodiode are displayed in the (a) x-y direction (b) y-z direction (c) x-z direction.

11.4.Summary

In this chapter, a photoplethysmography signal has been simulated using an innovative approach that combines the optical and mechanical properties of the phantom, which allows for more realistic simulations in the study of blood vessel dynamics. While this study holds positive implications for in-vitro validation in the field of physiological monitoring, it is particularly useful for future simulations intending to explore the effect of confounding factors, such as skin pigmentation, in the characterisation of PPG signals in controlled conditions.

CHAPTER 12: MONTE CARLO MODELLING OF THE EFFECT OF SKIN PIGMENTATION ON SIMULATED PHOTOPLETHYSMOGRAPHY SIGNALS

12.1.Introduction

By now we have established that studies have consistently indicated an overestimation of SpO_2 in subjects with darker skin, particularly evident in the shift of simulated calibration curves for both transmittance and/or reflectance pulse oximetry modes in comparison to light skin populations. While this research has been crucial for establishing the influence of red-light absorption by increasing levels of melanin, some improvements in the methodologies can help create more realistic models of the human finger which in effect can improve PPG data obtained for different skin types. Consequently, this study aims to examine the effect of skin pigmentation on simulated Monte Carlo PPG signals using red light (660 nm) and infrared light (940 nm). The aim is to directly explore how skin pigmentation affects PPG signals through an in silico investigation, which provides complementary insights to the studies that have focused on simulated pulse oximeter calibrations for different skin types [223], [229], [269], [279] and to those in this thesis. Whilst they have been crucial for understanding variations in the ratio of ratios values, analysing the initial signal distortions caused by skin pigmentation provides clarity to the overall knowledge base. This approach allows for observing the signal's amplitude and quality with different skin types, offering insights that can lead to more precise adjustments in calibration algorithms before the raw PPG data is processed.

Additionally, another novelty in this study is to improve the modelling of skin pigmentation. One of the key advancements is the use of spectrophotometrically obtained optical properties for different skin tones, rather than relying on mathematical equations (Chapter 3.2, Chapter 6). Also, previous discussions on the limitations of the Fitzpatrick scale should be considered, specifically its relevance to UV-induced skin changes, which is not entirely applicable in the context of this study. Hence, greater accuracy in the methodology approach should be achieved when objectively quantifying skin pigmentation.

12.2.Method for execution

The finger model implemented in this study is adapted from Chapters 9 and 10, including the optical properties of the fat, muscle and bone layers, and the dimensions of the stratum

corneum, epidermis, dermal layers, fat, muscle, and bone. Further modifications to the simulated finger model are provided below.

First, a block diagram of the different layers in the human finger was created for implementation in the current Monte Carlo model (Figure 12-1). This included the stratum corneum, epidermis, a dermis layer containing five blood vessels positioned 1 mm apart in the lateral (x) direction, fat, and muscle containing a cylindrical bone perpendicular to the vessels, in alternate order. This way, adequate blood perfusion was modelled by including a sufficient number of blood vessels, which also covered the area where the light would travel between the source and detector in reflectance mode (3 mm). thicknesses of each layer were extracted from the literature and used in previous models, including the Monte Carlo algorithm used to simulate photons and model the different light–tissue interaction mechanisms.

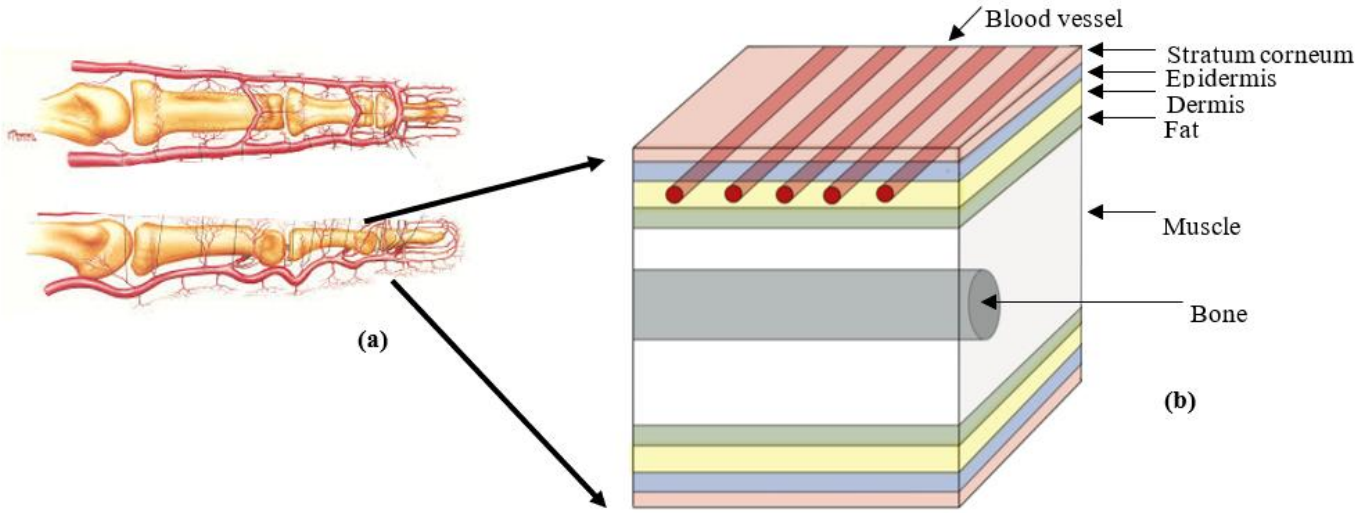

Figure 12-1. Anatomical structure of the region of interest. (a) Diagram of a finger showing the vasculature network to implement in the MC model. (b) Block diagram of the finger showing the stratum corneum, epidermis, dermis and vessels, fat, muscle, and bone in alternate order. In transmittance, the source is placed directly above the central vessel and the detector directly beneath it on the lower stratum corneum. In reflectance mode, the source and detector are placed 3 mm apart, above the second and fourth blood vessel, respectively. Vascular network adapted from [297].

Next, three silicone skin layers were prepared using different concentrations of Bismark Brown as the absorber along with a fixed concentration of titanium dioxide in Sylgard 184, specifically designed to mimic the optical and mechanical characteristics of skin. These pigmented silicone skin samples were then placed in an optical-grade cuvette and positioned inside the LAMBDA 1050+ UV/VIS/NIR spectrophotometer to also measure diffuse reflectance. After machine calibration, light was directed through a monochromator to the sample, and reflected light was captured by detectors for wavelengths ranging between 400 nm and 1000 nm. The diffuse reflectance spectrum was calculated by comparing the sample's reflected light to the baseline, enabling detailed analysis of the light scattering and absorption influenced by pigmentation. After that, the spectra was processed with the same IAD algorithm used in Chapter 11 to derive the absorption and reduced scattering coefficients of the epidermal layers using an input anisotropy value of 0.8 [280]. Additionally, the L*a*b* values of the developed skin layers were calculated from the reflectance spectra, which is a colour representation system that describes colours in a three-dimensional space [281] (Chapter 3.2). The optical properties of the bloodless dermis and blood vessels were calculated to reflect changes in the anatomy presented in the current model. The absorption coefficient and scattering coefficient of arterial blood (μ_{a_A} and μ_{s_A}, respectively) and venous blood (μ_{a_V} and μ_{s_V}, respectively) were calculated using eqs. (12-1a) – (12-1d) for arterial oxygen saturation levels of 70% and 100%, adapted from Jacques (1998) [173] to reflect different in red blood cell concentration and size, respectively:

$$\mu_{a\_A} = sat_A * \mu_{a_{Hbo}} + (1 - sat_A) * \mu_{a\_HHb} \quad (12\text{-}1a)$$

$$\mu_{a\_V} = sat_V * \mu_{a_{Hbo}} + (1 - sat_V) * \mu_{a\_HHb} \quad (12\text{-}1b)$$

$$\mu_{s\_A} = sat_A * \mu_{s_{Hbo}} + (1 - sat_A) * \mu_{s\_HHb} \quad (12\text{-}1c)$$

$$\mu_{s\_V} = sat_V * \mu_{s_{Hbo}} + (1 - sat_V) * \mu_{s\_HHb} \quad (12\text{-}1d)$$

sat_A = arterial oxygen saturation level (70% and 100%);
sat_V = venous oxygen saturation level (60% and 90%);
$\mu_{a_{Hbo}}$ = absorption coefficient of oxygenated blood;
$\mu_{a_{HHb}}$ = absorption coefficient of deoxygenated blood;
$\mu_{s_{Hbo}}$ = scattering coefficient of oxygenated blood;

$\mu_{s_{HHb}}$ = scattering coefficient of deoxygenated blood.

Then, the overall absorption coefficient and scattering coefficient of each vessel was calculated by taking the mean of these coefficient values to account for overall contribution from the arterial and venous blood. Lastly, the absorption coefficient of the dermal layer was calculated by taking the average of the papillary dermis, upper blood net dermis, reticular dermis, and deep blood net dermis using their respective water concentrations (Table 9-1):

$$\mu_{a\_dermis} = \sum \mu_{a_W}(n) \times v_w(n) + (1 - v_W(n)) \times \mu_{a\_baseline} \,/a \qquad (12\text{-}2)$$

μ_{a_W} = absorption coefficient of water;
v_w = water concentration;
n = papillary dermis (1), upper blood net dermis (2), reticular dermis (3), and deep blood net dermis (4);
a = number of dermal sublayers (4).

To simulate the characteristics of the AC component of the PPG signal, it was important to understand how the vessel volume changes when inducing different levels of internal pressure. Therefore, a custom-built phantom body with a 0.5 mm vessel channel was created by mixing 20 g of Part A Platsil Gel 00 (Polytek Development Corp, Easton, Pennsylvania, USA) with 0.6 g of retarder (1.5% of the total silicone used) to extend the working time from 6 min to 10–12 min. This allowed for sufficient time to combine all components before the silicon started to harden. After that, 20 g of Part B Platsil Gel 00 was incorporated into the mixture for approximately one minute before placing it in a vacuum to remove any air bubbles. A 3D-printed 40-by-77 mm mould (width by length) was used to insert a 0.5 mm diameter wire through pre-made holes. The wire was carefully straightened and secured with weighted objects at both ends to ensure the channel remained as straight as possible. The silicone mixture was then poured into the mould and left to cure for 24 h. Once cured, the phantom was removed from the mould and the wire was extracted by pulling it to expose the channel. Figure 12-2 shows the vessel channel highlighted with blue ink for enhanced visualisation.

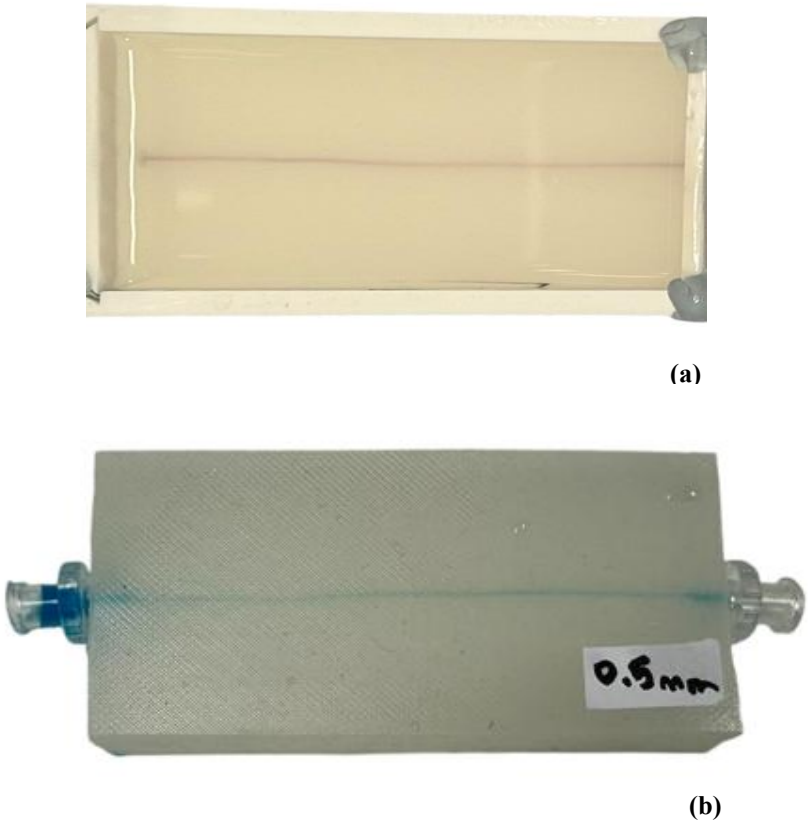

Figure 12-2. Phantom development process. (a) A secured 40 by 77 mm mould with a 0.5 mm diameter wire inserted through the holes on each side to create the vessel channel. Silicon is poured into the mould and left to cure for 24 hours. (b) Cured phantom with attached connectors to supply with fluid to induce pressure. Blue ink is used to visualise the vessel channel.

Subsequently, the phantom was connected to a pump (Legato 180, KD Scientific Inc, Massachusetts, USA) via small connectors and attached to a syringe containing blue ink, which was injected into the channel in 20-microliter increments. This was considered a suitable increment to find a balance between reliable data collection, time, and system stability. Initially, one end of the channel was left open until it was filled with blue ink to establish a baseline volume at 0 mmHg pressure. The channel was then sealed with the other connector and an additional 20-microliter of blue ink was injected into the closed system. Each increase in volume corresponded to a specific pressure value displayed on a screen, which was recorded from the pressure sensor after 10 seconds from when fluid was injected into the vessel channel (Figure 12-3). This procedure was repeated twice for a total of seven readings, and the average pressure was plotted against the channel diameter. The diameter was calculated using the following equation:

$$V = \pi {r_v}^2 L_v \quad (12\text{-}3a)$$

Which was then rearranged to:

$$r_v = \sqrt{V/\pi L_v} \quad (12\text{-}3b)$$

V = the volume of vessel channel;

r_v = the radius of the vessel channel;

L_v = the length of the vessel channel.

After that, the diameter was calculated by doubling the value of each radius.

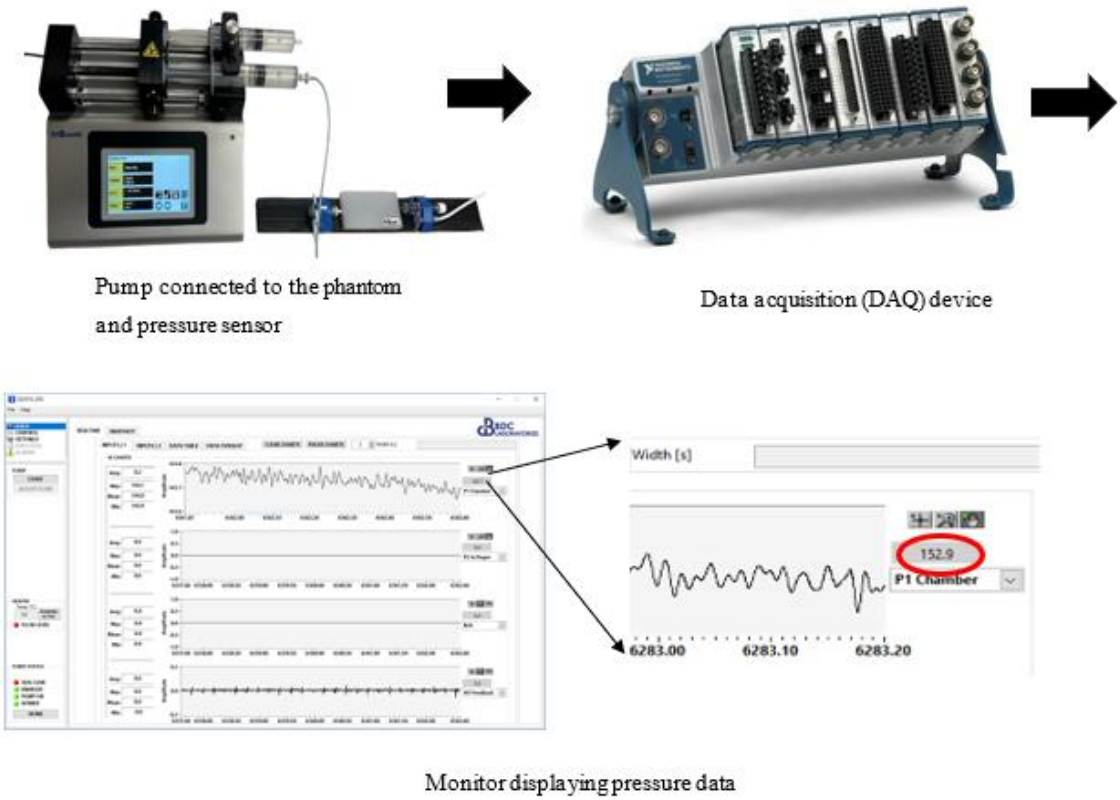

Figure 12-3. The phantom set up for a pressure–volume experiment. A pump (Legato 180, KD Scientific Inc., MA, USA) has a syringe mechanism containing blue ink to inject into the phantom. The other end of the phantom is connected to a pressure sensor to measure pressure in the vessel channel as 20 µL of blue ink is injected each time. The pressure sensor is connected to a data acquisition device (CompactDAQ−9178, National Instruments Corp.) to process the data and display pressure readings on the monitor.

12.3.Results

12.3.1. Optical properties of the pigmented skin layers

The L* and b* values of the silicone pigmented skin layers, corresponding to the lightness of the colour and the colour's position between blue and yellow, respectively, are presented in Figure 12-4. As observed, there is a similar trend to the L* and b* values reported in the literature for light, intermediate, and brown skin tones corresponding to light, moderate, and dark skin, respectively. After validating the pigmented skin layers against the L*a*b* scale, the optical properties were calculated and incorporated into the model. These are presented in Table 12-1 along with the optical properties of the stratum corneum, fat, muscle, and bone from the literature.

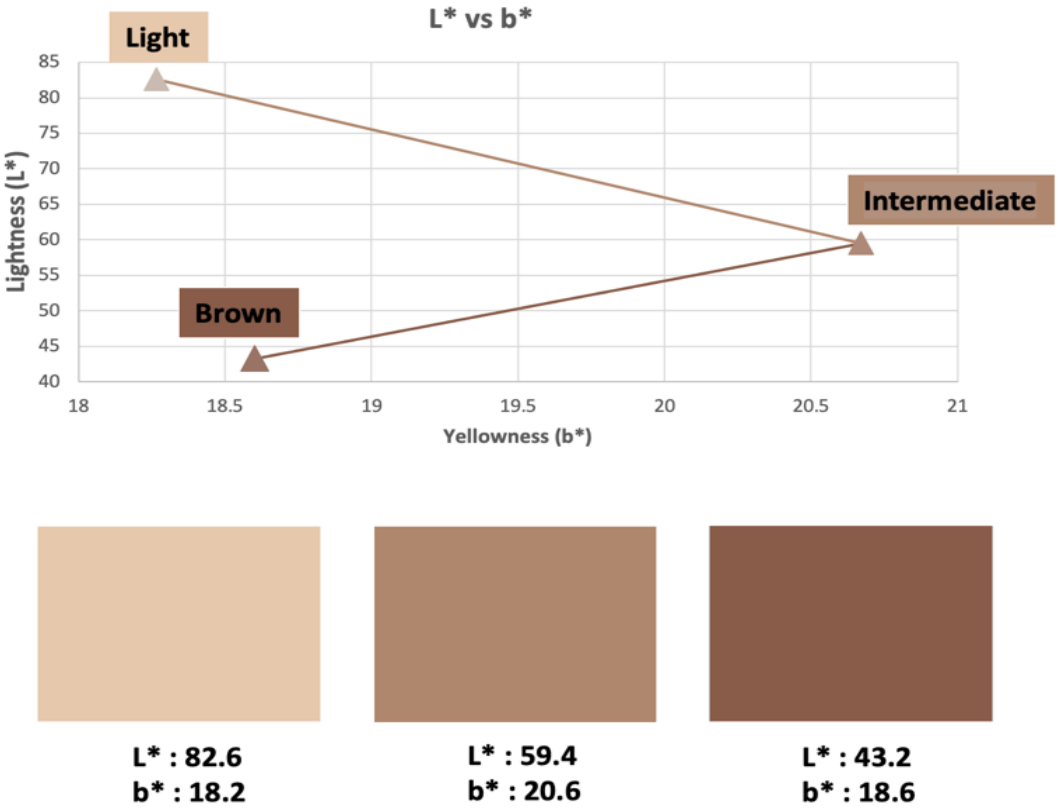

Figure 12-4. Quantification of pigmented silicon skin layers against the L*a*b* scale. (a) L*b* plane values for six skin types ranging between very light and dark. (b) L* and b* values calculated from the reflectance spectra of the developed skin layers in the Research Centre for Biomedical Engineering at City St George's, University of London, using Microsoft Excel. The results show a similar trend to the L* and b* values reported in the literature for light, intermediate, and brown skin tones.

Table 12-1: Optical properties of the finger layers, including the blood vessels, at 70% and 100% oxygen saturation.

Tissue Layer/Component	μ_a (mm^{-1})		μ_s (mm^{-1})		g	
	660 nm	**940 nm**	**660 nm**	**940 nm**	**660 nm**	**940 nm**
Stratum corneum	0.0495	0.0170	25.6	5.68	0.910	0.940
Light epidermis	0.00964	0.00571	13.8	7.79	0.800	0.800
Moderate epidermis	0.0195	0.00567	12.3	7.10	0.800	0.800
Dark epidermis	0.0396	0.00627	12.9	7.70	0.800	0.800
Dermis (Bloodless)	0.0135	0.0209	25.6	5.68	0.910	0.940
Blood vessels (O2 = 70%)	0.672	0.573	60.6	37.1	0.985	0.977
Blood vessels (O2 = 100%)	0.225	0.639	87.8	54.1	0.985	0.977
Fat	0.0104	0.0170	6.20	5.42	0.900	0.900
Muscle	0.0816	0.0401	8.61	5.81	0.880	0.910
Bone	0.0351	0.0457	34.5	24.7	0.920	0.930

12.3.2. Mechanical Properties

Changes in pressure were recorded from the pressure transducer as more and more ink was injected into the vessel channel. These values were recorded and then plotted against their respective calculated vessel diameter in MATLAB. Since there was a clear linear relationship between the two variables, a linear equation was extracted using in -built MATLAB tools for the maximum possible pressure that the system was able to withstand. This accurately represented pressure variations with vessel volume before the system was no longer functioning in a closed loop:

$$Pressure = 576 * diameter - 237 \quad (12\text{-}4)$$

This equation is rearranged and used to convert variations in a normotensive blood pressure pulse (Figure 12-5) to changes in vessel diameter (Figure 12-6). The pressure pulse consists of approximately 7000 data points, which corresponds to 7000 vessel diameter values. However, simulating all these points would be computationally inefficient, so 15 key points were selected

to represent the features of a PPG signal. First, the onsets of the pressure signal were identified, followed by key inflexion points, including the systolic peak and points before and after the dicrotic notch. Additional points were then chosen between these key locations to accurately capture the overall shape of the PPG signal. This vessel diameter data was inputted into the Monte Carlo model to simulate the dynamic response of a PPG signal.

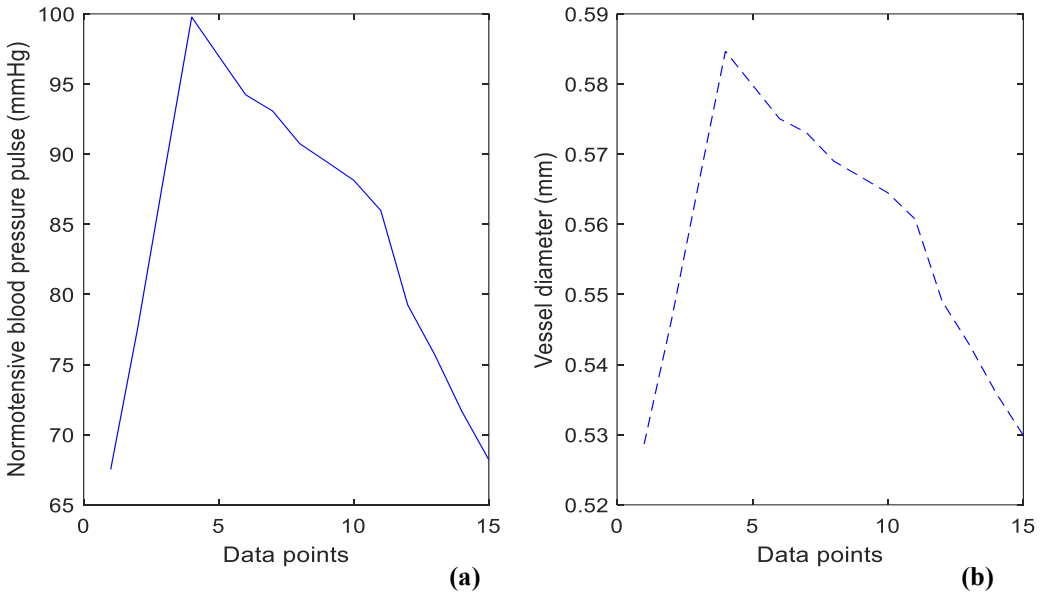

Figure 12-5. Pressure pulse used to convert volumetric blood changes into vessel diameter data using equation 12-4. These 15 vessel diameter values are inputted into the Monte Carlo model to simulate characteristic points of a PPG waveform in synchrony with pressure. (a) Normotensive blood pressure waveform (b) Calculated vessel diameter values.

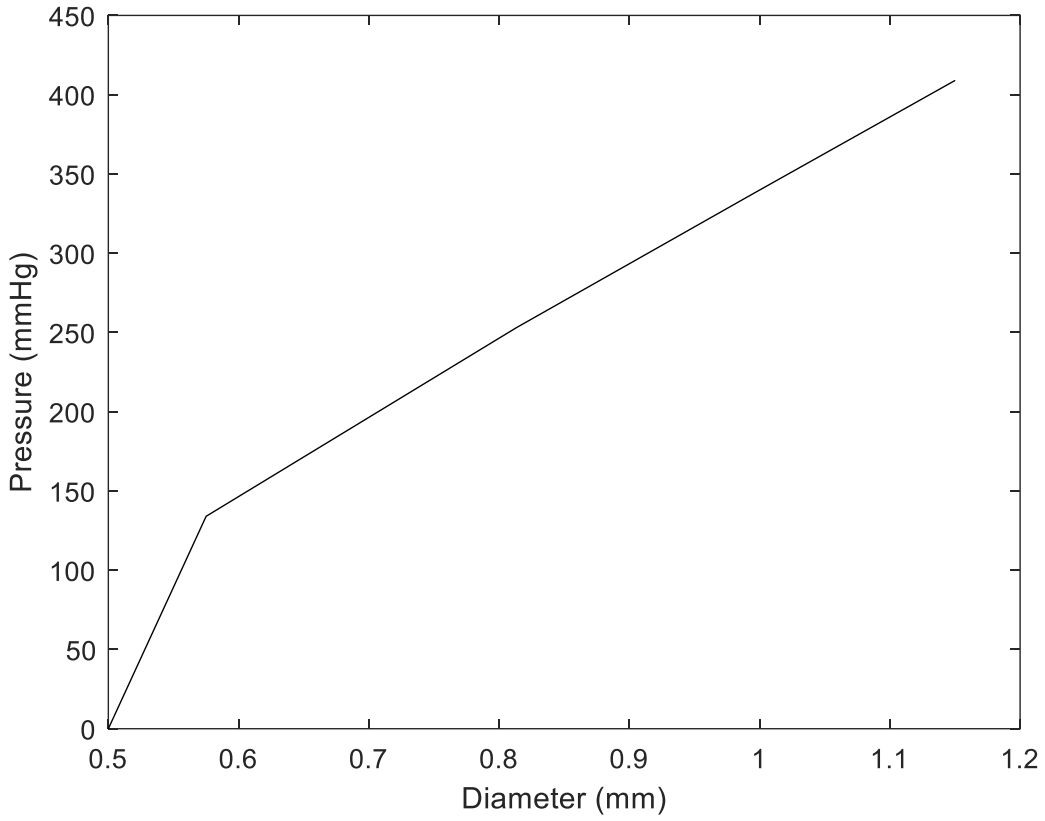

Figure 12-6. The relationship between pressure and vessel diameter in a closed-loop system. This was used to derive a linear equation to calculate variations in vessel diameter as pressure changes.

12.3.3. Simulation outcomes

First, the trajectories of detected photons in transmittance mode were stored in *x, y,* and *z* vectors to plot the photon profiles at 660 nm and 940 nm in Figure 12-7. As shown, the scattering behaviour of red light is more pronounced in the dermal and bone layers due to their higher scattering coefficients compared to other layers, which are also lower at 940 nm. The highest scattering is observed in the central vessel, emphasising the significance of sensor positioning to obtain more bio-optical information from specific regions of interest. In this case, we are concerned with ensuring optimal interactions in the vessels during volumetric changes to simulate the characteristic points of the simulated PPG signal more accurately. Overall, these photon profiles align with the anticipated photon propagation and behaviour.

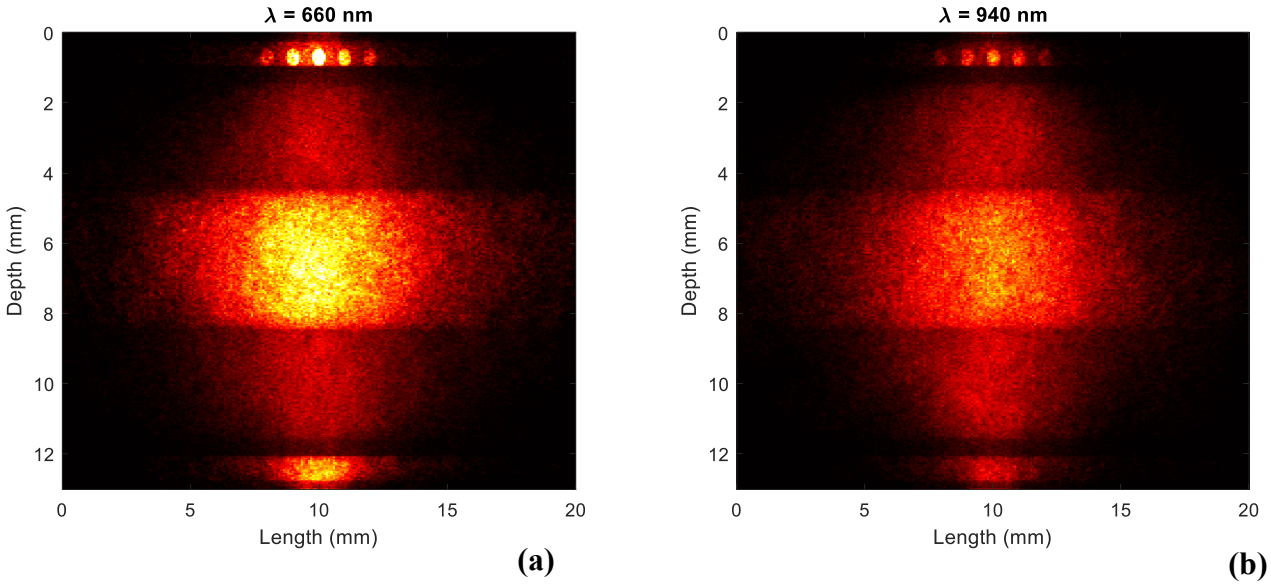

Figure 12-7. Photon profiles of the finger model in transmittance mode. (a) 660 nm. (b) 940 nm.

By employing the methodology outlined in this study, PPG characteristic points were successfully simulated from the Monte Carlo model. The raw intensity points, represented by dots in Figure 12-8 were processed using a second-order digital Butterworth filter with a cut-off frequency of 4 Hz to smooth the signals and remove noise from the raw data, as shown by the solid lines. Hence, in transmittance mode, detecting more than one million photons in this scenario is crucial for improving the accuracy of the characteristic points, including the systolic and diastolic slopes, systolic peaks, onsets, and dicrotic notches by reducing randomness. Further analysis of PPG parameters such as the perfusion index is therefore not recommended due to the variability in intensity values during the systolic and diastolic peaks, which are critical for calculating the AC and DC components. This is comparable to how clinicians are required to retake oximeter readings until signal quality is improved before confirming a patient's SpO_2 status. However, despite this, the simulation replicates the overall shape of the PPG waveform after filtering and reveals distinct trends at both wavelengths.

However, at 660 nm, the detected intensity is seen to decrease as skin pigmentation becomes darker. Additionally, the intensity at 100% saturation is greater than at 70%, since deoxygenated haemoglobin absorbs more light at this wavelength compared to oxygenated haemoglobin, resulting in reduced detected intensity at lower oxygen levels. In contrast, with infrared light, higher intensities are observed at 70% oxygen saturation since deoxygenated

haemoglobin absorbs less light. However, changes in detected intensity are minimal as skin pigmentation increases, suggesting that this absorber has a lesser effect on PPG amplitude compared to red light.

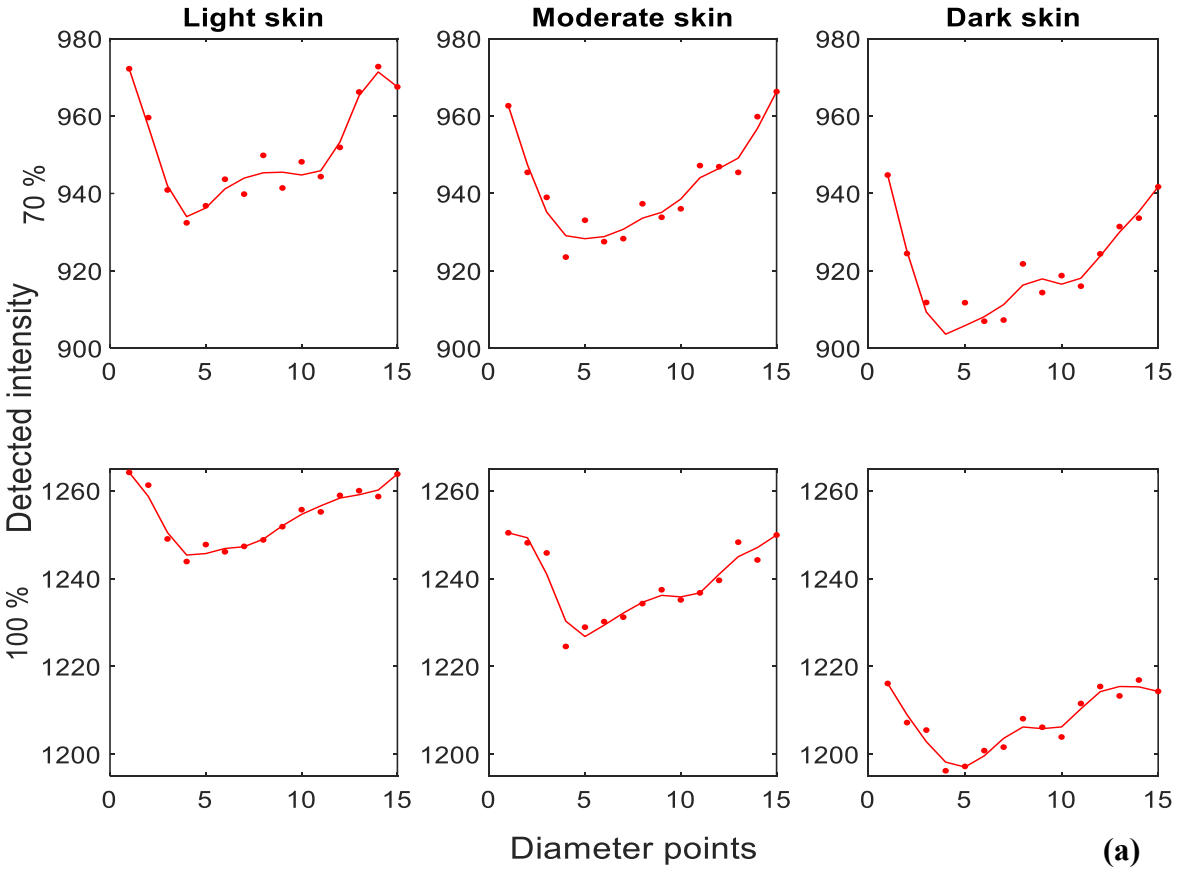

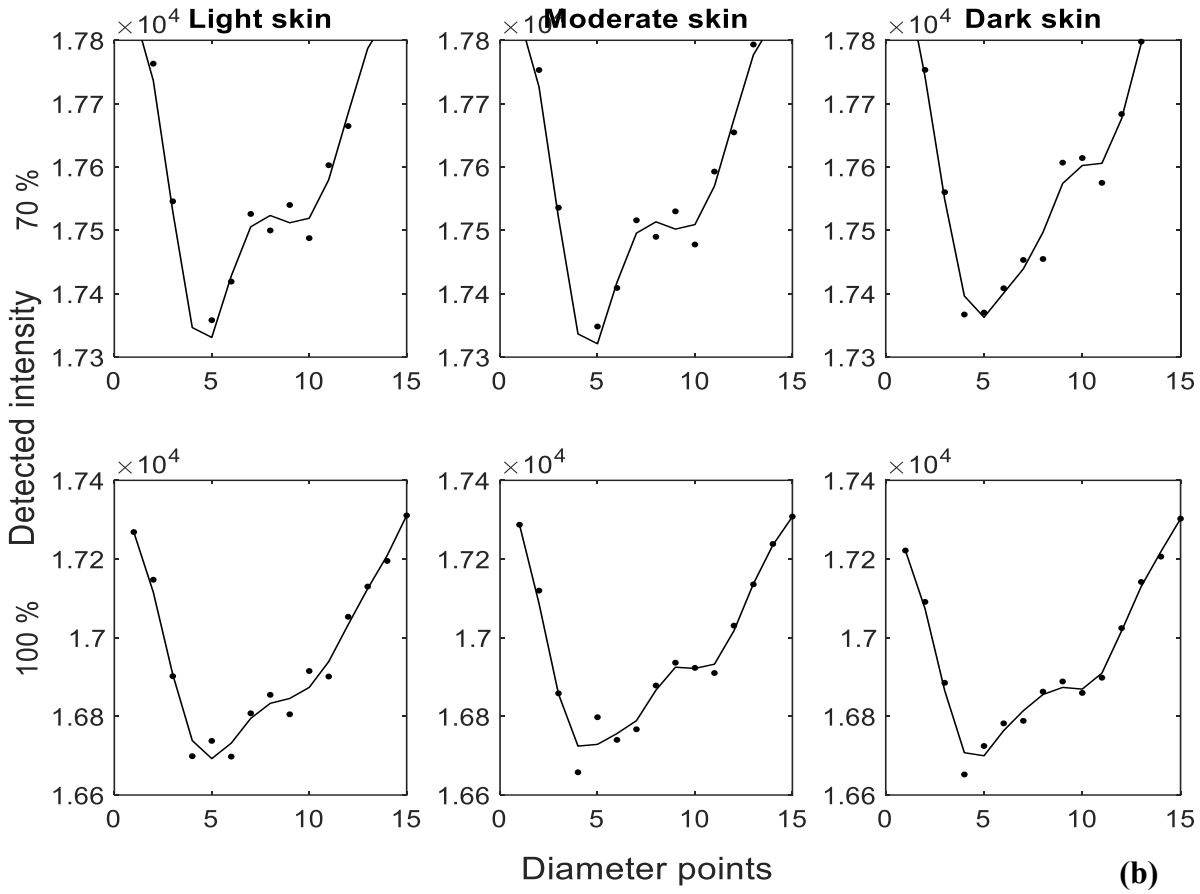

Figure 12-8. Simulated PPG characteristic points for light, moderate, and dark skin at 70% and 100% oxygen saturation levels. Digital filtering is applied to the simulated data points to visualise the shape of the PPG. (a) Red light. (b) Infrared light.

In reflectance mode at both wavelengths, the scattering density is notably high within the vessels, particularly at 660 nm, which aligns with the observations seen in transmittance mode. Although photon penetration depth is quite limited to the skin layers in reflectance mode, the photons are seen to travel across a sufficient width of the finger and through the vessels. This interaction is essential for generating reproducible characteristic points where the key features of the PPG signal are visibly clear and well distinguished. The high scattering coefficient facilitates photon transport and interaction with the blood in the vessels, which enhances the signal-to-noise ratio by increasing the light modulation corresponding to pulsatile blood flow. However, it should be noted that the scattering coefficient alone does not directly minimise noise but rather supports conditions conducive to a higher-quality PPG signal.

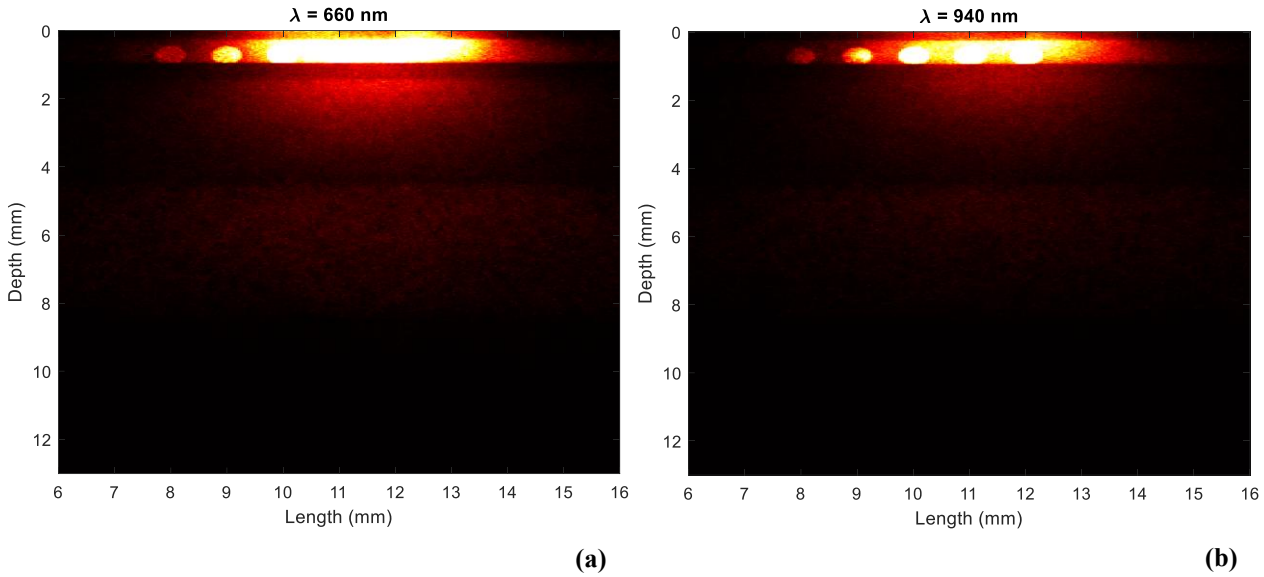

Figure 12-9. Photon profiles showing the scattering density of photons as they travel from the source to the detector in reflectance mode. Brighter regions show higher scattering density and vice versa. (a) Red light. (b) Infrared light.

Furthermore, the PPG signals generated for light, moderate, and dark skin at 70% and 100% oxygen saturation with red and infrared light show more clearly the characteristics of a PPG signal (Figure 12-10). In this scenario, the signal was not filtered because the number of scattering events in the blood, which is where the PPG is sought to primarily be generated from as vessel volume changes with pressure, is much higher than in transmittance mode, reducing the level of randomness. Additionally, reflectance is approximately 1111 to 1267 times higher with red light and 70 to 73 times higher with infrared light across all skin pigmentation types than transmittance mode. This demonstrates that the weight of photon packets backscattered to the photodetector is significantly greater than that of transmitted photons, highlighting the impact of absorption and scattering in the other tissue layers of the finger as photons travel a longer path. As the data generated by the model in reflectance mode was reproducible, the percentage difference in systolic intensities between light, moderate, and dark skin can be calculated to reflect contributions in the DC component, as shown in Table 12-2. For red light, the percentage difference between light and moderate skin exceeds 1% and rises to over 4–5% between light and dark skin. However, even for dark skin, the maximum percentage difference for infrared light is just above 0.1%, implying that the impact on the systolic peak with infrared light is approximately 50 times less than red light. Furthermore, changes in oxygen saturation

result in a 0.11% and 0.27% difference between light and moderate skin and light and dark skin, respectively, at 660 nm, and 0.13% and 0.031% at 940 nm. These findings once again confirm the trends in haemoglobin absorption spectra at the two wavelengths consistently across different skin pigmentations.

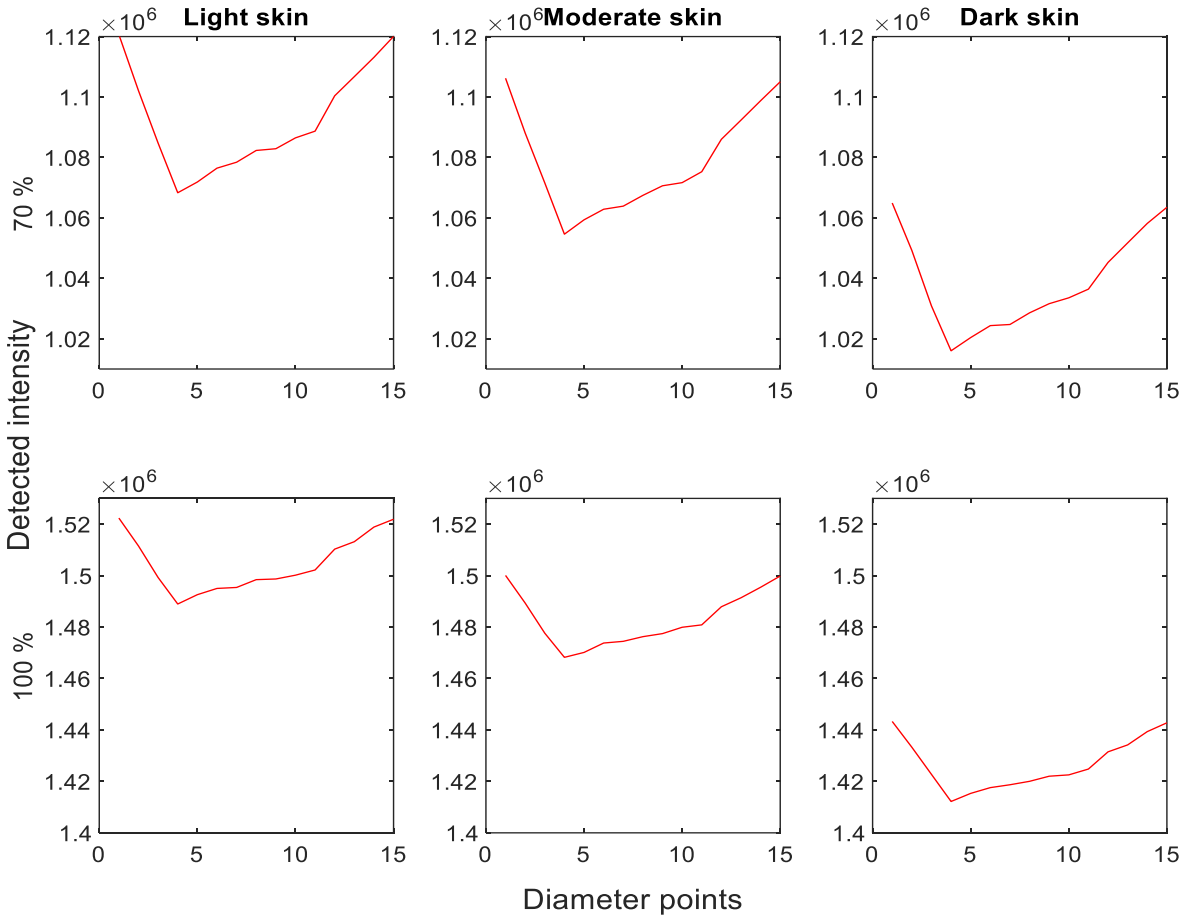

(a)

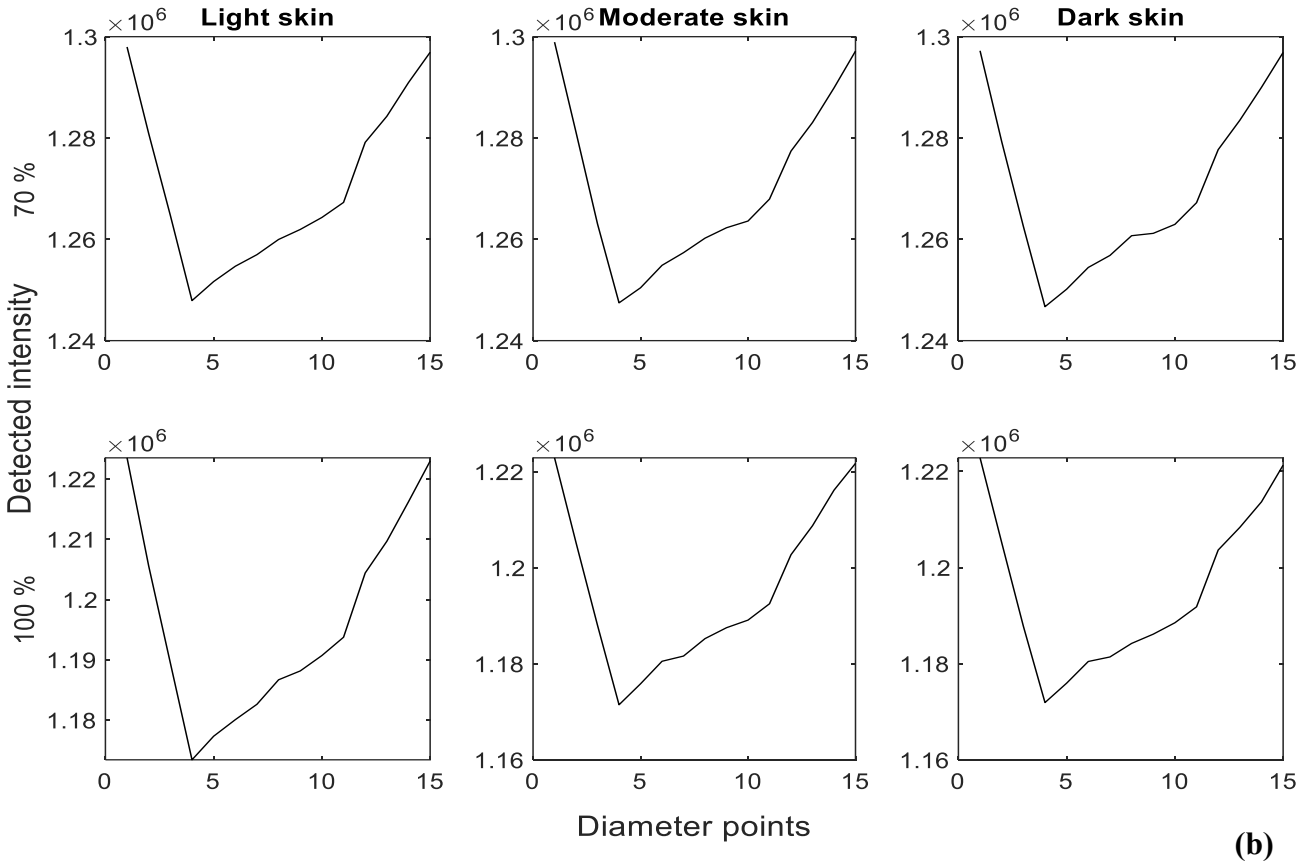

Figure 12-10. Simulated photoplethysmography signals from the Monte Carlo model for light, moderate and dark skin at 70% and 100% oxygen saturation level in reflectance mode. (a) Red light. (b) Infrared light.

Table 12-2: The percentage difference in systolic intensities between light skin (reference) and moderate skin and light skin and dark skin at 660 nm and 940 nm for 70% and 100% oxygen saturation. All values are rounded to three significant figures.

	Red		**Infrared**	
	70%	**100%**	**70%**	**100%**
Light–Moderate skin	1.28	1.39	0.0356	0.166
Light–Dark skin	4.89	5.16	0.0966	0.128

Lastly, further analysis examined the calculated perfusion index values, which represent the ratio between the AC and direct current (DC) components of the simulated PPG signals for red and infrared light at 70% and 100% oxygen saturation for light, moderate, and dark skin (Table

12-3). At 70% oxygen saturation, the perfusion index decreases with red light as skin pigmentation becomes darker; it then increases with infrared light. Consequently, the overall ratio of ratios decreases as pigmentation increases, as shown in Figure 12-11a. However, at 100% oxygen saturation, there is no direct relationship between the perfusion index and skin type. This can be attributed to the differences in the optical properties of blood when it is more oxygenated in addition to the non-linearity of the scattering coefficients of the epidermal layers. This increase in scattering may result in it being a more dominant mechanism of the light–tissue interactions taking place in dark epidermis and hence increasing the random redirection of the photons. Despite this, the importance of analysing the ratio of ratios instead of solely examining intensity changes or perfusion indices at individual wavelengths is highlighted. The ratio method captures the interplay between contributions from different tissue components at both wavelengths, showing that skin pigmentation has a minimal impact on pulse oximeter calibration at 100% oxygen saturation compared to 70%. While there are a number of studies relating the perfusion index to several biomarkers, including oxygen, lactate, glucose, etc., a potential area of research could involve the assessment of the perfusion index at specific wavelengths of interest. This would serve as a useful validation tool to compare with such data derived from computational models. Additionally, the calibration curves presented here also indicate that skin pigmentation must first be quantified to apply the appropriate correction factor if required, which would differ from those proposed in Chapter 10, due to the different pigmentation modelling approach employed. This is shown from the relatively minor differences in simulated SpO2 level between the different skin types in Figure 12-11c.

Table 12-3: Simulated perfusion index (AC/DC) values for light, moderate, and dark skin at 70% and 100% oxygen saturation with 660 nm and 940 nm light sources. L = light skin, M = moderate skin, and D = dark skin.

SaO_2 (%)	**Red (660 nm)**			**Infrared (940 nm)**		
	L	**M**	**D**	**L**	**M**	**D**
70	0.0484	0.0478	0.0467	0.0393	0.0398	0.0403
100	0.0221	0.0215	0.0217	0.0422	0.0429	0.0421

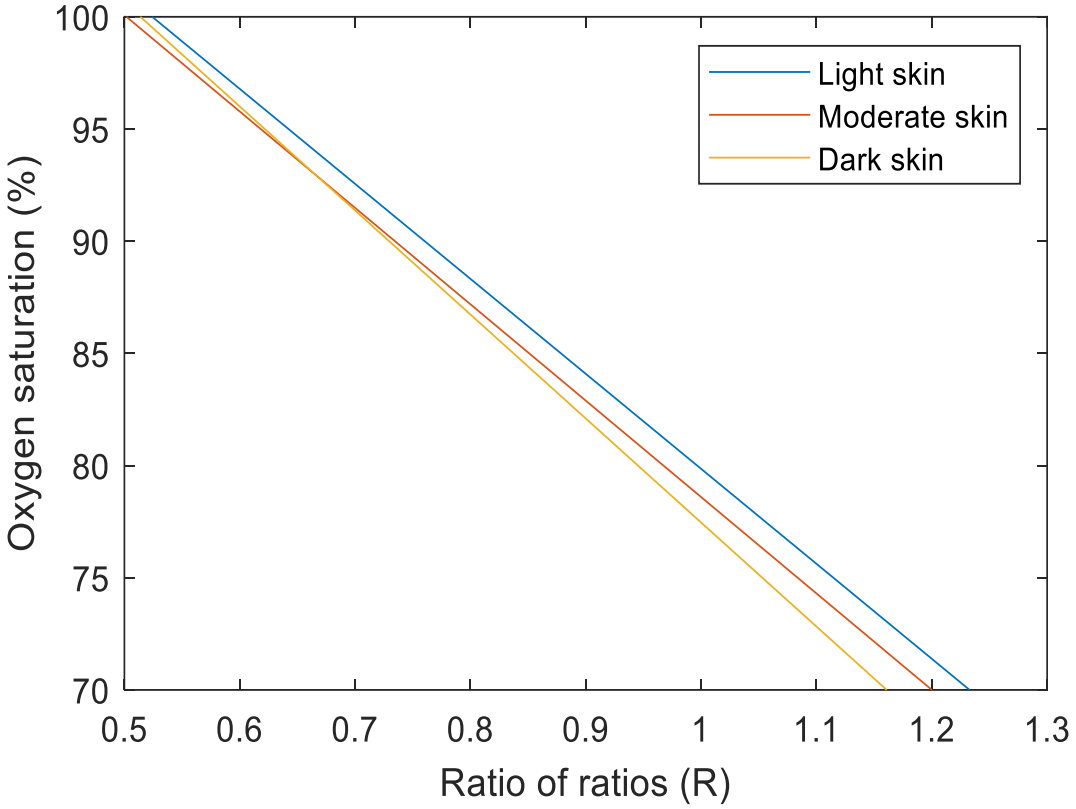
Light skin
Moderate skin
Dark skin
Oxygen saturation (%)
Ratio of ratios (R)
100
95
90
85
80
75
70
0.5
0.6
0.7
0.8
0.9
1
1.1
1.2
1.3

(a)

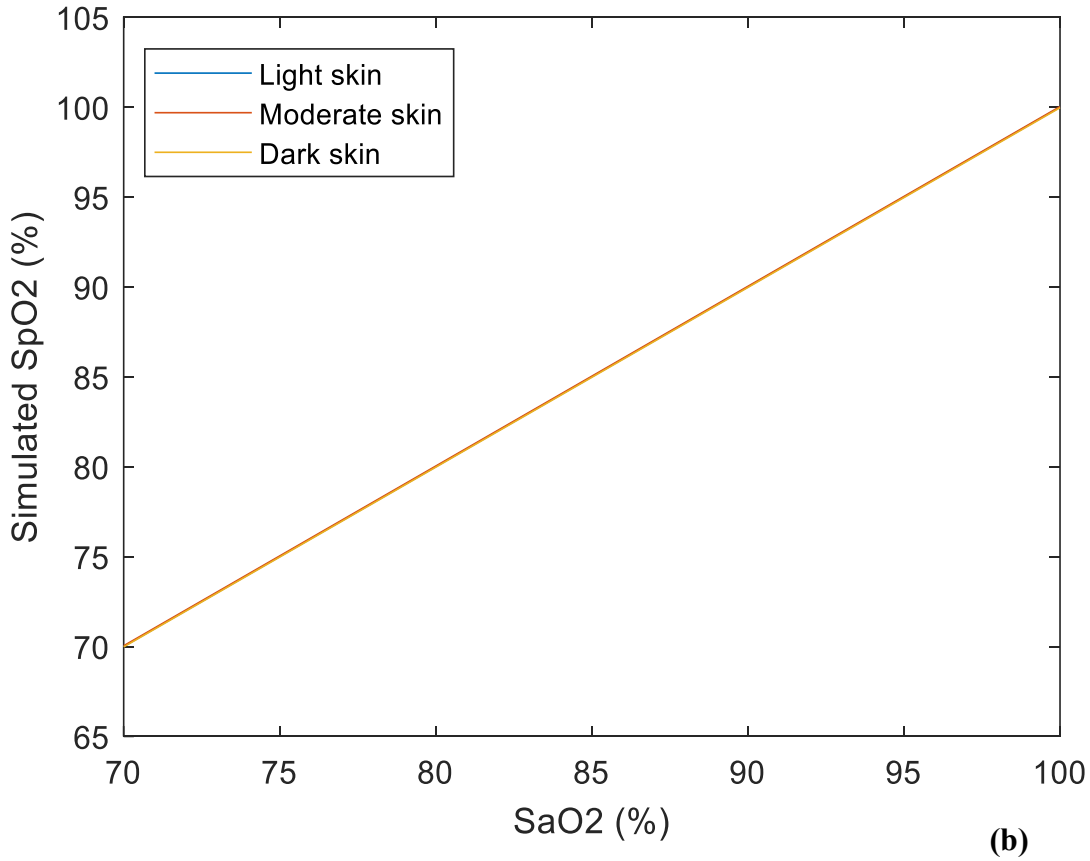
Light skin
Moderate skin
Dark skin
Simulated SpO2 (%)
SaO2 (%)
105
100
95
90
85
80
75
70
65
70
75
80
85
90
95
100

(b)

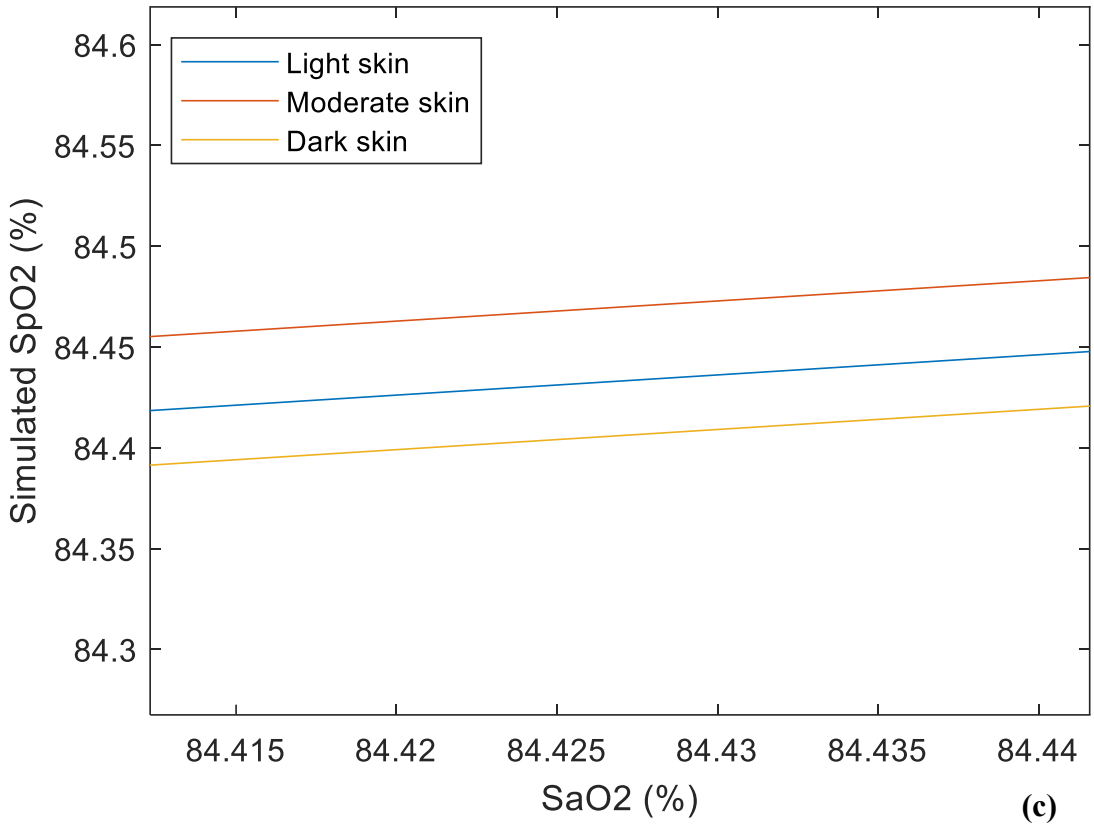

Figure 12-11. (a) Simulated ratios of ratios plotted against arterial oxygen saturation for light, moderate, and dark skin in reflectance mode. (b) Simulated oxygen saturation against true oxygen saturation for light, moderate and dark skin (c) Magnified plot of (b).

12.4.Summary

This study presents a detailed Monte Carlo model of the human finger, demonstrating the effects of skin pigmentation on simulated PPG signals at two oxygen saturation levels. By incorporating the spectrophotometry measurements of developed pigmented skin layers, and the anatomical structure and elastic properties of vessels in the dermis, the model improves upon previous methodologies, offering more accurate input parameters. The results highlight how skin pigmentation alters signal intensity in transmittance and reflectance modes, particularly at 660 nm, and how the perfusion index varies between skin types at different oxygen saturation levels. These findings underscore the importance of considering diverse patient populations in device calibration or integrating post-processing algorithms to adjust for variations to promote inclusivity in healthcare technology.

CHAPTER 13: DISCUSSIONS AND CONCLUSIONS

13.1.Light tissue interactions

The computational investigation of light-tissue interactions began with a monolayer model of the epidermis to isolate the effects of melanin concentration on key optical parameters. This provided a controlled environment to validate the model's behaviour with established theoretical principles such as the Beer-Lambert Law. Key findings suggested that melanin concentration is a critical factor in determining photon behaviour in the visible range, including the extent to which light is absorbed, scattered, and reflected. In reflectance mode, shorter wavelengths such as blue light exhibited higher sensitivity to changes in melanin levels, which limited their ability to penetrate deeper into the tissue layer. In contrast, red light demonstrated resilience to absorption by melanin, making it more suitable for probing deeper structures. These wavelength-dependent interactions justify the use of red light from the visible range to optimise photon detection during the presence of high melanin levels at a fixed source-detector separation. Furthermore, photon detection increased at shorter separations but restricted the depth of their penetration through the tissue layer. Meanwhile, longer separations facilitated deeper tissue penetration but at the cost of reduced photon detection, particularly in highly pigmented skin. Similarly, the analysis of optical pathlength further revealed how melanin modulates photon trajectories, with longer pathlengths achieved with red light in comparison to blue and green light, where photons were confined to the superficial region of the epidermis. These trends reflect the need for careful selection of sensor configurations to achieve both sensitivity and accuracy, particularly in diverse populations with darker skin pigmentation.

With this, the model was extended to capture the complexity of light propagation through heterogeneous tissue layers by including the dermis to simulate blood perfusion, and other underlying layers and structures. By progressively increasing model complexity, this study enabled a deeper understanding of how specific layers contribute to light attenuation. The human finger was chosen as the anatomical region of interest in the MC simulation due to its practicality and popularity in assessing peripheral perfusion, and the common site for pulse oximetry. Hence, this led to focus on investigating the light-tissue interactions at the two operating wavelengths used in pulse oximetry: red and infrared light. Since pulse oximeters used in hospitals and clinical settings are predominantly designed in transmittance mode, the increasing popularity of consumer health wearables, which primarily use reflectance PPG, has highlighted the need to study the impact of melanin concentration in both sensor

configurations. Additionally, the model was optimised to launch photons simultaneously, leveraging the computational resources available in order to enhance simulation speed.

Moreover, three distinct skin types were simulated by using volume fractions that correlated with the Fitzpatrick scale, rather than inputting arbitrary melanin levels. When this study was conducted in 2022, the Fitzpatrick scale was the most practical, widely used, and FDA approved method for stratifying skin pigmentation. Hence, using this scale was the preferred approach for simulating pigmentation levels in the model. The photon profiles revealed the significant prevalence of scattering when simulating infrared light, despite dark skin having an 11-fold higher photon absorption capacity per mm compared to light skin. Melanin, particularly at higher concentrations, absorbed more red light than infrared light in both transmittance and reflectance PPG modes. As a consequence, the magnitudes of the AC and DC components were smaller compared to infrared light, which were derived from the predicted systolic and diastolic intensities. Even though infrared photons had a higher probability of localising in the epidermis at a fixed melanin level first (eq. (7-6e)), their output intensity was higher than red light intensity due to the lower absorption coefficient of the epidermis as this wavelength, and greater likelihood of reaching the detector due to photons travelling relatively larger distances after every scattering event. In reflectance mode, only increases in the source-detector separation decreased the number of scattering events, enabling photons to penetrate deeper into the finger model and thus increasing their optical pathlength, a trend also observed in the monolayer model (Chapter 8). Although the relationship between penetration depth, optical pathlength, source-detector spacing and near infrared spectroscopy (NIRS) is known [282], this study has additionally shown the effect of melanin concentration on these optical parameters.

In principle, there is no reason for the AC/DC ratio to be affected by melanin absorption because the contribution of melanin absorption to systolic absorbance should be cancelled out with the contribution of melanin absorption to diastolic absorbance under Beer Lambert's law. However, it may be, that there is a threshold to which light can behave similarly or within a narrow deviation across all skin types in accordance with optical theory. The differences in magnitude between transmittance and reflectance AC and DC values imply sensitivities to changes in skin chromophores such as melanin. However, it is important to note that transmittance PPGs are generally more accurate than reflectance PPGs since they exhibit a much higher probability of measuring absorption in all the arteries in the anatomical site.

Overall, these studies were conducted to explore individually the behaviour of confounding factors influencing photoplethysmography signals and to assess their relative impact. The fundamental science underpinning the ongoing concern of the impact of skin pigmentation on the accuracy of physiological measurements were revealed from both monolayer and multilayer models, which align with the trends presented by Hu et al [279]. Specifically, all studies showed that (a) the AC and DC components increased with decreasing melanin concentration and (b) the effect of melanin concentration on the red-light PPG characteristics should be paid more attention when predicting blood oxygen saturation. These findings offered valuable insights into the behaviour of light in three distinct skin colours from 'healthy' individuals to serve as a reference for the forthcoming application-based simulations.

13.2. Pulse oximetry

As highlighted in Chapter 5, the discrepancies observed in pulse oximeter measurements have undoubtedly impacted clinical outcomes. Many of the in vivo studies reviewed in this thesis experienced inconsistencies in data collection and retrieval of poor-quality data especially from darker individuals, which resulted in inaccurate data sets for conclusive analyses. There is also a lack of adequate training provided to clinicians to recognise inequity issues when monitoring patients' oxygen saturation levels during and after hospital admission, or in providing guidance to patients in the use of pulse oximeters at home. Therefore, an independent review initiated by the UK Secretary of State for Health and Social Care was formed to consult a group of healthcare professionals dedicated to achieving equity in healthcare [283]. They proposed several recommendations, including:

"Innovators, researchers and manufacturers should cooperate with public and patient participants to design better, smarter oximeters using innovative technologies to produce devices that are not biased by skin tone. This could include developing enhanced algorithms for oximeter device software to address measurement bias".

Aligned with this recommendation, the model was adapted to simulate calibration curves for the same three skin types, after having established the impact of melanin concentration on PPG parameters and light-tissue interactions in the finger. The goal was to determine whether the discrepancies observed in SpO_2 measurements arise from the algorithms used in pulse oximeters, which are sought to be calibrated in a predominantly White population. Evidently,

the data generated from this model suggested that a single pulse oximeter algorithm may not be universally acceptable for all skin types, since greater absorption of red light exhibited by higher concentrations of melanin lead to major differences in the perfusion index as oxygen saturation increases from 70% to 100% in comparison to the perfusion indices with infrared light. Moreover, the data derived from the simulated calibration curves in transmittance mode were validated against experimental data to ensure consistency with observations of oxygen saturation variations relative to skin pigmentation in clinical settings. The ratio of the mean biases between White and Black subjects from the cohort study approximately matched the ratio from the simulation study between light and dark skin mean biases, with a difference of 1.13%. Consequently, further analysis explored the feasibility of adjusting pulse oximeter calibration across diverse skin types to suggest potential solutions for measurement bias. The simulated dark skin calibration curve was only fully adjusted with respect to the light skin curve after applying an exponential multiplication factor to account for the larger bias arising from the combined effects of lower oxygen saturation and high melanin level. However, for moderate skin, applying a linear multiplication factor was sufficient for the correction process, suggesting that the integration of different corrective measures can minimise bias level between difference skin pigmentation groups. Other solutions could include the greater enrolment of individuals with higher levels of pigmentation in the calibration process to minimise bias [229].

Furthermore, the same protocols were conducted in reflectance mode as there is a growing demand for health wearables to perform as well as medical grade devices [272]. Similarly, the results suggested that bias between simulated transmittance and reflectance SpO_2 data was greater for dark skin in comparison to light and moderate skin, especially at lower oxygen saturation levels. It was also observed that applying similar correction factors to the simulated calibration curves in reflectance mode requires further investigation, as additional aspects of photon behaviour in this configuration need to be considered. Specifically, ensuring consistent penetration depth across the three skin types is crucial to normalise the data and account for variations in light-tissue interactions, potentially by decreasing the source-detector separation as melanin concentration increases.

Other computational studies adopted a similar approach in attempt to provide insight into the variations in SpO_2 measurements based on differences in skin pigmentation. For instance, Bolic [223] conducted an examination of the influence of skin colour and the depth of the air gap on SpO_2 levels during contactless sensor placement in reflectance mode, focusing on melanin

concentrations ranging from 0.3% to 16% [223]. Similar trends in the simulated calibration algorithms were observed, specifically higher levels of absorption at 660 nm as melanin concentration increased. Some limitations of the study included an anomalous calibration outcome at 8% melanin concentration, whereby a satisfactory explanation was not provided. Additionally, the study focused on the exclusive representation of light and moderate skin types, which neglects individuals with darker skin tones [249], including a significant portion of African populations. Therefore, this could explain the smaller difference in the y-intercepts of the best fit lines, similar to the differences between light and moderate skin in this MC simulation with 2.55% and 15.5% melanin concentrations respectively. Furthermore, Jung et al [284] conducted a study to characterise and evaluate the estimation of oxygen saturation measured by a wrist-worn reflectance pulse oximeter during sleep. While the study had a number of limitations, the accuracy of the smartwatch was said to comply with the FDA and ISO standards. In the context of skin pigmentation as the limitation explored in this study, the 97 participants enrolled in the investigation were reported as 'Asian'. Since ethnicity may not serve as a precise method for stratifying skin pigmentation, the probability of not meeting FDA and ISO standards was low, assuming uniform skin pigmentation levels across all participants and a maximum RMSE of ±8% with co-oximetry as a reference. Therefore, future studies are advised to recruit an adequate number of participants with quantified skin pigmentation levels and assess SpO_2 measurement using reflectance pulse oximeters. This can, in addition to providing insight into the effect of skin pigmentation in reflectance pulse oximeters, serve as a validation study to compare with the simulated results from the current Monte Carlo model. Meanwhile, the generated data should be interpreted with caution.

13.3. Monte Carlo simulated PPG signals

After exploring the light-finger interactions in the presence of different melanin concentrations, which provided justifications to the differences in the simulated calibration curves, the final studies set out to develop another Monte Carlo model to generate PPG characteristic points reflecting the shape of a PPG signal. This approach enabled the visualisation of the AC and DC components, specifically the effect of skin pigmentation on 'amplitude' at 660 nm and 940 nm. First, a preliminary model of a silicon phantom body with an indwelling vessel was created to establish an approach to simulating PPG signals from the MC model. The optical properties of the tissue components were acquired spectroscopically, which improved on previous

methods of acquiring those properties from the literature. The elastic properties of the vessel were obtained by measuring the diameter at different blood pressures to simulate geometrical changes in the model reflecting the dynamic response of a PPG signal. Previous attempts of Monte Carlo simulated PPGs have been documented by Boonya et al. [245], where they obtained PPG signals from an artery located 4.5 mm deep from the surface. To model the mechanical behaviour of the artery, finite element analysis (FEA) was used to visualise the motion of the arterial wall under applied internal pressure. While this approach may be preferred to visualise stress and strain patterns, conducting a vessel diameter test in this context offers several advantages over FEA. This includes a simpler, faster, and more cost-effective method which does not rely on material assumptions, avoiding unnecessary use of computational resources and expertise whilst capturing the behaviour of the vessel more accurately. It is also important to consider that such vessel diameter tests can serve as valuable validation benchmark for FEA simulations to ensure the models align with experimental outcomes. Therefore, the methodology employed in the MC model presented in this thesis is intended to be recognised as a more appropriately efficient approach for the objectives of the study. The shape of the PPG signal was successfully achieved using approximately 0.2% of the diameter data, including the identification of key features, including onsets, peaks, and downslopes, etc. Therefore, this approach allows for significant utilisation of time and computational resources to obtain results in shorter periods of time. For this specific model, projecting one billion photons was sufficient to capture small fluctuations in the simulated detected intensities, reflecting the small magnitudes of the AC component of a PPG signal.

With this work providing the basis for simulating PPG signals, additional physiological factors were incorporated into the model, including the implementation of oxygenated blood in the vascular network of the finger, and skin pigmented layers. Hence, the final study in this thesis presented a comprehensive Monte Carlo model of the human finger to examine the effects of skin pigmentation on simulated characteristic points of PPG signals at 70% and 100% oxygen saturation. Firstly, the elastic properties of the vessel were characterised using the same methodology employed in Chapter 11, with a custom phantom comprising a 0.5 mm diameter vessel channel. Secondly, a key innovation of this work lies in its methodological improvements for characterising the optical properties of the skin layers, producing a more realistic finger model. The pigmented skin layers were validated against the L*a*b* scale, which is a more objective method for stratifying skin pigmentation in comparison to the Fitzpatrick scale, as discussed in Chapter 4. As a result, the optical properties incorporated into

the current Monte Carlo model reflected more real-world variations in skin pigmentation. This is an advancement from the previous studies presented in this thesis and more, where the optical properties of the epidermis are conventionally calculated using equations from the literature. Although variations in the perfusion index at 940 nm in reflectance mode were consistent with the study presented in Chapter 10, the perfusion indices at 660 nm were significantly more affected. This is likely attributed to the greater magnitude in the calculated absorption coefficients (0.73 mm^{-1}, 4.21 mm^{-1}, and 8.24 mm^{-1} for light, moderate, and dark skin, respectively) in comparison to those spectroscopically obtained (0.00964 mm^{-1}, 0.0195 mm^{-1}, 0.0396 mm^{-1}). Nevertheless, this further confirms the minimal influence of skin pigmentation on the PI values in the infrared region, and that optically characterising skin colour beyond simple equations is required especially in the visible range, since the percentage differences in systolic intensities were significantly higher for red light. This characterisation was essential for generating more representative magnitudes of simulated detected intensities which better reflect the effect of light absorption and scattering with different skin types.

Moreover, the photon profiles revealed that scattering density is notably higher in the blood vessels and superficial layers of the finger in reflectance mode, particularly at 660 nm. This is a phenomena also observed in previous studies [173], [230], and aligns with the known scattering properties of blood. Consequently, the PPG signals displayed consistent features across different skin types and oxygen saturation levels, indicating that the number of photon iterations was sufficient to capture the volumetric changes in the vessel. Visually, skin pigmentation was seen to effect detected intensity, which is indicative of differences in amplitudes from experimental-based PPG signals. Overall, the findings once again highlighted the importance of accounting for skin pigmentation in pulse oximeter calibration at different oxygen saturation levels. However, this requires the accurate quantification of skin pigmentation of very large and representative cohort using spectroscopic-based techniques to understand the type of corrective measures required to minimise bias. Whilst a number of signal processing techniques have been introduced in pulse oximeter technology to minimise the effects of other known limitations, including motion artefact reduction [285], [286], [287], baseline drift correction [288], etc., the same is proposed to account for physiological differences in diverse populations. In addition to the integration of classification algorithms to estimate skin colour, this could also include applying pre-defined correction factors tailored to pigmentation levels as suggested in Chapter 10 or consider scaling the absorption differences due to differences in melanin, particularly for the red-light source.

13.4. Limitations and Future Work

Computational and experimental studies are often used interchangeably, independently, or in combination to test various hypotheses, and both come with their own limitations. Therefore, despite the robust findings generated by the Monte Carlo models presented in this thesis, it is essential to acknowledge the inherent limitations of this technique.

Firstly, this thesis presents a set of novel Monte Carlo simulations based on established methodologies outlined in the literature, and its performance was validated against other published models. While this approach allowed for complete control over the modelling framework and computational optimisations, it inevitably required substantial development time. Hence, a potential avenue for future research would be to implement the modelling framework using highly optimised, widely used Monte Carlo platforms such as MCX, offering advantages in speed by GPU acceleration to achieve higher photon counts, and enabling the simulation of more complex geometries. Its extensive documentation and large user community also facilitate troubleshooting and reproducibility. However, such pre-built frameworks may limit flexibility in modifying the photon propagation algorithms or in implementing unconventional optical property definitions i.e. in non-homogenous tissue layers, which can be important when exploring more realistic tissue models. Accounting for these advantages and disadvantages may suggest the use of a hybrid approach which leverages MCX for computational efficiency while maintaining some capacity for customised algorithmic development. This would be particularly useful when simulating dark skin and all skin pigmentation models in transmittance mode, since the number of photon projections and/or detections can exceed the amounts used in the current models to minimise randomness and noise. Nevertheless, while the data generated from the model was reproducible, an improvement would involve running the model multiple times to reduce the deviations of the data points from the best-fit lines, as seen in the simulated calibration curves (Chapter 10).

Secondly, scattering density plots were generated to investigate photon paths, survival rates, and detection characteristics within the tissue. This approach was chosen because it provides detailed insight into how factors such as skin pigmentation and tissue geometry influence photon behaviour and signal strength, which is critical for understanding variations in detector output. However, fluence, which is commonly computed in Monte Carlo models, also offer a complementary perspective by quantifying the total light energy available at each tissue location regardless of detection. It is often favoured for validating Monte Carlo simulations

because it enables direct comparison with analytical or finite element solutions. Therefore, future models could benefit from a fluence tally to quantify the total photon availability at each location, allowing more accurate assessment of light–tissue interactions. Such data would enable better interpretation of how variations in skin pigmentation or tissue structure affect overall light propagation, complementing the insights gained from scattering behaviour analysis. Evidently, the red wavelength was particularly affected by increased skin pigmentation, which can compromise the accuracy of pulse oximetry in individuals with darker skin tones relative to infrared light. Hence, exploring the use of multiple wavelength light sources to improve measurement robustness across diverse skin pigmentation levels would be useful, especially for the concept of partial pathlengths [289]. The partial pathlength factor (PPF) method would make it possible to separate the effects of superficial melanin from deeper blood absorption, quantify how melanin alters light penetration and pathlength through blood, and assess how these errors vary across wavelengths. This enables a clearer understanding of how melanin-induced attenuation contributes to oxygen saturation bias and informs wavelength choices that minimise error in pulse oximetry measurements, instead of using the standard DPF.

Thirdly, while they offer valuable insights, computational models may overlook uncontrollable experimental factors, such as motion artifacts, and can only replicate certain parameters to a relative degree. In the context of skin pigmentation, it can be challenging to model this highly complex tissue component that is influenced by both intrinsic and extrinsic factors and vary significantly among individuals (Chapter 4). This is especially the case given the limited research on skin property variability across large and diverse populations, including knowledge of the non-uniform distribution of melanin on both sides of the finger, and the greater thickness of the epidermis in darker skin types which would increase photon absorption even further.

Similarly, another area for improvement is the modelling of haemodynamic related activity presented in Chapters 9 and 10. Prior to incorporating the vessels into the finger model, the assumption of doubling the diastolic blood volume to simulate systolic blood volume and equally distributing it between arterial and venous compartments could have been refined. Even though the accurate simulation of blood was an important component of the model, it was considered a constant factor across all skin pigmentation models. Hence, any differences in the output were attributed solely to changes in melanin concentration, which was the primary focus of the studies. As a result, this aspect was refined in the models developed for generating PPG

characteristic points, by simulating the relationship between pressure and vessel volume in synchrony with the cardiac cycle in vitro. Additionally, attention should be given to capturing other mechanical changes in the blood vessels for better modelling of peripheral haemodynamics. This can include accounting for vasodilation and vasoconstriction, the non-linear stiffness of vessel walls under varying pressures, more realistic blood flow dynamics which vary with race [213], and viscosity effects. For instance, instead of measuring vessel diameter and internal pressure, compliance can be derived from a volume-pressure graph to calculate more minor changes in vessel volume overtime. These advancements could improve the model's ability to simulate physiological conditions with greater accuracy and realism. To further strengthen these findings, a correlation study could be conducted across a range of melanin levels with controlled physiological factors i.e. in vitro, for cross validation. Ultimately, the novel Monte Carlo models presented in this thesis have shown for the first time to a be a powerful tool for investigating the effect of skin pigmentation on pulse oximeter accuracy, and that ongoing advancements can bridge the gap even more between simulated tissue models and real-world biological complexity.

APPENDIX: COMPUTATIONAL PROGRAM

```
clc;clear;
lambda=940;
mua_bl=7.84*10^7*(lambda^-3.255);
mua_mel=(6.6*10^10)*(lambda^(-3.33));
fibrad2=1;
ni=1.4; %internal refractive index of tissue
nt=1; %external refractive index of air
rad1=1; %Gaussian beam radius
Rsp=((ni-nt)/(ni+nt))^2;
k=0; %number of position of photon
s=3;
.....................................................

    detect=0;entry=0;N_phot=1E8;
    %mua_W=0.0004; %660nm;
    mua_W=0.02674; %940nm;
    %mua_HHb=1.64; %660 nm
    %mua_Hbo=0.15; %660 nm
    mua_HHb=0.43; %940 nm
    mua_Hbo=0.65; %940 nm

    Sat_A=0.7;
    Sat_V=Sat_A-0.1;
    mua_A=Sat_A*mua_Hbo+(1-Sat_A)*mua_HHb;
    mua_V=Sat_V*mua_Hbo+(1-Sat_V)*mua_HHb;

.....................................................
        vW=0.05;
    mua_sc=mua_W*vW+(1-vW)*mua_bl;%stratum croneum

.....................................................
..
        vW=0.2;
    vmel=0.305; %Type I-II Very fair, IV-V Medium, VI Dark
    mua_epi=vmel*mua_mel+mua_W*vW+(1-vmel-vW)*mua_bl;

.....................................................
..
        %papder
    vW=0.5; %volume of Water (=50%)
    v=0.04; %total blood volume (=4%)
    vA=v/2; %volume of arterial blood
    vV=v/2; %volume of venous blood
    mua_papder=mua_A*vA+mua_V*vV+mua_W*vW+(1-(vA+vV+vW))*mua_bl;

.....................................................
..
```

```
        %upbloodnetplexus
    vW=0.6; %volume of W6ater (=60%)
    v=0.3; %total blood volume (=30%)
    vA=v/2; %volume of arterial blood
    vV=v/2; %volume of venous blood
    mua_upblder=mua_A*vA+mua_V*vV+mua_W*vW+(1-(vA+vV+vW))*mua_bl;

.....................................................................
..
        %retderm
    vW=0.7; %volume of W6ater (=70%)
    v=0.04; %total blood volume (=4%)
    vA=v/2; %volume of arterial blood
    vV=v/2; %volum of arterial blood
    mua_retder=mua_A*vA+mua_V*vV+mua_W*vW+(1-(vA+vV+vW))*mua_bl;

.....................................................................
..
        %deepbloodnetplexus
    vW=0.7;
    v=0.1; %total blood volume (=10%)
    vA=v/2; %volume of arterial blood
    vV=v/2; %volume of venous blood
    mua_dpblder=mua_A*vA+mua_V*vV+mua_W*vW+(1-(vA+vV+vW))*mua_bl;

.....................................................................
..

    %% Skin
    %mus1_skin=2.562; %660nm
    mus1_skin=1.568; %940nm
    g_skin=0.9;

    %% Fat
    %mus1_fat=1.24; %660 nm
    mus1_fat=1.085; %940nm
    %mua_fat=0.0104; %660 nm
    mua_fat=0.0170;%940 nm
    g_fat=0.8;

    %% Muscle
    %mus1_musc=4.305; %660nm
    mus1_musc=2.905; %940nm
    %mua_musc=0.0816; %660 nm
    mua_musc=0.0401;%940 nm
    g_musc=0.5;

    %% Bone
    %mus1_bone=2.756; %660nm
```

```
mus1_bone=1.976; %940nm
%mua_bone=0.0351; %660 nm
mua_bone=0.0457;%940 nm
g_bone=0.92;
d_bone=3;
r_bone=2;

.......finger model: total thicknes 1.3 cm.....................
    t1=0.02; % all measurements in mm
t2=t1+0.25;
t3=t2+0.1;
t4=t3+0.08;
t5=t4+0.2;
t6=t5+0.3;
t7=t6+0.5;
t8=t7+10.1; %muscle and bone
t9=t8+0.5;
t10=t9+0.3;
t11=t10+0.2;
t12=t11+0.08;
t13=t12+0.1;
t14=t13+0.25;
t15=t14+0.02;
.............................................................

%% Initialising vectors
%X=zeros;Y=zeros;Z=zeros;
XYZ=zeros(3,1);I=0;test=0;OP=0;threshold=1E6;

while detect<threshold
    disp(detect);
    if test==0
        delete(gcp('nocreate'))
        parpool;
        test=1;
    end
    if detect >= 930000 && detect < 990000
        N_phot=1E7;
    elseif detect >= 970000 && detect < 995000
        N_phot=1E6;
    elseif detect>= 995000
        N_phot=1;
        if test==1
            delete(gcp('nocreate'))
            test=2;
        end
    else
    end
    parfor q=1:N_phot
```

```
            %disp([q idk])
            k=0;Scat=0;entry=entry+1;
            X=zeros;Y=zeros;Z=zeros;
            alpha=2*pi*rand; %cylinidrical co-ord angle
            r_source=rad1*sqrt(-log(rand));
            x_source=r_source*cos(alpha);
            y_source=r_source*sin(alpha);
            w=1-Rsp;
            x=x_source; %Gaussian distribution
            y=y_source;
            z=0;ux=0;uy=0;uz=1;n_ent=1;
            k=k+1;
            X(k)=x;Y(k)=y;Z(k)=z;
            L=0; %total pathlength of a single photon
            mu_a=mua_sc;
            g=g_skin;
            mu_s=mus1_skin/(1-g);
            while n_ent==1
                theta=acos(abs(uz));
                l=-log(rand)/(mu_a+mu_s);
                L=L+l;
                x2=x+(l*ux);
                y2=y+(l*uy);
                z2=z+(l*uz);
                k=k+1;
                Scat=0;
                if (w<=10^-4)%Roullet
                    if(rand<=1/10)
                        w=10*w;
                    else
                        n_ent=0;k=0;
                    end
                %
%.................Reflectance.............................
                % elseif (z2<0)%exit below
                %     x3=z*(ux/uz)+x;
                %     y3=z*(uy/uz)+y;
                %     if (((x3-s)^2+y3^2)<=fibrad2^2)

%.................Transmittance...........................
                elseif (z2>t15)%exit below
                    x3=(t15-z)*(ux/uz)+x;
                    y3=(t15-z)*(uy/uz)+y;
                    if (((x3-s)^2+y3^2)<=fibrad2^2)
                        I=I+w;
                        w=0;k=k+1;
                        %X(k)=x3;Y(k)=y3;Z(k)=0; %ref
                        X(k)=x3;Y(k)=y3;Z(k)=t15; %trans
                        OP=[OP L];
```

```
                    XYZ=[XYZ [X(1,:); Y(1,:); Z(1,:)]];
                    detect=detect+1;
                    k=0;n_ent=0;

                    %% Internal reflection
                elseif (abs(uz)==1||theta>asin(nt/ni)) %OI/TIR
                    uz=-uz;
                    z2=-z2;
                    %X(k)=x2;Y(k)=y2;Z(k)=z2;
                else
                    theta_t=asin(ni*sin(theta));
                    a=theta-theta_t;
                    b=theta+theta_t;
                    aa=sin(a)/sin(b);
                    bb=tan(a)/tan(b);
                    r_fres=(aa^2+bb^2)*0.5;
                    if(rand>r_fres) %photon exits tissue
                        k=0;n_ent=0;w=0;
                    else %photon reflects back in tissue
                        uz=-uz;
                        z2=-z2;%internal reflection
                        x=x2;y=y2;z=z2;
                        %X(k)=x2;Y(k)=y2;Z(k)=z2;
                    end
                end
            % elseif (z2>t15) %exit below in reflectance mode
            %     if (abs(uz)==1||theta>asin(nt/ni)) %OI/TIR
            %         uz=-uz;
            %         z2=-z2;
            %         %X(k)=x2;Y(k)=y2;Z(k)=z2;
            %     else
            %         theta_t=asin(ni*sin(theta));
            %         a=theta-theta_t;
            %         b=theta+theta_t;
            %         aa=sin(a)/sin(b);
            %         bb=tan(a)/tan(b);
            %         r_fres=(aa^2+bb^2)*0.5;
            %         if(rand>r_fres) %photon exits tissue
            %             k=0;n_ent=0;w=0;
            %         else %photon reflects back in tissue
            %             uz=-uz;
            %             z2=-z2;%internal reflection
            %             x=x2;y=y2;z=z2;
            %             %X(k)=x2;Y(k)=y2;Z(k)=z2;
            %         end
            %     end

.....................................................................
..
```

```
                    %goes in order of skin layers
                elseif((z2>=0)&&(t1>z2))% stratum croneum
                    mu_a=mua_sc;g=g_skin;mu_s=mus1_skin/(1-
g);Scat=1;
                elseif ((z2>=t1)&&(t2>z2))%epidermis
                    g=g_skin;mu_a=mua_epi;mu_s=mus1_skin/(1-
g);Scat=1;
                elseif ((z2>=t2)&&(t3>z2))%papilary dermis
                    mu_a=mua_papder;g=g_skin;mu_s=mus1_skin/(1-
g);Scat=1;
                elseif ((z2>=t3)&&(t4>z2))%upper blood net dermis
                    mu_a=mua_upblder;g=g_skin;mu_s=mus1_skin/(1-
g);Scat=1;
                elseif ((z2>=t4)&&(t5>z2))%reticular dermis
                    mu_a=mua_retder;g=g_skin;mu_s=mus1_skin/(1-
g);Scat=1;
                elseif ((z2>=t5)&&(t6>z2))%deep blood net dermis
                    mu_a=mua_dpblder;g=g_skin;mu_s=mus1_skin/(1-
g);Scat=1;
                elseif ((z2>=t6)&&(t7>z2))%fat
                    mu_a=mua_fat;g=g_fat;mu_s=mus1_fat/(1-g);Scat=1;
                elseif ((z2>=t7)&&(t8>z2))%muscle and bone
                    if ((y2^2+(z2-
(t7+d_bone+r_bone))^2)<=(r_bone^2))%bone
                        mu_a=mua_bone;g=g_bone;mu_s=mus1_bone/(1-
g);Scat=1;
                    else
                        mu_a=mua_musc;g=g_musc;mu_s=mus1_musc/(1-
g);Scat=1;
                    end
                elseif ((z2>=t8)&&(t9>z2))%fat
                    mu_a=mua_fat;g=g_fat;mu_s=mus1_fat/(1-g);Scat=1;
                elseif ((z2>=t9)&&(t10>z2))%deep blood net
                    mu_a=mua_dpblder;g=g_skin;mu_s=mus1_skin/(1-
g);Scat=1;
                elseif ((z2>=t10)&&(t11>z2))%reticular dermis
                    mu_a=mua_retder;g=g_skin;mu_s=mus1_skin/(1-
g);Scat=1;
                elseif ((z2>=t11)&&(t12>z2))%upper blood net
                    mu_a=mua_upblder;g=g_skin;mu_s=mus1_skin/(1-
g);Scat=1;
                elseif ((z2>=t12)&&(t13>z2))%papilary dermis
                    mu_a=mua_papder;g=g_skin;mu_s=mus1_skin/(1-
g);Scat=1;
                elseif ((z2>=t13)&&(t14>z2))%epidermis
                    mu_a=mua_epi;g=g_skin;mu_s=mus1_skin/(1-
g);Scat=1;
                elseif ((z2>=t14)&&(t15>z2)) %strat croneum
```

```
                    mu_a=mua_sc;g=g_skin;mu_s=mus1_skin/(1-
g);Scat=1;
                else
                    n_ent=0;w=0;k=0;Scat=0;
                end
                if Scat==1
                    p=(1-g^2)/(1-g+2*g*(rand));
                    costheta=(1+g^2-p^2)/(2*g);
                    sintheta=sqrt(1-costheta^2);
                    temp=sqrt(1-uz^2);
                    phi=2*(rand)*pi;
                    if abs(uz)==1
                        ux1=sintheta*cos(phi);
                        uy1=sintheta*sin(phi);
                        uz1=sign(uz)*costheta;
                    else
                        ux1=(sintheta*(ux*uz*cos(phi)-
uy*sin(phi))/temp)+ux*costheta;

uy1=(sintheta*(uy*uz*cos(phi)+ux*sin(phi))/temp)+uy*costheta;
                        uz1=-temp*sintheta*cos(phi)+uz*costheta;
                    end
                    ux=ux1;uy=uy1;uz=uz1;
                    X(k)=x2;Y(k)=y2;Z(k)=z2;
                    x=x2;y=y2;z=z2;
                    dw=w*mu_a/(mu_a+mu_s); %fractional absorption at
site
                    w=w-dw; %new weight
                    Scat=0;
                end
            end
        end
    end
save(['sat',num2str(Sat_A*100),'ird.mat']);
```

BIBLIOGRAPHY

[1] P. A. Kyriacou and J. Allen, *Photoplethysmography: Technology, Signal Analysis and Applications*. Academic Press, 2021.

[2] K. K. Tremper and S. J. Barker, "Pulse oximetry," *Anesthesiology*, vol. 70, no. 1, pp. 98–108, Jan. 1989, doi: 10.1097/00000542-198901000-00019.

[3] J. F. Kelleher, "Pulse oximetry," *J. Clin. Monit.*, vol. 5, no. 1, pp. 37–62, Jan. 1989, doi: 10.1007/BF01618369.

[4] J. A. Wahr, K. K. Tremper, and M. Diab, "Pulse oximetry," *Respir. Care Clin. N. Am.*, vol. 1, no. 1, pp. 77–105, Sep. 1995.

[5] S. T. Lawless, "Crying wolf: false alarms in a pediatric intensive care unit," *Crit. Care Med.*, vol. 22, no. 6, pp. 981–985, Jun. 1994.

[6] C. Dumas, J. A. Wahr, and K. K. Tremper, "Clinical evaluation of a prototype motion artifact resistant pulse oximeter in the recovery room," *Anesth. Analg.*, vol. 83, no. 2, pp. 269–272, Aug. 1996, doi: 10.1097/00000539-199608000-00012.

[7] N. Shah, H. B. Ragaswamy, K. Govindugari, and L. Estanol, "Performance of three new-generation pulse oximeters during motion and low perfusion in volunteers," *J. Clin. Anesth.*, vol. 24, no. 5, pp. 385–391, Aug. 2012, doi: 10.1016/j.jclinane.2011.10.012.

[8] R. J. Falconer and B. J. Robinson, "Comparison of pulse oximeters: accuracy at low arterial pressure in volunteers," *Br. J. Anaesth.*, vol. 65, no. 4, pp. 552–557, Oct. 1990, doi: 10.1093/bja/65.4.552.

[9] J. H. Eichhorn, "Pulse oximetry as a standard of practice in anesthesia," *Anesthesiology*, vol. 78, no. 3, pp. 423–426, Mar. 1993.

[10] C. J. Wilkins, M. Moores, and C. D. Hanning, "COMPARISON OF PULSE OXIMETERS: EFFECTS OF VASOCONSTRICTION AND VENOUS ENGORGEMENT," *Br. J. Anaesth.*, vol. 62, no. 4, pp. 439–444, Apr. 1989, doi: 10.1093/bja/62.4.439.

[11] R. W. Morris, M. Nairn, and T. A. Torda, "A comparison of fifteen pulse oximeters. Part I: A clinical comparison; Part II: A test of performance under conditions of poor perfusion," *Anaesth. Intensive Care*, vol. 17, no. 1, pp. 62–73, Feb. 1989, doi: 10.1177/0310057X8901700113.

[12] S. Shah *et al.*, "Novel Use of Home Pulse Oximetry Monitoring in COVID-19 Patients Discharged From the Emergency Department Identifies Need for Hospitalization," *Acad. Emerg. Med. Off. J. Soc. Acad. Emerg. Med.*, vol. 27, no. 8, pp. 681–692, Aug. 2020, doi: 10.1111/acem.14053.

[13] C. Rodriguez, "Using pulse oximetry to monitor high-risk patients with COVID-19 at home," *Nursing (Lond.)*, vol. 50, no. 11, pp. 15–16, Nov. 2020, doi: 10.1097/01.NURSE.0000718376.94916.eb.

[14] R. M. Levitan, "Pulse Oximetry as a Biomarker for Early Identification and Hospitalization of COVID-19 Pneumonia," *Acad. Emerg. Med. Off. J. Soc. Acad. Emerg. Med.*, vol. 27, no. 8, pp. 785–786, Aug. 2020, doi: 10.1111/acem.14052.

[15] D. B. Gootenberg *et al.*, "Developing a pulse oximetry home monitoring protocol for patients suspected with COVID-19 after emergency department discharge," *BMJ Health Care Inform.*, vol. 28, no. 1, p. e100330, Jul. 2021, doi: 10.1136/bmjhci-2021-100330.

[16] J. N. Ngiam, N. W. S. Chew, C.-H. Sia, W. K.-F. Kong, and K. K. Poh, "Silent hypoxia: pulse oximetry and its relation to COVID-19 in Singapore," *Singapore Med. J.*, vol. 64, no. 4, p. 222, Sep. 2021, doi: 10.11622/smedj.2021134.

[17] K. E. J. Philip *et al.*, "Working accuracy of pulse oximetry in COVID-19 patients stepping down from intensive care: a clinical evaluation," *BMJ Open Respir. Res.*, vol. 7, no. 1, p. e000778, Dec. 2020, doi: 10.1136/bmjresp-2020-000778.

[18] T. Greenhalgh, M. Knight, M. Inda-Kim, N. J. Fulop, J. Leach, and C. Vindrola-Padros, "Remote management of covid-19 using home pulse oximetry and virtual ward support," *BMJ*, vol. 372, p. n677, Mar. 2021, doi: 10.1136/bmj.n677.

[19] V. Quaresima and M. Ferrari, “COVID-19: efficacy of prehospital pulse oximetry for early detection of silent hypoxemia,” *Crit. Care*, vol. 24, p. 501, Aug. 2020, doi: 10.1186/s13054-020-03185-x.
[20] P. Brouqui *et al.*, “Asymptomatic hypoxia in COVID-19 is associated with poor outcome,” *Int. J. Infect. Dis. IJID Off. Publ. Int. Soc. Infect. Dis.*, vol. 102, pp. 233–238, Jan. 2021, doi: 10.1016/j.ijid.2020.10.067.
[21] R. Cajanding, “Oxygen use and saturation targets in patients with COVID-19: Are we giving too much or aiming too low?,” *Nurs. Crit. Care*, vol. 27, no. 2, pp. 282–285, Mar. 2022, doi: 10.1111/nicc.12709.
[22] “Early Detection of Silent Hypoxia in Covid-19 Pneumonia Using Smartphone Pulse Oximetry - PMC.” Accessed: Nov. 07, 2024. [Online]. Available: https://pmc.ncbi.nlm.nih.gov/articles/PMC7305055/
[23] N. Wilson-Baig, T. McDonnell, and A. Bentley, “Discrepancy between SpO2 and SaO2 in patients with COVID-19,” *Anaesthesia*, vol. 76, no. Suppl 3, p. 6, Aug. 2020, doi: 10.1111/anae.15228.
[24] E. A. Lancet *et al.*, “Prehospital hypoxemia, measured by pulse oximetry, predicts hospital outcomes during the New York City COVID-19 pandemic,” *J. Am. Coll. Emerg. Physicians Open*, vol. 2, no. 2, p. e12407, Apr. 2021, doi: 10.1002/emp2.12407.
[25] A. Cysewska-Sobusiak, “Problems with evaluating readings of pulse oximeters used at home during the ongoing COVID-19 pandemic,” *Photonics Lett. Pol.*, vol. 13, p. 19, Mar. 2021, doi: 10.4302/plp.v13i1.1093.
[26] A. M. Luks and E. R. Swenson, “Pulse Oximetry for Monitoring Patients with COVID-19 at Home. Potential Pitfalls and Practical Guidance,” *Ann. Am. Thorac. Soc.*, vol. 17, no. 9, pp. 1040–1046, Sep. 2020, doi: 10.1513/AnnalsATS.202005-418FR.
[27] F. Michard, K. Shelley, and E. L’Her, “COVID-19: Pulse oximeters in the spotlight,” *J. Clin. Monit. Comput.*, vol. 35, no. 1, pp. 11–14, Feb. 2021, doi: 10.1007/s10877-020-00550-7.
[28] M. J. Tobin, F. Laghi, and A. Jubran, “Why COVID-19 Silent Hypoxemia Is Baffling to Physicians,” *Am. J. Respir. Crit. Care Med.*, vol. 202, no. 3, pp. 356–360, Aug. 2020, doi: 10.1164/rccm.202006-2157CP.
[29] Y. T. Wang and S. C. Poh, “Noninvasive oximetry in pigmented patients,” *Ann. Acad. Med. Singapore*, vol. 14, no. 3, pp. 427–429, Jul. 1985.
[30] M. R. Gabrielczyk and R. J. Buist, “Pulse oximetry and postoperative hypothermia. An evaluation of the Nellcor N-100 in a cardiac surgical intensive care unit,” *Anaesthesia*, vol. 43, no. 5, pp. 402–404, May 1988, doi: 10.1111/j.1365-2044.1988.tb09025.x.
[31] W. T. Cecil, K. J. Thorpe, E. E. Fibuch, and G. F. Tuohy, “A clinical evaluation of the accuracy of the Nellcor N-100 and Ohmeda 3700 pulse oximeters,” *J. Clin. Monit.*, vol. 4, no. 1, pp. 31–36, Jan. 1988, doi: 10.1007/BF01618105.
[32] A. L. Ries, L. M. Prewitt, and J. J. Johnson, “Skin color and ear oximetry,” *Chest*, vol. 96, no. 2, pp. 287–290, Aug. 1989, doi: 10.1378/chest.96.2.287.
[33] C. Cahan, M. J. Decker, P. L. Hoekje, and K. P. Strohl, “Agreement between noninvasive oximetric values for oxygen saturation,” *Chest*, vol. 97, no. 4, pp. 814–819, Apr. 1990, doi: 10.1378/chest.97.4.814.
[34] K. H. Lee, K. P. Hui, W. C. Tan, and T. K. Lim, “Factors influencing pulse oximetry as compared to functional arterial saturation in multi-ethnic Singapore,” *Singapore Med. J.*, vol. 34, no. 5, pp. 385–387, Oct. 1993.
[35] P. A. Bothma *et al.*, “Accuracy of pulse oximetry in pigmented patients,” *South Afr. Med. J. Suid-Afr. Tydskr. Vir Geneeskd.*, vol. 86, no. 5 Suppl, pp. 594–596, May 1996.
[36] J. N. Adler, L. A. Hughes, R. Vivilecchia, and C. A. Camargo, “Effect of skin pigmentation on pulse oximetry accuracy in the emergency department,” *Acad. Emerg. Med. Off. J. Soc. Acad. Emerg. Med.*, vol. 5, no. 10, pp. 965–970, Oct. 1998, doi: 10.1111/j.1553-2712.1998.tb02772.x.

[37] S. J. Ebmeier *et al.*, “A two centre observational study of simultaneous pulse oximetry and arterial oxygen saturation recordings in intensive care unit patients,” *Anaesth. Intensive Care*, vol. 46, no. 3, pp. 297–303, May 2018, doi: 10.1177/0310057X1804600307.
[38] M. D. Wiles *et al.*, “The effect of patient ethnicity on the accuracy of peripheral pulse oximetry in patients with COVID-19 pneumonitis: a single-centre, retrospective analysis,” *Anaesthesia*, vol. 77, no. 2, pp. 143–152, Feb. 2022, doi: 10.1111/anae.15581.
[39] E. E. Foglia *et al.*, “The Effect of Skin Pigmentation on the Accuracy of Pulse Oximetry in Infants with Hypoxemia,” *J. Pediatr.*, vol. 182, pp. 375-377.e2, Mar. 2017, doi: 10.1016/j.jpeds.2016.11.043.
[40] P. E. Bickler, J. R. Feiner, and J. W. Severinghaus, “Effects of skin pigmentation on pulse oximeter accuracy at low saturation,” *Anesthesiology*, vol. 102, no. 4, pp. 715–719, Apr. 2005, doi: 10.1097/00000542-200504000-00004.
[41] J. R. Feiner, J. W. Severinghaus, and P. E. Bickler, “Dark skin decreases the accuracy of pulse oximeters at low oxygen saturation: the effects of oximeter probe type and gender,” *Anesth. Analg.*, vol. 105, no. 6 Suppl, pp. S18–S23, Dec. 2007, doi: 10.1213/01.ane.0000285988.35174.d9.
[42] K. Baker *et al.*, “Performance of five pulse oximeters to detect hypoxaemia as an indicator of severe illness in children under five by frontline health workers in low resource settings - A prospective, multicentre, single-blinded, trial in Cambodia, Ethiopia, South Sudan, and Uganda,” *EClinicalMedicine*, vol. 38, p. 101040, Aug. 2021, doi: 10.1016/j.eclinm.2021.101040.
[43] A. Jubran and M. J. Tobin, “Reliability of pulse oximetry in titrating supplemental oxygen therapy in ventilator-dependent patients,” *Chest*, vol. 97, no. 6, pp. 1420–1425, Jun. 1990, doi: 10.1378/chest.97.6.1420.
[44] O. Dyer, “Pulse oximetry may underestimate hypoxaemia in black patients, study finds,” *BMJ*, vol. 371, p. m4926, Dec. 2020, doi: 10.1136/bmj.m4926.
[45] “Pulse Oximetry May Be Inaccurate in Patients with Darker Skin,” *Am. J. Nurs.*, vol. 121, no. 4, p. 16, Apr. 2021, doi: 10.1097/01.NAJ.0000742448.35686.f9.
[46] V. S. M. Valbuena *et al.*, “Racial Bias in Pulse Oximetry Measurement Among Patients About to Undergo Extracorporeal Membrane Oxygenation in 2019-2020: A Retrospective Cohort Study,” *Chest*, vol. 161, no. 4, pp. 971–978, Apr. 2022, doi: 10.1016/j.chest.2021.09.025.
[47] Z. Vesoulis, A. Tims, H. Lodhi, N. Lalos, and H. Whitehead, “Racial discrepancy in pulse oximeter accuracy in preterm infants,” *J. Perinatol. Off. J. Calif. Perinat. Assoc.*, vol. 42, no. 1, pp. 79–85, Jan. 2022, doi: 10.1038/s41372-021-01230-3.
[48] A.-K. I. Wong *et al.*, “Analysis of Discrepancies Between Pulse Oximetry and Arterial Oxygen Saturation Measurements by Race and Ethnicity and Association With Organ Dysfunction and Mortality,” *JAMA Netw. Open*, vol. 4, no. 11, p. e2131674, Nov. 2021, doi: 10.1001/jamanetworkopen.2021.31674.
[49] C. Shi *et al.*, “The accuracy of pulse oximetry in measuring oxygen saturation by levels of skin pigmentation: a systematic review and meta-analysis,” *BMC Med.*, vol. 20, no. 1, p. 267, Aug. 2022, doi: 10.1186/s12916-022-02452-8.
[50] M. J. Knight, C. P. Subbe, and M. Inada-Kim, “Racial discrepancies in oximetry: where do we stand?,” *Anaesthesia*, vol. 77, no. 2, pp. 129–131, Feb. 2022, doi: 10.1111/anae.15635.
[51] M. J. Tobin and A. Jubran, “Pulse oximetry, racial bias and statistical bias,” *Ann. Intensive Care*, vol. 12, p. 2, Jan. 2022, doi: 10.1186/s13613-021-00974-7.
[52] S. J. Barker and W. C. Wilson, “Racial effects on Masimo pulse oximetry: a laboratory study,” *J. Clin. Monit. Comput.*, vol. 37, no. 2, pp. 567–574, 2023, doi: 10.1007/s10877-022-00927-w.
[53] C. J. Crooks *et al.*, “Pulse oximeter measurements vary across ethnic groups: an observational study in patients with COVID-19,” *Eur. Respir. J.*, vol. 59, no. 4, p. 2103246, Apr. 2022, doi: 10.1183/13993003.03246-2021.

[54] O. E. Okunlola, M. S. Lipnick, P. B. Batchelder, M. Bernstein, J. R. Feiner, and P. E. Bickler, “Pulse Oximeter Performance, Racial Inequity, and the Work Ahead,” *Respir. Care*, vol. 67, no. 2, pp. 252–257, Feb. 2022, doi: 10.4187/respcare.09795.
[55] M. N. Bangash *et al.*, “Impact of ethnicity on the accuracy of measurements of oxygen saturations: A retrospective observational cohort study,” *EClinicalMedicine*, vol. 48, p. 101428, Jun. 2022, doi: 10.1016/j.eclinm.2022.101428.
[56] M. Hunasikatti, “Racial bias in accuracy of pulse oximetry and its impact on assessments of hypopnea and T90 in clinical studies,” *J. Clin. Sleep Med. JCSM Off. Publ. Am. Acad. Sleep Med.*, vol. 17, no. 5, p. 1145, May 2021, doi: 10.5664/jcsm.9178.
[57] K. E. J. Philip, R. Tidswell, and C. McFadyen, “Racial bias in pulse oximetry: more statistical detail may help tackle the problem,” *BMJ*, vol. 372, p. n298, Feb. 2021, doi: 10.1136/bmj.n298.
[58] A. C. Ralston, R. K. Webb, and W. B. Runciman, “Potential errors in pulse oximetry. III: Effects of interferences, dyes, dyshaemoglobins and other pigments,” *Anaesthesia*, vol. 46, no. 4, pp. 291–295, Apr. 1991, doi: 10.1111/j.1365-2044.1991.tb11501.x.
[59] T. Whitehead-Clarke, “More on Racial Bias in Pulse Oximetry Measurement,” *N. Engl. J. Med.*, vol. 384, no. 13, p. 1278, Apr. 2021, doi: 10.1056/NEJMc2101321.
[60] “More on Racial Bias in Pulse Oximetry Measurement,” *N. Engl. J. Med.*, vol. 384, no. 13, pp. 1278–1278, Mar. 2021, doi: 10.1056/NEJMc2101321.
[61] R. N. Smith and R. Hofmeyr, “Perioperative comparison of the agreement between a portable fingertip pulse oximeter v. a conventional bedside pulse oximeter in adult patients (COMFORT trial),” *South Afr. Med. J. Suid-Afr. Tydskr. Vir Geneeskd.*, vol. 109, no. 3, pp. 154–158, Feb. 2019, doi: 10.7196/SAMJ.2019.v109i3.13633.
[62] M. D. Witting and S. M. Scharf, “Diagnostic room-air pulse oximetry: effects of smoking, race, and sex,” *Am. J. Emerg. Med.*, vol. 26, no. 2, pp. 131–136, Feb. 2008, doi: 10.1016/j.ajem.2007.04.002.
[63] S. M. Murphy and S. Omar, “The Clinical Utility of Noninvasive Pulse Co-oximetry Hemoglobin Measurements in Dark-Skinned Critically Ill Patients,” *Anesth. Analg.*, vol. 126, no. 5, pp. 1519–1526, May 2018, doi: 10.1213/ANE.0000000000002721.
[64] J. L. Reuss, “Multilayer modeling of reflectance pulse oximetry,” *IEEE Trans. Biomed. Eng.*, vol. 52, no. 2, pp. 153–159, Feb. 2005, doi: 10.1109/TBME.2004.840188.
[65] K. Badgujar, A. Badgujar, D. Dhangar, and V. Badgujar, “Importance and use of pulse oximeter in COVID-19 pandemic: general factors affecting the sensitivity of pulse oximeter,” *Indian Chem. Eng.*, vol. 62, pp. 1–11, Nov. 2020, doi: 10.1080/00194506.2020.1845988.
[66] M. Ferrari, V. Quaresima, and F. Scholkmann, “Pulse oximetry, racial bias and statistical bias: further improvements of pulse oximetry are necessary,” *Ann. Intensive Care*, vol. 12, p. 19, Feb. 2022, doi: 10.1186/s13613-022-00992-z.
[67] A. Guber, G. Epstein Shochet, S. Kohn, and D. Shitrit, “Wrist-Sensor Pulse Oximeter Enables Prolonged Patient Monitoring in Chronic Lung Diseases,” *J. Med. Syst.*, vol. 43, no. 7, p. 230, Jun. 2019, doi: 10.1007/s10916-019-1317-2.
[68] D. Leasa, “Noninvasive blood gas monitoring: a review for use in the adult critical care unit. Technology Subcommittee of the Working Group on Critical Care, Ontario Ministry of Health.,” *CMAJ Can. Med. Assoc. J. J. Assoc. Medicale Can.*, 1992, Accessed: Feb. 26, 2025. [Online]. Available: https://www.semanticscholar.org/paper/Noninvasive-blood-gas-monitoring%3A-a-review-for-use-Leasa/334dc87024bc4355d6c33a1a34bf793bdabd1249
[69] A. L. Holder and A.-K. I. Wong, “The big consequences of small discrepancies: Why racial differences in pulse oximetry errors matter,” *Crit. Care Med.*, vol. 50, no. 2, p. 335, Feb. 2022, doi: 10.1097/CCM.0000000000005447.
[70] N. R. Henry *et al.*, “Disparities in Hypoxemia Detection by Pulse Oximetry Across Self-Identified Racial Groups and Associations With Clinical Outcomes,” *Crit. Care Med.*, vol. 50, no. 2, pp. 204–211, Feb. 2022, doi: 10.1097/CCM.0000000000005394.

[71] G. W. Burnett *et al.*, “Self-reported Race/Ethnicity and Intraoperative Occult Hypoxemia: A Retrospective Cohort Study,” *Anesthesiology*, vol. 136, no. 5, pp. 688–696, May 2022, doi: 10.1097/ALN.0000000000004153.
[72] A. Fawzy *et al.*, “Racial and Ethnic Discrepancy in Pulse Oximetry and Delayed Identification of Treatment Eligibility Among Patients With COVID-19,” *JAMA Intern. Med.*, vol. 182, no. 7, pp. 730–738, Jul. 2022, doi: 10.1001/jamainternmed.2022.1906.
[73] M. W. Sjoding, R. P. Dickson, T. J. Iwashyna, S. E. Gay, and T. S. Valley, “Racial Bias in Pulse Oximetry Measurement,” *N. Engl. J. Med.*, vol. 383, no. 25, pp. 2477–2478, Dec. 2020, doi: 10.1056/NEJMc2029240.
[74] G. A. Volgyesi and I. Spahr-Schopfer, “DOES SKIN PIGMENTATION AFFECT THE ACCURACY OF PULSE OXIMETRY? AN IN VITRO STUDY,” *Anesthesiology*, vol. 75, p. A406, 1991.
[75] H. Ruppel *et al.*, “Evaluating the Accuracy of Pulse Oximetry in Children According to Race,” *JAMA Pediatr.*, vol. 177, no. 5, pp. 540–543, May 2023, doi: 10.1001/jamapediatrics.2023.0071.
[76] F. Savorgnan, A. Hassan, N. Borges, and S. Acosta, “Pulse Oximetry and Arterial Saturation Difference in Pediatric COVID-19 Patients: Retrospective Analysis by Race*,” *Pediatr. Crit. Care Med.*, vol. 24, no. 6, pp. 458–462, Jun. 2023, doi: 10.1097/PCC.0000000000003208.
[77] M. Meira e Cruz, C. Zhou, M. H. Kryger, and H. Wang, “Validation of a Smart Ring Oximeter in Individuals With Dark Skin Pigment,” *Mayo Clin. Proc. Digit. Health*, vol. 1, no. 3, pp. 357–365, Sep. 2023, doi: 10.1016/j.mcpdig.2023.06.012.
[78] A. Fawzy *et al.*, “Skin Pigmentation and Pulse Oximeter Accuracy in the Intensive Care Unit: A Pilot Prospective Study,” *Am. J. Respir. Crit. Care Med.*, vol. 210, no. 3, pp. 355–358, Aug. 2024, doi: 10.1164/rccm.202401-0036LE.
[79] A. K. Khanna, J. Beard, S. Lamminmäki, J. Närväinen, N. Antaki, and H. O. Yapici, “Assessment of skin pigmentation-related bias in pulse oximetry readings among adults,” *J. Clin. Monit. Comput.*, vol. 38, no. 1, pp. 113–120, Feb. 2024, doi: 10.1007/s10877-023-01095-1.
[80] S. Hao *et al.*, “Utility of skin tone on pulse oximetry in critically ill patients: a prospective cohort study,” *medRxiv*, p. 2024.02.24.24303291, Feb. 2024, doi: 10.1101/2024.02.24.24303291.
[81] G. Leeb *et al.*, “The performance of 11 fingertip pulse oximeters during hypoxemia in healthy human participants with varied, quantified skin pigment,” *eBioMedicine*, vol. 102, Apr. 2024, doi: 10.1016/j.ebiom.2024.105051.
[82] S. Haxha *et al.*, “Effect of Skin Pigmentation and Finger Choice on Accuracy of Oxygen Saturation Measurement in an IoT-Based Pulse Oximeter,” *Sensors*, vol. 24, no. 11, Art. no. 11, Jan. 2024, doi: 10.3390/s24113301.
[83] G. Blaney, J. Frias, F. Tavakoli, A. Sassaroli, and S. Fantini, “Dual-ratio approach to pulse oximetry and the effect of skin tone,” *J. Biomed. Opt.*, vol. 29, no. S3, p. S33311, Oct. 2024, doi: 10.1117/1.JBO.29.S3.S33311.
[84] F. Azam, A. Roshan, and L. Siddiqui, “Pulse Oximeter And Different Skin Tones In Pakistan,” *JPMA J. Pak. Med. Assoc.*, vol. 73, no. 7, p. 1563, Jul. 2023, doi: 10.47391/JPMA.7899.
[85] O. M. P. Jolobe, “Defining the role of skin pigmentation in the accuracy of pulse oximetry in COVID-19 subjects receiving domiciliary oxygen supplementation,” *Am. J. Emerg. Med.*, vol. 68, p. 187, Jun. 2023, doi: 10.1016/j.ajem.2023.04.026.
[86] P. J. Maher, N. N. Goel, C. R. Horowitz, M. Rea, M. G. Figueiro, and L. D. Richardson, “Survey in emergency medicine of skin pigmentation bias in pulse oximeters,” *Am. J. Emerg. Med.*, vol. 79, pp. 209–211, May 2024, doi: 10.1016/j.ajem.2024.03.002.
[87] A. C. Argent, “Pulse Oximetry Bias and Skin Tone, What We Know, What We Need to Do About It,” *Pediatr. Crit. Care Med. J. Soc. Crit. Care Med. World Fed. Pediatr. Intensive Crit. Care Soc.*, vol. 25, no. 10, pp. 967–969, Oct. 2024, doi: 10.1097/PCC.0000000000003600.
[88] J. W. Jacobs and E. Abels, “The potential for unnecessary medical interventions due to inaccurate pulse oximetry measurements,” *Heart Lung J. Crit. Care*, vol. 58, pp. 238–239, 2023, doi: 10.1016/j.hrtlng.2022.09.016.

[89] J. J. Brownscombe, H. Loane, and B. Honan, “COVID-19 highlights the need for action on pulse oximeter accuracy in people with dark skin,” *Med. J. Aust.*, vol. 216, no. 10, p. 539, Jun. 2022, doi: 10.5694/mja2.51522.
[90] M. D. Keller, B. Harrison-Smith, C. Patil, and M. S. Arefin, “Skin colour affects the accuracy of medical oxygen sensors,” *Nature*, vol. 610, no. 7932, pp. 449–451, Oct. 2022, doi: 10.1038/d41586-022-03161-1.
[91] V. Sharma, S. J. Barker, J. Novak, and W. C. Wilson, “Pulse Oximetry Performance in Darkly Pigmented Skin: Methodological Concerns,” *Anesth. Analg.*, vol. 139, no. 6, pp. e62-64, Oct. 2024, doi: 10.1213/ANE.0000000000007224.
[92] M. Sharma *et al.*, “Racial and skin color mediated disparities in pulse oximetry in infants and young children,” *Paediatr. Respir. Rev.*, vol. 50, pp. 62–72, Jun. 2024, doi: 10.1016/j.prrv.2023.12.006.
[93] A. D. Pal, “Limitations in the Use of Pulse Oximetry in Patients of Color,” *J. Perianesth. Nurs.*, vol. 38, no. 6, pp. 943–944, Dec. 2023, doi: 10.1016/j.jopan.2023.08.018.
[94] A. W. Fogarty, C. Crooks, I. Adejumo, A. Binegdie, and D. Shaw, “Increasing awareness of the racial bias of pulse oximetry measurements in populations with darker skin,” *J. Pan Afr. Thorac. Soc.*, vol. 4, pp. 113–114, Sep. 2023, doi: 10.25259/JPATS_22_2023.
[95] A. Oza, “Fingertip oxygen sensors can fail on dark skin — now a physician is suing,” *Nature*, Jan. 2024, doi: 10.1038/d41586-024-00089-6.
[96] O. O. Nafiu, C. Mpody, S. S. Kim, J. C. Uffman, and J. D. Tobias, “Race, Postoperative Complications, and Death in Apparently Healthy Children,” *Pediatrics*, vol. 146, no. 2, p. e20194113, Aug. 2020, doi: 10.1542/peds.2019-4113.
[97] A. Jubran, “Pulse oximetry,” *Crit. Care Lond. Engl.*, vol. 19, no. 1, p. 272, Jul. 2015, doi: 10.1186/s13054-015-0984-8.
[98] “The use and regulation of pulse oximeters (information for healthcare professionals),” GOV.UK. Accessed: Nov. 08, 2024. [Online]. Available: https://www.gov.uk/guidance/the-use-and-regulation-of-pulse-oximeters-information-for-healthcare-professionals
[99] E. Austin *et al.*, “Visible Light Part I. Properties and Cutaneous Effects of Visible Light,” *J. Am. Acad. Dermatol.*, vol. 84, no. 5, pp. 1219–1231, May 2021, doi: 10.1016/j.jaad.2021.02.048.
[100] C. Ash, M. Dubec, K. Donne, and T. Bashford, “Effect of wavelength and beam width on penetration in light-tissue interaction using computational methods,” *Lasers Med. Sci.*, vol. 32, no. 8, pp. 1909–1918, 2017, doi: 10.1007/s10103-017-2317-4.
[101] M. Nitzan, A. Romem, and R. Koppel, “Pulse oximetry: fundamentals and technology update,” *Med. Devices Auckl. NZ*, vol. 7, pp. 231–239, Jul. 2014, doi: 10.2147/MDER.S47319.
[102] T. A. Henderson and L. D. Morries, “Near-infrared photonic energy penetration: can infrared phototherapy effectively reach the human brain?,” *Neuropsychiatr. Dis. Treat.*, vol. 11, pp. 2191–2208, Aug. 2015, doi: 10.2147/NDT.S78182.
[103] H. Zhang, D. Salo, D. M. Kim, S. Komarov, Y.-C. Tai, and M. Y. Berezin, “Penetration depth of photons in biological tissues from hyperspectral imaging in shortwave infrared in transmission and reflection geometries,” *J. Biomed. Opt.*, vol. 21, no. 12, p. 126006, Dec. 2016, doi: 10.1117/1.JBO.21.12.126006.
[104] H. Woerdman, “Reflection revisited,” Jun. 2009. [Online]. Available: https://www.nature.com/articles/nphoton.2009.91.pdf
[105] R. S. Fishman, “Perish, Then Publish: Thomas Harriot and the Sine Law of Refraction,” *Arch. Ophthalmol.*, vol. 118, no. 3, pp. 405–409, Mar. 2000, doi: 10.1001/archopht.118.3.405.
[106] E. Hecht, *Optics*, 5 ed. Boston: Pearson Education, Inc, 2017.
[107] I. Oshina and J. Spigulis, “Beer–Lambert law for optical tissue diagnostics: current state of the art and the main limitations,” *J. Biomed. Opt.*, vol. 26, no. 10, p. 100901, Oct. 2021, doi: 10.1117/1.JBO.26.10.100901.
[108] R. Splinter and B. A. Hooper, *An Introduction to Biomedical Optics*. Taylor & Francis, 2006.

[109] K. Jansen, M. Wu, A. F. W. van der Steen, and G. van Soest, “Photoacoustic imaging of human coronary atherosclerosis in two spectral bands,” *Photoacoustics*, vol. 2, no. 1, pp. 12–20, Mar. 2014, doi: 10.1016/j.pacs.2013.11.003.
[110] D. T. Delpy, M. Cope, P. van der Zee, S. Arridge, S. Wray, and J. Wyatt, “Estimation of optical pathlength through tissue from direct time of flight measurement,” *Phys. Med. Biol.*, vol. 33, no. 12, pp. 1433–1442, Dec. 1988, doi: 10.1088/0031-9155/33/12/008.
[111] L. G. Henyey and J. L. Greenstein, “Diffuse radiation in the galaxy.” 1941.
[112] S. Batool, M. Nisar, F. Mangini, F. Frezza, and E. Fazio, “Scattering of Light from the Systemic Circulatory System,” *Diagnostics*, vol. 10, no. 12, p. 1026, Nov. 2020, doi: 10.3390/diagnostics10121026.
[113] M. D. Humzah, “Tyndall, Rayleigh, Mei, and Raman scattering: Understanding their role in aesthetics,” *J. Cosmet. Dermatol.*, vol. 23, no. 11, pp. 3493–3496, Nov. 2024, doi: 10.1111/jocd.16470.
[114] P. P. Naik and S. N. Farrukh, “Influence of Ethnicities and Skin Color Variations in Different Populations: A Review,” *Skin Pharmacol. Physiol.*, vol. 35, no. 2, pp. 65–76, 2022, doi: 10.1159/000518826.
[115] T. Hida *et al.*, “Elucidation of Melanogenesis Cascade for Identifying Pathophysiology and Therapeutic Approach of Pigmentary Disorders and Melanoma,” *Int. J. Mol. Sci.*, vol. 21, no. 17, Art. no. 17, Jan. 2020, doi: 10.3390/ijms21176129.
[116] T. H. Nasti and L. Timares, “Invited Review MC1R, Eumelanin and Pheomelanin: their role in determining the susceptibility to skin cancer,” *Photochem. Photobiol.*, vol. 91, no. 1, pp. 188–200, Jan. 2015, doi: 10.1111/php.12335.
[117] L. Bento-Lopes, L. C. Cabaço, J. Charneca, M. V. Neto, M. C. Seabra, and D. C. Barral, “Melanin’s Journey from Melanocytes to Keratinocytes: Uncovering the Molecular Mechanisms of Melanin Transfer and Processing,” *Int. J. Mol. Sci.*, vol. 24, no. 14, Art. no. 14, Jan. 2023, doi: 10.3390/ijms241411289.
[118] M. I. Koster, “Making an epidermis,” *Ann. N. Y. Acad. Sci.*, vol. 1170, pp. 7–10, Jul. 2009, doi: 10.1111/j.1749-6632.2009.04363.x.
[119] A. V. Rawlings, “Ethnic skin types: are there differences in skin structure and function?,” *Int. J. Cosmet. Sci.*, vol. 28, no. 2, pp. 79–93, Apr. 2006, doi: 10.1111/j.1467-2494.2006.00302.x.
[120] K. Toda, M. A. Pathak, J. A. Parrish, T. B. Fitzpatrick, and W. C. Quevedo, “Alteration of racial differences in melanosome distribution in human epidermis after exposure to ultraviolet light,” *Nature. New Biol.*, vol. 236, no. 66, pp. 143–145, Apr. 1972, doi: 10.1038/newbio236143a0.
[121] G. Szabó, A. B. Gerald, M. A. Pathak, and T. B. Fitzpatrick, “Racial differences in the fate of melanosomes in human epidermis,” *Nature*, vol. 222, no. 5198, pp. 1081–1082, Jun. 1969, doi: 10.1038/2221081a0.
[122] B. L. Johnson, R. L. Moy, and G. M. White, *Ethnic Skin: Medical and Surgical*. Mosby, 1998.
[123] B. Jothishankar and S. L. Stein, “Impact of skin color and ethnicity,” *Clin. Dermatol.*, vol. 37, no. 5, pp. 418–429, Sep. 2019, doi: 10.1016/j.clindermatol.2019.07.009.
[124] J. Ancans, D. J. Tobin, M. J. Hoogduijn, N. P. Smit, K. Wakamatsu, and A. J. Thody, “Melanosomal pH controls rate of melanogenesis, eumelanin/phaeomelanin ratio and melanosome maturation in melanocytes and melanoma cells,” *Exp. Cell Res.*, vol. 268, no. 1, pp. 26–35, Aug. 2001, doi: 10.1006/excr.2001.5251.
[125] H. Watabe *et al.*, “Regulation of tyrosinase processing and trafficking by organellar pH and by proteasome activity,” *J. Biol. Chem.*, vol. 279, no. 9, pp. 7971–7981, Feb. 2004, doi: 10.1074/jbc.M309714200.
[126] B. B. Fuller, D. T. Spaulding, and D. R. Smith, “Regulation of the catalytic activity of preexisting tyrosinase in black and Caucasian human melanocyte cell cultures,” *Exp. Cell Res.*, vol. 262, no. 2, pp. 197–208, Jan. 2001, doi: 10.1006/excr.2000.5092.
[127] Y. Mantri and J. V. Jokerst, “Impact of skin tone on photoacoustic oximetry and tools to minimize bias,” *Biomed. Opt. Express*, vol. 13, no. 2, p. 875, Jan. 2022, doi: 10.1364/BOE.450224.

[128] J. E. Fitzpatrick, W. A. High, and W. L. Kyle, “Chapter 27 - Discolorations of the Skin,” in *Urgent Care Dermatology: Symptom-Based Diagnosis*, J. E. Fitzpatrick, W. A. High, and W. L. Kyle, Eds., Elsevier, 2018, pp. 441–460. doi: 10.1016/B978-0-323-48553-1.00027-6.
[129] “Skin Optics Summary.” Accessed: Jul. 17, 2023. [Online]. Available: https://omlc.org/news/jan98/skinoptics.html
[130] N. Ahmad, H. Alqahtani, S. Al-Terary, A. Laref, and A. Haseeb, “Control of optical absorption and fluorescence spectroscopies of natural melanin at different solution concentrations,” *Opt. Quantum Electron.*, vol. 51, Jun. 2019, doi: 10.1007/s11082-019-1936-3.
[131] C. So-Ling and L. Li, “A multi-layered reflection model of natural human skin,” in *Proceedings. Computer Graphics International 2001*, Jul. 2001, pp. 249–256. doi: 10.1109/CGI.2001.934681.
[132] opencriticalcare.org, “Skin pigmentation Archives,” Open Critical Care. Accessed: Nov. 14, 2024. [Online]. Available: https://opencriticalcare.org/faq-category/skin/
[133] A. N. Sharma and B. C. Patel, “Laser Fitzpatrick Skin Type Recommendations,” in *StatPearls*, Treasure Island (FL): StatPearls Publishing, 2024. Accessed: Nov. 28, 2024. [Online]. Available: http://www.ncbi.nlm.nih.gov/books/NBK557626/
[134] M. Langeveld, L. S. van de Lande, E. O’ Sullivan, B. van der Lei, and J. A. van Dongen, “Skin measurement devices to assess skin quality: A systematic review on reliability and validity,” *Skin Res. Technol.*, vol. 28, no. 2, pp. 212–224, 2022, doi: 10.1111/srt.13113.
[135] M. Wilkes, C. Y. Wright, J. L. du Plessis, and A. Reeder, “Fitzpatrick Skin Type, Individual Typology Angle, and Melanin Index in an African Population: Steps Toward Universally Applicable Skin Photosensitivity Assessments,” *JAMA Dermatol.*, vol. 151, no. 8, pp. 902–903, Aug. 2015, doi: 10.1001/jamadermatol.2015.0351.
[136] S. Y. He, C. E. McCulloch, W. J. Boscardin, M.-M. Chren, E. Linos, and S. T. Arron, “Self-Reported Pigmentary Phenotypes and Race are Significant but Incomplete Predictors of Fitzpatrick Skin Phototype in an Ethnically Diverse Population,” *J. Am. Acad. Dermatol.*, vol. 71, no. 4, p. 731, Jun. 2014, doi: 10.1016/j.jaad.2014.05.023.
[137] L. K. Pershing *et al.*, “Reflectance spectrophotometer: the dermatologists’ sphygmomanometer for skin phototyping?,” *J. Invest. Dermatol.*, vol. 128, no. 7, pp. 1633–1640, Jul. 2008, doi: 10.1038/sj.jid.5701238.
[138] A. Treesirichod, S. Chansakulporn, and P. Wattanapan, “Correlation Between Skin Color Evaluation by Skin Color Scale Chart and Narrowband Reflectance Spectrophotometer,” *Indian J. Dermatol.*, vol. 59, no. 4, pp. 339–342, 2014, doi: 10.4103/0019-5154.135476.
[139] H. E. MCCREATH *et al.*, “Use of Munsell Color Charts to Measure Skin Tone Objectively in Nursing Home Residents at Risk for Pressure Ulcer Development,” *J. Adv. Nurs.*, vol. 72, no. 9, pp. 2077–2085, Sep. 2016, doi: 10.1111/jan.12974.
[140] S. Mosca and A. Morrone, “Human Skin Pigmentation: From a Biological Feature to a Social Determinant,” *Healthcare*, vol. 11, no. 14, Art. no. 14, Jan. 2023, doi: 10.3390/healthcare11142091.
[141] L. Gevaux, “3D-hyperspectral imaging and optical analysis of skin for the human face,” phdthesis, Université de Lyon, 2019. Accessed: Nov. 29, 2024. [Online]. Available: https://theses.hal.science/tel-02881115
[142] J. W. Severinghaus, “ARTERIAL BLOOD GASES,” in *Encyclopedia of Respiratory Medicine*, Academic Press, 2006, pp. 144–150.
[143] J. G. Webster, Ed., *Design of Pulse Oximeters*. Boca Raton: CRC Press, 1997. doi: 10.1201/9780367802592.
[144] J. T. B. Moyle, *Principles and Practice Series: Pulse Oximetry*. BMJ Publishing Group, 1994.
[145] P. D. Mannheimer, M. E. Fein, and J. R. Casciani, “Physio-optical considerations in the design of fetal pulse oximetry sensors,” *Eur. J. Obstet. Gynecol. Reprod. Biol.*, vol. 72 Suppl, pp. S9-19, Mar. 1997, doi: 10.1016/s0301-2115(97)02713-9.
[146] M. Nitzan, I. Nitzan, and Y. Arieli, “The Various Oximetric Techniques Used for the Evaluation of Blood Oxygenation,” *Sensors*, vol. 20, no. 17, p. 4844, Aug. 2020, doi: 10.3390/s20174844.

[147] A. Bashkatov *et al.*, “Optical properties of melanin in the skin and skinlike phantoms,” *Proc. SPIE - Int. Soc. Opt. Eng.*, vol. 4162, Nov. 2000, doi: 10.1117/12.405946.
[148] G. Zonios, J. Bykowski, and N. Kollias, “Skin melanin, hemoglobin, and light scattering properties can be quantitatively assessed in vivo using diffuse reflectance spectroscopy,” *J. Invest. Dermatol.*, vol. 117, no. 6, pp. 1452–1457, Dec. 2001, doi: 10.1046/j.0022-202x.2001.01577.x.
[149] J. R. Feiner, M. D. Rollins, J. W. Sall, H. Eilers, P. Au, and P. E. Bickler, “Accuracy of carboxyhemoglobin detection by pulse CO-oximetry during hypoxemia,” *Anesth. Analg.*, vol. 117, no. 4, pp. 847–858, Oct. 2013, doi: 10.1213/ANE.0b013e31828610a0.
[150] C. J. Coté, E. A. Goldstein, W. H. Fuchsman, and D. C. Hoaglin, “The effect of nail polish on pulse oximetry,” *Anesth. Analg.*, vol. 67, no. 7, pp. 683–686, Jul. 1988.
[151] G. Hakverdioğlu Yönt, E. Akin Korhan, and B. Dizer, “The effect of nail polish on pulse oximetry readings,” *Intensive Crit. Care Nurs.*, vol. 30, no. 2, pp. 111–115, Apr. 2014, doi: 10.1016/j.iccn.2013.08.003.
[152] H. Sütçü Çiçek *et al.*, “Effect of nail polish and henna on oxygen saturation determined by pulse oximetry in healthy young adult females,” *Emerg. Med. J. EMJ*, vol. 28, no. 9, pp. 783–785, Sep. 2011, doi: 10.1136/emj.2010.096073.
[153] K. Balaraman *et al.*, “1167: EFFECT OF NAIL POLISH ON OXYGEN SATURATION READINGS,” *Crit. Care Med.*, vol. 48, no. 1, p. 561, Jan. 2020, doi: 10.1097/01.ccm.0000643592.11619.5c.
[154] A. M. Rodden, L. Spicer, V. A. Diaz, and T. E. Steyer, “Does fingernail polish affect pulse oximeter readings?,” *Intensive Crit. Care Nurs.*, vol. 23, no. 1, pp. 51–55, Feb. 2007, doi: 10.1016/j.iccn.2006.08.006.
[155] L. G. Yamamoto, J. A. Yamamoto, J. B. Yamamoto, B. E. Yamamoto, and P. P. Yamamoto, “Nail polish does not significantly affect pulse oximetry measurements in mildly hypoxic subjects,” *Respir. Care*, vol. 53, no. 11, pp. 1470–1474, Nov. 2008.
[156] A. M. Mathes, S. Kreuer, S. O. Schneider, S. Ziegeler, and U. Grundmann, “The performance of six pulse oximeters in the environment of neuronavigation,” *Anesth. Analg.*, vol. 107, no. 2, pp. 541–544, Aug. 2008, doi: 10.1213/ane.0b013e31817e6778.
[157] T. E. Schulte, J. R. Ohnoutka, and A. Agrawal, “BrainLAB interference with pulse oximetry during stereotactic brain biopsy,” *J. Clin. Anesth.*, vol. 24, no. 8, p. 675, Dec. 2012, doi: 10.1016/j.jclinane.2012.03.010.
[158] J. Saito, M. Kitayama, R. Kato, and K. Hirota, “Interference with pulse oximetry by the Stealth Station™ Image Guidance System,” *JA Clin. Rep.*, vol. 3, no. 1, p. 6, 2017, doi: 10.1186/s40981-017-0076-7.
[159] C. F. Poets and V. A. Stebbens, “Detection of movement artifact in recorded pulse oximeter saturation,” *Eur. J. Pediatr.*, vol. 156, no. 10, pp. 808–811, Oct. 1997, doi: 10.1007/s004310050719.
[160] G. W. J. Clarke, A. D. C. Chan, and A. Adler, “Effects of motion artifact on the blood oxygen saturation estimate in pulse oximetry,” in *2014 IEEE International Symposium on Medical Measurements and Applications (MeMeA)*, Jun. 2014, pp. 1–4. doi: 10.1109/MeMeA.2014.6860071.
[161] M. T. Petterson, V. L. Begnoche, and J. M. Graybeal, “The effect of motion on pulse oximetry and its clinical significance,” *Anesth. Analg.*, vol. 105, no. 6 Suppl, pp. S78–S84, Dec. 2007, doi: 10.1213/01.ane.0000278134.47777.a5.
[162] P. Banik, S. Hossain, T.-H. Kwon, H. Kim, and K.-D. Kim, “Development of a Wearable Reflection-Type Pulse Oximeter System to Acquire Clean PPG Signals and Measure Pulse Rate and SpO2 with and without Finger Motion,” *Electronics*, vol. 9, p. 1905, Nov. 2020, doi: 10.3390/electronics9111905.
[163] P. J. Chacon *et al.*, “A Wearable Pulse Oximeter With Wireless Communication and Motion Artifact Tailoring for Continuous Use,” *IEEE Trans. Biomed. Eng.*, vol. 66, no. 6, pp. 1505–1513, Jun. 2019, doi: 10.1109/TBME.2018.2874885.

[164] A. Louie, J. R. Feiner, P. E. Bickler, L. Rhodes, M. Bernstein, and J. Lucero, “Four Types of Pulse Oximeters Accurately Detect Hypoxia during Low Perfusion and Motion,” *Anesthesiology*, vol. 128, no. 3, pp. 520–530, Mar. 2018, doi: 10.1097/ALN.0000000000002002.
[165] J. M. Goldman, M. T. Petterson, R. J. Kopotic, and S. J. Barker, “Masimo signal extraction pulse oximetry,” *J. Clin. Monit. Comput.*, vol. 16, no. 7, pp. 475–483, 2000, doi: 10.1023/a:1011493521730.
[166] T. Ishiyama *et al.*, “The effects of Patent Blue dye on peripheral and cerebral oxyhaemoglobin saturations,” *Anaesthesia*, vol. 70, no. 4, pp. 429–433, Apr. 2015, doi: 10.1111/anae.12932.
[167] K. Sriganesh, B. Vinay, and V. Bhadrinarayan, “Indocyanine green dye administration can cause oxygen desaturation,” *J. Clin. Monit. Comput.*, vol. 27, no. 3, pp. 371–371, Jun. 2013, doi: 10.1007/s10877-012-9423-4.
[168] P. A. Ross, C. J. L. Newth, and R. G. Khemani, “Accuracy of pulse oximetry in children,” *Pediatrics*, vol. 133, no. 1, pp. 22–29, Jan. 2014, doi: 10.1542/peds.2013-1760.
[169] W. T. Mahle *et al.*, “Role of pulse oximetry in examining newborns for congenital heart disease: a scientific statement from the American Heart Association and American Academy of Pediatrics,” *Circulation*, vol. 120, no. 5, pp. 447–458, Aug. 2009, doi: 10.1161/CIRCULATIONAHA.109.192576.
[170] R. J. Rosychuk, A. Hudson-Mason, D. Eklund, and T. Lacaze-Masmonteil, “Discrepancies between arterial oxygen saturation and functional oxygen saturation measured with pulse oximetry in very preterm infants,” *Neonatology*, vol. 101, no. 1, pp. 14–19, 2012, doi: 10.1159/000326797.
[171] R. Chen *et al.*, “Monte Carlo simulation of cutaneous reflectance and fluorescence measurements – The effect of melanin contents and localization,” *J. Photochem. Photobiol. B*, vol. 86, no. 3, pp. 219–226, Mar. 2007, doi: 10.1016/j.jphotobiol.2006.11.001.
[172] P. D. Cook, J. N. Bixler, R. J. Thomas, and E. A. Early, “Prediction of tissue optical properties using the Monte Carlo modeling of photon transport in turbid media and integrating spheres,” *OSA Contin.*, vol. 3, no. 6, pp. 1456–1476, Jun. 2020, doi: 10.1364/OSAC.377805.
[173] S. Chatterjee and P. A. Kyriacou, “Monte Carlo Analysis of Optical Interactions in Reflectance and Transmittance Finger Photoplethysmography,” *Sensors*, vol. 19, no. 4, p. 789, Feb. 2019, doi: 10.3390/s19040789.
[174] I. Meglinski and A. Doronin, “Monte Carlo Modeling of Photon Migration for the Needs of Biomedical Optics and Biophotonics,” in *Advanced Biophotonics: Tissue Optical Sectioning*, 2012, pp. 1–72. doi: 10.1201/b15256-2.
[175] D. J. Durian and J. Rudnick, “Photon migration at short times and distances and in cases of strong absorption,” *JOSA A*, vol. 14, no. 1, pp. 235–245, Jan. 1997, doi: 10.1364/JOSAA.14.000235.
[176] C. Zhu and Q. Liu, “Review of Monte Carlo modeling of light transport in tissues,” *J. Biomed. Opt.*, vol. 18, no. 5, p. 050902, May 2013, doi: 10.1117/1.JBO.18.5.050902.
[177] I. Krasnikov, A. Seteikin, and B. Roth, “Advances in the simulation of light–tissue interactions in biomedical engineering,” *Biomed. Eng. Lett.*, vol. 9, no. 3, pp. 327–337, Jul. 2019, doi: 10.1007/s13534-019-00123-x.
[178] E. Nikolaidis, V. Pandey, and Z. Mourelatos, “Managing the Computational Cost in a Monte Carlo Simulation by Considering the Value of Information,” SAE International, Warrendale, PA, SAE Technical Paper 2012-01–0915, Apr. 2012. doi: 10.4271/2012-01-0915.
[179] Z. Klanecek, R. Hren, U. Simončič, B. T. Muc, M. Lukač, and M. Milanič, “Finite Element Method (FEM) Modeling of Laser-Tissue Interaction during Hair Removal,” *Appl. Sci.*, vol. 13, no. 14, Art. no. 14, Jan. 2023, doi: 10.3390/app13148553.
[180] H.-J. Kim *et al.*, “Laser–tissue interaction simulation considering skin-specific data to predict photothermal damage lesions during laser irradiation,” *J. Comput. Des. Eng.*, vol. 10, no. 3, pp. 947–958, Jun. 2023, doi: 10.1093/jcde/qwad033.

[181] J. Jiang *et al.*, "Validation and Comparison of Monte Carlo and Finite Element Method in Forward Modeling for Near Infrared Optical Tomography," in *Oxygen Transport to Tissue XLI*, P.-D. Ryu, J. C. LaManna, D. K. Harrison, and S.-S. Lee, Eds., Cham: Springer International Publishing, 2020, pp. 307–313. doi: 10.1007/978-3-030-34461-0_39.

[182] N. Ortega-Quijano, O. G. Romanov, F. Fanjul-Vélez, I. Salas-García, A. L. Tolstik, and J. L. Arce-Diego, "Numerical modeling of light propagation in biological tissues: time-resolved 3D simulations based on light diffusion model and FDTD solution of Maxwell's equations," in *Diffuse Optical Imaging III (2011), paper 80881R*, Optica Publishing Group, May 2011, p. 80881R. doi: 10.1364/ECBO.2011.80881R.

[183] A. H. Hielscher, R. E. Alcouffe, and R. L. Barbour, "Comparison of finite-difference transport and diffusion calculations for photon migration in homogeneous and heterogeneous tissues," *Phys. Med. Biol.*, vol. 43, no. 5, pp. 1285–1302, May 1998, doi: 10.1088/0031-9155/43/5/017.

[184] Y. Zhao, A. Raghuram, H. K. Kim, A. H. Hielscher, J. T. Robinson, and A. Veeraraghavan, "High Resolution, Deep Imaging Using Confocal Time-of-flight Diffuse Optical Tomography," *IEEE Trans. Pattern Anal. Mach. Intell.*, vol. 43, no. 7, pp. 2206–2219, Jul. 2021, doi: 10.1109/TPAMI.2021.3075366.

[185] V. Venugopalan, J. S. You, and B. J. Tromberg, "Radiative transport in the diffusion approximation: An extension for highly absorbing media and small source-detector separations," *Phys. Rev. E*, vol. 58, no. 2, pp. 2395–2407, Aug. 1998, doi: 10.1103/PhysRevE.58.2395.

[186] V. Quaresima, F. Scholkmann, and M. Ferrari, "Skin pigmentation bias in regional brain oximetry measurements?," *Crit. Care Lond. Engl.*, vol. 27, no. 1, p. 10, Jan. 2023, doi: 10.1186/s13054-022-04295-4.

[187] X. Sun, J. Ellis, P. J. Corso, P. C. Hill, F. Chen, and J. Lindsay, "Skin pigmentation interferes with the clinical measurement of regional cerebral oxygen saturation," *Br. J. Anaesth.*, vol. 114, no. 2, pp. 276–280, Feb. 2015, doi: 10.1093/bja/aeu335.

[188] A. Afshari *et al.*, "Evaluation of the robustness of cerebral oximetry to variations in skin pigmentation using a tissue-simulating phantom," *Biomed. Opt. Express*, vol. 13, no. 5, pp. 2909–2928, Apr. 2022, doi: 10.1364/BOE.454020.

[189] X. Huang, M. D. Protheroe, A. M. Al-Jumaily, A. N. Chalmers, S. P. Paul, and X. Fu, "Simulation of UV power absorbed by follicular stem cells during sun exposure and possible implications for melanoma development," *JOSA A*, vol. 36, no. 4, pp. 628–635, Apr. 2019, doi: 10.1364/JOSAA.36.000628.

[190] J. Zhao, H. Lui, D. I. McLean, and H. Zeng, "Chapter 12 - Rapid Real-Time Raman Spectroscopy and Imaging-Guided Confocal Raman Spectroscopy for In Vivo Skin Evaluation and Diagnosis," in *Imaging in Dermatology*, M. R. Hamblin, P. Avci, and G. K. Gupta, Eds., Boston: Academic Press, 2016, pp. 119–139. doi: 10.1016/B978-0-12-802838-4.00012-1.

[191] S. Chatterjee, K. Budidha, and P. A. Kyriacou, "Investigating the origin of photoplethysmography using a multiwavelength Monte Carlo model," *Physiol. Meas.*, vol. 41, no. 8, p. 084001, Sep. 2020, doi: 10.1088/1361-6579/aba008.

[192] I. V. Meglinskii, "Monte Carlo simulation of reflection spectra of random multilayer media strongly scattering and absorbing light," *Quantum Electron.*, vol. 31, no. 12, p. 1101, Dec. 2001, doi: 10.1070/QE2001v031n12ABEH002108.

[193] Z. X. Ying, Y. B. Zhao, D. Li, Y. L. Shang, B. Chen, and W. C. Jia, "The influence of morphological distribution of melanin on parameter selection in laser thermotherapy for vascular skin diseases," *Lasers Med. Sci.*, vol. 35, no. 4, pp. 901–917, Jun. 2020, doi: 10.1007/s10103-019-02882-6.

[194] T. Maeda, N. Arakawa, M. Takahashi, and Y. Aizu, "Monte Carlo simulation of spectral reflectance using a multilayered skin tissue model," *Opt. Rev.*, vol. 17, no. 3, pp. 223–229, May 2010, doi: 10.1007/s10043-010-0040-5.

[195] R. Akaho, M. Hirose, N. Ojima, T. Igarashi, and N. Tsumura, “Component analysis and synthesis of dark circles under the eyes using a spectral image,” in *Proceedings of SPIE - The International Society for Optical Engineering*, San Francisco, California, United States, Feb. 2017.
[196] L. Quintanar, D. Fabila, S. Stolik, and J. M. de la Rosa, “An irradiation system for photodynamic therapy with a fiber-optic sensor for measuring tissue oxygen,” in *8th Iberoamerican Optics Meeting and 11th Latin American Meeting on Optics, Lasers, and Applications*, SPIE, Nov. 2013, pp. 1457–1464. doi: 10.1117/12.2021715.
[197] A. E. Karsten and A. Singh, “Quantifying the influence of the epidermal optical properties on laser treatment parameters,” in *Medical Laser Applications and Laser-Tissue Interactions VI (2013), paper 88030J*, Optica Publishing Group, May 2013, p. 88030J. Accessed: Feb. 10, 2025. [Online]. Available: https://opg.optica.org/abstract.cfm?uri=ECBO-2013-88030J
[198] P. Ghassemi, Q. Wang, and T. J. Pfefer, “Dynamic thermal effects of epidermal melanin and plasmonic nanoparticles during photoacoustic breast imaging,” in *Design and Quality for Biomedical Technologies IX*, SPIE, Mar. 2016, pp. 82–90. doi: 10.1117/12.2214870.
[199] H. Liu, M. Kohl-Bareis, and X. Huang, “Design of a tissue oxygenation monitor and verification on human skin,” vol. 8087, p. 80871Y, Jul. 2011, doi: 10.1117/12.889197.
[200] C.-T. Chen, S.-H. Tseng, B.-H. Sung, Y.-Y. Chen, and H.-C. Cheng, “Noninvasive transcutaneous bilirubin measurement in adults using skin diffuse reflectance,” *Biomed. Opt. Express*, vol. 14, no. 10, pp. 5405–5417, Oct. 2023, doi: 10.1364/BOE.500833.
[201] J. Fine, M. J. McShane, G. L. Coté, and C. G. Scully, “A Computational Modeling and Simulation Workflow to Investigate the Impact of Patient-Specific and Device Factors on Hemodynamic Measurements from Non-Invasive Photoplethysmography,” *Biosensors*, vol. 12, no. 8, p. 598, Aug. 2022, doi: 10.3390/bios12080598.
[202] C. M. Robbins, S. Tabassum, M. F. Baumhauer, J. Yang, J. F. Antaki, and J. M. Kainerstorfer, “Two-layer spatial frequency domain imaging of compression-induced hemodynamic changes in breast tissue,” *J. Biomed. Opt.*, vol. 26, no. 5, p. 056005, May 2021, doi: 10.1117/1.JBO.26.5.056005.
[203] J. A. Swearingen, S. H. Holan, M. M. Feldman, and J. A. Viator, “Photoacoustic discrimination of vascular and pigmented lesions using classical and Bayesian methods,” *J. Biomed. Opt.*, vol. 15, no. 1, p. 016019, 2010, doi: 10.1117/1.3316297.
[204] Ajmal, T. Boonya-Ananta, A. J. Rodriguez, V. N. Du Le, and J. C. Ramella-Roman, “Monte Carlo analysis of optical heart rate sensors in commercial wearables: the effect of skin tone and obesity on the photoplethysmography (PPG) signal,” *Biomed. Opt. Express*, vol. 12, no. 12, pp. 7445–7457, Nov. 2021, doi: 10.1364/BOE.439893.
[205] M. Denstedt, A. Bjorgan, M. Milanič, and L. L. Randeberg, “Wavelet based feature extraction and visualization in hyperspectral tissue characterization,” *Biomed. Opt. Express*, vol. 5, no. 12, pp. 4260–4280, Dec. 2014, doi: 10.1364/BOE.5.004260.
[206] N. Verdel, A. Marin, M. Milanič, and B. Majaron, “Physiological and structural characterization of human skin in vivo using combined photothermal radiometry and diffuse reflectance spectroscopy,” *Biomed. Opt. Express*, vol. 10, no. 2, pp. 944–960, Feb. 2019, doi: 10.1364/BOE.10.000944.
[207] M. Althobaiti, “In Silico Investigation of SNR and Dermis Sensitivity for Optimum Dual-Channel Near-Infrared Glucose Sensor Designs for Different Skin Colors,” *Biosensors*, vol. 12, no. 10, Art. no. 10, Oct. 2022, doi: 10.3390/bios12100805.
[208] M. Reiser, O. Amft, and A. Breidenassel, “Analysis of Melanin Concentration on Reflective Pulse Oximetry Using Monte Carlo Simulations,” IEEE, Feb. 2025, pp. 24454–24462.
[209] T. R. Else, L. Hacker, J. Gröhl, E. V. Bunce, R. Tao, and S. E. Bohndiek, “Effects of skin tone on photoacoustic imaging and oximetry,” *J. Biomed. Opt.*, vol. 29, no. Suppl 1, p. S11506, Jan. 2024, doi: 10.1117/1.JBO.29.S1.S11506.

[210] I. Nishidate, “Chapter 5 - Camera-based blood oxygen measurement,” in *Contactless Vital Signs Monitoring*, W. Wang and X. Wang, Eds., Academic Press, 2022, pp. 99–116. doi: 10.1016/B978-0-12-822281-2.00013-5.
[211] J. C. Ramella-Roman and J. M. Hidler, “The impact of autonomic dysreflexia on blood flow and skin response in individuals with spinal cord injury,” *Adv. Opt. Technol.*, p. 797214, 2008, doi: 10.1155/2008/797214.
[212] I. Fredriksson, M. Larsson, and T. Strömberg, “Measurement depth and volume in laser Doppler flowmetry,” *Microvasc. Res.*, vol. 78, no. 1, pp. 4–13, Jun. 2009, doi: 10.1016/j.mvr.2009.02.008.
[213] V. Dremin, N. Golubova, E. Potapova, and A. Dunaev, “Influence of Melanin Content on Laser Doppler Flowmetry and Tissue Reflectance Oximetry Signal Formation,” *J. Biomed. Photonics Eng.*, vol. 7, no. 4, Art. no. 4, Nov. 2021, doi: 10.18287/JBPE21.07.040306.
[214] J. M. Burns, W. Jia, J. S. Nelson, B. Majaron, and B. Anvari, “Photothermal treatment of port-wine stains using erythrocyte-derived particles doped with indocyanine green: a theoretical study,” *J. Biomed. Opt.*, vol. 23, no. 12, p. 121616, Dec. 2018, doi: 10.1117/1.JBO.23.12.121616.
[215] D. Yudovsky, J. Q. M. Nguyen, and A. J. Durkin, “In vivo spatial frequency domain spectroscopy of two layer media,” *J. Biomed. Opt.*, vol. 17, no. 10, p. 107006, Oct. 2012, doi: 10.1117/1.JBO.17.10.107006.
[216] M. Larsson, M. Ewerlöf, E. G. Salerud, T. Strömberg, and I. Fredriksson, “Artificial neural networks trained on simulated multispectral data for real-time imaging of skin microcirculatory blood oxygen saturation,” *J. Biomed. Opt.*, vol. 29, no. Suppl 3, p. S33304, Jun. 2024, doi: 10.1117/1.JBO.29.S3.S33304.
[217] B. K. Harrison-Smith, M. S. Arefin, A. Dumont, and C. Patil, “Reducing racial bias in transcutaneous measurements with mobile phone camera based spatially resolved diffuse reflectance,” in *Optical Interactions with Tissue and Cells XXXIII; and Advanced Photonics in Urology*, SPIE, Mar. 2022, pp. 16–21. doi: 10.1117/12.2610519.
[218] C. Li, V. Brost, Y. Benezeth, F. Marzani, and F. Yang, “Design and evaluation of a parallel and optimized light–tissue interaction-based method for fast skin lesion assessment,” *J. Real-Time Image Process.*, vol. 15, no. 2, pp. 407–420, Aug. 2018, doi: 10.1007/s11554-015-0494-6.
[219] F. H. Mustafa, P. W. Jones, and A. L. McEwan, “Near infrared spectroscopy for body fat sensing in neonates: quantitative analysis by GAMOS simulations,” *Biomed. Eng. OnLine*, vol. 16, no. 1, p. 14, Jan. 2017, doi: 10.1186/s12938-016-0310-y.
[220] V. Colas, W. Blondel, G. Khairallah, C. Daul, and M. Amouroux, “Proposal for a Skin Layer-Wise Decomposition Model of Spatially-Resolved Diffuse Reflectance Spectra Based on Maximum Depth Photon Distributions: A Numerical Study,” *Photonics*, vol. 8, no. 10, Art. no. 10, Oct. 2021, doi: 10.3390/photonics8100444.
[221] J. Huang, S. Zhang, S. Gnyawali, C. K. Sen, and R. X. Xu, “Second derivative multispectral algorithm for quantitative assessment of cutaneous tissue oxygenation,” *J. Biomed. Opt.*, vol. 20, no. 3, p. 036001, Mar. 2015, doi: 10.1117/1.JBO.20.3.036001.
[222] L. Hernández-Quintanar, D. A. Fabila-Bustos, M. Hernández-Chávez, A. Valor, J. M. de la Rosa, and S. Stolik, “Fiber-optic pulseoximeter for local oxygen saturation determination using a Monte Carlo multi-layer model for calibration,” *Comput. Methods Programs Biomed.*, vol. 187, p. 105237, Apr. 2020, doi: 10.1016/j.cmpb.2019.105237.
[223] M. Bolic, “Simulating the Effects of Melanin and Air Gap Depth on the Accuracy of Reflectance Pulse Oximeters:,” in *Proceedings of the 16th International Joint Conference on Biomedical Engineering Systems and Technologies*, Lisbon, Portugal: SCITEPRESS - Science and Technology Publications, 2023, pp. 64–71. doi: 10.5220/0011749300003414.
[224] P. Naglič, L. Vidovič, M. Milanič, L. L. Randeberg, and B. Majaron, “Suitability of diffusion approximation for an inverse analysis of diffuse reflectance spectra from human skin in vivo,” *OSA Contin.*, vol. 2, no. 3, pp. 905–922, Mar. 2019, doi: 10.1364/OSAC.2.000905.

[225] X. U. Zhang, P. van der Zee, I. Atzeni, D. J. Faber, T. G. van Leeuwen, and H. J. C. M. Sterenborg, "Multidiameter single-fiber reflectance spectroscopy of heavily pigmented skin: modeling the inhomogeneous distribution of melanin," *J. Biomed. Opt.*, vol. 24, no. 12, p. 127001, Dec. 2019, doi: 10.1117/1.JBO.24.12.127001.
[226] H. Van Lankveld, A. Q. Mai, L. Lim, N. Hosseinkhah, P. Cassano, and J. Jean Chen, "Simulation-based dosimetry of transcranial and intranasal photobiomodulation of the human brain: the roles of wavelength, power density and skin colour," Apr. 2024, doi: 10.1101/2024.04.05.588330.
[227] H. Hou, G. Du, Y. Wang, C. Su, L. Guo, and X. Chen, "Noninvasive in vivo study of NADH fluorescence and its real-time intrinsic dynamical changes: Experiments and seven-layered skin model Monte Carlo simulations," *J. Innov. Opt. Health Sci.*, vol. 15, no. 03, p. 2230006, May 2022, doi: 10.1142/S1793545822300063.
[228] T. Okamoto, T. Kumagawa, M. Motoda, T. Igarashi, and K. Nakao, "Monte Carlo simulation of light reflection from cosmetic powder particles near the human skin surface," *J. Biomed. Opt.*, vol. 18, no. 6, p. 61232, Jun. 2013, doi: 10.1117/1.JBO.18.6.061232.
[229] M. S. Arefin, A. P. Dumont, and C. A. Patil, "Monte Carlo based simulations of racial bias in pulse oximetry," in *Design and Quality for Biomedical Technologies XV*, SPIE, Mar. 2022, pp. 8–12. doi: 10.1117/12.2610483.
[230] S. K. Narayana Swamy, C. Liu, R. Correia, B. R. Hayes-Gill, and S. P. Morgan, "Exploring the bias: how skin color influences oxygen saturation readings via Monte Carlo simulations," *J. Biomed. Opt.*, vol. 29, no. Suppl 3, p. S33308, Jun. 2024, doi: 10.1117/1.JBO.29.S3.S33308.
[231] M. Keller, B. Harrison-Smith, C. Patil, and M. Arefin, "Skin colour affects the accuracy of medical oxygen sensors," *Nature*, vol. 610, pp. 449–451, Oct. 2022, doi: 10.1038/d41586-022-03161-1.
[232] C. R. Malskies, E. Eibenberger, and E. Angelopoulou, *The Recognition of Ethnic Groups based on Histological Skin Properties*. The Eurographics Association, 2011. Accessed: Feb. 23, 2025. [Online]. Available: https://doi.org/10.2312/PE/VMV/VMV11/353-360
[233] Albany Cosmetic And Laser Center and K. Alhallak, "Skin, Light and their Interactions, an In-Depth Review for Modern Light-Based Skin Therapies," *Clin. Dermatol. Ther.*, vol. 7, no. 2, pp. 1–15, Sep. 2021, doi: 10.24966/CDT-8771/100081.
[234] L. Wang, S. L. Jacques, and L. Zheng, "MCML—Monte Carlo modeling of light transport in multi-layered tissues," *Comput. Methods Programs Biomed.*, vol. 47, no. 2, pp. 131–146, Jul. 1995, doi: 10.1016/0169-2607(95)01640-F.
[235] S. L. Jacques, "Monte Carlo Modeling of Light Transport in Tissue (Steady State and Time of Flight)," in *Optical-Thermal Response of Laser-Irradiated Tissue*, A. J. Welch and M. J. C. van Gemert, Eds., Dordrecht: Springer Netherlands, 2011, pp. 109–144. doi: 10.1007/978-90-481-8831-4_5.
[236] E.D. Cashwell and C.J.Everett, *A Practical Manual on the Monte Carlo Method for Random Walk Problems*. 1959. Accessed: Dec. 13, 2024. [Online]. Available: http://archive.org/details/a_practical_manual_on_the_Monte_Carlo_Method_for_Random_Walk_Problems
[237] B. Lapeyre, É. Pardoux, and R. Sentis, "The Monte-Carlo method for the transport equations," in *Introduction to Monte-Carlo Methods for Transport and Diffusion Equations*, B. Lapeyre, É. Pardoux, and R. Sentis, Eds., Oxford University Press, 2003, p. 0. doi: 10.1093/oso/9780198525929.003.0003.
[238] T. G. Mayerhöfer, S. Pahlow, and J. Popp, "The Bouguer-Beer-Lambert Law: Shining Light on the Obscure," *ChemPhysChem*, vol. 21, no. 18, pp. 2029–2046, 2020, doi: 10.1002/cphc.202000464.
[239] J. P. Phillips, P. A. Kyriacou, and D. P. Jones, "Calculation of photon path changes due to scatter in Monte Carlo simulations," *Annu. Int. Conf. IEEE Eng. Med. Biol. Soc. IEEE Eng. Med. Biol. Soc. Annu. Int. Conf.*, vol. 2010, pp. 4959–4962, 2010, doi: 10.1109/IEMBS.2010.5627216.

[240] Z. Wang, L. Wang, Y. T. Zhang, and X. D. Chen, “Monte Carlo simulation of light propagation in human tissue models,” in *Proceedings - The 3rd International Conference on Bioinformatics and Biomedical Engineering (iCBBE 2009)*, Institute of Electrical and Electronics Engineers, Inc., Jun. 2009, p. 5163086. doi: 10.1109/ICBBE.2009.5163086.
[241] A. A. A. Halim, M. H. Laili, and M. Rusop, “Analysis of light absorption with variation of epidermis thickness in human skin model using Monte Carlo simulation,” *AIP Conf. Proc.*, vol. 2151, no. 1, p. 020008, Aug. 2019, doi: 10.1063/1.5124638.
[242] I. Matveeva and O. Myakinin, “Monte Carlo modelling of normal skin and skin cancer Raman spectra,” *J. Phys. Conf. Ser.*, vol. 1368, no. 4, p. 042084, Nov. 2019, doi: 10.1088/1742-6596/1368/4/042084.
[243] S. Wang, J. Zhao, H. Lui, Q. He, J. Bai, and H. Zeng, “Monte Carlo simulation of in vivo Raman spectral measurements of human skin with a multi-layered tissue optical model,” *J. Biophotonics*, vol. 7, no. 9, pp. 703–712, Sep. 2014, doi: 10.1002/jbio.201300045.
[244] A. Doronin and I. Meglinski, “Online Monte Carlo based calculator of human skin spectra and color,” *Prog. Biomed. Opt. Imaging - Proc. SPIE*, vol. 8337, p. 1, Oct. 2011, doi: 10.1117/12.923732.
[245] T. Boonya-Ananta *et al.*, “Synthetic photoplethysmography (PPG) of the radial artery through parallelized Monte Carlo and its correlation to body mass index (BMI),” *Sci. Rep.*, vol. 11, no. 1, p. 2570, Jan. 2021, doi: 10.1038/s41598-021-82124-4.
[246] J. Phillips, “Calculation of photon path changes due to scatter in Monte Carlo simulations,” *Conf. Proc. Annu. Int. Conf. IEEE Eng. Med. Biol. Soc. IEEE Eng. Med. Biol. Soc. Annu. Conf.*, Jan. 2010, Accessed: Dec. 04, 2024. [Online]. Available: https://www.academia.edu/79263527/Calculation_of_photon_path_changes_due_to_scatter_in_Monte_Carlo_simulations
[247] M. Elgendi *et al.*, “The use of photoplethysmography for assessing hypertension,” *Npj Digit. Med.*, vol. 2, no. 1, pp. 1–11, Jun. 2019, doi: 10.1038/s41746-019-0136-7.
[248] Y. Khan, C. Lochner, A. Pierre, and A. Arias, “System Design for Organic Pulse Oximeter,” Aug. 2015. doi: 10.1109/IWASI.2015.7184975.
[249] V. G. Kanellis, “A review of melanin sensor devices,” *Biophys. Rev.*, vol. 11, no. 6, pp. 843–849, Dec. 2019, doi: 10.1007/s12551-019-00581-8.
[250] A. Doronin, I. Fine, and I. Meglinski, “Assessment of the calibration curve for transmittance pulse-oximetry,” *Laser Phys.*, vol. 21, no. 11, pp. 1972–1977, Nov. 2011, doi: 10.1134/S1054660X11190078.
[251] J. L. Reuss and D. Siker, “The pulse in reflectance pulse oximetry: modeling and experimental studies,” *J. Clin. Monit. Comput.*, vol. 18, no. 4, pp. 289–299, Aug. 2004, doi: 10.1007/s10877-005-2909-6.
[252] J. M. Schmitt, G. X. Zhou, E. C. Walker, and R. T. Wall, “Multilayer model of photon diffusion in skin,” *J. Opt. Soc. Am. A*, vol. 7, no. 11, pp. 2141–2153, Nov. 1990, doi: 10.1364/josaa.7.002141.
[253] J. Fine *et al.*, “Sources of Inaccuracy in Photoplethysmography for Continuous Cardiovascular Monitoring,” *Biosensors*, vol. 11, no. 4, p. 126, Apr. 2021, doi: 10.3390/bios11040126.
[254] M. Hickey, J. P. Phillips, and P. A. Kyriacou, “Venous pooling and drainage affects photoplethysmographic signals at different vertical hand positions,” *Opt. Diagn. Sens. XV Point--Care Diagn.*, vol. 9332, Jan. 2015, doi: 10.1117/12.2076732.
[255] M. Nitzan and H. Taitelbaum, “The measurement of oxygen saturation in arterial and venous blood,” *IEEE Instrum. Meas. Mag.*, vol. 11, no. 3, pp. 9–15, Jun. 2008, doi: 10.1109/MIM.2008.4534373.
[256] S. V. Patwardhan, A. P. Dhawan, and P. A. Relue, “Monte Carlo simulation of light-tissue interaction: three-dimensional simulation for trans-illumination-based imaging of skin lesions,” *IEEE Trans. Biomed. Eng.*, vol. 52, no. 7, pp. 1227–1236, Jul. 2005, doi: 10.1109/TBME.2005.847546.

[257] G. I. Petrov, A. Doronin, H. T. Whelan, I. Meglinski, and V. V. Yakovlev, “Human tissue color as viewed in high dynamic range optical spectral transmission measurements,” *Biomed. Opt. Express*, vol. 3, no. 9, p. 2154, Sep. 2012, doi: 10.1364/BOE.3.002154.
[258] R. Simpson, J. Laufer, M. Kohl, M. Essenpreis, and M. Cope, “Near-infrared optical properties of ex-vivo human skin and subcutaneous tissues using reflectance and transmittance measurements,” *Proc SPIE*, vol. 2979, pp. 307–313, Aug. 1997, doi: 10.1117/12.280259.
[259] A. Bashkatov, E. Genina, and V. Tuchin, “Optical properties of skin, subcutaneous, and muscle tissues: A review,” *J. Innov. Opt. Health Sci.*, vol. 04, Jan. 2011, doi: 10.1142/S1793545811001319.
[260] M. Firbank, M. Hiraoka, M. Essenpreis, and D. T. Delpy, “Measurement of the optical properties of the skull in the wavelength range 650-950 nm,” *Phys. Med. Biol.*, vol. 38, no. 4, p. 503, Apr. 1993, doi: 10.1088/0031-9155/38/4/002.
[261] N. Bosschaart, G. J. Edelman, M. C. G. Aalders, T. G. van Leeuwen, and D. J. Faber, “A literature review and novel theoretical approach on the optical properties of whole blood,” *Lasers Med. Sci.*, vol. 29, no. 2, pp. 453–479, 2014, doi: 10.1007/s10103-013-1446-7.
[262] G. M. Hale and M. R. Querry, “Optical Constants of Water in the 200-nm to 200-µm Wavelength Region,” *Appl. Opt.*, vol. 12, no. 3, pp. 555–563, Mar. 1973, doi: 10.1364/AO.12.000555.
[263] M. Hickey, “Optimal spacing between transmitting and receiving optical fibres in reflectance pulse oximetry,” presented at the Journal of Physics: Conference Series, Nov. 2007, p. 012030. doi: 10.1088/1742-6596/85/1/012030.
[264] A. M. Cabanas, M. Fuentes-Guajardo, K. Latorre, D. León, and P. Martín-Escudero, “Skin Pigmentation Influence on Pulse Oximetry Accuracy: A Systematic Review and Bibliometric Analysis,” *Sensors*, vol. 22, no. 9, p. 3402, Apr. 2022, doi: 10.3390/s22093402.
[265] Nonin, “The Effects of Skin Pigmentation and Low Saturation in Oximetry.” Accessed: Feb. 26, 2025. [Online]. Available: https://www.nonin.com/resource/effects-of-skin-pigmentation-in-oximetry/
[266] V. Sharma, S. J. Barker, R. Sorci, L. Park, and W. C. Wilson, “Racial effects on masimo pulse oximetry: impact of low perfusion index,” *J. Clin. Monit. Comput.*, Jan. 2024, doi: 10.1007/s10877-023-01113-2.
[267] M. S. Rea and A. Bierman, “Light source spectra are the likely cause of systematic bias in pulse oximeter readings for individuals with darker skin pigmentation,” *Br. J. Anaesth.*, vol. 131, no. 4, pp. e101–e103, Oct. 2023, doi: 10.1016/j.bja.2023.04.018.
[268] A. M. Cabanas, P. Martín-Escudero, and K. H. Shelley, “Improving pulse oximetry accuracy in dark-skinned patients: technical aspects and current regulations,” *Br. J. Anaesth.*, vol. 131, no. 4, pp. 640–644, Oct. 2023, doi: 10.1016/j.bja.2023.07.005.
[269] M. Moradi, S. Vasudevan, A. Bhusal, S. Weininger, Y. Chen, and J. Pfefer, “Modeling light-tissue interactions in pulse oximetry: effect of device design and skin pigmentation,” in *Design and Quality for Biomedical Technologies XVII*, SPIE, Mar. 2024, p. 1283302. doi: 10.1117/12.3004189.
[270] H. H. and J. L. and X. Chen, “The effect of Skin Melanin Concentration on Wrist Reflectance Photoplethysmography based on Monte Carlo Simulation | EndNote Click.” Accessed: May 30, 2024. [Online]. Available: https://click.endnote.com/viewer?doi=10.1109%2Fcisp-bmei56279.2022.9979897&token=WzMxMDQxMDQsIjEwLjExMDkvY2lzcC1ibWVpNTYyNzkuMjAyMi45OTc5ODk3Il0.O8tQ0uOC58XV9rez9x1C6dNrl1s
[271] M. Moradi, S. Vasudevan, A. Bhusal, S. Weininger, Y. Chen, and J. Pfefer, “Modeling light-tissue interactions in pulse oximetry: effect of device design and skin pigmentation,” in *Design and Quality for Biomedical Technologies XVII*, SPIE, Mar. 2024, p. 1283302. doi: 10.1117/12.3004189.
[272] J. Rafl, T. E. Bachman, V. Rafl-Huttova, S. Walzel, and M. Rozanek, “Commercial smartwatch with pulse oximeter detects short-time hypoxemia as well as standard medical-grade device:

Validation study," *Digit. Health*, vol. 8, p. 20552076221132127, 2022, doi: 10.1177/20552076221132127.
[273] L. Piwek, D. A. Ellis, S. Andrews, and A. Joinson, "The Rise of Consumer Health Wearables: Promises and Barriers," *PLOS Med.*, vol. 13, no. 2, p. e1001953, Feb. 2016, doi: 10.1371/journal.pmed.1001953.
[274] K. Guk *et al.*, "Evolution of Wearable Devices with Real-Time Disease Monitoring for Personalized Healthcare," *Nanomaterials*, vol. 9, no. 6, p. 813, May 2019, doi: 10.3390/nano9060813.
[275] C. Akitegetse, P. Landry, J. Robidoux, N. Lapointe, D. Brouard, and D. Sauvageau, "Monte-Carlo simulation and tissue-phantom model for validation of ocular oximetry," *Biomed. Opt. Express*, vol. 13, no. 5, pp. 2929–2946, Apr. 2022, doi: 10.1364/BOE.458079.
[276] A. Schmocker, A. Khoushabi, C. Schizas, P.-E. Bourban, D. Pioletti, and C. Moser, "Photopolymerizable hydrogels for implants: Monte-Carlo modeling and experimental in vitro validation," *J. Biomed. Opt.*, vol. 19, no. 3, p. 035004, Mar. 2014, doi: 10.1117/1.JBO.19.3.035004.
[277] S. Lisenko and M. Kugeiko, "Determination of Constituent Composition of Hemoglobin and Structural/Morphological Parameters of Skin Based on Approximating Functions for Radiation Fluxes Backscattered from Skin," *J. Appl. Spectrosc.*, vol. 81, pp. 442–449, Jul. 2014, doi: 10.1007/s10812-014-9952-3.
[278] J. M. May, M. Nomoni, K. Budidha, C. Choi, and P. A. Kyriacou, "Mechanical Testing of Artificial Vessels and Tissues for Photoplethysmography Phantoms," *Annu. Int. Conf. IEEE Eng. Med. Biol. Soc. IEEE Eng. Med. Biol. Soc. Annu. Int. Conf.*, vol. 2022, pp. 629–632, Jul. 2022, doi: 10.1109/EMBC48229.2022.9871830.
[279] H. H. and J. L. and X. Chen, "The effect of Skin Melanin Concentration on Wrist Reflectance Photoplethysmography based on Monte Carlo Simulation | EndNote Click." Accessed: Nov. 28, 2024. [Online]. Available: https://click.endnote.com/viewer?doi=10.1109%2Fcisp-bmei56279.2022.9979897&token=WzMxMDQxMDQsIjEwLjExMDkvY2lzcC1ibWVpNTYyNzkuMjAyMi45OTc5ODk3Il0.O8tQ0uOC58XV9rez9x1C6dNrl1s
[280] S. A. Prahl, M. J. C. Van Gemert, and A. J. Welch, "Determining the optical properties of turbid media by using the adding–doubling method," *Appl. Opt.*, vol. 32, no. 4, p. 559, Feb. 1993, doi: 10.1364/AO.32.000559.
[281] B. Ly, E. Dyer, J. Feig, A. Chien, and S. Bino, "Research Techniques Made Simple: Cutaneous Colorimetry: A Reliable Technique for Objective Skin Color Measurement," *J. Invest. Dermatol.*, vol. 140, pp. 3-12.e1, Jan. 2020, doi: 10.1016/j.jid.2019.11.003.
[282] A. Patil, J. Safaie, H. Moghaddam, F. Wallois, and R. Grebe, "Experimental investigation of NIRS spatial sensitivity," *Biomed. Opt. Express*, vol. 2, pp. 1478–93, Jun. 2011, doi: 10.1364/BOE.2.001478.
[283] "Equity in medical devices: independent review - final report," GOV.UK. Accessed: Mar. 13, 2024. [Online]. Available: https://www.gov.uk/government/publications/equity-in-medical-devices-independent-review-final-report
[284] H. Jung *et al.*, "Performance evaluation of a wrist-worn reflectance pulse oximeter during sleep," *Sleep Health*, vol. 8, no. 5, pp. 420–428, Oct. 2022, doi: 10.1016/j.sleh.2022.04.003.
[285] Y. Yan, C. C. Poon, and Y. Zhang, "Reduction of motion artifact in pulse oximetry by smoothed pseudo Wigner-Ville distribution," *J. NeuroEngineering Rehabil.*, vol. 2, no. 1, p. 3, Mar. 2005, doi: 10.1186/1743-0003-2-3.
[286] M. Raghuram, S. Kosaraju, and K. Reddy, "Reduction of motion artifacts from Pulse oximeter's PPG signals using MSICA," Dec. 2016, pp. 491–494. doi: 10.1109/ICCICCT.2016.7988000.
[287] J. Lee, W. Jung, I. Kang, Y. Kim, and G. Lee, "Design of filter to reject motion artifact of pulse oximetry," *Comput. Stand. Interfaces*, vol. 26, no. 3, pp. 241–249, May 2004, doi: 10.1016/S0920-5489(03)00077-1.

[288] S. Sun *et al.*, “Finger and forehead photoplethysmography-derived pulse-pressure variation and the benefits of baseline correction,” *J. Clin. Monit. Comput.*, vol. 33, pp. 65–75, Feb. 2019, doi: 10.1007/s10877-018-0140-5.

[289] G. Strangman, M. A. Franceschini, and D. A. Boas, “Factors affecting the accuracy of near-infrared spectroscopy concentration calculations for focal changes in oxygenation parameters,” *NeuroImage*, vol. 18, no. 4, pp. 865–879, Apr. 2003, doi: 10.1016/S1053-8119(03)00021-1.